# Neutrino mass analysis and systematics of the KATRIN experiment, using CMKAT

by

Larisa A. Thorne

Submitted in partial fulfillment of the
requirements for the degree of
Doctor of Philosophy
at
Carnegie Mellon University
Department of Physics
Pittsburgh, Pennsylvania

Advised by Professors Gregg Franklin & Diana Parno

June 29, 2021

**Abstract**

The Karlsruhe Tritium Neutrino (KATRIN) experiment aims to make a precision measurement of the effective neutrino mass by leveraging the kinematics of tritium beta decay, with a 3-year sensitivity of 0.2eV (90% C.L.). Recent run campaigns, both in standard mode (using molecular tritium) and calibration mode (using $^{83m}$Kr ), have provided a wealth of data. This data was analyzed using the CMKAT analysis framework, which models the integrated spectra using a convolution of the source decay physics and the experiment's response function. Additional information relating to construction and validation of CMKAT is included. Finally, results from fits to the second neutrino mass measurement campaign (KNM2) are presented, and confidence intervals on the extracted effective neutrino mass are constructed; selected systematic studies are included.

# Acknowledgments

There are a fair number of people who've played a significant role in helping me get where I am today. In the interest of keeping my thanks down to a manageable size, let brevity be the order of the day. I would like to express my deepest gratitude to:

**Family:** My parents, grandparents, and extended family in the US and Germany. I'd like to say that my Grandpop had no influence in making me a physicist ("I'd be proud of you no matter what you choose to do"), but he is a wonderful role model. Regine, Bret, Grandpop, Linda, Carloee, Kares, Tamara, Eckhard+, Annika.

**Mentors:** My principle advisors, Gregg Franklin and Diana Parno. I was really fortunate to be stuck with such great advisors. When I made the difficult switch from Jefferson Lab physics to neutrino physics, Gregg came with me to join Diana's newly-formed group. Gregg and Diana are supportive, extremely knowledgeable, and not afraid to call me out if needed. I'd also like to thank my first physics teacher, Takashi Nakajima, for starting me down this road.

**Friends:** For providing balance and support in my life. Michael, Dacen, Aklant, Andresa, Ruairí, Matt, Sam, Alejandro, Amy, Deva, Markus, Teo, Malavika, Tassia+, Michael, Broto+, Jannik, Bartosz, Jason, Ryan, John, Derek, Joule, Knut+Tarja, Tartan Salsa.

**Colleagues:** It doesn't seem fair to put this as a separate category from friends, as most of my colleagues became my friends. Nonetheless, they also supported the academic facet of my graduate career, in a mutually beneficial way. Ana Paula, Juan Carlos, Naomi, Eric, Will, Mike, Alexa, Brian, Wonqook, Jan, all the Florians, Thomas, Beate+Lutz, Peter, Woo Jeong, Julian, all the Alexanders, Magnus, Björn, Dominik, Leo, Anton, Moritz, Raphael, all the Martins, Kathrin, Brazilian Summer School December 2019.

**Coffee:** The ambrosia of (thesis) life.

Thank you, all.

# Contents

# List of Figures

# List of Tables

# Chapter 1

# Introduction

## 1.1 Neutrino mass history and physics motivation

Some decades ago, in an attempt to rescue conservation of energy in beta decay processes, Wolfgang Pauli proposed the existence of the neutrino as the mysterious third party in the beta decay process. Beta decay is a weak decay process in which a neutron was then understood to convert into a proton and an electron[1], where the outgoing electron is the beta particle which gives the process its name. Before Pauli made his proposal in 1930, it had long been assumed that beta decay was just another two-body decay, because at the time it was discovered[1], the other two similar kinds of decay (alpha decay[1] and gamma decay[2]) were two-body decays. Their respective decay particles, the alpha particle and the gamma particle, carried away energies equal to the difference between final and initial nuclear states, and so had very narrow energy distributions. But upon measuring the energy spectrum of the beta particles, it became clear that something else was going on: the beta particles instead had a continuous energy spectrum[3]. This behavior would contradict conservation of energy for two-body decay, but could be explained with a three-body decay, as proposed by Pauli.

It wasn't until 26 years later that the first experimental evidence of Pauli's proposed (anti-electron) neutrino was seen by the Cowan-Reines experiment[4]. Physicists at the time were discovering additional members of the lepton family, so other experiments jumped into detection of neutrinos associated with the other leptons

[1]This statement reflects the state of 1930s knowledge, but today we know that beta decay converts a neutron into a proton and an electron, plus an anti-electron neutrino. Beta decay can also convert a proton into a neutron and a positron, plus an electron neutrino. The former type beta decay (neutron to proton and electron) will be the focus of this work.

(muon and eventually tau), leading to the discovery of the muon neutrino in 1962 at Brookhaven National Lab[5] and the tau neutrino in 2000 at the Stanford Linear Accelerator[6]. This expanded the lepton family to six members (the original electron, muon, and tau, and three corresponding "flavors" of neutrinos), which allowed for lepton flavor conservation in weak interactions.

But the elation of the electron neutrino discovery by Cowan-Reines was soon tempered by the results of the Homestake experiment[7] in the late 1960s, which brought to light what is now known as the solar neutrino problem: a deficit in the measurement of electron neutrinos compared to theoretical predictions[8]. Though it would be nearly another 40 years until a solution was found, the resulting explanation had a profound impact on the neutrino community: neutrinos undergo flavor oscillation[2]. And whereas it had always been believed that neutrinos were massless, this oscillation discovery meant that neutrinos had mass[11, 12]. The Standard Model of particle physics (SM) does not explicitly predict them to be massless, but the neutrinos' masses are sufficiently small compared to the fundamental fermions to be excluded from the minimal SM[13, 14].

### 1.1.1 Neutrino physics and properties

Neutrino flavor oscillation is a phenomenon in which a neutrino created initially in a lepton flavor eigenstate $l$ can be measured later in a different lepton flavor eigenstate $l'$, with a probability amplitude $P_{ll'}$. The oscillation arises due to the fact that neutrinos are created (and absorbed) in weak interactions in the lepton flavor eigenstate, but propagate in the mass eigenstate. There are three lepton flavor eigenstates, corresponding to the three charged lepton partners in weak interactions: electron, muon, and tau. Each lepton flavor eigenstate $\{\nu_e, \nu_\mu, \nu_\tau\}$ is a different superposition of mass eigenstates $\{\nu_1, \nu_2, \nu_3\}$, governed by the PMNS mixing matrix, $U$, in the following way:

$$\begin{bmatrix} \nu_e \\ \nu_\mu \\ \nu_\tau \end{bmatrix} = \begin{bmatrix} U_{e,i} & U_{e,2} & U_{e,3} \\ U_{\mu,i} & U_{\mu,2} & U_{\mu,3} \\ U_{\tau,i} & U_{\tau,2} & U_{\tau,3} \end{bmatrix} \begin{bmatrix} \nu_1 \\ \nu_2 \\ \nu_3 \end{bmatrix} \tag{1.1}$$

Where the PMNS mixing matrix, $U$, is parameterized like so[15]:

[2] Additionally, high-energy neutrinos propagating through high electron-density regions like the interior of the Sun undergo the Mikheyev–Smirnov–Wolfenstein (MSW) effect[9, 10] which accounts for their oscillation through matter.

$$U = \begin{pmatrix} c_{12}c_{13} & s_{12}c_{13} & s_{13}e^{-i\delta_{CP}} \\ -s_{12}c_{23} - c_{12}s_{13}s_{23}e^{i\delta_{CP}} & c_{12}c_{23} - s_{12}s_{13}s_{23}e^{i\delta_{CP}} & c_{13}s_{23} \\ s_{12}s_{23} - c_{12}s_{13}c_{23}e^{i\delta_{CP}} & -c_{12}s_{23} - s_{12}s_{13}c_{23}e^{i\delta_{CP}} & c_{13}c_{23} \end{pmatrix} P \quad (1.2)$$

Where $c_{ij} = \cos\theta_{ij}$ and $s_{ij} = \sin\theta_{ij}$. The $\theta_{ij}$ parameters are mixing angles between two mass eigenstates $i$ and $j$. The $\delta_{CP}$ is a phase factor describing the degree to which neutrino oscillation violates CP symmetry. The matrix $P$ depends on whether the neutrino is type Dirac or type Majorana. If Dirac, then $P$ is the identity matrix $\mathbf{1}$. If Majorana, then $P$ is a diagonal matrix which is parametrized by two Majorana phase factors. The form of $P$ in the Majorana case does not follow any particular standardized convention, so varies across the literature[15]. Regardless, $P$ does not enter into calculations of oscillation probabilities; it only plays a role in hypothesized lepton number violating processes, like neutrinoless double beta decay. Majorana and Dirac neutrino properties are discussed further in later sections. The PMNS matrix elements are determined by the $\theta_{ij}$ and $\delta_{CP}$ values from experiment. All of these mixing angles have been measured, and are listed in Section 1.1.3.

Different mass eigenstates propagate with different frequencies, and because the flavor eigenstates are combinations of mass eigenstates, there is interference. This shows up in the calculation of the probability amplitude $P_{ll'}$. The probabilities have phases which are proportional to $(\frac{\Delta m^2_{ij} L}{E})$, where $L$ is the distance between the points of neutrino creation and observation, $E$ is the neutrino energy, and $\Delta m^2_{ij}$ is the mass splitting between two mass eigenstates $i$ and $j$. The mass splitting $\Delta m^2_{ij}$ is defined as:

$$\Delta m^2_{ij} = m^2_i - m^2_j \quad (1.3)$$

By careful tuning of $L$ and $E$, an experiment can be built near a constructive interference region to observe a neutrino flavor change (given a particular mass splitting, which are now known from oscillation experiments and listed in Section 1.1.3).

A schematic of the relative contributions of the lepton flavor eigenstates per given mass state is shown in Figure 1.1, where the fractions can be calculated from Equation 1.1. When organizing the neutrino masses $m_i$ from smallest to largest, there are two possible kinds of orderings (described in more detail later in this section).

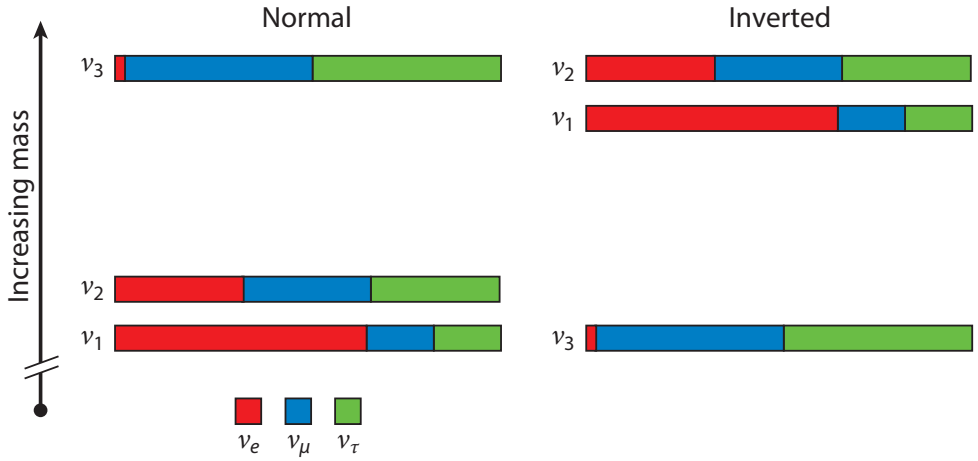


Figure 1.1: Mass eigenstate composition per lepton flavor eigenstate, for normal and inverted mass orderings. The two mass ordering options are discussed in more detail below. Adapted from [16].

At this point, it is important to note that while neutrino oscillation implies that neutrinos have mass, the only mass-related observables accessible to oscillation experiments are the mass splittings $\Delta m^2_{ij}$ as defined in Equation 1.3. The mass splittings contain no information about the absolute mass scale, in the sense that there is no information about the offset of the lightest neutrino mass from zero. Clearly another approach is needed to glean information on the absolute mass scale.

There are a few ways to get at the absolute neutrino mass scale, which are covered in more detail in Section 1.1.4. Since they can only be created and absorbed in the flavor eigenstate, neutrino mass experiments can't get at the $m_i$ directly. Instead, they can measure an effective neutrino mass $m_{\nu,eff}$, which is the incoherent weighted sum of the mass eigenstates. The example given below is for an experiment which measures electron-flavor neutrinos:

$$m^2_{\nu,eff} = \sum_{i=1}^{3} |U_{e,i}|^2 m_i^2 \tag{1.4}$$

The $m^2_{\nu,eff}$ term (for brevity later referred to as $m^2_\nu$) is the value extracted from neutrino mass experiments which use supernova time-of-flight (Section 1.1.4.2) and single beta decay (Section 1.1.4.4). If neutrinoless double beta decay is observed,

then the neutrino is of type Majorana, with a Majorana mass $m_{\beta\beta}$ defined as:

$$m_{\beta\beta} = \left| \sum_{i=1}^{3} |U_{e,i}|^2 m_i e^{i\alpha_i} \right| \tag{1.5}$$

Where $\alpha_i$ are linear combinations of the three CP-violating neutrino phases ($\delta_{CP}$ and two Majorana phases). The $m_\nu$ and $m_{\beta\beta}$ are the mass observables for laboratory experiment sensitive to the neutrino mass scale.

Massive neutrinos' interesting properties extend beyond the neutrino oscillation parameters and the absolute mass scale. Some other interesting and still unanswered questions surround neutrinos' type (Majorana versus Dirac), mass ordering (normal versus inverted) and whether more types of neutrinos exist (like sterile neutrinos).

The neutrino's Majorana or Dirac nature is decided by the relationship between the neutrino and its anti-particle partner, the anti-neutrino. If the neutrino is Majorana, the neutrino and anti-neutrino are treated as the same object. If the neutrino is Dirac, they are treated as different objects. An interesting property of the Dirac neutrino is that it would require lepton number conservation. Currently the only experimental means to conclusively determine the neutrino type is through searches for neutrinoless double beta decay.

Neutrino mass ordering (also called neutrino mass hierarchy) is another important feature related to mass. While results from neutrino oscillation experiments can provide some information, it's not enough to conclusively set the mass ordering. Given that the $m_1, m_2$ mass splitting ($\Delta m^2_{12}$) is the smallest mass splitting, and defining $m_1$ to be the smaller mass eigenstate of the two, Equation 1.3 is used to conclude that $\Delta m^2_{21} > 0$. However, there is no good information on the sign of the mass splitting between $m_2$ and $m_3$ ($\Delta m^2_{23}$). Because of this uncertainty in the sign of $\Delta m^2_{23}$, it's not clear how to order the mass eigenstates in terms of increasing mass. The two ordering possibilities are illustrated in Figure 1.1: in the normal ordering, the mass eigenstates are $m_1 < m_2 < m_3$. In the inverted ordering, the mass eigenstates are $m_3 < m_1 < m_2$. Current experimental evidence slightly favors the normal ordering [17].

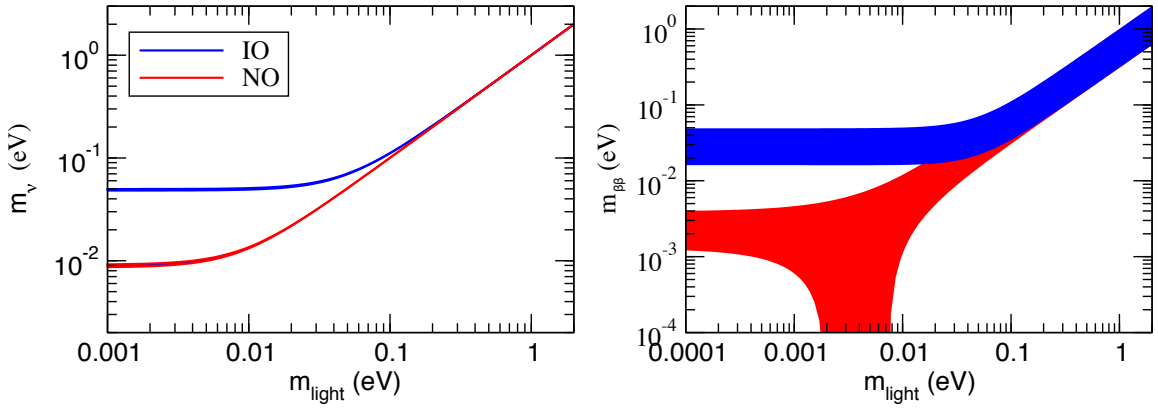


Figure 1.2: Neutrino mass ordering (NO = normal ordering, IO = inverted ordering) for single beta decay (left) and neutrinoless double beta decay (right). The plots relate the mass of the lightest mass eigenstate to the mass observable from single beta decay ($m_\nu$) and neutrinoless double beta decay ($m_{\beta\beta}$), which are described in more detail in Section 1.1.4. The area where NO and IO overlap is referred to as the quasi-degenerate regime. Adapted from [18], where the single beta decay plot is specific to one particular kind of single beta decay (using $^3$H).

Based on theoretical prediction, Figure 1.2 shows the extracted neutrino mass observable from two kinds of neutrino mass experiments ($m_\nu$ for $^3$H beta decay, and $m_{\beta\beta}$ for neutrinoless double beta decay; described in more detail in Section 1.1.4) assuming either a normal (NO) or an inverted ordering (IO) structure. An important caveat is that if no neutrinoless double beta decay signal is observed, it's possible that the neutrino isn't of type Majorana, thus no constraints on $m_{\beta\beta}$ can be made. The quasi degenerate regime is the area where the range of allowed mass observables corresponding to NO and IO overlap, and represents the case where $m_1 \simeq m_2 \simeq m_3$ (i.e., the orderings are indistinguishable).

Though there is evidence that there exist only three neutrino eigenstates (from measurements of Z decay partial-width to invisible final states at resonance in $e^+e^-$ collision experiments[19]), the possibility that other kinds of neutrinos exist has also been explored. One of the candidates is a sterile neutrino.

There is nothing ruling out an arbitrary number of these sterile neutrinos, but the simplest case is to start with just one; this is often called the "3+1 model". Adding one sterile-flavored neutrino would necessitate addition of a fourth member to the list of mass eigenstates: $m_4$. The sterile neutrino can be distinguished from the three

standard "active" neutrino flavor eigenstates by the fact that it doesn't participate in weak interactions, having no non-gravitational interaction with regular matter. This is also why this type of proposed fourth mass eigenstate is not in conflict with the Z decay data: they do not couple to the Z boson. In fact, its lack of weak, strong, or electromagnetic interaction means it has no weak hypercharge, color charge, or electric charge. This explains why the sterile neutrino hasn't been observed before: it cannot be directly detected.

Motivation for the sterile neutrino comes from a few sources. One of these is the significant difference between expected and detected neutrino fluxes from reactor-based experiments; this is the so-called reactor anti-neutrino anomaly[20]. In the anomaly, a deficit in electron anti-neutrinos is observed from nuclear reactor cores, which could be interpreted as an oscillation into another mass eigenstate. This suggests that a fourth neutrino would have a mass splitting on the order of $1\,\mathrm{eV}^2$ relative to the other states; this is much larger than the other mass splittings.

Depending on the value of $m_4$, there are a wide array of roles it could play across many fields, including: a possible warm dark matter candidate if the sterile neutrino mass is on the keV-scale[21], and explaining the matter-antimatter asymmetry by allowing baryogenesis via leptogenesis if the sterile neutrino mass is on the order of many GeV[22].

### 1.1.2 Motivation

Measuring the neutrino absolute mass scale is strongly motivated; it is a necessary component to get the full picture of neutrino properties. It is worth briefly highlighting why a measurement of the absolute neutrino mass scale is important to those outside the neutrino community, as it plays a role across many adjacent fields. In cosmology, for example, neutrinos' relative abundance in the universe affect the evolution of large-scale structure of the universe and the Cosmic Microwave Background (CMB). Current cosmological limits are model-dependent, so an absolute mass scale measurement would be crucial to inform model choice and break parameter degeneracies. In particle physics, the neutrino's massive nature suggests the need for a new mass-generation mechanism, of which the most popular is the seesaw mechanism[23], because neutrinos are at least $10^5$ times less massive than the next lightest fermion.

### 1.1.3 Neutrino oscillation experiments

Over the past decades, a number of experiments aimed at measuring these neutrino oscillation parameters have been carried out. These neutrino oscillation experiments are sensitive to $\theta_{ij}$ and the corresponding mass splitting $\Delta m^2_{ij}$. Below is a compilation of results from a few representative experiments; it is not meant to be an exhaustive list.

**Solar neutrino experiments** (SNO[24], SuperK[25]), which are sensitive to $\nu_e$ into $\nu_\mu$ and $\nu_\tau$ transitions, are used to determine $\theta_{12}$ and $\Delta m^2_{12}$. A 2018 global fit to world data yields $\sin^2\theta_{12} = 0.321^{+0.018}_{-0.016}$ and $\Delta m^2_{12} = (7.56 \pm 0.19) \times 10^{-5}\text{eV}^2$ [26].

**Reactor and accelerator experiments** (RENO[27], Double Chooz[28], Daya Bay[29], T2K[30]) are sensitive mainly to $\theta_{13}$ and $\Delta m^2_{13}$. Global fits to world data (2018) find $\sin^2\theta_{13} = (2.155^{+0.090}_{-0.075}) \times 10^{-2}$ and $\Delta m^2_{13} = (2.55 \pm 0.04) \times 10^{-3}\text{eV}^2$ [26].

**Atmospheric experiments** (IceCube[31], MINOS[32], SuperK[25]), which measure $\nu_\mu$ into $\nu_\tau$ transitions, are sensitive to $\theta_{23}$. Best fit values to the global data from 2018 is $\sin^2\theta_{23} = (4.30^{+0.20}_{-0.18}) \times 10^{-1}$[26].

All quoted values are for normal ordering. The only significant difference between the normal and inverted ordering results comes in the sign of $\Delta m^2_{23}$. As a new generation of oscillation experiments comes online, they are expected to focus more on pinning down the mass ordering and $\delta_{CP}$, which are currently the least well-understood neutrino parameters within reach of oscillation-type experiments.

### 1.1.4 Neutrino mass experiments

Though neutrino oscillation experiments have been enormously successful in quantifying the degree of mixing between different flavor and mass eigenstates, the absolute mass scale remains elusive. There are a few methods of extracting this absolute mass scale, including cosmological modeling using the CMB, time-of-flight measurements from supernovae, the search for neutrinoless double beta decay, and study of single beta decay processes.

#### 1.1.4.1 Cosmological modeling

Current cosmological limits, expressed as the sum of the mass eigenstates $\sum m_i$, come from analysis of the CMB and Baryon Acoustic Oscillations (BAO) by Planck: $\sum m_i \leq 0.12\,\text{eV}$ at 95% C.L.[33]. Such analyses focus on the CMB anisotropies, whose evolution can be influenced by massive neutrinos via (1) their contribution to the radiation density of the universe, and (2) suppression of structure growth on small scales. The BAO measurements are influenced by the additional anisotropic stress caused by neutrinos, which dampens the acoustic oscillations. This cosmological limit is the strictest limit on the absolute mass scale out there, but interpreting the results is tricky because of the strong model-dependence of the analysis, which manifests as a degeneracy between the sum of masses $\sum m_i$, the Hubble constant $H_0$, and the normalized matter fluctuation parameter $\sigma_8$ in the $\Lambda$CDM model[33].

#### 1.1.4.2 Supernova time-of-flight

Another approach uses the spread in arrival times of neutrinos created during a supernova event, assuming that all the neutrinos came from the same mechanism[34]. If the transit time of a neutrino is $t = \frac{d}{c}(1 - \frac{1}{2}\frac{m_\nu^2 c^4}{E^2})$, then the energy-correlated spread in arrival times has the form $\Delta t = \frac{d}{c} m_\nu^2 c^4 \frac{\Delta E}{E^3}$. Here, the distance from supernova to observer is $d$, the speed of light is $c$, the neutrino mass is $m_\nu^2$, the neutrino energy is $E$, and the neutrino energy dispersion (which is the cause of the arrival time dispersion) is $\Delta E$. From just the handful of electron anti-neutrinos arriving from supernova SN 1987A in the detectors of Kamiokande, IMB, and Baksan, a loose constraint of $m_\nu \leq 10\,\text{eV}$ at 95% C.L. was estimated[35]. While there is still much interest in this time-of-flight method and many detectors currently stand ready to detect these supernova-originating neutrinos, it is very much up to chance that a supernova within range of these detectors will go off. Interpretation of results is also reliant on accurate modeling of supernova core-collapse dynamics.

#### 1.1.4.3 Neutrinoless double beta decay

The third method is to search for neutrinoless double beta decay. This hypothetical nuclear transition occurs when a pair of neutrons in the parent nucleus convert into a pair of protons and a pair of electrons, such that the electrons are emitted with the entire share of the decay process's energy. The search for this condition amounts to finding a peak in the measured energy distribution around the decay's Q value. This underscores the need for an ultra-low background setup. If the peak is found, then using the number of nuclei available for double beta decay and the number of counts at

the peak, the equation for radioactive decay can be used to deduce the half-life. With the appropriate phase space factor and nuclear matrix elements, this half life can be used to calculate the Majorana mass, $m_{\beta\beta}$. To date, neutrinoless double beta decay has yet to be observed; the current lowest limits (from the GERDA experiment) are $m_{\beta\beta} \leq 79$–180meV (range is due to the spread in calculated nuclear matrix elements using different methods) at 90% C.L.[36]. Discovery of a neutrinoless double beta decay decay event would prove that neutrinos are Majorana type (i.e., that neutrinos are their own antiparticle), and would imply total lepton number violation.

#### 1.1.4.4 Kinematics of beta decay processes

The final category of neutrino mass experiment is to study the kinematics of beta decay processes. By studying beta decay of $^{3}$H (e.g., Troitsk[37], Mainz[38], KATRIN[39], and Project8[40]), $^{187}$Re (MARE[41]), and $^{115}$Sn[42], the neutrino mass can be extracted via a shape change in the endpoint region of the beta decay spectrum (shown in Figure 1.3).

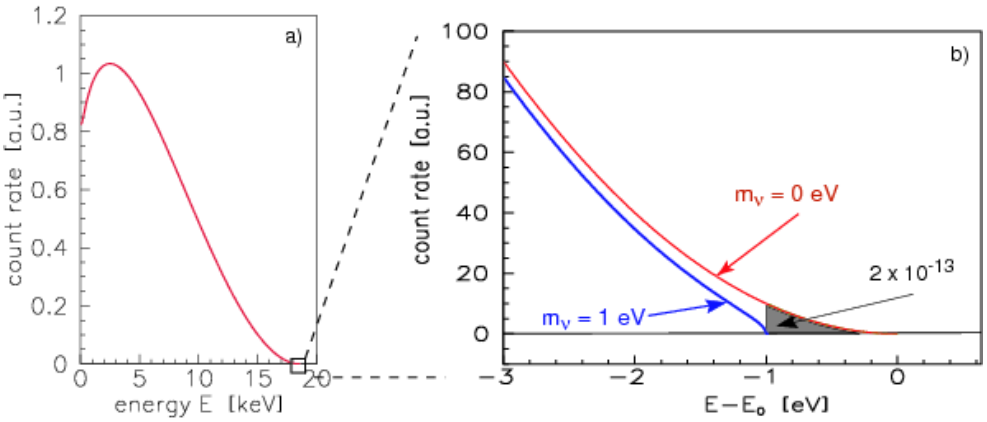


Figure 1.3: Beta decay spectrum near the endpoint, with inset demonstrating the shape change given at some sample neutrino mass values (0 and 1 eV) for $^{3}$H beta decay. Adapted from [43].

The current best limit from these beta decay experiments comes from the KATRIN experiment: $m_{\nu} \leq 0.9\,\text{eV}$ at 90% C.L.[44].

Another type of beta decay exists, in which an inner atomic electron is captured by a proton in the nucleus, thereby transforming it into a neutron (and emitting an electron neutrino). This process is called electron capture. The electron capture prospects all use $^{163}$Ho (EcHo[45], Holmes[46]), of which the EcHo experiment currently gives the best lower limit of $m_{\nu} \leq 10\,\text{eV}$[47]. These $^{163}$Ho-based experi-

ments are calorimetric measurements, which detect energy deposits in the form of small changes in temperature, which cause a change of magnetization and thus a flux change that can be read-out using a type of solid state (SQUID[48]) magnetometer.

While these kinematic experiments give the best model-independent constraints on the absolute neutrino mass scale and perform sterile neutrino searches, they can offer little information on other neutrino properties, such as the mass ordering. The KATRIN experiment, for example, is sensitive only in the quasi-degenerate regime.

The focus of this work will be on the $^3$H beta decay kinematic approach, with the KATRIN experiment. A brief introduction is given in Section 1.2, and a more detailed technical review is presented in Section 2.

## 1.2 Using the KATRIN experiment to extract neutrino mass

The KATRIN experiment is a neutrino experiment which examines the tritium beta decay process for clues to the absolute neutrino mass scale. At the most fundamental level, the physics of the KATRIN experiment can be described by decay of $^3$H (tritium):

$$^3\mathrm{H} \rightarrow ^3\mathrm{He} + \mathrm{e}^- + \bar{\nu}_e \tag{1.6}$$

Tritium is selected due to many favorable properties, including its relatively short half life (12.3 yr), relatively low endpoint energy (around 18.6 keV), simple electron shell configuration, and the fact that its decay is super-allowed (simpler nuclear matrix element). CPT symmetry is assumed, and so "neutrino" and "anti-neutrino" are used interchangeably, forthwith.

To get at the absolute mass scale, the KATRIN experiment extracts the effective anti-electron neutrino mass squared $m_\nu^2$ described in Equation 1.4, from the tritium beta decay. This is described in gory detail in Section 3.1.2. The KATRIN experiment is sensitive only to the effective neutrino mass because the energy resolution of the KATRIN experiment is larger than the mass splittings. This means it is not able to distinguish between different mass contributions.

The influence of $m_\nu^2$ is strongest near the endpoint of the tritium beta decay spectrum because the maximum energy the electron can carry away is capped by the rest energy of the neutrino. This region of greatest sensitivity to the neutrino mass is the region of interest for the KATRIN experiment, so it must be measured with

great precision. The effect manifests as a change in spectral shape, as is shown in the inset of Figure 1.3.

# Chapter 2

# The KATRIN experiment

The KArlsruhe TRitium Neutrino (KATRIN) experimental setup includes many subsystems, which work together to generate, guide, filter, and detect electrons originating from tritium beta decay. The experiment accomplishes this by utilizing an intense molecular tritium source as a source of beta decay electrons, which are magnetically guided through a high-resolution integrating spectrometer. The spectrometers impose a potential barrier to filter the beta electrons, and those which are transmitted are detected via segmented silicon pin diode. This process is repeated for several different spectrometer potential setpoints to build the integrated spectrum; it is this integrated spectrum which is fit to extract the neutrino mass.

A technical description of the KATRIN experiment is supplied in Section 2.1; measurement principle and various recent measurement campaigns are covered in Section 2.2.

A glossary of all the acronyms used here is given at the end of this work.

## 2.1 Experimental setup

The tritium gas, which is circulated and purified using a system of loops, is injected into the source system (Section 2.1.1 and Section 2.1.2). Beta electrons from the decay are guided through a transport system which filters out most non-electrons via two-step process: first actively (Section 2.1.3.1), and then passively (Section 2.1.3.2). Next, these electrons arrive at a set of filtering spectrometers, which allow only electrons with sufficient energy to pass through (Section 2.1.4). Finally, the remaining electrons which have successfully passed through the spectrometers are counted in

the detector system (Section 2.1.5). The complete KATRIN experiment beamline is shown in Figure 2.1. For orientation, note that downstream is from the perspective of the electron, which is traveling from the source decay chamber to the detector.

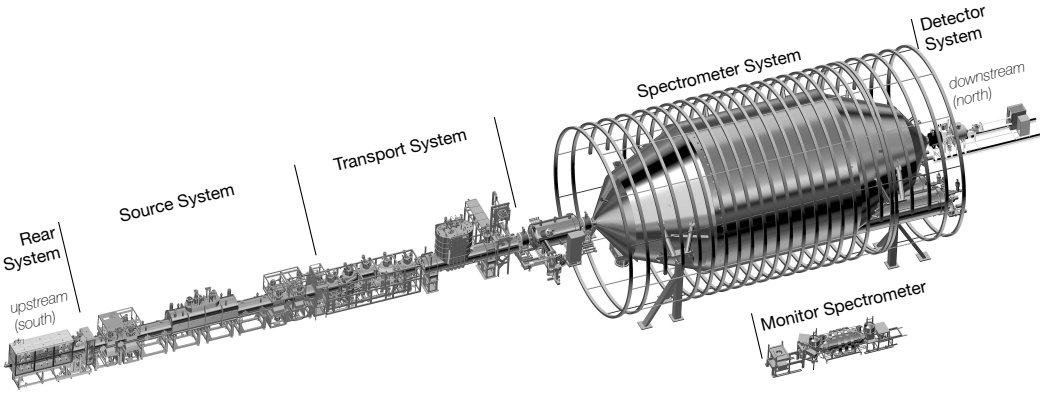


Figure 2.1: Complete KATRIN beamline. Adapted from [49].

Unless otherwise mentioned, all technical details come from the recently-released paper[49] and the references within.

### 2.1.1 Source section

The source section is referred to as the Windowless Gaseous Tritium Source (WGTS). Its main feature is a cylindrical chamber 10 m in length and 9 cm in diameter. The gas contained in the chamber is a high-purity molecular tritium gas ($T_2$), with an activity of up to $10^{11}$ Bq. The gas is injected via capillaries from an external loop system. The downstream end of the chamber is open (hence "windowless"), allowing the electrons to be guided into the transport section. A photo of the source system is shown in Figure 2.2.


Figure 2.2: KATRIN beamline at the source section. The source chamber is completely obscured by the superconducting magnets and secondary-containment glove boxes. The photograph is taken looking in the downstream direction. Adapted from [49].

To facilitate tritium beta decay, a 16 m-long magnet cryostat system surrounds the chamber with 7 warm-bore superconducting solenoids around the chamber, as well as two pairs of superconducting dipole magnets at either end of the chamber (for calibration and alignment). This provides a homogeneous 3.6 T magnetic field ($B_{\text{source}}$), with a stability of better than 0.03 %/month. The superconducting coils are kept cool in a liquid helium bath at 4.5 K, and are operated in driven mode. The value of $B_{\text{source}}$ was selected in order to satisfy adiabaticity requirements and to set the maximum transmitted electron starting angle.

The operating temperature of the tritium gas for neutrino mass measurement mode is nominally 30 K, though higher temperatures (80 K to 100 K) are needed during calibration mode (using krypton gas) to prevent the krypton from freezing. In order to achieve this with a stability of $10^{-5}\,\%\,\text{h}^{-1}$, a novel two-phase neon cooling system was developed. It is coupled to a 25 K gaseous helium system via a thermosiphon, which relies on vaporization/re-liquification of neon to keep the WGTS beamtube cool. The system is completely passive and has no mechanical parts, which is ideal for this high magnetic field environment.

There are two key parameters to the success of the KATRIN experiment which are controlled by the WGTS: column density and purity.

Column density is the number density of tritium molecules integrated over the length of the WGTS source column, and is expressed in units of molecules/cm$^2$. The nominal column density is around $5 \times 10^{17}$ molecules/cm$^2$. Commissioning campaigns have demonstrated that the design stability of the column density (less than $0.1\,\%{\cdot}\mathrm{h}^{-1}$) has been achieved.

The absolute column density comes from dedicated measurements with an electron gun (e-gun) used to measure the fraction of events with zero scatterings (the quantity extracted from these e-gun measurements is actually the product of the column density and the inelastic scattering cross section; since the response function only uses column density, the error on the inelastic scattering cross section is irrelevant here). This measurement provides absolute column density values. Column density cannot be measured parasitically during other measurement modes, but changes in column density relative to the results of the e-gun measurements are monitored by Beta-Induced X-Ray Spectroscopy (BIXS), a small electron detector before the spectrometers (Forward Beam Monitor (FBM)), and by tracking the Focal Plane Detector (FPD) detector rate in a high-rate regime ($-300\,\mathrm{eV}$ below the endpoint). Studies using these three methods for tracking the relative changes in column density between e-gun measurements are all in agreement.

Tritium purity describes the fraction of tritium atoms within the gas injected into the WGTS. The KATRIN experiment requires a tritium purity of more than 95 % in order to reach its design goals. In order to maintain this target level of tritium purity, it is vital that non-tritium contaminants are removed from the system, and that fresh tritium is brought in to replace it. In fact, the KATRIN experiment was installed at Karlsruhe Institute of Technology (KIT) partly because of the presence of previously-existing tritium handling infrastructure, which is part of the Tritium Laboratory Karlsruhe (TLK).

The TLK manages a tritium circulation system with various loops, and is responsible for tritium storage, isotope separation, and recovery/removal. The KATRIN Loop System, which includes an Inner Loop and Outer Loop, is integrated into the TLK. The Outer Loop acts as the middleman between the Inner Loop and the TLK: it brings purified molecular tritium gas from the TLK and introduces it into the Inner Loop, which injects the gas at the center of the WGTS chamber at a pressure of $3.35 \times 10^{-3}\,\mathrm{mbar}$. The gas is pumped out at the ends of the WGTS chamber, and into the Inner Loop. In the Inner Loop, the gas is run through a permeator to extract waste (oxygen, nitrogen, methane, etc); this extracted waste is replaced with fresh tritium gas to maintain high levels of tritium purity. In total, about 1.2 % of the tritium gas flow rate is removed into the Inner Loop system. The diagram in

Figure 2.3 illustrates this. The tritium gas injection pressure stability requirement of less than $10^{-3}$ % has been achieved.

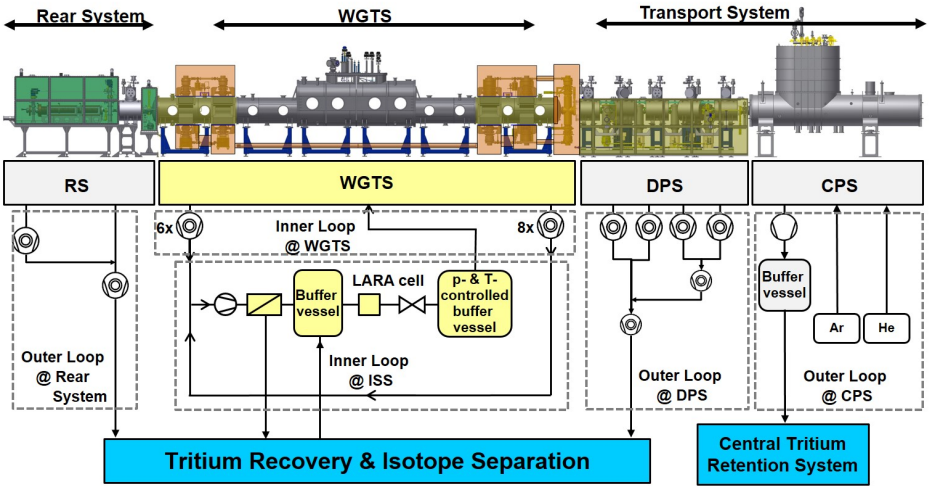


Figure 2.3: Schematic of tritium loops in the source and transport sections. Adapted from [49].

Additional WGTS operation modes include a calibration mode involving circulation of gaseous krypton (Gaseous Source (GKrS)), and a mode in which both gaseous tritium and krypton are simultaneously circulated. These modes are described in sec:kryptonAnalysis.

Further technical detail can be found in Sections 3.1-3.3 of [49].

### 2.1.2 Rear section

On the upstream side of the WGTS, the end of the beamtube is capped with a Rear Wall (RW) (arrow 2 in Figure 2.4). While the RW is the main part of the Rear System (RS), the RW also includes additional monitoring subsystems.

The RW is an important tool for determining and manipulating the space charge distribution in the WGTS. The RW is a 14.5 cm diameter gold-coated stainless steel disk. Whereas the WGTS beamtube walls are held at ground, the RW has a bias voltage applied to it. Thus, electrons created at the RW surface have a starting potential which is the sum of the potential created by the bias voltage and the work function (around 4.2 eV, with an average spread of 0.02 eV across the surface). The

bias voltage is adjustable within the range −500 V to 500 V, though current neutrino mass measurements are made with the RW bias set on the order of 0.1 V.

The RW disk has a small, 5 mm hole through its center (arrow 3 in Figure 2.4), which allows an e-gun sitting behind the RW to shoot a beam of mono-energetic electrons downstream. This e-gun is part of a commissioning and monitoring system, and has a myriad of uses. A flange with a ultra-high vacuum (UHV)-rated window faces the RW at a 55° angle, which allows for RW surface cleaning via ultra violet (UV) illumination. Illumination is achieved via a short-arc xenon CERMAX lamp which delivers light of wavelength 200 nm to 266 nm at 0.3 W ([49]: Section 7.7.4). X-ray radiation generated during the absorption of beta electrons in the RW gold coating is measured by BIXS ([49]: Section 7.3.1). The BIXS system is comprised of two Silicon Drift Detectors (SDDs), each with an active area of 92 $mm^2$ and energy resolution of 160 eV(FWHM) at 5.9 keV. This subsystem is used as a tritium activity monitor. The RW is kept at a slightly warmer temperature (0.5 K relative to the WGTS).

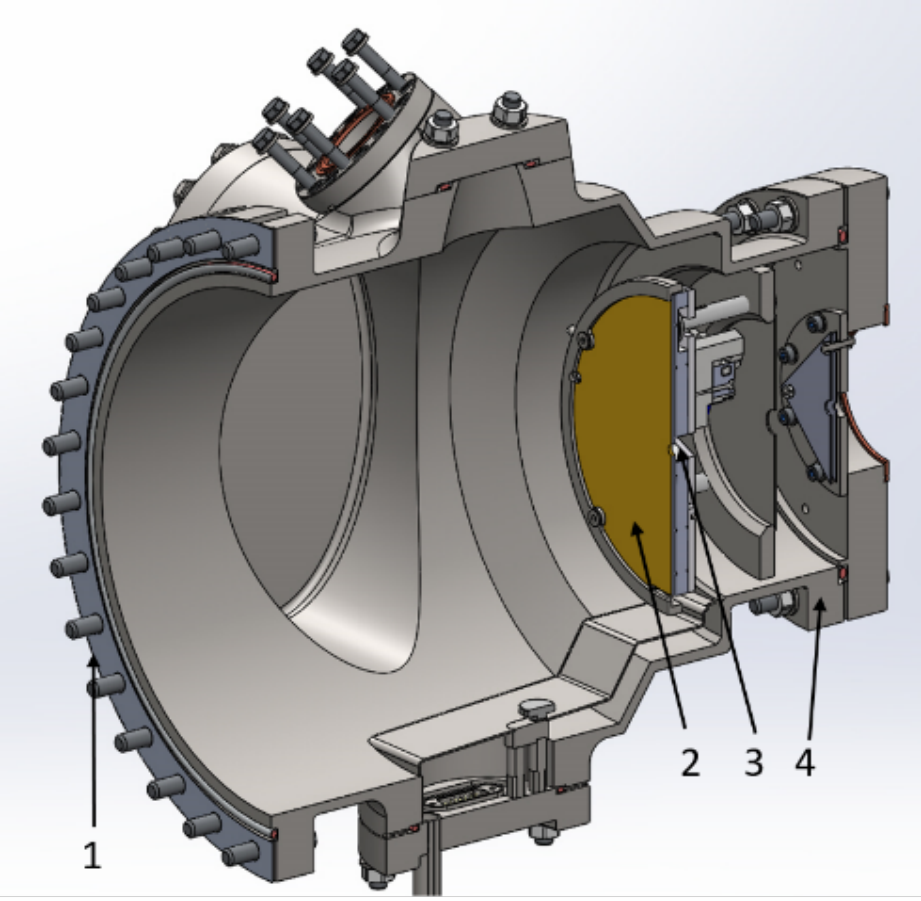


Figure 2.4: Cross section of the RW, including all support infrastructure. **1**: flange towards WGTS (i.e., downstream end). **2**: RW itself. **3**: e-gun hole. **4**: flange towards rear system. The e-gun is not depicted in this schematic, but would be located on the right side (upstream end). Adapted from [49].

More details are available in Section 3.4 of [49].

### 2.1.3 Transport section

The purpose of the transport section is two-fold: it must adiabatically guide electrons from the source section to the spectrometer section, and it must reduce the flow of tritium ($1\,\mathrm{mbar\,L\,s^{-1}}$ at the WGTS) by 14 orders of magnitude. To achieve this remarkable tritium reduction factor, two different pumping methods need to be employed, which effectively divide the section into two subsections: the DPS and the Cryogenic Pumping Section (CPS).

#### 2.1.3.1 Differential Pumping Section

The first section downstream from the WGTS is the Differential Pumping Section (DPS) (Figure 2.5). It uses differential pumping with the aim of reducing the neutral tritium flow rate by a factor of $10^7$ via turbo-molecular pumps (TMPs). Additionally, the 20° kinks in the horizontal plane (parallel to the ground) of the beamline create a chicane and thus help absorb the neutral tritium. A 2018 commissioning measurement confirmed that the total tritium reduction factor between DPS1-F (historically the downstream end of the WGTS) and DPS Pump Port 5 (PP5) was $1.4 \times 10^7$, with a 10 % uncertainty. This satisfies the tritium reduction factor requirement for the DPS.

Each of the five constituent beamtube components in the DPS has its own 1 m-long solenoidal superconducting magnet. Similar to the WGTS, they are liquid helium-cooled and have warm bores. However these magnets run in persistent current mode, and have two correction coils on either side of each magnet's main coil.

The DPS magnet support frame is made entirely of non-magnetic stainless steel, and was designed to withstand both the weight of the magnets and the forces between magnets. The horizontal and vertical positions of the magnets can easily be adjusted for alignment.

Additionally, the DPS contains several features for blocking and removing any ions which might be in the beamline. Ions which reach the detector would damage it; luckily, in standard neutrino mass measurement mode, ions cannot reach the detector. However, the ions can get trapped in the Main Spectrometer (MS), where they decay or interact with either residual gas or the vessel walls. These mechanisms can create secondary electrons, which pass through the MS and are collected together with beta decay electrons in the detector. Thus, these secondary electrons are a potential source of backgrounds for neutrino mass measurements. A recent commissioning campaign in 2019 successfully tested ion removal techniques[50] and showed that ion safety requirements were met ([49]: Section 7.4).

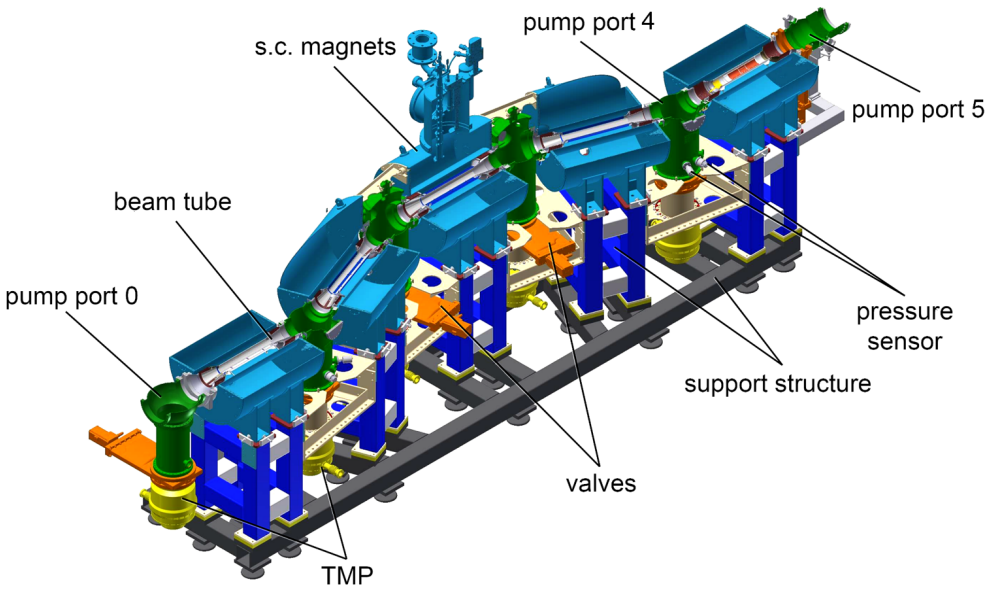


Figure 2.5: Overview of the DPS. Pump port 0 is the upstream end (connected to the WGTS), and has 2 TMPs connected to it. Pump port 5 is the downstream end (connected to the CPS). Pump ports 1-4 each have just one TMP per port. The light blue magnets are superconducting magnets. Adapted from [49].

For additional information, see Section 4.1 in [49].

#### 2.1.3.2 Cryogenic Pumping Section

The second part of the transport section is the Cryogenic Pumping Section (CPS) (Figure 2.6). This section uses a different pumping technique, because here the flow rate is low enough that TMPs are ineffective due to back-diffusion in the pumps. Therefore, in order to get the final factor of $10^7$ tritium flow reduction, a cryo-soption pump is the ideal candidate.

Cryo-sorption occurs via a cold trap. The cold trap is created by lining the inner surface of the beamtubes with gold, and coating that with a thin layer of argon. Beamtube segments 2-5 contain the cold trap, cooled to 3 K. In order to increase the cold trap surface area, 307 fins line the beamtube walls. To prepare the cryo-soption pump, 6 bar L of pure argon is fed into the beamtube, and allowed to freeze onto the gold-plated walls. This layer is referred to an argon frost, and any remaining tritium flowing past will be adsorbed with a sticking coefficient of 0.7. During standard operation mode, the cold trap is operated at 3 K. In order to empty the trap, the system is brought up to 80 K, and everything is pumped out. This process occurs

during a maintenance period, when the CPS is valved off from the up- and downstream sections.

The CPS also contains a chicane, oriented in the horizontal plane (parallel to the ground), with beamtube segments 2-4 tilted by 15°. This is to ensure greater probability of neutral gases hitting (and sticking to) the beamtube walls.

The CPS magnet system features 7 warm-bore solendoidal superconducting magnets, cooled by 4.5 K liquid helium, and operated in driven mode. There are just two pump ports in this section, but they allow for access to monitoring and calibration systems. The horizontal pump port allows the FBM to extend into the flux tube to take relative electron flux measurements (with an energy resolution of around 2 keV). The FBM ([49]: Section 7.3.2) consists of a small electron-counting detector on a long arm (vacuum manipulator on a 2 m-long bellows), which can be driven into the beamline with a precision of 0.1 mm in the x- and y-directions, relative to its starting position. The only drawback to monitoring the electron flux parasitically during a measurement is that the FBM detector board casts a shadow on the detector. The second CPS pump port is vertically oriented and allows a krypton calibration source to be lowered down into the beamline. This krypton calibration source is called the Condensed Source (CKrS), and takes the form of a thin film condensed onto a substrate; it is discussed in greater detail in Section 4.

Commissioning in 2017 showed that the temperatures along the beamtube varied between 3.4 K to 6.2 K, rather than the expected 3 K. COMSOL[51] heat load simulations found the temperature profile to be quite homogeneous with the exception of hot spots at the beamtube bends (due to the chicane) and bolts connecting the beamtube to the warmer inner radiation shield. Despite this, the CPS performed as desired. Simulations with the COMSOL temperature profile in MOLFLOW+[52] revealed that the tritium reduction factor was closer to $10^{11}$, which is four orders of magnitude better than the original requirement of ($10^{7}$).

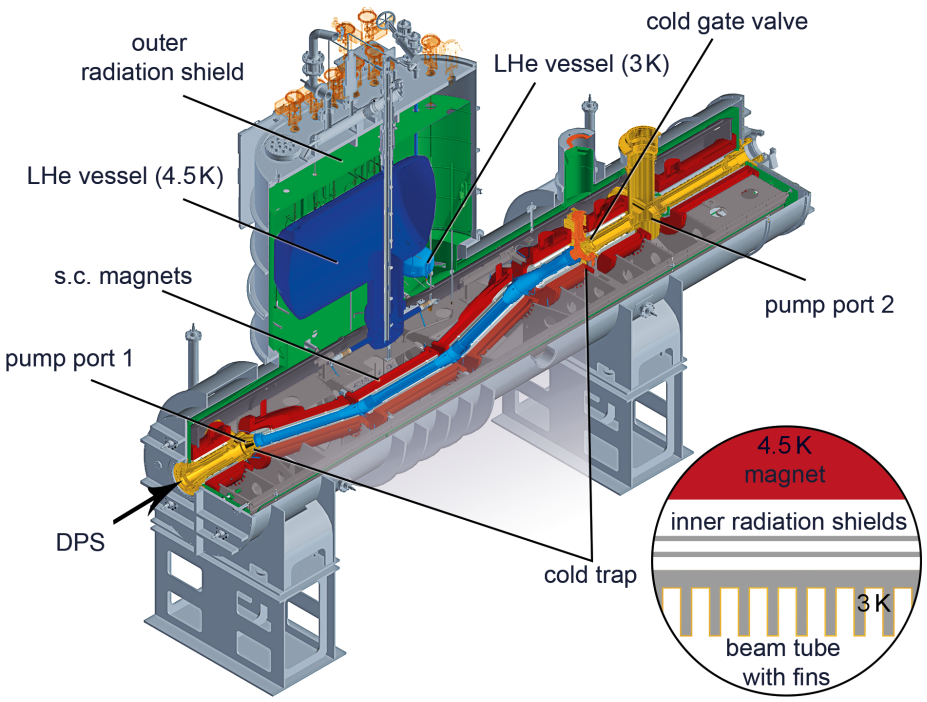


Figure 2.6: Overview of the CPS. The red magnets are superconducting magnets. Adapted from [49].

More technical information is available in Section 4.2 of [49].

### 2.1.4 Spectrometer section

As part of the measurement principle, the electrons must be filtered according to their energy. There are two spectrometers in series for this purpose, where the first acts analogous to a coarse filtering. This first spectrometer, the Pre-Spectrometer (PS), filters out the majority of the low energy electrons. The second spectrometer, the Main Spectrometer (MS), allows for fine control of the filtering. The filter technique for both spectrometers is a well-known technique called Magnetic Adiabatic Collimation with Electrostatic (MAC-E) filter, and uses a combination of magnetic fields and electric potentials to create a potential barrier of a particular height to filter the electrons. An explanation of the measurement principle is given later in Section 2.2. For more details on the physics behind the MAC-E filter, see Section 3.2.1.

Both spectrometers have similar vacuum systems and vessel design, which are presented below. Beyond these, the subsystems of PS and MS are presented separately.

Because vacuum conditions directly affect the storage time of trapped particles

and the production of secondary electrons that occur when trapped particles collide with residual gas molecules, it is important to get them right. Both spectrometers were designed with UHV systems which create pressure environments down to the $1 \times 10^{-11}$ mbar regime. This is accomplished via a combination of non-evaporable getter (NEG) pumps (operating at an effective pumping speed of $1 \times 10^{6}\,\mathrm{L\,s^{-1}}$) and cascaded TMPs. Later tests showed that these NEG pumps were a significant source of radon-induced backgrounds, by virtue of their construction from zirconium-vanadium-iron alloys. But by inserting a set of liquid nitrogen-cooled cryogenic baffles between the NEG pumps and the inner spectrometer volume, the radon-induced backgrounds could be attenuated to more acceptable levels. All vacuum gauges are installed behind their respective valves, to allow for ease of access to sensors without venting the entire vacuum vessel.

The vessel hulls are designed to be low radioactivity, low outgassing, and be able to operate on a huge temperature range (−20 °C to 350 °C) to accommodate cleaning via bake-out (at 200 °C for 4-6 weeks, depending on whether the NEG pumps are activated) and thermal activation of the NEG pumps (at 350 °C for 24 h). A type of stainless steel alloy (316LN) of thickness 10 mm in the PS and 32 mm in the MS was selected. As part of the high voltage system, both spectrometers have their own inner electrode systems, made from the same stainless steel. Both spectrometers feature conical ceramic insulators at their upstream and downstream ends to ground them.

#### 2.1.4.1 Pre Spectrometer

The Pre-Spectrometer (PS) served historically as the prototype for the eventual MS. Its current function in the KATRIN beamline is to filter out the majority of the lower energy beta electrons.

The PS vessel has dimensions of 3.38 m in length and an inner diameter of 1.68 m, as shown in Figure 2.7. These dimensions describe a vessel whose volume is 7.6 $\mathrm{m^3}$, and with an inner surface area of 25.6 $\mathrm{m^2}$. There are three ports with ConFlat flanges on the top of the PS for the high voltage feedthrough to an inner electrode system.

Because it functions primarily as a first step in filtering out the majority of low-energy electrons, high voltage precision is monitored but not critical to the experiment. Therefore, off-the-shelf power supplies are completely sufficient for the PS. The vessel is supplied by a 35 kV power supply, as well as some smaller 5 kV offset power supplies for the inner electrode system. Basic information on the PS high voltage system in the context of the main KATRIN high voltage systems is shown in Figure 2.9.

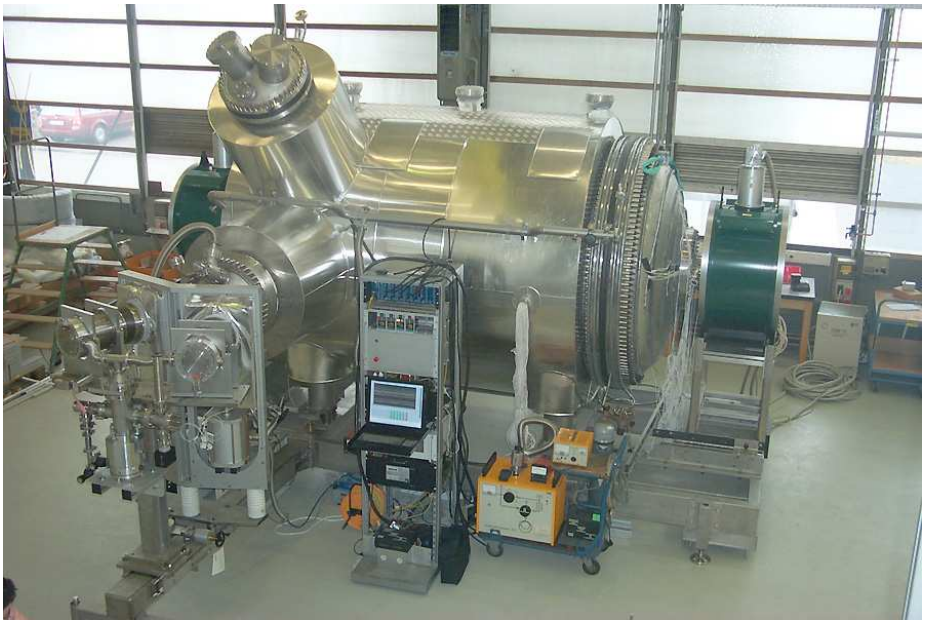

Figure 2.7: Photograph of the PS before it was inserted into the KATRIN beamline. The vessel pictured here includes the heating/cooling system tubing, thermal insulation, vacuum system, and two superconducting magnets. Adapted from [53].

#### 2.1.4.2 Main Spectrometer

The MS vessel has dimensions of 23.23 m in length and a maximum inner diameter of 9.8 m. These dimensions describe a vessel whose volume is 1240 $m^3$, with an inner surface area of 690 $m^2$.

There are 11 ports with ConFlat flanges on the top of the MS for high voltage feedthrough to the inner electrode system, pressure gauges, gas inlet system, and a sapphire window to shine UV light into the vessel.

The MS high voltage is extremely important to any energy analysis: for an electron in the MS, the effective filter voltage is defined by the retarding potential it encounters. For neutrino mass analyses, this retarding potential must be stable in the ppm-range, which translates to a stability of $\pm 20$ mV on an absolute scale of 18 600 kV. Figure 2.9 shows some basic information on the MS high voltage system in the context of the rest of the KATRIN experiment.

This retarding potential is achieved largely by applying a high negative voltage ($-18.6$ kV for neutrino mass measurements) on the vessel hull, and fine-tuning with a two layer system of inner electrodes (on the order of $-100$ V, relative to vessel

hull). The high voltage power supply to the hull is custom-built, and can provide a maximum of $-35\,\mathrm{keV}$, with a stability of 2 ppm over 8 h timescales.

The inner wire electrode system (IE) wire system is electrically isolated into segments, and prevents (background) electrons originating from the walls from entering the main MS volume by reflecting them back to the walls. A sample IE segment is shown in Figure 2.8. There are 248 such IE segments in the MS, arranged into 15 ring-sections. Some segments of the two-layer IE system became one effective layer due to unplanned short-circuiting during a past bake-out, but this does not present any significant drawbacks. Eleven IE ring-sections can still be independently controlled with their own dedicated power supply sources to shape the electric fields inside the MS.

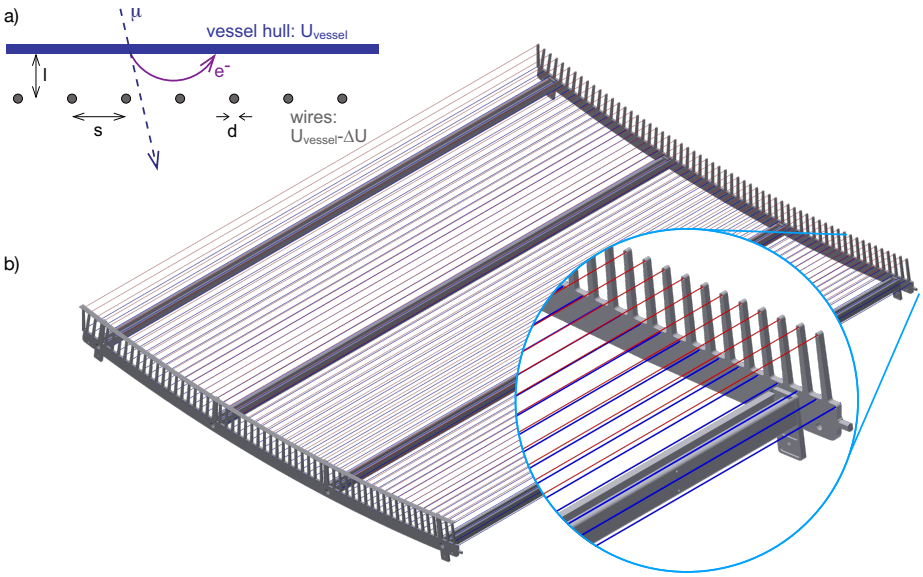


Figure 2.8: Sample IE wire segment from the MS. The wires have a diameter $d = 200\,\mu\mathrm{m}$ for the red wires, a diameter $d = 300\,\mu\mathrm{m}$ for the blue wires, and an average inter-wire spacing $s = 2.5\,\mathrm{cm}$. Outer IE layers are mounted a distance $l = 15\,\mathrm{cm}$ from the vessel walls. Subfigure (a) demonstrates how the electric field created by the IE wire segments cause secondary electrons created in the vessel walls to return to them, instead of continuing in to the MS volume. Adapted from [49].

Additional independent high voltages are applied on the IE mounted to the cone-shaped areas at the spectrometer's upstream and downstream ends. Their settings were optimized for shaping the electric potential within the spectrometer volume, and are quite close to the IE high voltage setpoint of $-200\,\mathrm{V}$. On top of all of this, a "post-regulation" control system is implemented to compensate for any high frequency noise in the system.

Because of the importance of knowing the high voltage extremely accurately, the voltage measurement must be high-precision. These high-precision voltage measurements are performed by a custom-made high voltage divider ("K35", which is calibrated by the German metrological institute, PTB) and two 8.5-digit precision precision digital voltmeters (DVMs). Additionally, an in-situ calibration method was successfully tested[54]. Offset and gain correction factors are recalculated twice per week to track any possible drifts and ensure the best possible high voltage precision.

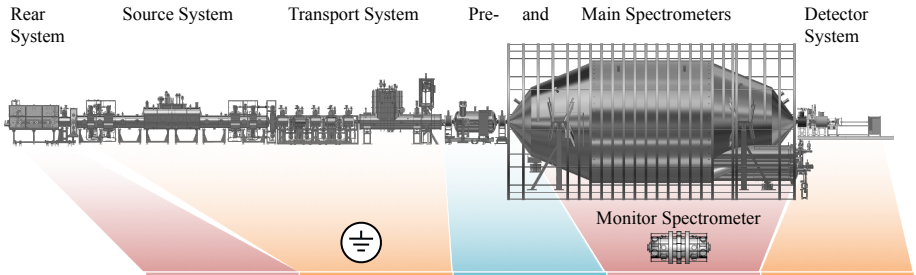


| | **angular selective electron gun** | **beam tube and condensed $^{83m}$Kr source** | **Pre Spectrometer** | **Main and Monitor Spectrometers** | **Post acceleration system** |
|---|---|---|---|---|---|
| Voltage | -20 kV | 0 | -35 kV | -35 kV | +10 kV |
| Stability | ± 20 mV | uncritical | uncritical | ± 20 mV | uncritical |
| Ripple and HF noise | shielded or compensated | grounded | uncritical | compensated | shielded |
| Relevance to $m_\upsilon$ | high | low | low, bg reduction | very high | low, bg reduction |
| Interfaces | coupled to main spectrometer potential, closed high voltage cage | no high voltage, but beam tube is overall reference ground | high voltage on surface, interlock system | high voltage on surface, interlock system, distributed high voltage | grounded housing, standalone system |

Figure 2.9: Overview of various KATRIN high voltage systems. Adapted from [49].

The MS uses a magnet system, comprising an aircoil system around the MS vessel and two superconducting magnets, one at either end of the MS vessel, to shape the magnetic fields in a manner consistent with the MAC-E filter concept. At the upstream end of the MS vessel is the Pre-Spectrometer magnet 2 (PS2): a 3.1 T cryogen-free, conduction-cooled superconducting magnet, operated in driven mode, and with a stability of $< 100$ ppm per 8 h. At the downstream end is the pinch magnet (PCH): a 4.2 T liquid helium-cooled superconducting magnet, operated in persistent current mode, and with a stability of <0.03% per month. The PCH magnet is part of the detector system.

There are two components to the aircoil system: one to compensate for the Earth's magnetic field (Earth Magnetic field Compensation System (EMCS)), and one to shape the magnetic fields in the MS (Low-Field Correction System (LFCS)). The EMCS has two sets of coils installed about the x- and y-axes of the MS. The more important of the two is the LFCS, which is a system of 14 rings, of 12.6 m diameter.

The rings are normal-conducting solenoids, and are installed as shown in Figure 2.10. Both EMCS and LFCS coils can be individually tuned, and the resulting magnetic field strengths around the outside of the MS are monitored by a system of Hall sensor-equipped mobile robots. A special feature of the LFCS is that their currents can be reversed to invert the magnetic field, drawing electrons to the walls of the MS instead of guiding them away. This "asymmetric" magnetic field mode is useful for removing stored electrons; it only takes a few seconds in this mode to accomplish this task, but cannot be done during a neutrino mass measurement[55].

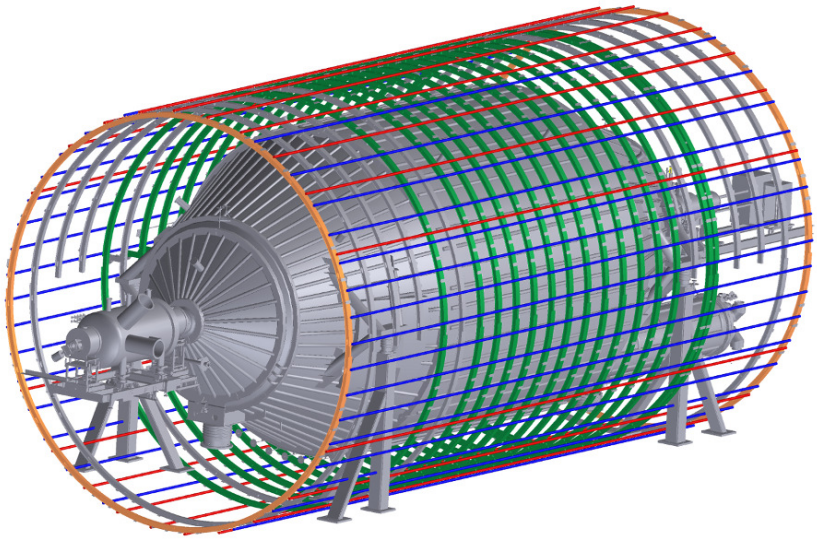

Figure 2.10: Aircoils in the MS: LFCS in green, and EMCS in blue and red. Adapted from [49].

More information can be found in Section 5 of [49].

### 2.1.5 Detector section

After being filtered in the MS, the remaining electrons are magnetically guided through a set of two collimating superconducting solenoids, accelerated, and aimed onto the Focal Plane Detector (FPD). The signals go to preamplifier cards, and are converted to optical signals via an optical sender board (OSB). From the OSB, they are transmitted via optical fibers out of the region of high magnetic field, to the data acquisition (DAQ) system. A cutout of the entire detector system is shown in Figure 2.11 below for orientation:

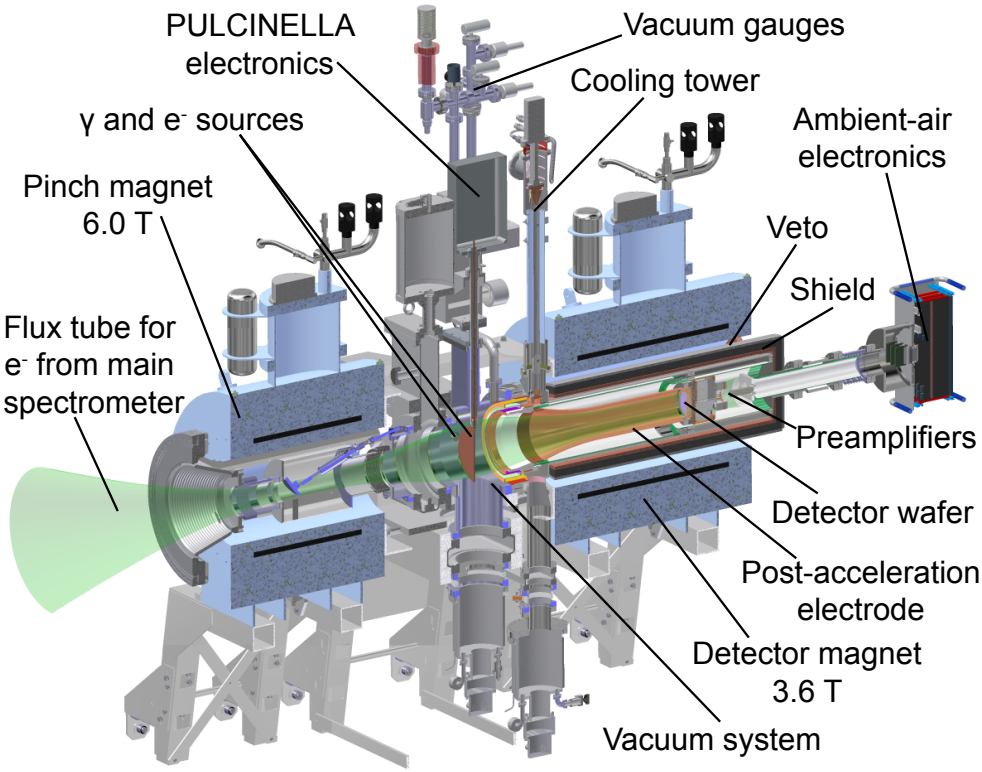


Figure 2.11: Overview of the detector system. The left side is the upstream side, where electrons from the MS enter. The right side (downstream) leads towards the DAQ rack. Note that the pinch magnet (PCH) and detector magnet (DET) magnetic field values quoted in the figure are the maximal fields considered for operation. Magnetic field values quoted in the text correspond to current neutrino mass measurement mode settings. Adapted from [56].

The two collimating magnets are the PCH (described in the Section 2.1.4) and DET magnets. The DET magnet is a 2.5 T liquid Helium-cooled superconducting magnet, operated in persistent current mode, and with a stability of <0.03% per month. The re-acceleration step is achieved via a Post Acceleration Electrode (PAE), which leads up to the DET. The PAE is a trumpet-shaped copper electrode held at −10 kV, and is used to shift the beta electrons' energies into a regime of lower intrinsic detector background.

Inside the warm bore of the DET magnet sits the FPD wafer. This detector is a monolithic silicon p-i-n diode which features 148 pixels of equal surface area (44 $mm^2$ each), fabricated by Canberra (Figure 2.13a). The detector wafer itself has a diameter

of 125 mm, with the sensitive area (the pixel-containing part) having a diameter of 90 mm. It has thickness 503 µm, an approximately 155 nm-thick dead layer, and is operated with a bias voltage of 120 V. The upstream (pixelated) side (Figure 2.12b) has a thin, non-oxidizing TiN coating to facilitate electrical connection.The pixels are connected on the downstream side (Figure 2.12c) to spring-loaded, gold-coated pogo pins (one pin per pixel) on a custom-built feedthrough flange.

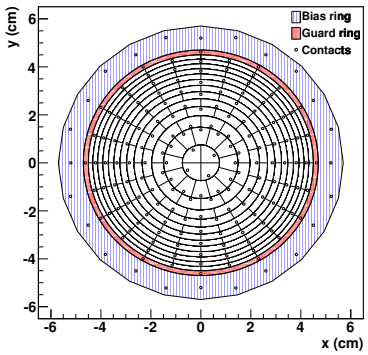


(a) FPD wafer schematic.

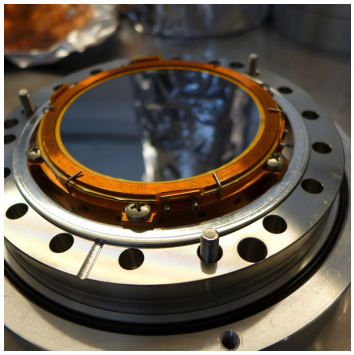

(b) FPD wafer (upstream).

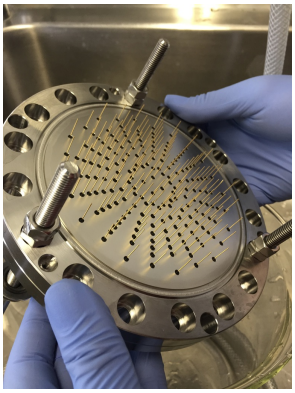

(c) Feedthrough flange (downstream).

Figure 2.12: Schematic and photographs of the FPD detector wafer.

The feedthrough flange demarcates the border between two different vacuum systems: everything upstream of this feedthrough flange is at the same UHV condition as the MS (up to $1 \times 10^{-11}$ mbar), while everything downstream is under regular high vacuum (HVac), which is around $1 \times 10^{-6}$ mbar because the UHV pressures are difficult to achieve in the presence of outgassing from the detector readout electronics. Downstream from the feedthrough flange, the pogo pins' ends pass through tiny holes in a copper plate, and connect electrically directly to the first detector readout stage: the preamplifier cards.

There are 24 of these preamplifier cards (blue objects in Figure 2.13b), each of which connects to either six or seven pogo pins, each corresponding to one channel. The preamplifier cards are arranged in a circular pattern, with one card every 15°. This entire structure is colloquially referred to as the "preamplifier carousel". In total, the channels include the 148 from each pixel, as well as 12 guard ring contacts and 24 bias ring contacts. The average heat dissipation per card is 0.72 W, which is conducted away via the mounting pins to the detector flange, and connected to an active cooling system. Heat flow management is important because it's been shown that there are some temperature-dependent effects on the FPD energy resolution, but they can be considered mostly negligible when the carousel temperature is stable around −30 °C[57].

(a) FPD wafer insertion by Florian and Larisa. Courtesy of Florian Fränkle.

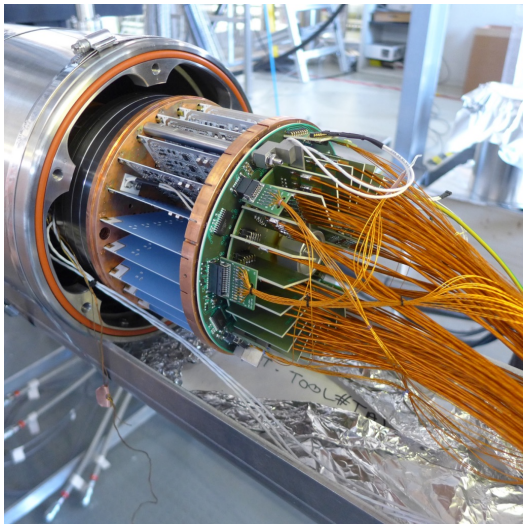

(b) FPD preamplifier carousel. Courtesy of Florian Fränkle.

Figure 2.13: Photographs taken during reassembly of the FPD system in 2017.

Downstream from the preamplifier card carousel, a copper alignment ring guides the cards into a power and control (PAC) distribution board, which in turn is plugged into the signal distribution board. At this point, the signal can be fed via thin, plastic-coated coaxial cables through another vacuum feedthrough into the ambient air electronics crate. Within this crate, the signals are sorted into four 37-channel OSBs and one PAC board. While this is all now outside the HVac region and within a Faraday cage, it is still in a high magnetic field region and floats at the PAE potential ($\mathcal{O}(10)$kV). To carry the signal to the (grounded) DAQ rack, located 2.5 m from the ambient air electronics crate (corresponding to the edge of the 7 mT "safe"[1] region), the signal is converted by the OSBs into an optical signal. The optical signals are carried via optical fiber into the optical receiver boards (ORBs) at the back panel of the DAQ. These ORBs carry out the final task of converting the optical signal into a digital one for processing by the DAQ.

[1]Safe for power supply fans to function reliably; also safe for humans with medical implants, cards with magnetic stripes, and graduate students.

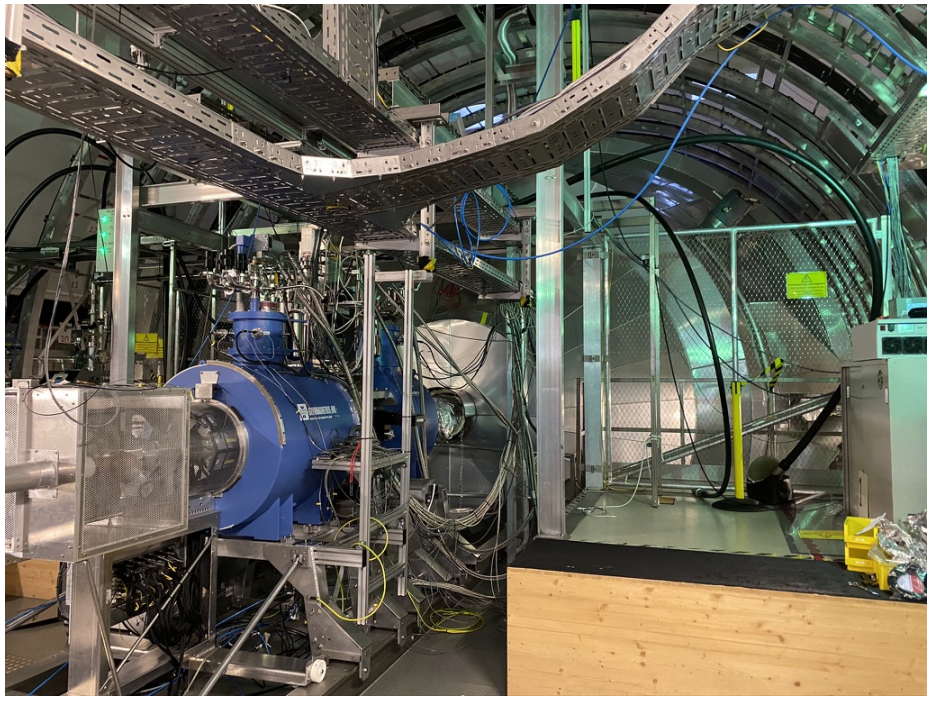

Figure 2.14: Photograph of the detector system during data taking, looking in the upstream direction. Courtesy of the author herself.

In order to do a calibration of the detector, the gate valve connecting the detector section to the MS is shut, and an $^{241}$Am source with 18 MBq activity is inserted into the space upstream of the detector. $^{241}$Am is an alpha emitter, with daughter products whose energy gamma spectrum is shown in Figure 2.15a. This allows for an absolute energy scale calibration based on the observed spectrum, a procedure which takes place every two weeks during normal neutrino mass operations.

The energy resolution of the detector can be attained by fitting the 59.54 keV $^{241}$Am peak with a gaussian; the detector energy resolution corresponds to the FWHM. Good energy resolution is the strongest criterion when it comes to FPD wafer selection. The currently installed wafer#143110 (installed February 2020) has a median energy resolution of 2.44 keV over the entire FPD[57], and no dead or shorted pixels. The distribution of energy resolution per pixel is shown in Figure 2.15b. Wafer maintenance, testing, and exchanges took place in 2017, 2018, and early 2020, with the assistance of the author.

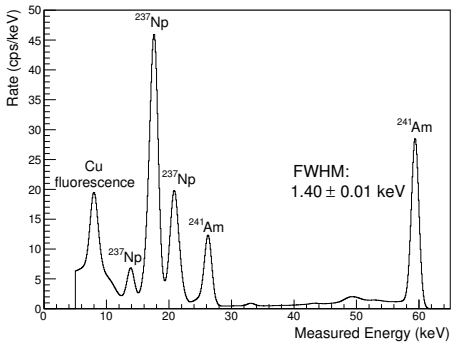


(a) Sample $^{241}$Am energy spectrum. Adapted from [56].

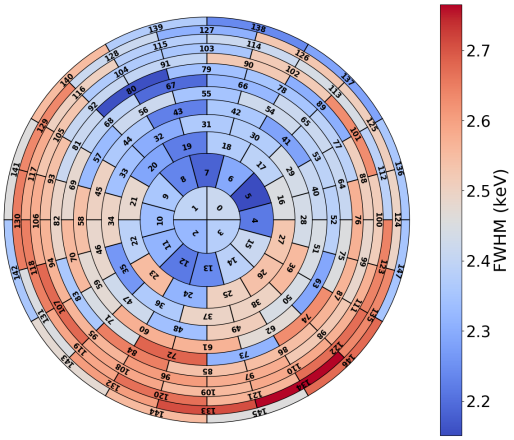


(b) Energy resolution per pixel, for wafer#143110. Data taken at −30 °C on 26 February, 2020. Adapted from [57].

Figure 2.15: Sample $^{241}$Am calibration data.

The only downside to this kind of calibration is that because $^{241}$Am is a gamma emitter, no information on dead layer effects can be gained. To get information on the FPD dead layer (which is an important ingredient in detector efficiency estimation), an electron calibration source is needed. This is where Precision Ultra-Low Current Integrating Normalization Electrometer for Low-Level Analysis (PULCINELLA) comes into play: electrons are created via the photoelectric effect by illuminating a titanium disk with an array of six UV LEDs, and the electron current is measured by PULCINELLA on the pA scale with 3% accuracy.

The careful reader will at this point note that two different energy resolutions have been presented: the MAC-E energy resolution (or "filter width", around 1 eV) and the detector energy resolution (around 1 keV). The detector resolution is less important to optimize because the energy deposited by the electrons on the detector isn't used for constructing the integrated beta spectrum. It is the retarding potential barrier information which is used to construct the integrated beta spectrum, so this is the value to minimize (by suitable choice of MAC-E filter conditions). However it's still important to know what the electron energies deposited in the detector are so regions of interest can be properly constructed to exclude regions with high background.

The final detector subsystem is the muon veto system, which consists of 4 pairs of scintillating panels watched by Silicon Photomultipliers (SiPMs) mounted directly to Wave-Length Shifting (WLS) fibers, in a coincidence configuration. This active veto system is complemented by passive (lead) shielding within the DET magnet bore, around the detector.

More information can be found in Section 6 of [49].

## 2.2 Measurement principle and campaigns

An integrated spectrum is constructed step by step, using an integrating spectrometer. At each step, the KATRIN integrating spectrometer is set at a particular high voltage value. The spectrometer acts equivalently to a high-pass filter: with the MS vessel on high voltage, only electrons with sufficient energy to pass the retarding potential barrier are transmitted and counted by the detector. For more details, see Section 3.2.1. For a set of MS high voltage values (qU values), there are corresponding detector counts. The amount of time spent counting electrons at each qU value allows us to calculate the detector count rate. This is the integrated spectrum.

A sample spectrum (Figure 2.16) demonstrates this measurement principle on one of the calibration (krypton) lines; using this source makes it much easier to see the difference between the differential spectrum (green line) and the integrated spectrum which the KATRIN experiment measures (blue data points).

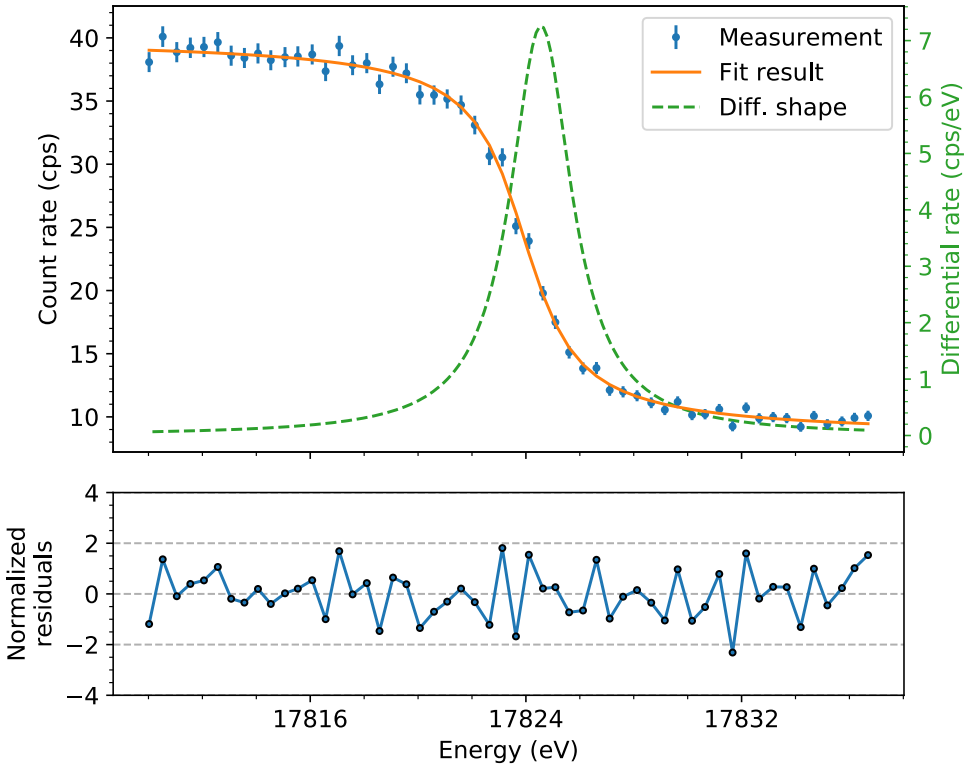


Figure 2.16: Krypton spectral measurement of the K-32 line. The KATRIN experiment measures the integrated spectrum (blue data points). Information from the fit to this data can be used to reconstruct its differential spectral shape (green curve). Adapted from [58].

For neutrino mass analysis runs, the region of interest is around the tritium beta decay endpoint region (around 18.6 keV). For characterization and calibration with krypton, the region of interest will center around individual krypton spectral lines.

A typical integrated spectrum measurement is about 2 hours in duration, and is referred to as a "run" throughout this work. KATRIN sources sometimes use the term "scan", which is interchangeable with "run". The amount of time spent at each qU value defines the Measurement Time Distribution (MTD), and is used to convert counts to rate. Each qU setting is called a "subrun".

In July 2017, the KATRIN experiment held its first krypton campaign. The objective here was to characterize the entire beamline and complete calibrations, using high-resolution krypton spectroscopy[59, 58]. The source used was $^{83m}$Kr , a commonly-used metastable form of krypton, which undergoes a two-step decay

(32 keV and 9.4 keV, respectively) and produces a set of well-defined lines of width comparable to the spectrometer's resolution around 1 eV. More information on the krypton source, its decay properties, and the krypton lines of interest is given in Section 3.1.1. This krypton source was available in gaseous and condensed form to test different properties of the system.

The first tritium gas was circulated in May 2018 during the First Tritium campaign[60]. This measurement campaign circulated much smaller amounts of tritium (with a deuterium carrier gas) to check safety measures and conduct other tests.

With these tests complete, a new era could begin: the KATRIN experiment has begun a cycle of routine neutrino mass measurement campaigns. This started with the "KNM1" measurement campaign in spring 2019, which was the first campaign with non-negligible amounts of tritium in circulation, and provided around 23 days' worth of data[61, 39]. Subsequent measurement campaigns are expected to last 60 days, working towards the fully 3 years' worth of total measurement time needed to reach the KATRIN experiment's target neutrino mass sensitivity of 0.2 eV[53].

For a more detailed breakdown of the various krypton and tritium measurement campaigns, as well as analysis of their data, refer to Section 4 and Section 5, respectively.

# Chapter 3

# CMKAT

While the KATRIN experiment measures the integrated tritium beta spectrum, the purpose of the analysis is to extract the effective neutrino mass by fitting the data with a very precise model of just a few free parameters.

The model constructed to fit the data has two major components: (1) the source and (2) the response function. The source contains a description of the relevant decay physics, whereas the experimental setup information is encoded in the response function. Their convolution gives the integrated spectrum model, which has been implemented into an analysis framework called the Carnegie Mellon-KATRIN ("CMKAT") framework. This model is shown schematically in Figure 3.1.

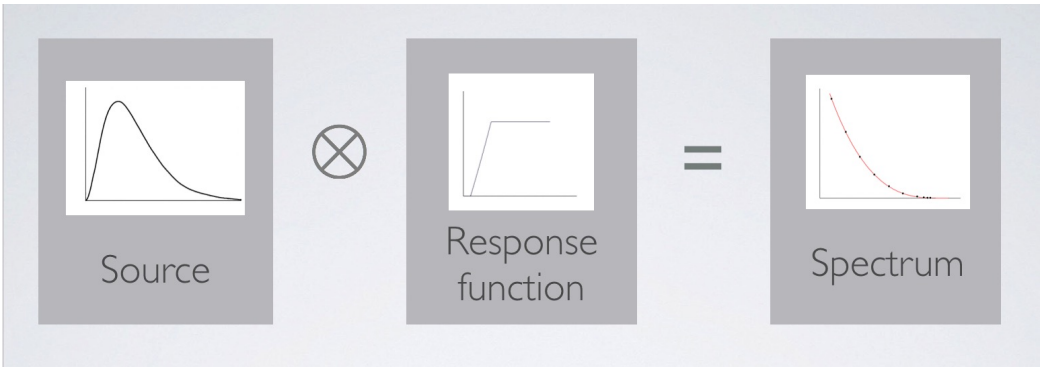


Figure 3.1: Schematic of CMKAT model.

CMKAT will be the focus of this work, though other fitters are also available. The main features of the framework are given below:

**Highlights of the CMKAT framework:**

- Written in C++, using ROOT[62] libraries
- Source models:
  - Tritium beta decay, based on equations from [63]
  - Krypton decay, based on equations from [58]
  - Simultaneous krypton and tritium decay
- $\chi^2$ minimization, via Minuit2
  - Custom parameter error estimation, in addition to standard Minuit error matrix
- Completely independent from all other analyses, except shared input (run summary, period summary)
- Fit optimization by taking advantage of linear terms

This chapter will cover the different input source models (krypton in Section 3.1.1, and tritium in Section 3.1.2). Details of the response function are presented in Section 3.2, and the final integrated spectrum in Section 3.3. The rest of the chapter is dedicated to technical details surrounding CMKAT-specific implementation: a brief introduction to the CMKAT classes (Section 3.4), a description of the available CMKAT fit parameters (Section 3.4.3), and fit modes (Section 3.4.6). With this groundwork laid, the chapter concludes with validation (Section 3.5) and convergence tests (Section 3.6).

## 3.1 Source models

For maximum flexibility, the source portion of CMKAT is designed to be modular. KATRIN run campaigns have used both $^{83m}$Kr (hereafter referred to as "krypton") and tritium, so both krypton and tritium decay models are implemented. For analysis, the user can set the source mode to krypton mode, tritium mode, or a combined krypton and tritium mode. It is important to note that the source models represent the differential spectra, not the integrated spectra. The integrated spectra are put together in Section 3.3, for both the tritium and krypton source models.

### 3.1.1 Krypton model

Krypton-83 in a special metastable state ($^{83m}$Kr ) is used as a calibration source in the KATRIN experiment. Created by the decay of parent $^{83}$Rb, it releases conversion electrons via the internal conversion mechanism at many different energies, with narrow line widths on the same order ($\sim 1\,\mathrm{eV}$) as the spectrometer energy resolution[64, 65].

Internal conversion is the process by which an excited nucleus interacts electromagnetically with one of its orbital electrons. The orbital electron is kicked out at high energies, leaving a hole in the shell. This hole is filled by an electron further out, causing a cascade to fill the vacancies, and resulting in the emission of X-ray photons and/or Auger electrons.

The $^{83m}$Kr is the second excited state of $^{83}$Kr, and undergoes a two-step decay via electromagnetic transitions to get to the ground state. The first step (dominated by the electric octopole term, E3, of the interaction Hamiltonian), which releases around 32.2 keV, and the second (M1 or E2 terms of the interaction Hamiltonian), which releases around 9.4 keV, each release a conversion electron. These conversion electrons can have different energies, depending on the shell (K, L, M, N) from which they originate, as shown in Figure 3.2. This results in an energy spectrum with peaks (later referred to as "lines") corresponding to electrons from different shells in the two-step decay.

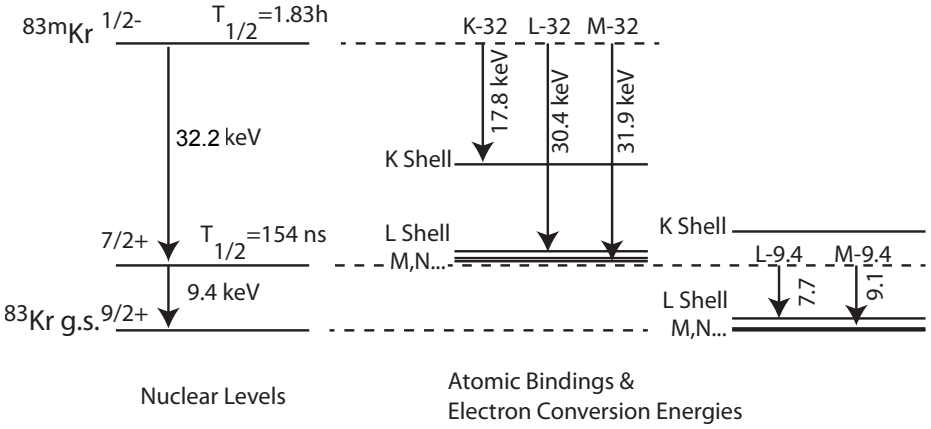


Figure 3.2: Two-step decay of $^{83m}$Kr to its ground state. Courtesy of Gregg Franklin.

The kinetic energy of an electron which originates in a state $\ell$, $E_{KE,\ell}$, can be calculated:

$$E_{KE,\ell} = E_{nucl} - E_{atomic,\ell} \tag{3.1}$$

Where $E_{nucl}$ is the nuclear transition energy (either 32.2 keV or 9.4 keV), and $E_{atomic,\ell}$ is the atomic binding energy of an electron in state $\ell$. Not included in Equation 3.1 are small corrections for the recoil energy of the nucleus, which is negligible[64]. The kinetic energies $E_{KE,\ell}$ are shown in Table 3.1, and correspond to the line positions.

| For 32.2 keV transition | | | | |
|---|---|---|---|---|
| **Shell:** | **State:** | $E_{atomic,\ell}$ [keV]**:** | $E_{KE,\ell}$ [keV]**:** | **Shorthand:** |
| K | $1s_{1/2}$ | 14.3 | 17.9 | K-32 |
| L | $2s_{1/2}$ | 1.9 | 30.3 | $L_1$-32 |
| | $2p_{1/2}$ | 1.7 | 30.5 | $L_2$-32 |
| | $2p_{3/2}$ | 1.6 | 30.6 | $L_3$-32 |
| M | $3s_{1/2}$ | 0.3 | 31.9 | $M_1$-32 |
| | $3p_{1/2}$ | 0.2 | 32.0 | $M_2$-32 |
| | $3p_{3/2}$ | 0.2 | 32.0 | $M_3$-32 |
| | ... | | | |
| N | $4s_{1/2}$ | 0.02 | $\sim 32.2$ | $N_1$-32 |
| | $4p_{1/2}$ | 0.01 | $\sim 32.2$ | $N_2$-32 |
| | $4p_{3/2}$ | 0.01 | $\sim 32.2$ | $N_3$-32 |
| | ... | | | |
| For 9.4 keV transition | | | | |
| **Shell:** | **State:** | $E_{atomic,\ell}$ [keV]**:** | $E_{KE,\ell}$ [keV]**:** | **Shorthand:** |
| K | $1s_{1/2}$ | 14.3 | | NO K line! |
| L | $2s_{1/2}$ | 1.9 | 7.5 | $L_1$-9.4 |
| | $2p_{1/2}$ | 1.7 | 7.7 | $L_2$-9.4 |
| | $2p_{3/2}$ | 1.6 | 7.8 | $L_3$-9.4 |
| M | $3s_{1/2}$ | 0.3 | 9.1 | $M_1$-9.4 |
| | $3p_{1/2}$ | 0.2 | 9.2 | $M_2$-9.4 |
| | $3p_{3/2}$ | 0.2 | 9.2 | $M_3$-9.4 |
| | ... | | | |
| N | $4s_{1/2}$ | 0.02 | $\sim 9.4$ | $N_1$-9.4 |
| | $4p_{1/2}$ | 0.01 | $\sim 9.4$ | $N_2$-9.4 |
| | $4p_{3/2}$ | 0.01 | $\sim 9.4$ | $N_3$-9.4 |
| | ... | | | |

Table 3.1: Kinetic energies of various $^{83m}$Kr lines. The atomic binding energies come from Table 2 of [64].

Some of the most experimentally interesting lines are the K-32 line (closest to tritium beta decay endpoint), $L_3$-32 (most intense line), and the $N_1$-32/$N_2$-32 "doublet" (extremely close together and each of negligible line width).

Each krypton line's (differential) shape can be modelled by a Breit-Wigner shape:

$$\frac{d^2N}{dEdt} = \frac{2}{\pi}\frac{R\Gamma}{4(E-E_0)^2+\Gamma^2} \tag{3.2}$$

Where $\frac{d^2N}{dEdt}$ is the differential spectrum, which is a function of the electron energy $E$.

Within the CMKAT framework, these variables map to the following variable names:

$$\begin{aligned}
\Gamma &= \text{Natural (or intrinsic) line width (FWHM), in eV} \\
&= \text{CMKAT variable } \texttt{WLine} \\
R &= \text{Decay rate for the krypton line, in cps} \\
&= \text{CMKAT variable } \texttt{RLine} \\
E_0 &= \text{Line position, in eV} \\
&= (\text{CMKAT variable } \texttt{E0Line}\ ) - (\text{CMKAT variable } \texttt{DeltaE}\ )
\end{aligned}$$

The CMKAT variable `E0Line` is regarded as the nominal krypton line position. The CMKAT fit parameter `DeltaE` is introduced to account for uncertainties in the true line position $E_0$ and spectrometer retarding potential. For more information on the CMKAT fit parameters, see Section 3.4.3.

The CMKAT krypton model only models one krypton line at a time. This means that relative line intensities need not be included in the model. Additionally, the satellite lines which appear near the main krypton lines described in Table 3.1 due to shake up and shake off effects[66] are not included in the model. This is fine for the krypton line analysis because these satellite lines appear $> 20\,\text{eV}$ below the main lines and are of sufficiently low transition probability that they can be excluded by suitable choice of fit range and a free background fit parameter.

This work will analyze the $L_3$-32 line because it is one of the most intense lines, and there is much data on this particular line under a variety of experimental conditions. Analysis of this line is presented in Section 4.

#### 3.1.1.1 Corrections

There exist a handful of effects which can broaden a krypton line. To take these into account, the line is convolved with a Gaussian of width $\sigma$. This Gaussian broadening term represents the total contributions from many sources, which add in quadrature. Multiple analyses over different experimental conditions are required to separate these contributions. Though there are two different implementations of the krypton source in the KATRIN experiment's main beamline (gaseous and condensed), this work will focus on what can be learned using the gaseous source.

The three largest known sources of Gaussian broadening are those due to fluctuations in the applied spectrometer high voltage[67], the Doppler effect, and the starting potential variations in the WGTS due to space charge. The broadening due to the Doppler effect is calculated below for different source temperature conditions, and WGTS starting potential variations are studied in Section 4.1; they are referred to as $\sigma_{Dopp}$ and $\sigma_P$, respectively.

**Doppler** The Doppler broadening depends only on the temperature within the WGTS; the corresponding $\sigma_{Dopp}$ encodes the amount of smearing due to the thermal motion of the parent $^{83m}$Kr . This $\sigma_{Dopp}$ can be directly calculated using [58] and the relativistic definition $(\gamma+1)m = E+2m$ (derived in Equation 3.26 and Equation 3.27):

$$\sigma_{Dopp} = \sqrt{\frac{(E_{kin} + 2m_e)E_{kin}k_BT}{m_{83Kr}}} \tag{3.3}$$

For the $L_3$-32 line (most intense calibration line; also used for systematic studies later in this thesis), these values correspond to:

$$
\begin{aligned}
E_{kin} &= \text{Kinetic energy of } L_3\text{-32 electrons, in center of mass frame} \\
&= 30472.0\text{eV} \\
k_B &= \text{Boltzmann constant [68]} \\
&= 8.617333262145 \times 10^{-5}\text{eV/K} \\
T &= \text{Temperature of } {}^{83}\text{Kr parent atom} \\
m_e &= \text{Electron mass [69]} \\
&= 5.1099895 \times 10^{5}\text{eV} \\
m_{83Kr} &= \text{Isotopic mass of } {}^{83}\text{Kr [70]} \\
&= 82.914136\text{Da} \times \frac{931.49410242\text{MeV}}{1\text{Da}} = 77234028691.25\text{eV}
\end{aligned}
$$

For the purposes of this calculation, we assume that the electrons have approximately the same energy: that of the $L_3$-32 line.

A table which evaluates the Doppler broadenings for different measurement campaigns based on the WGTS temperatures during those campaigns is given below:

| Temperature [K]: | Campaigns under these conditions: | $\sigma_{Doppler}$[eV]: |
|---|---|---|
| 78.8 | KNM3 krypton-only reference scans<br>KNM3 Kr+Tr extended MTD | 0.053101 |
| 98.9 | KNM2 Kr+Tr regular MTD | 0.059489 |

Table 3.2: $^{83m}$Kr Doppler broadening values $\sigma_{Dopp}$ by measurement campaigns at each temperature.

### 3.1.2 Tritium model

Tritium beta decay (first introduced in Section 1.2), is described by:

$$
{}^3\text{H} \rightarrow {}^3\text{He} + e^- + \bar{\nu_e} \tag{3.4}
$$

The rate of particles created in the kinetic energy range ($E$, $E$+d$E$) is described by Fermi's Golden Rule:

$$\frac{d^2N}{dEdt} = \frac{2\pi}{\hbar}|\mathcal{M}_{fi}|^2\rho(E_{tot,e}, E_{tot,\nu}) \tag{3.5}$$

Where:

$$\begin{aligned}
\mathcal{M}_{fi} &= \text{the matrix element } < f|H|i > \\
\rho(E_{tot,e}, E_{tot,\nu}) &= \text{Density of states for outgoing electron and neutrino} \\
E_{tot,e} &= \text{Total energy of outgoing electron} \\
E_{tot,\nu} &= \text{Total energy of outgoing neutrino}
\end{aligned}$$

The matrix element $\mathcal{M}_{fi}$, which maps the initial state $i$ to the final state $f$ via the interaction Hamiltonian $H$, can be further decomposed into:

$$\mathcal{M}_{fi} = G_F|V_{ud}|\mathcal{M}_{nuc}\mathcal{M}_{lept} \tag{3.6}$$

Where:

$$\begin{aligned}
G_F &= \text{Fermi coupling constant} \\
|V_{ud}| &= \text{Projection onto (u,d)-coupling by the Cabbibo angle } \theta_C \\
&= \text{Some texts refer to this as } \cos\theta_C \\
\mathcal{M}_{nuc} &= \text{Nuclear matrix element} \\
\mathcal{M}_{lept} &= \text{Leptonic matrix element}
\end{aligned}$$

Because tritium beta decay is super-allowed, the nuclear matrix element is (relatively) simple and, more importantly, does not depend on the electron's energy. The leptonic matrix element can be expressed in terms of the Fermi function, $F$:

$$|\mathcal{M}_{lept}|^2 = \frac{1}{V^2}F(Z, E) \tag{3.7}$$

This Fermi function accounts for the Coulomb interaction between the emitted beta electron and the final state of the remaining nucleus, where $V$ is the volume term,

$Z$ is the atomic charge of the daughter nucleus ($Z = 2$), and $E$ is the electron energy. Using the classical Fermi function, the fully relativistic Fermi function is analytically calculable if one approximates the wavefunctions to be spherically symmetric[71]:

$$\begin{aligned} F(Z,T) &= F_{classical} \times (1.002037 - 0.001427\beta) \\ &= \frac{2\pi\eta}{1 - e^{-2\pi\eta}} \times (1.002037 - 0.001427\beta) \end{aligned} \tag{3.8}$$

Where:

$$\begin{aligned} \eta &= \text{Sommerfeld parameter} \\ &= \frac{\alpha_{fs} Z}{\beta} \\ \alpha_{fs} &= \text{Fine structure constant} \\ \beta &= \frac{\sqrt{E^2 + 2Em_e}}{E + m_e} \\ Z &= \text{Atomic charge of daughter nucleus} \\ &= 2 \\ E &= \text{Kinetic energy of outgoing electron} \\ m_e &= \text{Electron mass} \end{aligned}$$

The final piece in the basic tritium model is to calculate the density of states, $\rho$. Each decay product will have its own $\rho$, which is of form:

$$\rho = \frac{dn}{dEd\Omega} \tag{3.9}$$

Where $E$ is the particle's kinetic energy, $n$ is the number of states, and $\Omega$ is its solid angle.

$$\begin{aligned} dn &= \frac{V}{(2\pi)^3} p^2 dp d\Omega \\ &= \frac{V}{(2\pi)^3} pE_{tot} dE_{tot} d\Omega \end{aligned} \tag{3.10}$$

Plugging Equation 3.10 into Equation 3.9 and evaluating for both the electron

and the neutrino:

$$\begin{aligned}\rho(E_{tot,e}, E_{tot,\nu}) &= \rho_e \rho_\nu \\ &= \frac{V}{(2\pi)^3} p_e E_{tot,e} \cdot \frac{V}{(2\pi)^3} p_\nu E_{tot,\nu}\end{aligned} \tag{3.11}$$

The recoiling $^3$He's momentum is fixed to $-(\vec{p}_e + \vec{p}_\nu)$, so it doesn't have an additional phase space to contribute. Defining the total neutrino energy as $\epsilon$ and combining Equation 3.11, Equation 3.5, Equation 3.6, and Equation 3.7:

$$\frac{d^2N}{dEdt} = \frac{G_F |V_{ud}|^2}{2\pi^3} |M_{nucl}|^2 F(Z,E) p_e (E + m_e) \epsilon \sqrt{\epsilon^2 - m_\nu^2} \tag{3.12}$$

It is clear from physics considerations that $\epsilon^2 - m_\nu^2 \geq 0$ to ensure that mass is real, so the Heaviside function is introduced to ensure that the kinetic energy remains positive:

$$\frac{d^2N}{dEdt} = \frac{G_F |V_{ud}|^2}{2\pi^3} |M_{nucl}|^2 F(Z,E) p_e (E + m_e) \epsilon \sqrt{\epsilon^2 - m_\nu^2} \Theta(\epsilon - m_\nu) \tag{3.13}$$

Within the CMKAT framework, the tritium fit parameters are `DeltaE` and `mnu2` , which relate to Equation 3.13 in the following way:

$$\begin{aligned} E &= \text{Kinetic energy of the electron, in eV} \\ m_\nu^2 &= \text{Neutrino mass squared, in eV}^2 \\ &= \texttt{mnu2} \\ \epsilon &= \text{Total neutrino energy, in eV}^2 \\ &= E_0 - E \\ &= (\texttt{E0Nominal} - \texttt{DeltaE}\ ) - E \end{aligned}$$

Where $E_0$ is the true tritium endpoint, `E0Nominal` is the nominal maximum kinetic energy of the electron (usually set to 18 574.0 eV). The CMKAT fit parameter `DeltaE` accounts for uncertainties in the true tritium endpoint $E_0$ and spectrometer retarding potential.

Equation 3.13 is then the tritium beta decay rate without any corrections. The largest corrections to the tritium model will be presented in the next sections: treatment of the final state distribution (Section 3.1.2.1), radiative corrections (Section 3.1.2.2), and Doppler broadening (Section 3.1.2.3). Additional theoretical corrections have been covered in literature[63, 72], but have negligible contributions at the level of recent results[39, 44].

The final section in the tritium model section (Section 3.1.2.4) deals with the negative $m_\nu^2$ extension, which is necessary for the fit.

#### 3.1.2.1 Final State Distribution

Up until now, the tritium model described in Equation 3.13 is valid for atomic tritium sources. However, the KATRIN experiment uses tritium in the molecular state $T_2$.

Because we are dealing with molecular rather than atomic tritium, it's important to keep in mind that there exist a spectrum of "rovibronic" (rotational, vibrational, and electronic) states which the excited daughter molecule is left in. One can imagine that, for each unique rovibronic state, there exists a unique beta decay spectrum with an endpoint that is slightly shifted due to the energy of this rovibronic state. This takes away from the total energy available to the outgoing neutrino, so we shift it like so:

$$\epsilon_f = \epsilon - V_{fi} \tag{3.14}$$

Where $V_{fi}$ is the energy going to the excitation of the molecule; this is the energy associated with transitioning from the initial state $|i>$ to final state $|f>$. It is sometimes called the final state energy. The notation buries in it all the quantum numbers, which are not the focus of this work.

There is an entire distribution of these final state energies. Taking them into account in the tritium beta decay model modifies $\epsilon \to \epsilon_f$ and introduces a sum over all the final states $f$ modified by the probability $P_f$ of transitioning to that final state. The $i$ notation is now dropped because the Final State Distributions (FSDs) are constructed by doing a weighted sum over different initial states.

$$\frac{d^2N}{dEdt} = \frac{G_F|V_{ud}|^2}{2\pi^3}|M_{nucl}|^2 F(Z,E) p_e(E+m_e) \sum_f P_f \epsilon_f \sqrt{\epsilon_f^2 - m_\nu^2}\Theta(\epsilon_f - m_\nu) \tag{3.15}$$

Another complication with applying this final state distribution correction comes,

again, from the fact that it is in a molecular form. And the other atom in the molecule is not necessarily another tritium: it could also be a deuterium or a hydrogen atom. It could also be other things, but the most common tritiated molecules by far in the KATRIN experiment are $T_2$, DT, and HT. For each of these molecules, we need a map of the final state energies $V_f$ to their associated probabilities $P_f$. These are referred to as the FSD, and can be evaluated computationally[73].

There is one FSD per parent molecule type and its associated rotational state (shown in Figure 3.3), and they must be properly combined into one overall FSD to use Equation 3.15. The FSDs are provided by the FSD working group. Each molecule's FSD is broken into $n_{bin}$ energy bins of variable size. Each energy bin corresponds to an energy $V_f$ and a probability of transitioning to the states included in that energy bin.

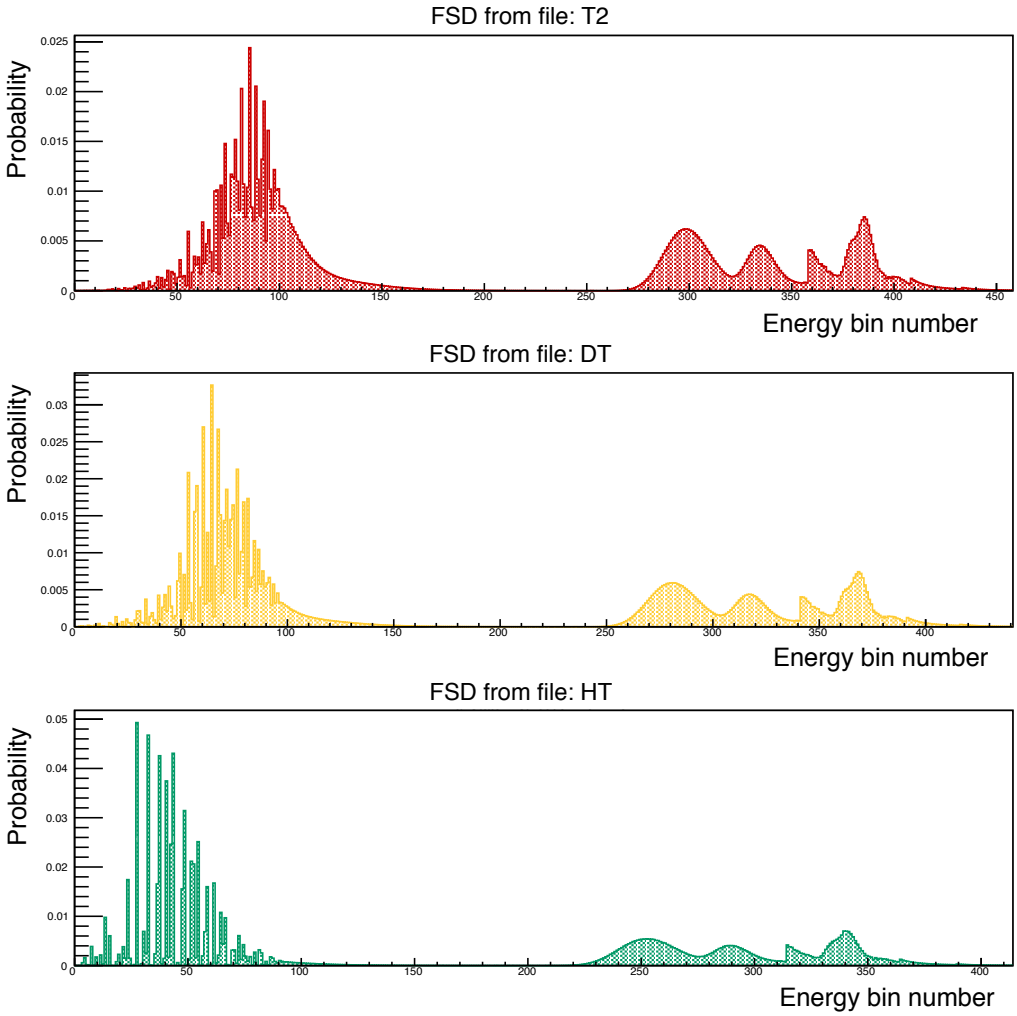


Figure 3.3: FSDs for $T_2$, DT, and HT, as evaluated by the FSD working group. The FSDs shown here are the ones calculated for use in the KNM1 neutrino mass analysis. To get a sense for the energy scale: the large peak in probability on the left is around 2 eV, and the onset of the peak groups on the right occurs around 20 eV (see [63]).

In order to combine the FSDs, we need to know what the relative fractions of the parent molecules are. This information comes from the concentrations, which are calculated by the Laser Raman Spectroscopy (LARA) group (Section 7.2 of [49]), and given in the standard RunSummary[74, 75].

Let $\{f_{T_2}, f_{DT}, f_{HT}\}$ represent the fraction of decays originating in tritiated molecules of type $\{T_2, DT, HT\}$, respectively. And so the fraction of decays in the gas column,

are:

$$f_{T_2} = \frac{2\eta_{T2}}{2\eta_{T2} + \eta_{DT} + \eta_{HT}} \tag{3.16}$$

$$f_{DT} = \frac{\eta_{DT}}{2\eta_{T2} + \eta_{DT} + \eta_{HT}} \tag{3.17}$$

$$f_{HT} = \frac{\eta_{HT}}{2\eta_{T2} + \eta_{DT} + \eta_{HT}} \tag{3.18}$$

Where $\eta_X$ is the concentration of type X in the gas column, and the fractions sum to unity: $f_{T_2} + f_{DT} + f_{HT} = 1$. The factor of 2 in $f_{T_2}$ is due to the two tritium atoms in $T_2$, whereas all the other tritiated molecules presented here have only one.

In order to construct the combined FSD, the probability of a particular state in energy bin $k$ due to a $\{T_2, DT, HT\}$ molecule is scaled by the fraction of decays $\{f_{T_2}, f_{DT}, f_{HT}\}$. These probabilities are added together for groups of energies which are within $E_{merge}$ of one another. The new energy bin $k$' now represents a weighted average of $V_f$. The typical value of $E_{merge}$ for most neutrino mass analyses is 0.1 eV, and its value is set in the ControlParams file (described in Section 3.4.2).

This is an important step because the input FSDs can have differ $n_{bin}$ and different energies assigned to each of their bins. Without consolidating bins which are close in energy, the combined FSD would have a huge number of bins ($\sim$ 1000), which according to Equation 3.15 would increase tritium spectrum computational time. The typical combined FSD has around 300 bins.

#### 3.1.2.2 Radiative correction

The radiative correction is to account for the electron energy lost due to interaction with virtual- and soft-real- photons. According to [63], exclusion of the radiative correction would result in one of the top five highest systematic effects on $m_\nu^2$ . Luckily this effect can be taken into account by calculating a multiplicative factor, $G$[76, 63]:

$$G(W, W_0) = (W_0 - W)^{\xi_0} \left(1 + \frac{2\alpha_{fs}}{\pi}(\xi_1 + \xi_2 + \xi_3)\right) \tag{3.19}$$

Where:

$$
\begin{aligned}
W &= \text{Electron total energy, in units of electron mass} \\
&= \frac{E_{kin} + m_e}{m_e} \\
W_0 &= \text{Endpoint energy, in units of electron mass} \\
&= \frac{E_0 - V_f + m_e}{m_e} \\
\xi_0 &= 2\frac{\alpha_{fs}}{\pi} \cdot t(\beta) \\
\xi_1 &= t(\beta)\left(ln(2) - \frac{3}{2} + \frac{W_0 - W}{W}\right) \\
\xi_2 &= \frac{1}{4}(t(\beta) - 1)\left(2(1+\beta^2) + 2ln(1-\beta) + \frac{(W_0 - W)^2}{6W^2}\right) \\
\xi_3 &= -2 + \frac{1}{2}\beta - \frac{17}{36}\beta^2 + \frac{5}{6}\beta^3
\end{aligned}
$$

And:

$$
\begin{aligned}
t(\beta) &= \frac{1}{\beta}\tanh\beta^{-1} - 1 \\
\alpha_{fs} &= \text{Fine structure constant} \\
V_f &= \text{Energy of the } f\text{th bin of the combined FSD} \\
m_e &= \text{Electron mass} \\
\beta &= \frac{p}{W} \\
p &= \text{Electron momentum, in units of electron mass} \\
&= \sqrt{W^2 - 1}
\end{aligned}
$$

This $G$ factor, which depends on the endpoint energy $E_0$, a final state energy $V_f$, and phase space of that same final state, is now referred to as $G_f$ and comes into play during the calculation over the summation of possible final states in Equation 3.13:

$$
\sum_f P_f \epsilon_f \sqrt{\epsilon_f^2 - m_\nu^2}\Theta(\epsilon_f - m_\nu) \rightarrow \sum_f G_f P_f \epsilon_f \sqrt{\epsilon_f^2 - m_\nu^2}\Theta(\epsilon_f - m_\nu) \tag{3.20}
$$

The values which $G_f$ can take on are $0 \leq G_f \leq 1$, where the lower and upper bounds correspond to:

- $G_f = 0$: occurs if $V_f$ is negative (not physical, but can occur if using blinded FSDs, which has been artificially broadened).
- $G_f = 1$: no radiative correction applied.

#### 3.1.2.3 Doppler correction

The Doppler broadening depends only on the temperature within the WGTS, and $\sigma_{Dopp}$ encodes the amount of smearing due to the thermal motion of the parent molecule. The value of $\sigma_{Dopp}$ can be calculated using the following equation[63]:

$$\sigma_{Dopp} = \sqrt{\frac{(E_{kin} + 2m_e)E_{kin}k_BT}{m_{T_2}}} \tag{3.21}$$

Where:

$$\begin{aligned}
E_{kin} &= \text{Kinetic energy of the electron, in the } \beta\text{-emitter's rest frame} \\
&= 18\,574\,\text{eV} \\
k_B &= \text{Boltzmann constant [68]} \\
&= 8.617\,333\,262\,145 \times 10^{-5}\,\text{eV K}^{-1} \\
T &= \text{Temperature of source gas} \\
m_e &= \text{Electron mass [69]} \\
&= 5.109\,989\,5 \times 10^{5}\,\text{eV} \\
m_{T_2} &= \text{Isotopic mass of } T_2 \text{ [77]} \\
&= (2 \times 3.016\,049\,281\,320\,\text{Da}) \times 931.494\,102\,42\,\text{eV Da}^{-1} \\
&= 5\,618\,864\,236.32\,\text{eV}
\end{aligned}$$

For the purposes of this calculation, we assume that the electrons have approximately the same kinetic energy: that of the tritium nominal endpoint, $E_0$. During the KNM2 neutrino mass measurement campaign, the WGTS temperature was $(30.065 \pm 0.001)$ K[44], corresponding to a Doppler broadening value:

$$\sigma_{Dopp} = 0.094\,\text{eV} \tag{3.22}$$

This value agrees with the 94 meV value calculated for similar conditions in [63].

#### 3.1.2.4 Negative $m_\nu^2$ extension

Previous experiments have shown that $m_\nu^2$ is close to zero. If the true value of $m_\nu^2$ were below the sensitivity of the experiment, then a best fit value to the data would return a positive fitted $m_\nu^2$ 50% of the time, and a negative fitted $m_\nu^2$ 50% of the time. In order to allow $m_\nu^2$ to statistically fluctuate into the negative $m_\nu^2$ regime, an extension must be built into the model. This is not to correct for any physical effect; it is purely for the fitting process.

The modification to Equation 3.13 is[63]:

$$\epsilon_f\sqrt{\epsilon_f^2 - m_\nu^2} \rightarrow \left(\epsilon_f + \mu e^{\frac{-\epsilon_f}{\mu}-1}\right)\sqrt{\epsilon_f^2 - m_\nu^2} \tag{3.23}$$

Where the behavior of the parameter $\mu$ is conditional on the sign of $m_\nu^2$:

$$\mu = \begin{cases} k\sqrt{-m_\nu^2} & m_\nu^2 < 0 \\ 0 & m_\nu^2 \geq 0 \end{cases} \tag{3.24}$$

The value of the tuning parameter, $k$, is calculated based on past studies which optimize for the most symmetric and continuous $\chi^2$ distribution around $m_\nu^2 = 0$[63]. This means that, if the true $m_\nu^2$ value were of negligible size, averaging the $m_\nu^2$ values extracted from multiple measurements would converge to zero. The $k$ value is unique to each experiment, so simply using the $k$ value from another experiment, say the predecessor Mainz experiment, is not feasible. Current KATRIN neutrino mass analyses use $k = 0.716$ (`NEGMASS_TUNING` variable in class cmFixedDefinitions).

## 3.2 Response function

We require a physical setup to observe beta decay, so we must model how true physics events are seen through the lens of the KATRIN experiment. This is the response function, whose ingredients include the experimental setup (settings and filters, etc).

At minimum, the ingredients to the response function include: a transmission condition (Section 3.2.1), correct angular acceptance (Section 3.2.2), implementation of the inelastic scattering probability (Section 3.2.3), and an energy loss function (Section 3.2.4). Section 3.2.5 brings it all together into the final response function. An additional correction is presented in Section 3.2.6.

### 3.2.1 Transmission condition

Consider a charged particle undergoing cyclotron motion about a magnetic field line. This motion is adiabatic if the change in magnetic field over the course of an orbit is small, and from this it can be shown that the orbital magnetic moment about the field line is conserved.

Let $\vec{p}$ be the total momentum of the electron, which can be decomposed into the longitudinal momentum $p_L$ (parallel to the magnetic field line) and the transverse momentum $p_T$ (perpendicular to the magnetic field line), such that $p^2 = p_T^2 + p_L^2$. The conservation of orbital magnetic moment (or the "adiabatic invariant of flux through the orbit of a particle", as given in Section 12.6 of Jackson[78]) can then be written as:

$$\frac{p_T^2}{B} = \text{constant} \tag{3.25}$$

In order to get this into a more useful form, we must transform $p_T^2$ into energy. We begin by using the relationship between total energy ($E_{tot} = E + m$), kinetic energy $E$, rest mass $m$, and momentum $p$:

$$\begin{aligned} E_{tot}^2 &= m^2 + p^2 \\ E + m &= \sqrt{m^2 + p^2} \\ E^2 + 2mE &= p^2 \end{aligned} \tag{3.26}$$

Given that $E+m = \gamma m$ (where $\gamma$ is the relativistic factor), Equation 3.26 becomes:

$$\begin{aligned} m(\gamma - 1)E + 2mE &= p^2 \\ (\gamma + 1)mE &= p^2 \end{aligned} \tag{3.27}$$

Let the pitch angle $\theta$ be the angle between the electron's $\vec{p}$ and $\vec{B}$. Transverse momentum can then be expressed as $p_T = p \sin\theta$. Using this relation in conjunction with Equation 3.27, and letting the constant $m$ drop out, Equation 3.25 becomes:

$$\frac{(\gamma + 1)E \sin^2\theta}{B} = \text{constant} \tag{3.28}$$

We now define two different points, Point 1 and Point 2; where $E_1$ is the electron energy at Point 1, $B_1$ the magnetic field value at Point 1, $\theta_1$ the electron pitch angle at Point 1, and $\gamma_1$ the relativistic factor at Point 1; and so forth for Point 2. Using Equation 3.28, the following relation is constructed:

$$\frac{(\gamma_1 + 1)E_1 \sin^2\theta_1}{B_1} = \frac{(\gamma_2 + 1)E_2 \sin^2\theta_2}{B_2} \tag{3.29}$$

The kinetic energy $E_2$ can be rewritten in terms of $E_1$, as $E_2 = E_1 - \Delta$, where $\Delta$ is the change in kinetic energy as the particle goes from Point 1 to Point 2.

As a particle moves towards a region of higher potential energy and/or increased magnetic field, it may be reflected back. Let Point 1 be the location at which the electron is created in the source, which is denoted with an $S$. Let Point 2 to be the reflection point, which is denoted with an $R$ (thus, $\sin\theta_R = 1$). Solving for the source angle $\theta_S$:

$$\sin^2\theta_S = \frac{\gamma_R + 1}{\gamma_S + 1}\,\frac{E_S - \Delta}{E_S}\frac{B_S}{B_R} \tag{3.30}$$

There are two points at which an electron can be reflected: in the spectrometer's analyzing plane, and in the detector system. These both impose constraints on the transmission condition.

**Reflection at the analyzing plane (AP):** At the analyzing plane, the magnetic field is at its minimum value ($B_{AP}$), and the electron kinetic energy is small (of order eV). This allows us to approximate $\gamma_R = 1$. Thus Equation 3.30 becomes:

$$\sin^2\theta_{S,AP} = \frac{2}{\gamma_S + 1}\,\frac{E_S - \Delta}{E_S}\frac{B_S}{B_{AP}} \tag{3.31}$$

**Reflection in the detector system:** Just upstream of the detector, the magnetic field achieves its maximum value ($B_{pinch}$), the electron kinetic energy is large, and $\gamma_R = \gamma_S$. Thus Equation 3.30 becomes:

$$\sin^2\theta_{S,pinch} = \frac{E_S - \Delta}{E_S}\frac{B_S}{B_{pinch}} \tag{3.32}$$

In conclusion, these two scenarios impose the following transmission conditions: that an electron will only be transmitted if $E_S > \Delta$, and if the pitch angle at the source $\theta_S$ is less than both $\theta_{S,AP}$ and $\theta_{S,pinch}$. Else it will be reflected. Using these requirements, the acceptance can defined.

### 3.2.2 Acceptance

The transmission function is defined as the fraction of electrons transmitted, and is a function of electron energy $E$ and potential $qU$ at the analyzing plane. For a source which radiates isotropically, the fraction of particles emitted downstream into the MAC-E filter (which accepts a maximum angular acceptance $\theta_{max}$, defined in Equation 3.36) is:

$$\begin{aligned} T_{un}(E, qU) &= \frac{1}{2\pi} \int_0^{2\pi} d\phi \int_{\cos\theta_{max}}^{1} d(\cos\theta) \\ &= 1 - \cos\theta_{max} \\ &= 1 - \sqrt{1 - \sin^2\theta_{max}} \end{aligned} \tag{3.33}$$

The transmission function $T_{un}(E, qU)$ is at this point not yet normalized. Using the conditions defined in Equation 3.31 and Equation 3.32, Equation 3.33 can be written as a piecewise function in for the three regions of interest:

$$T_{un}(E, qU) = 1 - \sqrt{1 - \sin^2\theta_{max}} = \begin{cases} 0 & \delta < 0 \\ 1 - \sqrt{1 - \frac{\delta}{E}\frac{B_S}{B_{AP}}\frac{2}{\gamma+1}} & 0 \leq \delta \leq \Delta E \\ \sqrt{1 - \frac{B_S}{B_{pinch}}} & \delta > \Delta E \end{cases} \tag{3.34}$$

Where the surplus energy is $\delta = E - qU$ and the filter width (sometimes called the MAC-E filter's energy resolution, although the transmission function is not Gaussian) is:

$$\Delta E = E \frac{B_{AP}}{B_{pinch}} \frac{\gamma + 1}{2} \tag{3.35}$$

Using Equation 3.34, it can be seen that the maximum angular acceptance $\theta_{max}$ is a function of the surplus energy $\delta$. Its value varies from $\theta_{max} = 0$ at $\delta = 0$, to its

maximum value $\theta_{max} = \theta'_{max}$ at $\delta > \Delta E$.

$$\theta_{max} = \begin{cases} 0 & \delta < 0 \\ \arcsin\left(\sqrt{1 - \frac{\delta}{E}\frac{B_S}{B_{AP}}\frac{2}{\gamma+1}}\right) & 0 \leq \delta \leq \Delta E \\ \arcsin\left(\sqrt{\frac{B_S}{B_{pinch}}}\right) & \delta > \Delta E \end{cases} \tag{3.36}$$

Finally, the transmission function is normalized such that it evaluates to 1 for surplus energies far above $\Delta E$:

$$\begin{aligned} T(E, qU) &= \frac{T_{un}(E, qU)}{1 - \sqrt{1 - \sin^2\theta_{pinch}}} \\ &= \frac{1 - \sqrt{1 - \sin^2\theta_{max}}}{1 - \sqrt{1 - \sin^2\theta_{pinch}}} = \begin{cases} 0 & \delta < 0 \\ \frac{1 - \sqrt{1 - \frac{\delta}{E}\frac{B_S}{B_{AP}}\frac{2}{\gamma+1}}}{1 - \sqrt{1 - \frac{B_S}{B_{pinch}}}} & 0 \leq \delta \leq \Delta E \\ 1 & \delta > \Delta E \end{cases} \end{aligned} \tag{3.37}$$

### 3.2.3 Scattering probability

The probability of an electron with pitch angle $\theta$ being scattered inelastically $S$ times on its journey out of the WGTS is described by the function $P_S(z, \theta)$. This probability can be modeled by a Poisson distribution:

$$P_S(z, \theta) = \frac{\mu(z, \theta)^S e^{-\mu(z,\theta)}}{S!} \tag{3.38}$$

Where:

$z$ = Electron starting position along the WGTS axis ($z = 0$ at WGTS center)
$\theta$ = Electron pitch angle
$\mu(z, \theta)$ = Mean number of inelastic scatterings for an electron starting at position $z$, with pitch angle $\theta$

Note that this work assumes that the pitch angle $\theta$ remains the same, even after a scattering event. This is not technically the case, but a previous study by [79]

showed that considering angular changes during scattering has a negligible effect on the response function shape, so it can be ignored.

The mean number of scatterings, $\mu(z, \theta)$, is calculated:

$$\mu(z, \theta) = \frac{\mu_0 G(z)}{\cos\theta} \tag{3.39}$$

Where:

$$\begin{aligned}
\mu_0 &= \text{Mean number of inelastic scatterings of an electron traversing the} \\
&\quad \text{entire WGTS, with zero pitch angle} \\
&= \sigma_{inel}\bar{\rho}d \\
G(z) &= \text{Effective integrated column density of the scattering gas (molecules/cm}^2) \\
&= \int_z^L g(z')dz' \\
g(z) &= \text{Scattering gas profile along } z \text{ direction (molecules/cm}^3) \\
\sigma_{inel} &= \text{Inelastic scattering cross section(cm}^2) \\
\bar{\rho}d &= \text{Integrated column density (molecules/cm}^2)
\end{aligned}$$

Introducing the variable $x = \cos\theta$ and changing to a normalized length scale to describe position along the source tube ($\xi = 2z/L$, where $L$ is the length of the WGTS beamtube and $z = 0$ is defined as the center of the WGTS beamtube), the scattering probabilities can be rewritten as:

$$P_S(\xi, x) = \frac{\left(\frac{\mu_0 G(\xi)}{x}\right)^S}{S!} e^{-\frac{\mu_0 G(\xi)}{x}} \tag{3.40}$$

In the case where the scattering gas is not the same as the source gas (e.g., combined krypton and tritium operation mode), then the source gas density profile $g(z)$ is specified as $g_\beta(z)$. This is an important distinction to make now, as later sections will discuss the special case of two different gases simultaneously occupying the WGTS. Integrating over $\xi$ gives the average scattering probability for electrons with a pitch angle corresponding to $x = \cos\theta$:

$$
\begin{aligned}
P_S(x) &= \int_{-1}^{1} d\xi g_\beta(\xi) P_S(\xi, x) \\
&= \int_{-1}^{1} d\xi g_\beta(\xi) \frac{\left(\frac{\mu_0 G(\xi)}{x}\right)^S}{S!} e^{-\frac{\mu_0 G(\xi)}{x}}
\end{aligned} \tag{3.41}
$$

In the case where the source gas is the scattering gas (e.g., tritium operation mode), then with suitable u-substitution choice ($u = \frac{\mu_0 G(\xi)}{x}$), the analytic solution to the integral can be written in terms of Gamma functions ($\Gamma(S)$) and incomplete Gamma functions ($\Gamma(S, x)$). The scattering probability can thus be evaluated:

$$
\begin{aligned}
P_S(x) &= \frac{\Gamma(1+S) - \Gamma(1+S, \frac{\mu_0}{x})}{\mu S!} x \\
&= \left(1 - \frac{\Gamma(1+S, \frac{\mu_0}{x})}{S!}\right) \frac{x}{\mu_0}
\end{aligned} \tag{3.42}
$$

An important note here is that this result (Equation 3.42) is independent of the scattering gas density profile, $g(\xi)$. However, if there are multiple gases with different gas density profiles simultaneously occupying the WGTS, then evaluation of $P_S(x)$ must be via numerical integration of Equation 3.41. An example of such a scenario occurred during the KNM2 and KNM3 measurement campaigns, where krypton calibration measurements were undertaken in the presence of both the GKrS and tritium gas in the WGTS. Under these conditions, the source and the scattering gas densities are not equal, so the calculation of scattering probabilities requires the input of both sources' gas profiles. Additional details pertaining to this "dual gas density" mode are given in Section 3.4.3.

If the beta decay emissions are isotropic, as they are in the KATRIN experiment, then $P_S$ can be averaged over $x_{min} = \cos\theta_{max}$ to $x_{max} = \cos(0) = 1$:

$$
\begin{aligned}
\bar{P}_S(x_{min}) &= \frac{1}{1 - x_{min}} \int_{x_{min}}^{1} dx P_S(x) \\
&= \frac{\Gamma(1+S) - \Gamma(1+S, \frac{\mu_0}{x})}{\mu S!} x \\
&= \{(1 - x_{min}^2)\Gamma(1+S) + \mu_0^2[\Gamma(S-1, \mu_0) - \Gamma(S-1, \mu_0/x_{min})] \\
&\quad - \Gamma(S+1, \mu_0) + x_{min}^2 \Gamma(S+1, \mu_0/x_{min})\}/\{2\mu_0(1 - x_{min})S!\}
\end{aligned} \tag{3.43}
$$

Where $\bar{P}_S$ is the angle-averaged probability of $S$ scatters.

### 3.2.4 Energy loss function

The energy loss function $f(\epsilon')$ represents the probability that $\epsilon'$-worth of energy is lost during scattering, and it comes from an empirical model. The superposition of the three Gaussians is a sufficient approximation at lower energies. The parametrization of this lower energy portion of the energy loss function is provided by the energy loss function working group, and can be found in [80, 81]. But above the $T_2$ ionization energy threshold $\epsilon_{ion}$=15.487 eV, the Binary Encounter Dipole model must be used (Eqn. 44 in [82]):

$$f(\epsilon') = \begin{cases} A_1 e^{-\frac{(\epsilon'-\mu_1)^2}{2\sigma_1^2}} + A_2 e^{-\frac{(\epsilon'-\mu_2)^2}{2\sigma_2^2}} + A_3 e^{-\frac{(\epsilon'-\mu_3)^2}{2\sigma_3^2}} & \epsilon' < \epsilon_{ion} \\ \left( A_1 e^{-\frac{(\epsilon_{ion}-\mu_1)^2}{2\sigma_1^2}} + A_2 e^{-\frac{(\epsilon_{ion}-\mu_2)^2}{2\sigma_2^2}} + A_3 e^{-\frac{(\epsilon_{ion}-\mu_3)^2}{2\sigma_3^2}} \right) \alpha & \epsilon' \geq \epsilon_{ion} \end{cases} \tag{3.44}$$

Where $\{A_i, \mu_i, \sigma_i\}$ are the amplitude, mean, and width of the three Gaussians, and $\alpha$ is the ratio of the differential ionization cross sections:

$$\alpha = \frac{\frac{d\sigma(\epsilon', E_0, \epsilon_{ion})}{dW}}{\frac{d\sigma(\epsilon_{ion}, E_0, \epsilon_{ion})}{dW}} \tag{3.45}$$

Where $E_0$ is the nominal tritium endpoint energy. The differential ionization cross sections ($\frac{d\sigma(\epsilon, E_0, \epsilon_{ion})}{dW}$) used in Equation 3.45 are evaluated using the $H_2$ power series fit parameters in Table 1 of [82].

From this, we can express the total energy loss function for $S$ scatterings as $S$ convolutions of Equation 3.44:

$$f_S(\epsilon') = f_1(\epsilon') \otimes f_1(\epsilon') \otimes ... \tag{3.46}$$

This parametrization for the energy loss function is shown in Figure 3.4 for the first 7 scatterings; the red curve corresponds to the energy loss function of a single scattering.

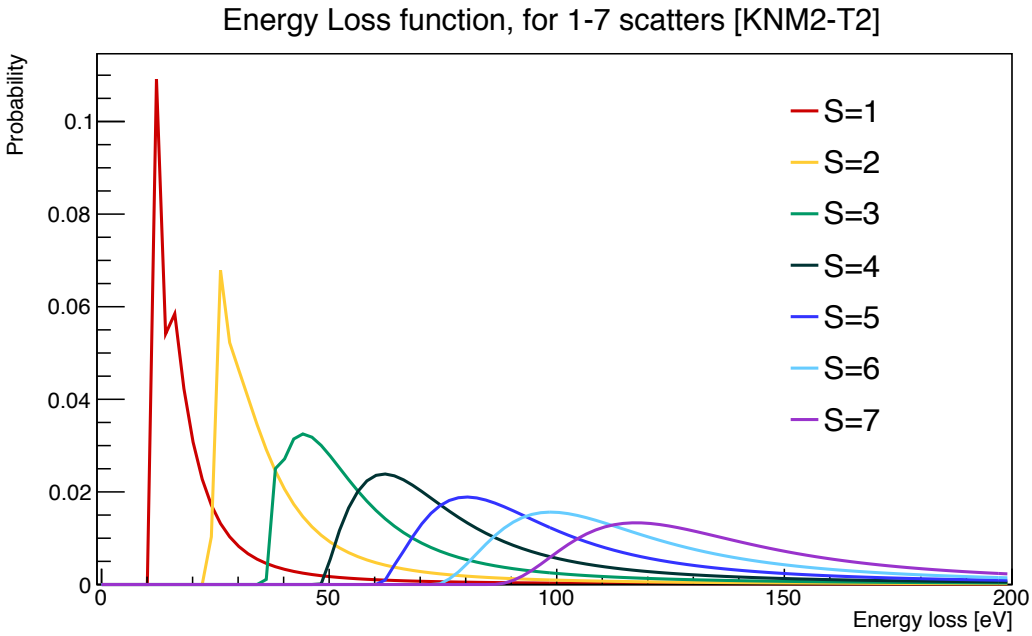


Figure 3.4: Energy loss functions for the first 7 scatterings. Parametrization of the lower energy portion is based on e-gun data gathered during KNM2 in the presence of $T_2$ gas[80].

Evaluation of $f_S(\epsilon')$ in the CMKAT framework is done in the ProbabilityELoss class, which performs the convolutions during its initialization stage by using Fast Fourier Transforms (FFTs) to build lookup tables.

Let the Fourier transform of $f_1$ be $\mathscr{F}(f_1) = \tilde{f}_1$. To make use of the convolution theorem, we first take the Fourier transform of Equation 3.46:

$$\begin{aligned} \mathscr{F}(f_S) &= \tilde{f}_1 \cdot \tilde{f}_1 \cdot ... \\ &= (\tilde{f}_1)^S \end{aligned} \tag{3.47}$$

Then, by taking the inverse Fourier transform of Equation 3.47, we have a quick way to evaluate $f_S$. These results are stored in lookup tables for use in generating the full response function.

$$f_S = \mathscr{F}^{-1}((\tilde{f}_1)^S) \tag{3.48}$$

### 3.2.5 Construction of the Response Function

Finally, the response function can be constructed:

$$R(E, qU) = \int_0^{E-qU} d\epsilon \int_{x_{min}}^{1} dx\ T(E-\epsilon, x, qU) \cdot \sum_S \bar{P}_S(x_{min}) f_s(\epsilon) \tag{3.49}$$

Near the tritium endpoint, the response function can be approximated $R(E, qU) = R(\delta)$, where $\delta$ is the electron surplus energy at the analyzing plane ($\delta = E - qU$, as introduced in Section 3.2.2). Note that $\bar{P}_S(x_{min})$ is a function of the maximum acceptance angle $\theta_{max}$, which takes on values of $\theta_{max}$=0 to $\theta_{max} = \theta'_{max}$, as defined in Equation 3.36.

A response function showing all the major features is shown in Figure 3.5.

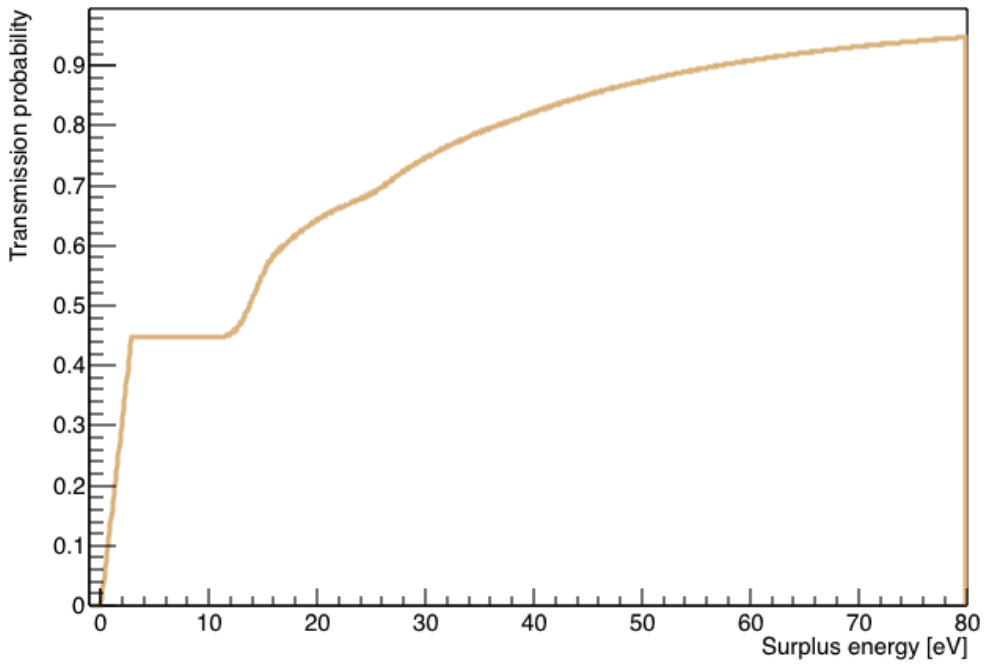


Figure 3.5: Response function generated using FirstTritium measurement campaign settings[83]. It is expressed in terms of the electrons' surplus energy at the analyzing plane of the MS. The finite filter width can be observed in the sharp transmission edge below 5 eV. The bumps above the transmission edge are evidence of the $S$-fold scatterings.

For more technical details on the implementation of the response function in the context of CMKAT, see Section 3.4.4.

### 3.2.6 Correction: synchrotron radiation loss

If energy losses due to synchrotron radiation are considered in the construction of the response function, then the synchrotron radiation energy losses are a function of position $\xi$ in the WGTS. This necessitates an additional step before doing the integral over $x$. The synchrotron radiation energy loss $E_{synch}$ can be expressed as:

$$E_{synch}(x, \xi) = E_{s_0}(x) + \xi E_{s_1}(x) \tag{3.50}$$

Where $E_{s_0}(x)$ is the total synchrotron radiation energy lost for an electron created with pitch angle $x = \cos\theta$ in the middle of the WGTS ($\xi = 0$), and $E_{s_1}(x) = \frac{dE(x)}{d\xi}$. These energy losses can be used as an adjustment to $x$, which is a function of energy. Because of the dependence on $\xi$, when implementing the synchrotron radiation corrections to $x$, the WGTS must be divided into longitudinal segments. For most analyses in the following sections, the simplest case of just one segment is used, as the synchrotron radiation losses aren't the leading order correction. In this case, the position used for evaluation is the midpoint of WGTS segment. Details on the implementation can be found in the CMKAT `cmSynchRad` class, and its documentation [84].

## 3.3 Integrated Spectrum

To generate the final integrated spectrum, we combine the source information (Section 3.1.1, Section 3.1.2) with the response function (Section 3.2) via convolution:

$$\begin{aligned} S_{FPD}(qU) &= \frac{d^2N}{dEdt} \otimes R(E, qU) \\ &= \int_{qU}^{E_{max}} dE \frac{d^2N}{dEdt} R(E, qU) \end{aligned} \tag{3.51}$$

The rate $S_{FPD}(qU)$ is the rate of electrons which have passed through the analyzing plane and have reached the detector. $E$ is the electron energy, and $qU$ the retarding potential energy in the MS.

### 3.3.1 Tritium

For the integrated tritium spectrum, $S_{FPD}(qU)$ is the rate per triton per pixel, so it must be normalized by the decay rate into the accepted flux tube ($C_{\mathrm{FT,acc}}$), the fraction of the flux tube mapped to a single pixel ($C_{\mathrm{FT,pix}}$), and any changes to the nominal column density via the column density adjustment term term ($C_{\texttt{ColAdj}}$ , where the `ColAdj` term is described in more detail in Section 3.4.3). This new, normalized $S_{FPD,norm}(qU)$ is defined as:

$$S_{FPD,norm}(qU) = C_{\mathrm{FT,acc}} C_{\mathrm{FT,pix}} C_{\texttt{ColAdj}}\ S_{FPD}(qU) \tag{3.52}$$

The accepted flux tube normalization factor $C_{\mathrm{FT,acc}}$ is:

$$\begin{aligned}
C_{\mathrm{FT,acc}} &= \epsilon_{det}\eta_{triton}\text{ꓤ}_{FT} \qquad (3.53)\\
\epsilon_{det} &= \text{Detector efficiency}\\
\eta_{triton} &= \text{Number of tritons in the flux tube}\\
&= 2\epsilon_T\bar{\rho}d\sigma_{WGTS}\\
\epsilon_T &= \text{Tritium purity}\\
&= \eta_{T_2} + \frac{1}{2}\left(\eta_{DT} + \eta_{HT}\right)\\
\{\eta_{T_2}, \eta_{DT}, \eta_{HT}\} &= \text{Concentrations of } T_2\text{, DT, and HT, respectively}\\
\bar{\rho}d &= \text{Integrated column density}\\
\sigma_{WGTS} &= \text{Columnar cross sectional area of the WGTS beamtube}\\
&= \frac{\pi d_{FT}^2}{4}\\
d_{FT} &= \text{Flux tube diameter}\\
&= 9\,\text{cm}\\
\text{ꓤ}_{FT} &= \text{Fraction of beta electrons in the flux tube (see Section 3.2.1)}\\
&= \frac{1}{2}\left(1 - \sqrt{1 - \frac{B_S}{B_{max}}}\right)
\end{aligned}$$

The pixel flux tube normalization factor $C_{\mathrm{FT,pix}}$ is:

$$\begin{aligned}
C_{\mathrm{FT,pix}} &= \frac{A_{pix}B_{FPD}}{\sigma_{WGTS}B_S} \qquad (3.54)\\
A_{pix} &= \text{Detector pixel area}\\
&= 44\,\text{mm}^2
\end{aligned}$$

The $B_{FPD}$ necessary for this pixel flux tube normalization is estimated in Section 3.4.3.5.

The column density normalization factor $C_{\texttt{ColAdj}}$ is:

$$C_{\texttt{ColAdj}} = 1 + \texttt{ColAdj} \tag{3.55}$$

Where `ColAdj` is a fit parameter described in more detail in Section 3.4.3.2.

Finally, we take into account an extra normalization factor $A$ and a constant, energy-independent background term $B$:

$$S(qU) = A \cdot S_{FPD,norm}(qU) + B \tag{3.56}$$

Where $S(qU)$ is the final detected integrated spectrum for tritium. The normalization factor $A$ scales with activity and corresponds to the CMKAT fit parameter `AScale` (unitless). The value of $B$ captures the total background over the entire FPD, which corresponds to the per-pixel CMKAT fit parameter `Bkgnd` (cps/pixel), multiplied by the number of active pixels.

### 3.3.2 Krypton

Without information on the total krypton decay rate in the flux tube, it isn't feasible to construct the proper normalization factors, as was done in the tritium case. We therefore allow all the normalization to be taken care of by the $R$ factor (corresponding to the CMKAT fit parameter `RLine` ) in Equation 3.2. Using the rate of electrons at the detector (Equation 3.51), the final detected integrated spectrum for a krypton source is:

$$S(qU) = S_{FPD}(qU) + B \tag{3.57}$$

Where the `RLine` (cps) parameter within the $S_{FPD}(qU)$ term scales with activity, and $B$ is the constant background term, corresponding to the CMKAT fit parameter `Bkgnd` (cps/pixel).

## 3.4 CMKAT classes and other inputs

The CMKAT framework uses a set of custom classes and data inputs, which are called by scripts written by the analyst, to fit the data. These scripts can be written to suit the needs of the analysis, but in general include calls to at least four classes: betaData (holds data, both real and simulated), cmKatrin (model of the KATRIN experiment which returns a count rate, given a set of parameters), cmM2Fit (fitting algorithm, described in more detail in Section 3.4.6), and pixelSelection (container for information on active pixels and mapping pixels to regions). Additional classes exist, and are used as helper classes; they are listed in Section 3.4.1.

A sample fit script is given in Appendix A.2.1. This is to demonstrate the flow of a typical analysis fitting script:

1. Initialization of class instances.
2. Define desired input data files (RunSummaries) and fit settings information file (ControlParams). These files are described in Section 3.4.2.
3. Give classes access to RunSummaries and ControlParams files by invoking the updateParams() function in each class. This allows class instances to read in parameters and initialize themselves. Note that updateParams() does not load data files into the betaData; this is done during a later step.
4. Build response function tables.
5. Load RunSummary information to betaData class, using addRunData() member function. This can be either real data (from one or more RunSummaries) or Monte Carlo-generated data.
6. Instruct the fit class cmM2Fit instance on which fit mode to use, using the setFit() member function.
7. Fix and free fit parameters, using the cmM2Fit helper functions FixGlobalParameter() and ReleaseGlobalParameter().
8. Start the fit by calling cmM2Fit to minimize().
9. Save fit results to file, if desired, using the FitContainer class.

### 3.4.1 CMKAT classes

The following is a list of existing CMKAT classes:

- **betaData**: retrieves and handles the KATRIN tritium data. Dependencies: pixelSelection, KatrinParams.
- **cmFixedDefinitions**: centralized lookup for physics and experiment constants.
- **cmKatrin**: combines response function and selected differential source model to calculate the integrated counts.
- **cmM2Fit**: performs fit. This is where the chi square calculation (with optional pull term) lives. Makes use of the Minuit2 minimizer. Errors can be calculated with Minuit error matrix or custom CMKAT method (Section 3.4.6).
- **cmMonte**: produces Monte Carlo data.
- **cmResponseFunction**: response function class (based on Section 3.2). Dependencies: ProbabilityELoss, ProbabilityScatter, and cmSynchRad.
- **cmSynchRad**: handles calculation of energy loss due to synchrotron radiation in the source and transport sections (based on Section 3.2.6).
- **FitContainer**: data structure to organize fit parameters.
- **fitPixelTerms**: for linear algebra used in the Level 2 and Level 3 fit modes.
- **fpdCanvas**: draws results into an FPD canvas, for visualization purposes.
- **KatrinParams**: retrieves values from data file (.ktf, .txt) and loads them to their respective classes. "Interprets the data".
- **kryptonSource**: contains information on the Krypton differential source model (based on Section 3.1.1).
- **pixelSelection**: handles selection of active pixels and how they should be combined.
- **ProbabilityELoss**: calculation of the energy loss function (Section 3.2.4).
- **ProbabilityScatter**: calculation of inelastic scattering probabilities (based on Section 3.2.3).
- **tritiumSource**: contains information on the tritium differential source model (based on Section 3.1.2).

### 3.4.2 Data inputs to CMKAT

The CMKAT classes are the workhorses of the CMKAT framework, but in order to run a fit, a few input files must be provided for data and fit setting information.

The data is provided in the form of RunSummaries. These are data files which include not only the count and livetime information for the detector (separated by pixel), but also the column density, molecular concentrations, MS potential $qU$, and many other values for each subrun. These and other values in the RunSummaries come from slow control systems or dedicated subsystem analyses. There exists a dedicated working group to process the data (including some preliminary data cuts and quality checks) and create RunSummaries for analysis with version numbers to track changes.

Some experimental settings cannot be extracted directly from individual runs. These are listed in PeriodSummaries, which are valid over a defined period of time, for a particular setting. The values in the PeriodSummary include magnetic and electric potential maps of the MS analyzing plane, which come from simulation. These PeriodSummaries are generated by a dedicated working group.

Using the information from RunSummaries and PeriodSummaries, custom CMKAT RunSummaries are generated using a script to extract relevant data into a database that can be accessed by the individual CMKAT classes using the KatrinParams class.

For analysis of tritium data, input FSD files are required. They are described in Section 3.1.2.1. For blinded neutrino mass analyses, the FSDs are blinded by convolving them with an additional Gaussian of width $\sigma_{blind}$[85], which is unknown to the analysts until unblinding.

For analysis of combined krypton and tritium data, input gas density profile files are required. This is a map of the column densities of tritium and krypton (listed separately) evaluated by simulation at points along the z direction in the WGTS. More details in Section 3.2.4 and Section 3.4.3.3.

Beyond these various data inputs, CMKAT also needs to know fit settings. The ones most typically accessed for high-level analysis tasks have their own associated member functions (for example, fixing or freeing a fit parameter). In order to avoid hardcoding fit settings which aren't as regularly accessed, they are read in from a ControlParams file. Some examples of values that can be set in the ControlParams file include choice of energy loss model, how many inelastic scatterings to include, whether to allow CMKAT classes access to subrun-level column density information, fit parameter initialization values, and pixel selection. A sample ControlParams file is given in Appendix A.2.2.

### 3.4.3 Fit parameters

As stated earlier, the cmKatrin class is designed to return the integrated model count rate for given values of qU and an array of fit parameters, the KatPar array. This output is used by the fitting class, cmM2Fit. Member functions of the cmKatrin class require passing of a value $qUDiff = qU$ - `qUOffset` , so that the spectrum can be plotted versus $qU$ on a relative scale or on an absolute scale. If plotting on a relative scale, then it is relative to the `qUOffset` value: the endpoint of the spectrum would correspond to $qUDiff = 0$, where `qUOffset` =`E0Nominal`. If plotting on an absolute scale, then the endpoint of the spectrum would be plotted as $qUDiff =$ `E0Nominal`, where `qUOffset` =0). The value of `E0Nominal` is set in the ControlParams file.

The KatPar array contains 16 parameters. Three of these are "meta-parameters", which are not varied during the fit. The calling member function uses these meta-parameters to select the desired fit mode, for example pixel grouping. The other 13 KatPar parameters are fitting parameters, which can be varied or fixed to a predefined value during the fitting procedure. The KatPar parameter array members are described in Table 3.3. Some fit parameters are exclusive to either the krypton model (Section 3.4.3.1), the tritium model (Section 3.4.3.2), or the combined krypton and tritium ("Kr+Tr") model (Section 3.4.3.3). Other parameters can be used in any of these modes (`Bkgnd` , as well as `BSlope` in Section 3.4.3.4). These are indicated by the checkmarks in the "type" box.

| Param: | Description: | Type: | | | Free: |
|---|---|---|---|---|---|
| | | Meta | Tr | Kr | |
| qUOffset | Potential offset for plotting. Units of eV. | ✓ | | | |
| pixelGrouping | Selects pixel mode. Options are single, region, or sum over all active pixels. | ✓ | | | |
| pixel | Pixel or region number. Ignored in summed mode. | ✓ | | | |
| BSlopeOffset | Anchor for background slope correction. Units of eV. | | ✓ | ✓ | |
| DeltaE | Adjustment to nominal endpoint (tritium mode) or line position (krypton mode). Units of eV. | | ✓ | ✓ | ✓ |
| mnu2 | Effective neutrino mass squared. Units of $eV^2$. | | ✓ | | ✓ |
| AScale | Tritium activity adjustment (normalization) factor. | | ✓ | | ✓ |
| Bkgnd | Constant (energy-independent) background term. In cps/pixel. | | ✓ | ✓ | ✓ |
| SigmaTr | Gaussian tritium broadening term. Units of eV. | | ✓ | | |
| E0Line | Krypton line position. Units of eV. | | | ✓ | |
| WLine | Krypton line width (FWHM). Units of eV. | | | ✓ | ✓ |
| RLine | Krypton rate. Units of cps. | | | ✓ | |
| SigmaKr | Gaussian krypton broadening term. Units of eV. | | | ✓ | ✓ |
| ColAdj | Integrated column density adjustment. In units of %. | | ✓ | | ✓ |
| BSlope | Energy-dependent background slope. In units of cps/pixels. | | ✓ | ✓ | ✓ |
| Delta10 | Mean difference in plasma potential between 0th and 1st scattering. | | * | * | |

Table 3.3: Menu of all available fit parameters. Note that Delta10 is special: it is used for Kr+Tr runs only.

CMKAT uses a chi squared method of fit. The chi square is twice the log likelihood in the case where the errors are assumed to be Gaussian (Gaussian probability density of the measurements) and are assumed to be independent of each other.

There are some options for fit parameter error estimation. The CMKAT fit parameters fall into two categories: they are either linear or nonlinear in the model (discussed in more detail in Section 3.4.6). The estimated errors on the linear parameters can be evaluated directly by taking advantage on the CMKAT fitting algorithm (Section 3.4.6). For reporting the estimated errors on the nonlinear fit parameters, there are two options: use the standard built-in Minuit error matrix, or a custom CMKAT error estimation method.

The built-in Minuit error matrix evaluates the fit parameter errors by inversion of the error matrix and calculating second derivatives. This process assumes the chi square distribution to be parabolic close to the minimum, and quotes symmetric $1\sigma$ errors. The CMKAT error estimation does not assume the chi square distribution to be parabolic close to the minimum; it calculates the points above $\chi^2_{min}$ where the $\chi^2$ has increased by 1. By definition, this defines the $1\sigma$ estimated errors. It is discussed in more detail in Section 6.

#### 3.4.3.1 Krypton fit parameters

For Krypton, the CMKAT parameters `E0Line`, `DeltaE` and `WLine` have already been introduced in Section 3.1.1. Since both `E0Line` and `DeltaE` are used to calculate the true line position, one must be kept constant. We choose to keep `E0Line` fixed, referring to it as the nominal line position (30 472.0 eV for the $L_3$-32 line, which can be set in the ControlParams file), and `DeltaE` to be the fit parameter.

As shown in Section 3.3, we require a normalization and energy-independent background term as well. This information is captured by `RLine` and `Bkgnd` , respectively.

Finally, the additional Gaussian broadening term `SigmaKr` is taken into account. This involves an additional convolution step before the normalization and background terms are considered:

$$\frac{d^2N}{dEdt}_{\texttt{SigmaKr}} = \frac{d^2N}{dEdt} \otimes Gaussian(\texttt{SigmaKr}\ ) \tag{3.58}$$

Where $\frac{d^2N}{dEdt}$ is the krypton source model (Section 3.1.1). The convolution of a Gaussian and a Breit-Wigner is a Voigt function, so in CMKAT, Equation 3.58 is

implemented using ROOT's normalized TMath::Voigt function. Using this method, Equation 3.58 can be calculated analytically.

#### 3.4.3.2 Tritium fit parameters

For Tritium, the CMKAT parameters `DeltaE` and `mnu2` have already been introduced in Section 3.1.2. The normalization and background terms required in Section 3.3 are `AScale` and `Bkgnd` , respectively.

The additional Gaussian broadening term `SigmaTr` is taken into account in the same manner as in the Krypton model described in Equation 3.58, except that it must be evaluated numerically.

The `ColAdj` term, called the column density adjustment, is implemented to allow for small changes of the column density. A technical description of the implementation of this parameter is given here, and systematic studies are covered later on in Section 6.6.

**`ColAdj` in the CMKAT context** As discussed in Section 2, the column density is one of the key parameters of the KATRIN experiment: it must be known precisely and be stable (on the $<0.1\,\%\,\mathrm{h}^{-1}$ level) over time [49].

There are a few systems in place to monitor the column density: BIXS for electrons moving upstream, and FBM for electrons moving downstream. These subsystems actually measure the activity rates, but combined with the tritium purity obtained from LARA and some other constants, this can be converted into a column density value (see Eqn 7.1 in [49]).

To simulate the effect of various column density uncertainties on the neutrino mass, the CMKAT fit parameter `ColAdj` is used. It represents how much the column density measurement over/underestimates the true column density ($\bar{\rho}d$):

$$\bar{\rho}d_{true} = \bar{\rho}d_{measured} \times (1 + \texttt{ColAdj}\ ) \tag{3.59}$$

The `ColAdj` parameter is unitless. As an example on how to interpret the value: 0.2% underestimation of the column density would require a `ColAdj` $= +0.002$ to obtain a response function corresponding to the correct column density.

The column density is proportional to the mean number of scatters for electrons of pitch angle $\theta$, so the scattering probability will increase with a higher column density

(see Equation 3.38). Thus the value of `ColAdj` plays a big role in the response function part of the model generation. Response function tables generated with a nonzero `ColAdj` are designed to be numerically accurate for `ColAdj` values up to a few percent (any more than that, and it would signal bigger problems, like column density stability problems).

**`ColAdj` for developers** The `ColAdj` parameter appears in many places in the model:

- cmKatrin::signalRateAtDetector_Tr(): after convolution of response function and tritium model, there is an additional normalization factor of (1+`ColAdj` ) applied to the rate.
- cmM2Fit::chiSquaredAllGlobal(): for top level fit (more information in Section 3.4.6), if using subrun column density values, then need to recalculate the value of `ColAdj` for each subrun.
- cmM2Fit::chiSquaredWithPixelTerms(): when calculating final chi square, add pull term as shown in Equation 3.60.
- cmM2Fit::chiSquaredWithPixelTerms(): when handing off fitting to the fitPixelTerms class, set (boolean) flag for using subrun column density values.
- cmM2Fit: can set or get (boolean) flag, which controls whether the column density pull term is included.
- cmResponseFunction::tableLookup(): if `ColAdj` not 0, then do second order Taylor expansion and calculate response function tables with first and second derivatives.
- cmResponseFunction: build single pixel response function. Use single pixel tables to build summed pixel response function. For single pixel derivative tables, need to evaluate response function at `IntegratedColumnDensity`$*(1.0\pm$ `DerivativeStepSize`) Where `DerivativeStepSize` (0.005) is on order of the column density measurement error.
- fitPixelTerms::ThreeParamLinearFit(): if using subrun column density values, then need to recalculate value of `ColAdj` for each subrun.
- fitPixelTerms::TwoParamLinearFit(): same as for the ThreeParamLinearFit above.

**`ColAdj` for analysts** There are two ways in which the column density values can be manipulated by the user, via `ColAdj` :

1. Via the fit parameter `ColAdj` : either freed or fixed.
2. Inclusion of the pull term in chi square.

The first item is fairly straightforward, and can be set explicitly in the analyst's fitting script via the usual Minuit-like incantation.

For the second method, `ColAdj` can be set to appear in the column density ($\bar{\rho}d$) pull term:

$$\begin{aligned}
\chi^2_{tot} &= \chi^2 + \chi^2_{pull,\texttt{ColAdj}} \\
&= \chi^2 + \frac{(\bar{\rho}d - \bar{\rho}d_{measured})^2}{\sigma^2_{\bar{\rho}d,err}} \\
&= \chi^2 + \frac{(\bar{\rho}d - (\bar{\rho}d(1 + \texttt{ColAdj}\ )))^2}{\sigma^2_{\bar{\rho}d,err}} \\
&= \chi^2 + \frac{\texttt{ColAdj}^{\ 2}}{\sigma^2_{\bar{\rho}d,err}}
\end{aligned} \tag{3.60}$$

Where $\chi^2$ represents the chi squared contribution of all non-pull terms, and $\sigma_{\bar{\rho}d,err}$ is the measurement error on the column density. For KNM2, $\sigma_{\bar{\rho}d,err}$ was 0.29%; for KNM3, it was 0.2% [86]. Note that including the pull term increases the fit degrees of freedom by one, as this measured value constitutes an additional data point in the fit.

For completeness, there exists a third way to control how CMKAT uses the column density information. This third way is to choose whether the column density values per subrun or the run-averaged column density is used. The flag which controls this setting is `fit.SubrunColumnDensityAdjustment` in the ControlParams file.

#### 3.4.3.3 Combined krypton and tritium fit parameters

This third measurement mode involves both tritium and krypton gases being present in the WGTS simultaneously. The main purpose of this measurement mode is to characterize the tritium source conditions. One kind of characterization analysis (exploring the plasma-induced properties of the tritium gas) is explored in Section 4.

According to [87], in order to model this type of measurement mode, we must introduce a "dual gas" setup. This requires two additional ingredients:

1. Dual gas density profile
2. `Delta10`

The dual gas density profile comes from simulating a mixture of tritium and krypton gas in the WGTS, and evaluating the column density of each gas separately, as a function of position within the WGTS[66]. It is important here to distinguish the tritium as the scattering gas, and the krypton as the source gas. There is more tritium than krypton gas in this measurement mode, and the measurements of interest are across a krypton line ($L_3$-32), which is far above the tritium endpoint. This changes how the scattering probabilities, $P_s(x)$, are calculated: we need to use Equation 3.41 and perform the integral numerically.

There is a different mean starting potential for $S$=1 scattered electrons than unscattered ($S$=0) electrons because there is a higher probability that the $S$=1 scattered electrons originate from the upstream half of the WGTS. This difference in the mean starting potentials can contribute to plasma-related effects (discussed in Section 4). Some fairly accurate approximations can be made to take into account these scattering-dependent starting potentials, using only the knowledge of the difference between the maximum scattering peaks of $S$=0 and $S$=1. This difference is encoded in the CMKAT parameter `Delta10` [87]. According to recent studies[87], the value of `Delta10` is consistent with zero within one standard deviation. Therefore it is fixed to zero for all CMKAT studies at this time.

#### 3.4.3.4 Background slope

A background slope parameter `BSlope` was implemented to take into account a linear, energy-dependent increase in background, with units of cps/eVpixel. The value of `BSlope` is meaningless without some kind of "anchor"; this anchor is the CMKAT parameter `BSlopeOffset`. This value is set by the ControlParams file variable `E0BkgndSlope`, and is typically the same as the `E0Nominal` value.

The effect of a nonzero background slope comes as an adjustment to the detector rate:

$$S'_{FPD}(E, qU) = S_{FPD}(E, qU) - N_{pix}\texttt{BSlope}\ (qU - \texttt{BSlopeOffset}) \tag{3.61}$$

Where $S_{FPD}(E, qU)$ is the original, unadjusted detector rate, $S'_{FPD}(E, qU)$ is the adjusted detector rate, $N_{pix}$ is the number of active pixels in the region, `BSlope` is the background slope, $qU$ is the retarding potential set by the MS, and `BSlopeOffset` is the "anchor" CMKAT parameter described in Table 3.3.

For an integrated spectrum, which we expect to be monotonically decreasing, one would naiively expect a positive BSlope to be unphysical. However, this is only true for electrons which are created in the WGTS. If electrons are being created further downstream in the spectrometers, they could contribute to the background rate in a qU-dependent way. These are not beta decay electrons, but secondary electrons created by background processes, like the Rydberg background[88].

The effect of including a nonzero `BSlope` is explored in greater detail in Section 4.1. Recent results[44] have found `BSlope` to be consistent with zero, but this could change once more neutrino mass measurement data is collected. This parameter can be fitted in either krypton or tritium mode.

#### 3.4.3.5 Flux tube normalization at the detector

In tritium signal rate evaluation, there is some normalization by the size of the flux tube at the detector before `AScale` is applied. If the flux tube normalization is done correctly, it pushes the value of `AScale` closer to 1. An `AScale` close to 1 implies good understanding of the system.

The missing ingredient to the flux tube normalization is the magnetic field at the detector $B_{FPD}$: it is not given in the RunSummary. It can be estimated by its effect on the size of the flux tube, assuming the electron motion to be adiabatic:

$$\frac{B_{source}}{B_{FPD}} = \frac{\text{Flux tube diameter at source}}{\text{Flux tube diameter at FPD}} \tag{3.62}$$

Whereas the flux tube diameter at the source is just the diameter of the WGTS beamtube, the flux tube diameter at FPD is found by looking at a heat map of detector rates. We identify the ring at which the detected rates exhibit a steep and sudden drop. In this case, the two outer rings had hardly any rates compared to the inner rings, allowing us to estimate the diameter of the FPD flux tube to be 85 mm. Solving for $B_{FPD}$:

$$
\begin{aligned}
B_{FPD} &= B_{source} \cdot \frac{\text{Flux tube diameter at FPD}}{\text{Flux tube diameter at source}} \\
&= 2.52\,\text{T} \cdot \frac{85\,\text{mm}}{90\,\text{mm}} \\
&= 2.38\,\text{T}
\end{aligned} \tag{3.63}
$$

Getting the most precise value of $B_{FPD}$ isn't a high priority, because the `AScale` fit parameter can compensate for the rest of the rate normalization. However, it is a nice check of our understanding of the system, and fit results in Section 5 indeed show that `AScale` is close to 1. Recent simulations for the KNM2 measurement campaign have estimated a mean $B_{FPD}$=(2.381 ± 0.003) T over the active detector region[89].

### 3.4.4 Response function generation

During the initialization stage of the response function, the energy loss function class ProbabilityELoss constructs energy loss probability lookup tables using the convolution theorem method described in Section 3.2.4.

The response function class cmResponseFunction contains a member function responseFunction(), which evaluates the response function as a function of the electron energy $E$ and the retarding potential $qU$; it also passes along information on the column density (combination of the inputted nominal column density and the `ColAdj` parameter) and the `Delta10` parameter. Additionally, it has the capability to do an extra convolution of the resulting response function with a gaussian of fixed width (set by `FixedGaussianSigma` in the ControlParams file), or a flat distribution of fixed width (set by `FixedFlatWidth` in the ControlParams file).

During the CMKAT fitting process, the response function class (cmResponseFunction) is called repeatedly. Therefore, CMKAT implements the response function in the form of lookup tables, which use Equation 3.49 for fast lookup. The resultant lookup tables allow for faster computation of the response function, and are accurate as long as the column density values are within a few percent of the inputted nominal column density.

Two kinds of response functions are generated, based on the fit settings (Section 3.4.6): the single-pixel and the summed-pixel response functions. The single-pixel response function is just a function of the surplus energy $\delta$. The summed-pixel response function sums the response functions of all enabled pixels, whose surplus energies $\delta$ are the difference between the electron energy and the $qU$ of the 0th pixel

(near the center of the analyzing plane). This has the effect of smearing out the transmission edge a little bit (varies depending on settings, but is usually 1 eV-2 eV), because the constituent pixels map to slightly different retarding potential values in the analysing plane[90].

Tables are also created for the first- and second-order derivatives of the response function with respect to the nominal column density, so that responseFunctionFast() returns the response function value for a column density $\bar{\rho}d = \bar{\rho}d_{nominal}(1 + \texttt{ColAdj})$. It is designed to be numerically accurate for `ColAdj` values on the order of a few percent. For more information, see Section 3.4.3.2.

When fitting multiple runs together, a single response function is generated. The settings necessary to generate the response function, which include magnetic fields and nominal column density, are taken from the first run in the list.

### 3.4.5 Run and pixel combination

A fit mode refers to how the data is combined for fitting purposes. CMKAT features three kinds of run combinations and three kinds of pixel combinations.

The run combination options are: individual, appending, and stacking.

1. **Individual:** no combination. Each spectrum is fit independently of the other spectra, and there are no shared fit parameters. This kind of analysis is ideal for exploring time-dependent effects. These fits are generally faster because each individual fit has only $N_{subrun}$ data points, and make the least amount of assumptions. The major disadvantage is the lack of statistical power in one run.

2. **Appending:** simply appends all data points in the set of runs together, such that each appended spectrum will have $N_{subrun} \times N_{run}$ data points. Clearly these fits have greater statistical power, but runs must be carefully selected for stability of slow control parameters.

3. **Stacking:** data points whose $qU$ values are separated from each other on the same order as the high voltage's precision (of order 10 meV) are combined. This reduces the stacked spectrum to $N_{subrun}$ data points, whose $qU$ values come from the mean of a Gaussian fit of the $qU$ distribution, and whose counts are added for each $qU$ bin. There is lots of statistical power to be gained by combining runs in this manner, as long as the runs are carefully selected for stability of slow control parameters.

Typically, the number of subruns $N_{subrun}$ and the amount of time spent at each subrun (MTD) are the same for each run in a measurement campaign.

The pixel combination options are: summed, region, and individual. Within the CMKAT framework, the meta fit parameter `pixelGrouping` dictates which pixel combination mode is selected. Region selections must be defined within the ControlParams file.

1. **Summed:** the rates of all active pixels are summed. All fit parameters are shared (global). This mode is usually used as a first, quick fit.
2. **Region:** the detector is divided into different segments. These can be rings, pseudorings, quadrants, or any other configuration. The region rate is the sum of the rates of each active pixel belonging to that region. Fit parameters can either be shared (global) between regions, or unique to that region. This mode is usually used to explore spatial effects. It's also a middle ground between the high statistical power of summed mode versus the lower statistical power of individual mode.
3. **Individual:** special case of region mode, where each pixel is its own region. This mode has the least amount of assumptions built in about the relationship of fit parameters between pixels, but also takes a long time to fit due to high number of degrees of freedom. The caveat here is that there must be enough measurement time to ensure that there is enough statistical power to ensure stable fits for each pixel.

Choice of run and pixel combinations depend on the goal of the analysis.

### 3.4.6 Fit Modes

With the run and pixel combinations defined, we must consider whether the free fit parameters are shared between all regions, or unique to each region. A fit parameter which is shared between all regions is called a global fit parameter. A fit parameter which is unique to each region is called a region-dependent fit parameter.

Given the large number of fit parameters described in Table 3.3, it is both useful and necessary to optimize the fitting procedure. To demonstrate the necessity, let us consider a tritium fit in which the pixels are grouped into 8 regions, where two fit parameters (`mnu2` , `ColAdj` ) are global, three are region-dependent fit parameters (`AScale` , `Bkgnd` , and `DeltaE` ), and the rest are fixed. In such a scheme, the total

number of parameters to optimize is $2+3\times8 = 26$. Performing a $\chi^2$ minimization with 26 free parameters using a generalized nonlinear algorithm is inefficient. The CMKAT framework uses a three-level algorithm which is designed to take advantage of two major properties of the model: (1) the total $\chi^2$ is the sum of the $\chi^2$ of each region, and (2) two of the fit parameters are linear in the model (described in Section 3.4.6.1).

The three-level fit algorithm accomplishes this by breaking the minimization into top, intermediate, and lowest levels. At the **top level**, the CMKAT code invokes Minuit to perform a nonlinear minimization routine and find the values of the global fit parameters. This is done within the fit class cmM2Fit, by calling on cmM2Fit::minimize(). The values of the region-dependent parameters and the $\chi^2$ for each region are returned by the function cmM2Fit::chiSquaredWithPixelTerms(), which calls on the intermediate level fit. During Minuit's search for the best global fit parameters, the region-dependent parameters are set to the best-fit values from the intermediate level. Upon conclusion of the top level fit, all fit parameters (global and region-dependent) are reported, and the total $\chi^2$ (sum of $\chi^2$ for each region) is returned.

The **intermediate level** determines the region-dependent fit parameters (`DeltaE` , `Bkgnd` , and the normalization `AScale` or `RLine` ) and the $\chi^2$ for each region using the fitPixelTerms class to call fitPixelTerms::fitPixelDeltaEandLinearTerms(). This function does a one-dimensional search on the nonlinear parameter `DeltaE` , such that the $\chi^2$ returned from calls to the lowest level fit is minimized. During the one-dimensional search for `DeltaE` , the global parameters are set to their best-fit values from the top level fit, and the pixel-dependent linear parameters are set to their best-fit values, as determined by the lowest level fit.

At the **lowest level**, the values of the region-dependent linear parameters `Bkgnd` and (`AScale` or `RLine` ) and the respective region-dependent $\chi^2$ are found. This is done within the fitPixelTerms class, by the member function fitPixelTerms::TwoParamLinearFit(). During the fit, the global parameters are set to their best-fit values from the top level fit, and the `DeltaE` value is fixed to the current value from the one-dimensional search in the intermediate level. Details on how the lowest level fit works are discussed in Section 3.4.6.1. This section also gives the error estimation on the linear parameters, and tests how good the error estimation is.

While not all 13 fit parameters can be individually set to both global or region-specific mode, the analysis needs and model linearity were taken into account to design a few pre-set combinations of global and region-specific fit parameters. They are sorted into three types:

- Level 1: all fit parameters are global.

- Level 2: region-dependent `Bkgnd` , and (`AScale` , `RLine` ) for (tritium, krypton) fitting. Global `DeltaE` and (`mnu2` , `WLine` ) for (tritium, krypton).
- Level 3: region-dependent `DeltaE` , `Bkgnd` , and (`AScale` , `RLine` ) for (tritium, krypton) fitting. Global (`mnu2` , `WLine` ) for (tritium, krypton).

Given this description of the three-level algorithm, the connection between the "Level X" schemes listed above and how many fit levels are used should become clear: the "Level 1" fit only needs access to the top level, because all fit parameters are global; the "Level 2" fit only needs access to the top and lowest levels, because the `DeltaE` term is not region-dependent; and the "Level 3" fit needs access to the top, intermediate, and lowest levels.

#### 3.4.6.1 Lowest level fit derivation

In the two-parameter linear fit, the region-dependent linear terms (`AScale` , `RLine` ) and `Bkgnd` for (tritium, krypton) mode are extracted, along with the region-dependent $\chi^2$ term. Here the normalization will be generalized as $A$, and the background will be denoted as $B$. The $B$ used in the following derivation is the background per region, which corresponds to the CMKAT fit parameter `Bkgnd` scaled by the number of active pixels in the region: $B = N_{\text{activePix}} \times$ `Bkgnd` .

Let:

$y_i$ = Measured rate in the region, for subrun **i**
$A$ = Normalization (or scaling term), given by `AScale`
$B$ = Background rate per region
$x_i$ = Parameter-dependent, region-dependent model rate calculation, for fixed `DeltaE` and `mnu2` , for subrun **i**
$\sigma_i$ = Measured region-dependent rate error (RMS), for subrun **i**

A region-dependent chi square for these two (nuisance) parameters, $A$ and $B$, can then be expressed as:

$$\chi^2(A, B; x_i, y_i) = \sum_{i=0}^{N} \frac{(y_i - (Ax_i + B))^2}{\sigma_i^2} \tag{3.64}$$

Where $N$ is the total number of subruns considered. Note that each subrun has a corresponding potential energy, $qU_i$.

The optimum $A$, $B$ values are located at the minima of Equation 3.64:

$$\frac{\partial \chi^2}{\partial A} = \sum_{i=0}^{N} \frac{2 \cdot (y_i - (Ax_i + B)) \cdot x_i}{\sigma_i^2} = 0 \tag{3.65}$$

$$\frac{\partial \chi^2}{\partial B} = \sum_{i=0}^{N} \frac{2 \cdot (y_i - (Ax_i + B))}{\sigma_i^2} = 0 \tag{3.66}$$

That's just a system of 2 equations with 2 unknowns, so can be described with the following 2x2 matrix operation:

$$\begin{bmatrix} \beta & \delta \\ \delta & \epsilon \end{bmatrix} \begin{bmatrix} A \\ B \end{bmatrix} = \begin{bmatrix} \alpha \\ \gamma \end{bmatrix} \tag{3.67}$$

Where:

$$\alpha = \sum_{i=0}^{N} \frac{x_i \cdot y_i}{\sigma_i^2} \tag{3.68}$$

$$\beta = \sum_{i=0}^{N} \frac{x_i^2}{\sigma_i^2} \tag{3.69}$$

$$\gamma = \sum_{i=0}^{N} \frac{y_i}{\sigma_i^2} \tag{3.70}$$

$$\delta = \sum_{i=0}^{N} \frac{x_i}{\sigma_i^2} \tag{3.71}$$

$$\epsilon = \sum_{i=0}^{N} \frac{1}{\sigma_i^2} \tag{3.72}$$

$$\eta = \sum_{i=0}^{N} \frac{y_i^2}{\sigma_i^2} \tag{3.73}$$

The solutions of $A$, $B$ are then:

$$A = \frac{\begin{vmatrix} \alpha & \delta \\ \gamma & \epsilon \end{vmatrix}}{\begin{vmatrix} \beta & \delta \\ \delta & \epsilon \end{vmatrix}}, \; B = \frac{\begin{vmatrix} \beta & \alpha \\ \delta & \gamma \end{vmatrix}}{\begin{vmatrix} \beta & \delta \\ \delta & \epsilon \end{vmatrix}} \tag{3.74}$$

Where the final result comes from evaluation of the determinants:

$$A = \frac{\gamma\delta - \alpha\epsilon}{-\beta\epsilon + \delta^2} \tag{3.75}$$

$$B = \frac{-\beta\gamma + \delta\alpha}{-\beta\epsilon + \delta^2} \tag{3.76}$$

Due to the linear relationship of $A$, $B$ in the chi square described in Equation 3.64, this part of the fit is called a linear least squares fit. This is in contrast to the global level of the fit, where `DeltaE` and `mnu2` are highly nonlinear: that level of the fit is a nonlinear least squares fit, and does not have a closed-form solution.

In the code, it is much faster to evaluate $\chi^2$ by using the shorthand:

$$\chi^2 = \eta + A^2\beta - 2A\alpha + 2AB\delta - 2B\gamma + B^2\epsilon$$

**Errors on A, B:** Taking advantage of the linear nature of this fit, we can calculate the errors on $A$, $B$ analytically, assuming linear propagation of errors.

$$\sigma_A^2 = \sum_{i=0}^{N} \left(\frac{\partial A}{\partial y_i}\right)^2 \sigma_i^2 \tag{3.77}$$

$$\sigma_B^2 = \sum_{i=0}^{N} \left(\frac{\partial B}{\partial y_i}\right)^2 \sigma_i^2 \tag{3.78}$$

Using Equation 3.75 and Equation 3.76 to calculate the partial derivatives for each subrun $i$:

$$\frac{\partial A}{\partial y_i} = \frac{1}{-\beta\epsilon + \delta^2}\frac{\delta + x_i\epsilon}{\sigma_i^2} \tag{3.79}$$

$$\frac{\partial B}{\partial y_i} = \frac{1}{-\beta\epsilon + \delta^2}\frac{-\beta + x_i\delta}{\sigma_i^2} \tag{3.80}$$

Plugging Equation 3.79 into Equation 3.77, and Equation 3.80 into Equation 3.78:

$$\sigma_A^2 = \frac{\beta}{\epsilon\beta - \delta^2} \tag{3.81}$$

$$\sigma_B^2 = \frac{\epsilon}{\epsilon\beta - \delta^2} \tag{3.82}$$

**Testing error calculation:** For calculating the error on the parameters $A$ and $B$ there are typically three ways to skin the cat[91]:

1. Using Equation 3.81 and Equation 3.82. Call this the "error matrix" method.
2. Generating many Monte Carlo spectra with statistical fluctuation included, and examine the width of the extracted fit parameter distribution. Call this the "Monte Carlo" method.
3. Only for $B$: use the measurement points beyond the end of the beta spectrum. Call this the "background region" method.

We choose to test the estimated error calculation on $B$, because of the plethora of ways to test it.

The first step is to prepare Monte Carlo spectra that mimic the run conditions of run 56279 (KNM2 tritium mode measurement, RunSummary version 4b), which was selected at random. The set of potential setpoints, $qU$, the amount of time spent at each $qU$ (measurement time distribution), and all experimental settings (magnetic fields, etc) for the Monte Carlo mimic those found in run 56279. The measurement time distribution of the Monte Carlo was scaled up such that the total measurement time was 5 hours. Any less than this, and the minimizer has trouble fitting due to low statistics. The amount of time spent in the 'background region' (set of potential setpoints $qU$ above the nominal tritium endpoint region) for this 5 hour

run is 4648.18 s, which accounts for about 25.8% of the total measurement time. The Monte Carlo truth of $B$ was set to 0.001 53 cps/pixel, which is the fitted `Bkgnd` value of the real data.

For the error matrix method: one Asimov (not statistically fluctuated[1]) Monte Carlo-generated spectrum is generated and fit. The estimated error on $B$ comes from the Minuit error matrix calculation. The output per-pixel background error from fitting this run is:

$$\sigma_{\text{B, per pixel}} = 4.86 \times 10^{-5}\,\text{cps} \tag{3.83}$$

For the Monte Carlo method: 10000 statistically-fluctuated MC samples are generated with the same settings described above. Each of these 10000 samples is fit, and their fitted `Bkgnd` values are histogrammed (Figure 3.6).

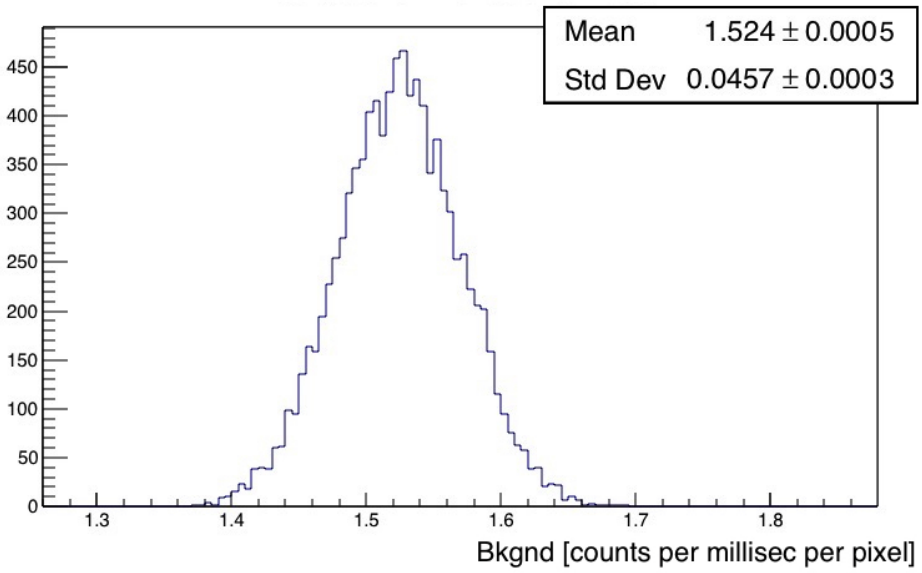


Figure 3.6: Histogram of `Bkgnd` values, from fit to MC-generated spectra, for 10000 MC trials.

The distribution of `Bkgnd` values in Figure 3.6 are fit by a Gaussian, where:

[1] An Asimov spectrum isn't *technically* "Monte Carlo", because there is no statistical fluctuation.

$$
\begin{aligned}
R_{\text{B, per pixel}} &= \text{Background rate per pixel} \\
&= \text{Mean of the histogram in Figure 3.6} \\
&= (152.40 \pm 0.05) \times 10^{-5}\text{cps} \\
\sigma_{\text{B, per pixel}} &= \text{Background rate error} \\
&= \text{Standard deviation of the histogram in Figure 3.6} \\
&= (4.570 \pm 0.003) \times 10^{-5}\text{cps}
\end{aligned} \tag{3.84}
$$

Finally, the background region method is checked. This method uses real data from the run 56279 RunSummary. There are 5 measurement points in the background region, where no tritium beta decay electrons are detected (or else they would have kinetic energy greater than the Q value, which is energetically disallowed).

From the RunSummary:

$$
\begin{aligned}
N_{\text{summed}} &= \text{Counts in the background region, summed over all active pixels} \\
&= 321\,\text{counts} \\
\Delta t &= \text{Total time spent in the background region} \\
&= 1788\,\text{s} \\
R_{\text{B, summed}} &= \text{Rate in the background region, summed over active pixels} \\
&= \frac{N_{\text{summed}}}{\Delta t} \\
&= 1.80 \times 10^{-1}\,\text{cps} \\
\sigma_{\text{B, summed}} &= \text{Fluctuation in rate in the background region, summed over active pixels} \\
&= \frac{\sqrt{N_{\text{summed}}}}{\Delta t} \\
&= 1.00 \times 10^{-2}\,\text{cps} \\
R_{\text{B, per pixel}} &= \text{Rate in the background region, per pixel} \\
&= \frac{R_{\text{B, summed}}}{117\text{ active pixels}} \\
&= 1.53 \times 10^{-3}\,\text{cps} \\
\sigma_{\text{B, per pixel}} &= \text{Fluctuation in rate in the background region, per pixel} \\
&= \frac{\sigma_{\text{B, summed}}}{117\text{ active pixels}} \\
&= 8.56 \times 10^{-5}\,\text{cps}
\end{aligned} \tag{3.85}
$$

Note that $R_{\text{B, per pixel}}$ matches the Monte Carlo truth value for `Bkgnd` (a requirement for the error estimation testing).

Compare the error on the extracted fit parameter $B$ per pixel between the three methods (Equation 3.83,Equation 3.84,Equation 3.85):

| Method: | $\sigma_{\text{B, per pixel}}$ [cps]: |
|---|---|
| Error matrix | $4.86 \times 10^{-5}$ |
| Monte Carlo | $4.57 \times 10^{-5}$ |
| Background region | $8.56 \times 10^{-5}$ |

Table 3.4: Comparison of calculated error on B per pixel, across three different methods.

The background region method's estimated background error per pixel is larger, suggesting that data points outside this region do provide some additional information on the background rate. But generally, the estimated error values are close. Compared to the per pixel background rate which they describe ($\approx 1 \times 10^{-3}$ cps), the error is on the percent level. Given this, we are free to choose the most time- and calculation-efficient method for calculating the errors on $A$, $B$: the error matrix method. This method has the advantage that it can be done *in situ* (within the same class that fits the $A$, $B$ values: fitPixelTerms), and does not require additional studies with Monte Carlo.

## 3.5 Validation

The purpose of validating the CMKAT framework is many-fold. The top reasons for undergoing validation is to establish trust in the validity of the results and for the sake of error catching. Trust is established by getting similar fit results, given the same input conditions, as compared to other parallel KATRIN fitting frameworks[61] (KaFit, Fitrium, and Samak). It is important to stress that the other fitting efforts are not assumed to be correct; only that there is an increased likelihood that our analysis methods are correct if all four fitters agree, within some uncertainty.

Preliminary validation steps were completed in cooperation with the KaFit team. This revealed the importance of a common fitting setting language. Final validation occurred during the data challenge phase of the official KNM2 neutrino mass analysis, in which all fitting teams were required to show that their respective frameworks could produce similar results, given a common set of Monte Carlo truths.

The validation was shown during a presentation[92] and was based on KNM2-like

conditions. This was done as part of the KNM2 data challenge, whose goals were:

1. Given the same experimental settings, compare the level of agreement for each model component, such that...
2. ...each team shall extract `mnu2` from another team's Asimov Monte Carlo-generated integrated tritium spectra, which is no further than $0.02\,\mathrm{eV}^2$ from the MC truth.

The first item is covered in Section 3.5.1. The second item, fitting benchmarking on MC-generated spectra, is covered in Section 3.5.2.

### 3.5.1 Compare model components

The model components to be compared are the source tritium spectrum and the response function. The ingredients to the response function (inelastic scattering probabilities, transmission function, and energy loss function) are tested individually before the full response function is calculated.

**Inelastic scattering probabilities** These values were calculated with script `teProbScat.C`. The relevant inputs for the calculation are given in the table below:

| CMKAT settings | | |
|---|---|---|
| **Category:** | **Setting:** | **Comments:** |
| $B_S$ [T]: | 2.52 | - |
| $B_{max}$ [T]: | 4.238 | - |
| $B_A$ [T]: | 0.0006308 | - |
| $\bar{\rho}d$ [molecule/cm$^2$]: | $4.2 \times 10^{17}$ | - |
| $\sigma_{scatter,inel}$ [cm$^2$]: | $3.642 \times 10^{-18}$ | Standard CMKAT setting is $3.64 \times 10^{-18}$ |
| Max num scatters: | 7 | - |

Table 3.5: Settings for inelastic scattering probability validation.

Two additional values of physical significance are calculated as an intermediate step:

$$\begin{aligned} \theta_{max} &= \text{Maximum accepted electron pitch angle, in radians} \\ &= 0.881 \\ \mu &= \text{Mean number of scatters at zero pitch angle} \\ &= 1.53 \end{aligned}$$

Using the values in Table 3.5, we can calculate the scattering probabilities for $S$ scatters. Since the probabilities decrease with increasing $S$, only the first three terms are calculated:

| Inelastic scattering probabilities, $P_S$ | | | | |
|---|---|---|---|---|
| $P_S$: | **CMKAT:** | **KaFit** | **Fitrium:** | **Samak:** |
| $P_0$ | 0.450100239 | 0.45009960151278972 | 0.45010023891625 | 0.450100239122969 |
| $P_1$ | 0.296113709 | 0.29611363743078756 | 0.29611370860149 | 0.296113708662095 |
| $P_2$ | 0.154287613 | 0.15428783669660842 | 0.15428761310708 | 0.154287613062644 |

Table 3.6: Let $P_S$ be the probability of scattering $S$ times. CMKAT probabilities agree with Fitrium and Samak on the $1 \times 10^{-9}$ level. This is because CMKAT only calculates to nine significant figures, and it seems unnecessary to go to more decimal places.

**Transmission function** The transmission function can be generated next, using script `teTransmissionFunction.C`. The settings are listed in Table 3.7, to match the settings required for the data challenge[93].

The transmission function is the simplest version of the response function because it doesn't include treatment of inelastic scattering and the energy loss function.

For this comparison of the transmission function, the synchrotron radiation loss corrections (recall Section 3.2.6) were included. To include these, the magnetic fields and effective lengths of the source and transport sections (WGTS and DPS+CPS, respectively) were needed. They are listed in Table 3.7. The last ingredient is the number of WGTS segments, because it is necessary to segment to WGTS in order to evaluate the synchrotron radiation losses. The number of segments was set to the

most simple case for this study (one segment). Later tests showed negligible changes to the agreement between the fitters' transmission functions when the segmentation was increased to 10 segments.

| CMKAT settings | | |
|---|---|---|
| **Category:** | **Setting:** | **Comments:** |
| $B_S$ [T]: | 2.52 | - |
| $B_{max}$ [T]: | 4.238 | - |
| $B_A$ [T]: | 0.0006308 | - |
| $B_T$ [T]: | 3.6 | Magnetic field in the transport section |
| $\bar{\rho}d$ [molecule/cm$^2$]: | $4.2 \times 10^{17}$ | - |
| $\sigma_{scatter,inel}$ [cm$^2$]: | $3.642 \times 10^{-18}$ | Standard CMKAT setting is $3.64 \times 10^{-18}$ |
| Max num scatters: | 0 | - |
| Lookup table E0Nominal [eV]: | 18545 | - |
| Synchrotron treatment: | ON | Num WGTS segments = 1<br>Analytic treatment (Groh PhD, Section 6.5.3)<br>$L1$ (eff. source length) = 5.041 m<br>$L2$ (transport section length) = 14.0 m |

Table 3.7: Settings for benchmarking the transmission function.

Two additional values of physical significance are calculated as an intermediate step:

$$\begin{aligned} \cos\theta_{max} &= \text{Acceptance factor } (=x_{min}) \\ &= 0.637 \\ \Delta E &= \text{MAC-E filter width (single central pixel), in eV} \\ &= 2.81 \end{aligned}$$

Note that the transmission function has been normalized by a factor of $\frac{1}{P_0(x_{min})}$ so that the probability goes to 1 (for large excess energy) in this comparison:

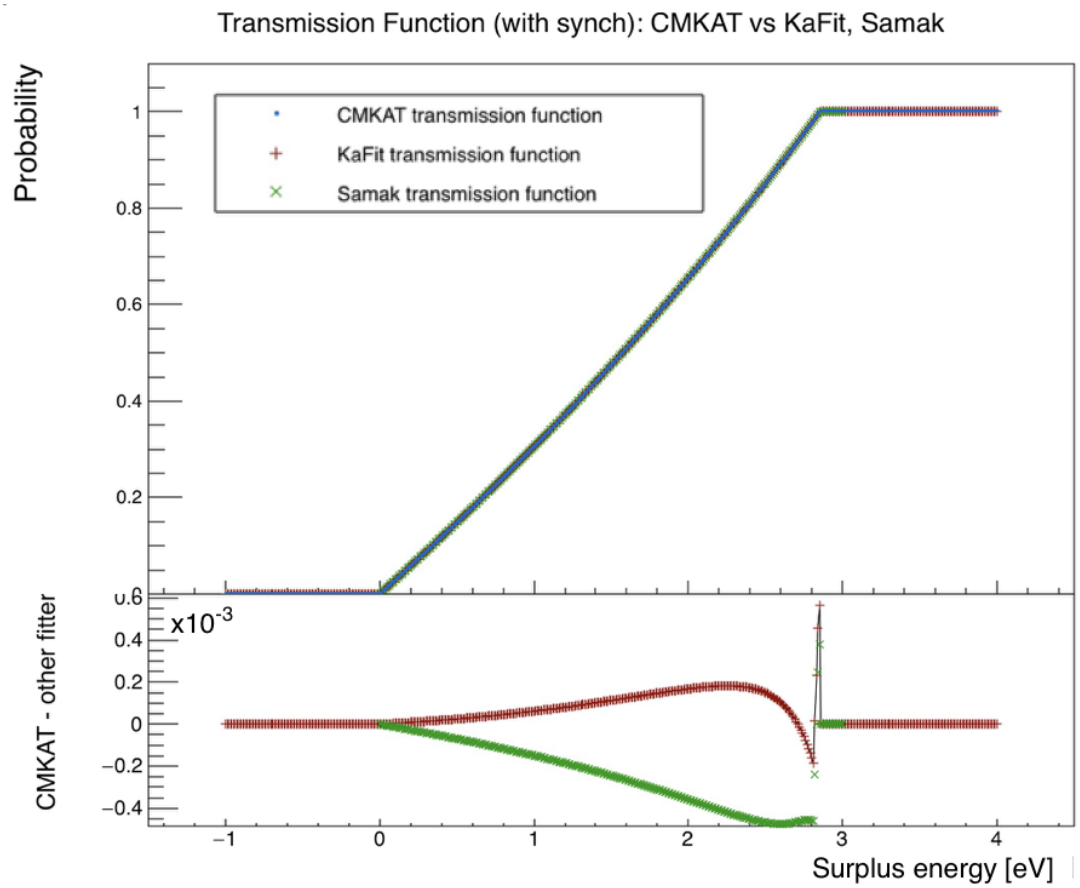


Figure 3.7: Transmission function, compared between CMKAT and other fitters. Agreement is on the $1 \times 10^{-4}$ level, with the CMKAT response function results lying between the other two.

**Energy loss function** Because the energy lost during the first scattering ($S$=1) is the greatest, the $S$=1 energy loss function is compared first. The test script is `teELoss.C`.

This was to test each fitter's implementation of the "KNM1-T2" parametrization[94] of the energy loss function (Section 3.2.4), as given by the energy loss function working group. An `E0Nominal` different from the usual nominal tritium `E0Nominal` is specified simply as a test to make sure that the individual fitters' codes could track changes to inputted `E0Nominal` values.

| CMKAT settings | | |
|---|---|---|
| **Category:** | **Setting:** | **Comments:** |
| Energy loss range [eV]: | (0,90) | In 0.1 eV increments |
| Max num scatters: | 1 | - |
| E0Nominal [eV]: | 18573.0 | - |
| Energy loss parametrization: | KNM1-T2 | See Section 3.2.4 |

Table 3.8: Settings for benchmarking energy loss function.

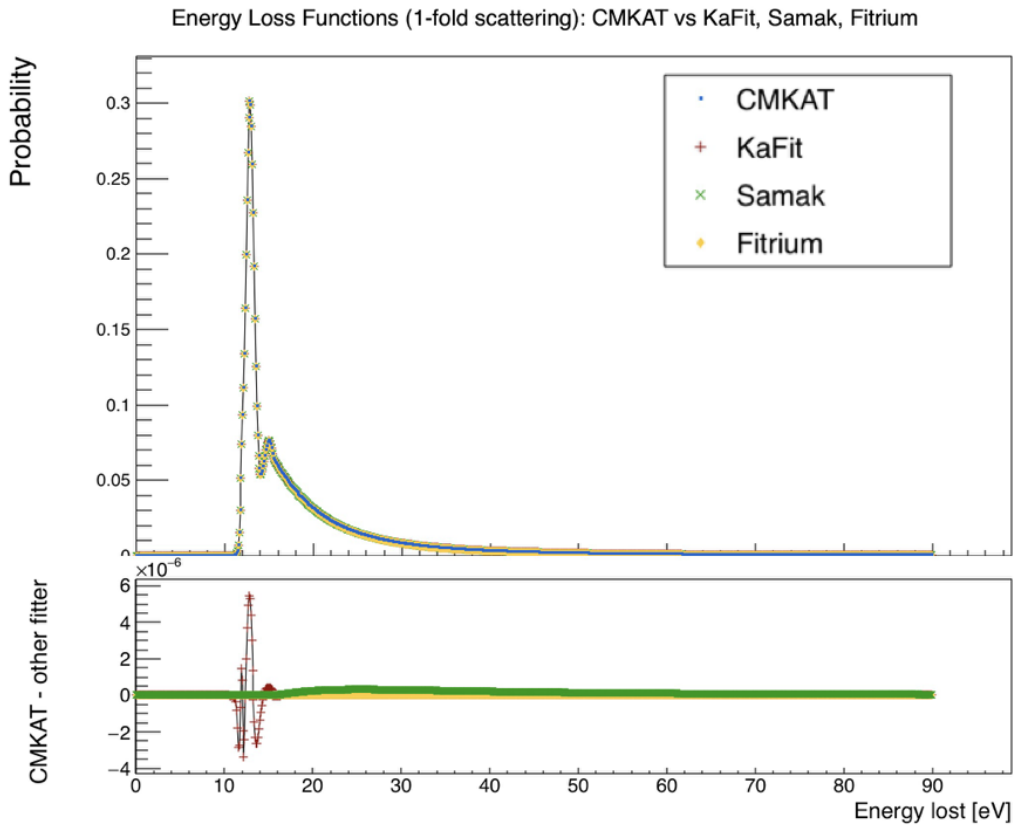


Figure 3.8: Energy loss function ($S$=1 only because this provides the largest contribution), compared between CMKAT and other fitters. Agreement is on the $1 \times 10^{-6}$ level.

At this stage, the validation team decided not to test higher scattering energy loss functions because the $S$=1 contribution showed agreement on the $1 \times 10^{-6}$ level, and the target agreement level for the final validation step (fitting MC data to extract a neutrino mass) was set to the $1 \times 10^{-2}$ level. Clearly the transmission function agreement ($1 \times 10^{-4}$) is the limiting factor thus far, so it seemed unnecessary to check the higher scattering energy loss functions.

**Response function** With the inelastic scattering probabilities, transmission function, and energy loss functions checked, the response function can be generated. The script for that is `teResponseFunction.C`.

| CMKAT settings | | |
|---|---|---|
| **Category:** | **Setting:** | **Comments:** |
| $B_S$ [T]: | 2.52 | - |
| $B_{max}$ [T]: | 4.238 | - |
| $B_A$ [T]: | 0.0006308 | - |
| $B_T$ [T]: | 3.6 | Magnetic field in the transport section |
| $\bar{\rho}d$ [molecule/cm$^2$]: | $4.2 \times 10^{17}$ | - |
| Energy loss function | KNM1-$T_2$ | See Section 3.2.4 |
| $\sigma_{scatter,inel}$ [cm$^2$]: | $3.642 \times 10^{-18}$ | Standard CMKAT setting is $3.64 \times 10^{-18}$ |
| Max num scatters: | 7 | - |
| Lookup table E0Nominal [eV]: | 18545 | - |
| Synchrotron treatment: | ON | Num WGTS segments = 1<br>Analytic treatment (Groh PhD, Section 6.5.3)<br>$L1$ (eff. source length) = 5.041 m<br>$L2$ (transport section length) = 14.0 m |
| Angular-dependent scattering probability treatment: | OFF | Non-standard CMKAT configuration setting (described below) |

Table 3.9: Settings for benchmarking the response function.

There is one particular setting to highlight: the angular-dependence of the scattering probability $P_S$. For this response function validation step only, the scattering probability is **not** angle dependent. The "angle-independent scattering probability" is defined by the following adjustment to the response function, where the scattering probability is a constant (evaluated at $\theta'_{max}$, which is independent of the surplus energy $\delta$):

$$R(\delta, \theta_{max}) = (1 - \cos(\theta_{max}(\delta))) \times \bar{P}_S(\theta'_{max}) \tag{3.86}$$

This is in contrast to the "angle-dependent scattering probability", where the scattering probability is evaluated at each $\theta_{max}$ (which is dependent on the surplus energy $\delta$, as shown in Equation 3.36):

$$R(\delta, \theta_{max}) = (1 - \cos(\theta_{max}(\delta))) \times \bar{P}_S(\theta_{max}) \tag{3.87}$$

This second approach (Equation 3.87) is consistent with the response function derivation in Section 3.2. Note that standard operating procedure with CMKAT is to include the treatment of angle-dependent scattering probabilities.

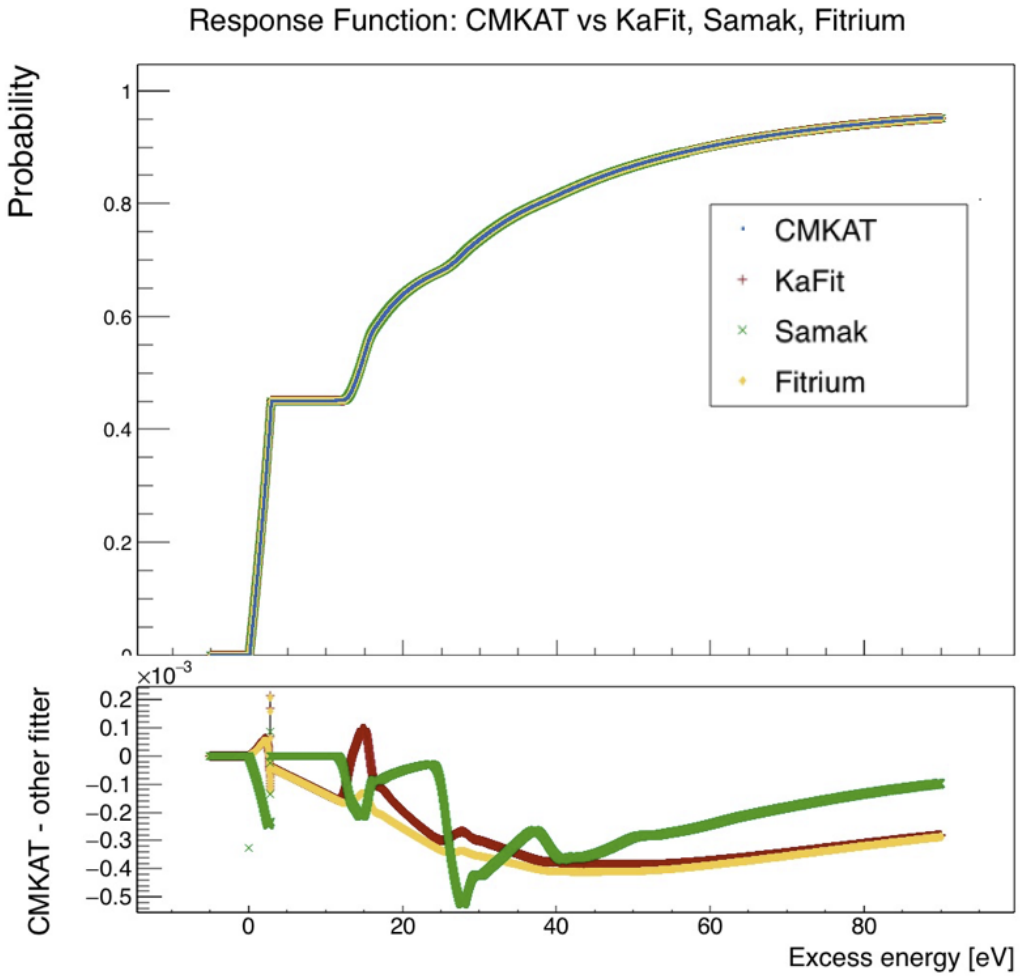


Figure 3.9: Response function, compared between CMKAT and other fitters. Agreement is on the $1 \times 10^{-4}$ level.

Figure 3.9 shows the results of the comparison between CMKAT and the other fitters, with agreement on the $1 \times 10^{-4}$ level.

**Source spectrum** The final step before combining into the integrated spectrum is to compare the source spectrum. The source spectrum here is the differential tritium beta decay spectrum, and includes the FSD treatment, which was still blinded at the time of the validation. The script used for this analysis is `teDiffSpec_withFSD.C`.

| CMKAT settings | | |
|---|---|---|
| **Category:** | **Setting:** | **Comments:** |
| E0Nominal [eV]: | 18573.7 | - |
| `mnu2` : | 0 | MC truth |
| Concentrations: | $T_2$=0.9754677<br>DT=0.0052227<br>HT=0.0185701 | - |
| FSD treatment: | ON | Using blinded KNM2 values ($T_2$, DT, HT) on GitLab |
| FSD $E_{merge}$ [eV]: | 0.05 | FSD number of final states after rebinning = 133 |
| $\bar{\rho}d$ [molecule/cm$^2$]: | $4.2 \times 10^{17}$ | - |
| $\sigma_{scatter,inel}$ [cm$^2$]:: | $3.642 \times 10^{-18}$ | Standard CMKAT setting is $3.64 \times 10^{-18}$ |
| Electron energy range [eV]: | (18483.7,18708.7) | Range of values at which the differential spectrum is evaluated<br>In 0.1 eV increments |

Table 3.10: Differential spectrum benchmark settings.

The comparison of differential spectra using the settings in Table 3.10 is shown in Figure 3.10. Agreement between fitters ranges between $1 \times 10^{-8}$ to $1 \times 10^{-11}$ level.

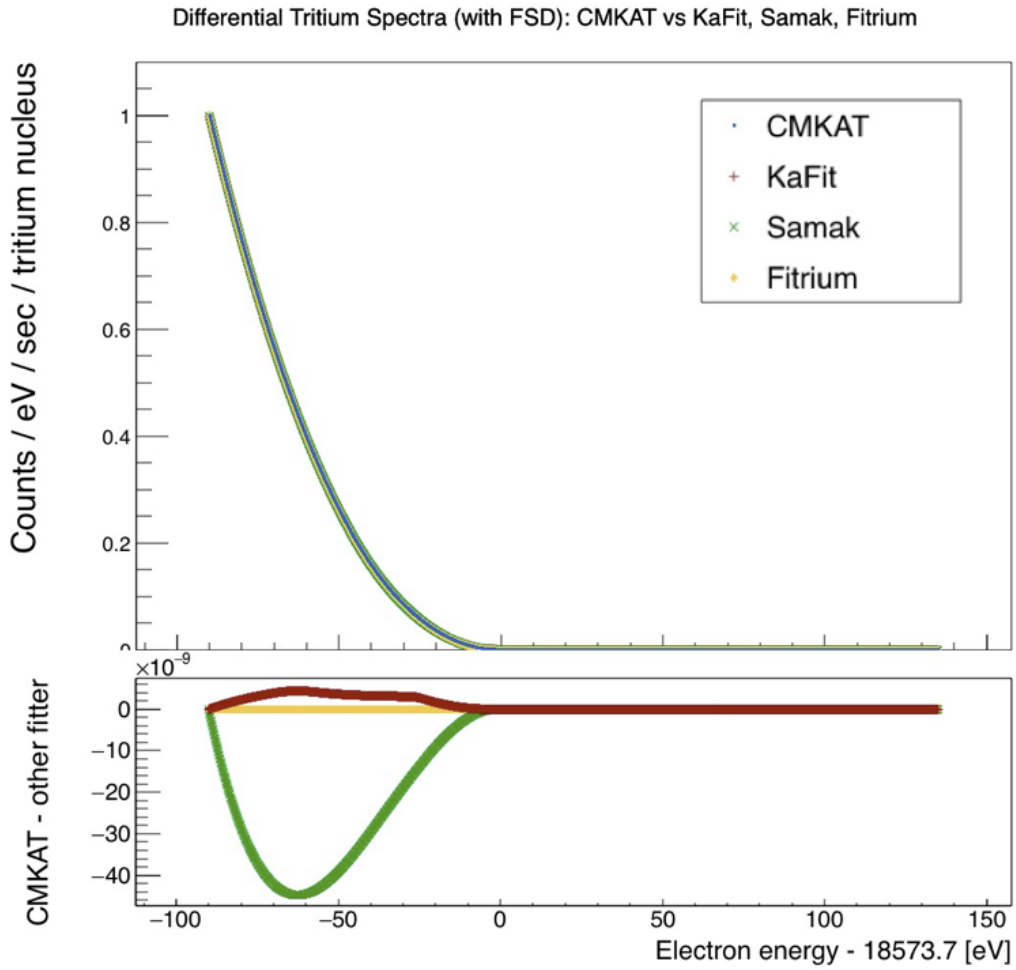


Figure 3.10: Differential spectra, compared between CMKAT and other fitters. Agreement is on the $1 \times 10^{-8}$ level for Samak, $1 \times 10^{-9}$ level for KaFit, and $1 \times 10^{-11}$ level for Fitrium.

### 3.5.2 Fitting MC-generated spectra

The final step in the validation process is to combine the source and response functions into an MC-generated integrated tritium spectrum, fit the spectrum, and measure the shift in `mnu2` . The MC spectrum is generated using the following settings in Table 3.11, without any statistical fluctuation.

| CMKAT MC-generation settings | | |
|---|---|---|
| **Category:** | **Setting:** | **Comments:** |
| MC truths | `DeltaE` = 0.7<br>`mnu2` = 0<br>`AScale` = 1.1<br>`Bkgnd` = 0.0001<br>`BSlope` = 0<br>`SigmaTr` = 0<br>`ColAdj` = 0<br>`Delta10` = 0 | All Kr-related parameters set to 0.<br>E0Nominal = 18 573.0 eV. |
| MTD | Scaled version of real 2 h run | Copy of MTD from reference RunSummary (Run 56341).<br>Counts and LiveTime values scaled by x100, to get a spectrum equivalent to a 200 hour measurement. |
| Energy loss function | KNM1-$T_2$ | See Section 3.2.4 |
| FSD | KNM2 blinded | - |
| Corrections | Synchrotron radiation loss = ON<br>Radiative correction = ON<br>Angle-dep scattering probability = FALSE | Num WGTS segments = 1<br>Analytic treatment (Groh PhD, Section 6.5.3)<br>L1 (eff. source length) = 5.041 m<br>L2 (transport section length) = 14.0 m |

Table 3.11: CMKAT validation Monte Carlo settings.

Fit settings are given below in Table 3.12.

| CMKAT fit settings | | |
|---|---|---|
| **Category:** | **Setting:** | **Comments:** |
| Fit level | 2 | Summed fit mode |
| Free params | `DeltaE` , `mnu2` , `AScale` , `Bkgnd` | - |
| Fixed params | `BSlope` = 0<br>`SigmaTr` = 0<br>`ColAdj` = 0<br>`Delta10` = 0 | All krypton parameters set to zero |
| Pixel selection | KNM2 Golden pixels | 117 active pixels |
| Fit pixel combination | Summed | - |
| Fit range ($qU$) | (-40, +50) eV around E0Nominal | E0Nominal = 18 573.7 eV<br>This corresponds to 28 subruns |
| Error type | Minuit | - |
| FSD $E_{merge}$ | 0.10 eV | - |

Table 3.12: CMKAT validation fit settings.

Generating an Asimov MC data set with CMKAT according to Table 3.11 and fitting it with CMKAT according to Table 3.12 demonstrates how well the original MC truth values can be recovered (first row of Table 3.13). Additionally, KaFit fit the CMKAT-generated MC data (second row of Table 3.13). KaFit also generated its own Asimov MC data set with the settings shown in Table 3.11, which CMKAT fit (third row of Table 3.13). Let $\Delta$`DeltaE` and $\Delta$`mnu2` stand for the difference between extracted fit value and MC truth values `DeltaE` and `mnu2` , respectively.

| Fit to CMKAT-generated MC data | | | |
|---|---|---|---|
| **Fitter:** | Δ `DeltaE` [eV]**:** | Δ `mnu2` [eV$^2$]**:** | $\chi^2$**:** |
| CMKAT | $-0.00009^{+0.044}_{-0.044}$ | $-0.025^{+0.53}_{-0.53}$ | 0.0037 |
| KaFit | $-0.014^{+0.044}_{-0.044}$ | $0.047^{+0.53}_{-0.53}$ | 0.0040 |
| Fit to KaFit-generated MC data | | | |
| **Fitter:** | Δ `DeltaE` [eV]**:** | Δ `mnu2` [eV$^2$]**:** | $\chi^2$**:** |
| CMKAT | $-0.012^{+0.041}_{-0.041}$ | $0.084^{+0.49}_{-0.49}$ | 0.00018 |
| KaFit | $-0.0001^{+0.043}_{-0.043}$ | $0.0032^{+0.63}_{-0.63}$ | 0.00026 |

Table 3.13: Results from fit: difference between MC truth and extracted fit value, for both CMKAT-generated and KaFit-generated MC data. Small $\chi^2$ values are expected because these fits are to Asimov spectra, so there are no statistical fluctuations. Additional details available[93].

The results are similar to others' MC value recovery results: the `mnu2` values are recovered on the $1 \times 10^{-2}$ level, with errors on the $1 \times 10^{-1}$ level; this is deemed sufficient for our validation purposes.

An additional MC validation check on the full 12.86 days' worth of KNM2-like data was passed, and is presented in Section 6.1.1.

## 3.6 Convergence tests

To test CMKAT convergence, we generate Asimov MC data and fit it with the exact same conditions. Ideally, the resulting $m_\nu^2$ would be exactly the MC truth, but because the modelled count rate isn't an analytical function, it's expected to begin deviating from the MC truth due to numerical noise at some level. This is done for different pixel combinations (summed and three kinds of regions: rings, patches, and individual pixels) and with either global or individual (region-specific) `mnu2` fit parameter treatment.

Since both the generated data and the fit model have all the same experimental inputs and corrections, they will not be listed here. What is important is the total measurement time and the set of MC truth values. They are given in Table 3.14.

| Convergence test settings | | |
|---|---|---|
| Category: | Setting: | Comments: |
| MC truth values | `DeltaE` =-0.7<br>`mnu2` =0.1<br>`AScale` =1.0<br>`Bkgnd` =0.0018 | All other fit parameters are set to zero. |
| Total measurement time | 1000 days | Approximately 3 years, which is the total KATRIN measurement time. |

Table 3.14: CMKAT convergence test settings.

During the fit, all four of these parameters are freed. The fit range is −40 eV to 10 eV around 18 573.0 eV. All 148 pixels are included, except in the case of the patch-regions because they were defined in a data-driven manner which excluded some pixels[95]. FPD pixel to region maps are shown in Figure 3.11; the excluded pixels are shown in white in Figure 3.11b. Fit results for different fit modes are listed in Table 3.15 below.

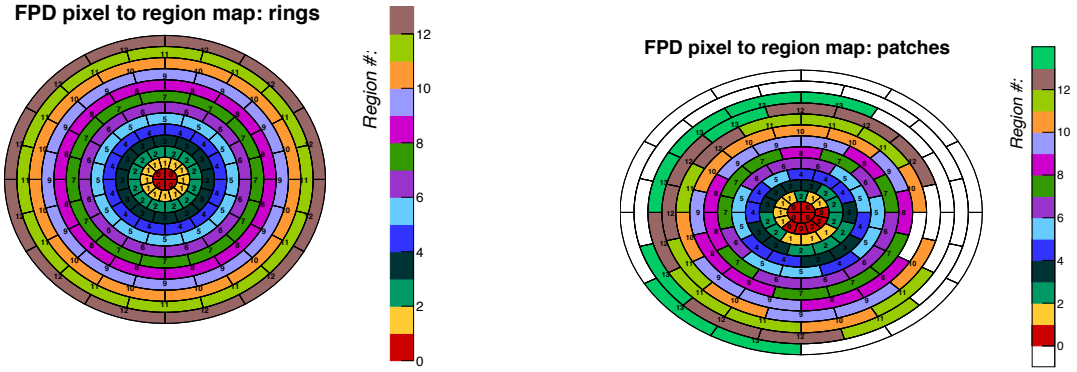


(a) The 13 ring regions.

(b) Patch regions.

Figure 3.11: FPD pixel to region maps.

| **Fit mode:** | $m^2_{fit} - m^2_{MC}$ [eV$^2$]**:** | $\binom{\textbf{upper error}}{\textbf{lower error}}$ **of** $m^2$ [eV$^2$]**:** | $\chi^2$**:** |
|---|---|---|---|
| Summed | 0.0023 | $^{+0.047}_{-0.047}$ | 0.00004/21 |
| Region: rings (individual $m^2_\nu$ ) | −0.0006* | $^{+0.002}_{-0.002}$ | 0.00000001/21 |
| Region: patches (individual $m^2_\nu$ ) | −0.0012* | $^{+0.0027}_{-0.0027}$ | 0.00000007/21 |
| Region: rings (global $m^2_\nu$ ) | −0.0007 | $^{+0.0080}_{-0.0080}$ | 0.00009/285 |
| Region: patches (global $m^2_\nu$ ) | −0.0012 | $^{+0.052}_{-0.051}$ | 0.0003/307 |
| Region: pixels (global $m^2_\nu$ ) | 0.00 | $^{+0.048}_{-0.047}$ | 0.000001/3255 |

Table 3.15: Comparison of extracted `mnu2` ($m^2_{fit}$) proximity to its MC truth ($m^2_{MC}$). For region fits with individual `mnu2` , each region is fit individually with its own unique `mnu2` . For this fit mode, the extracted `mnu2` fit value is the error-weighted average over all regions (marked with *), and the $\chi^2$ is that of Region 0. For region fits with global `mnu2` , there is just one `mnu2` (which is shared between all regions), and just one total $\chi^2$. All reported errors are CMKAT errors.

It is clear that summed fit mode gives the least accurate fit results. This can be attributed to the construction of the response function during the fitting process, which is a bit smeared due to the electric potential depression in the analyzing plane (additional radial electric potential offsets in the analyzing plane; see Section 3.2). For this reason, the pixel fit mode with global $m^2_\nu$ should give the most accurate reproduction of the data (and indeed, it does).

Although the pixel fit mode with global $m^2_\nu$ gives the most accurate results, it takes at least an order of magnitude more time than the next most accurate results (ring fit and patch fit with global $m^2_\nu$ ). Compromising between fitting time and fitting accuracy, any $m^2_\nu$ systematic studies shall use pseudoring fit mode with a global $m^2_\nu$ (see Section 6).

## 3.7 Conclusions

This chapter has introduced the analysis framework CMKAT. The modelling portion of CMKAT consists of the differential decay source models for krypton and tritium (Section 3.1), the response function (Section 3.2), and the final integrated spectrum (Section 3.3). The integrated spectrum model is a model of a few fit parameters, which is fit to data using custom classes described in Section 3.4.

CMKAT was successfully validated during a benchmarking step of the KNM2 campaign (Section 3.5). It showed that, for the same input settings, the response function was in agreement with other fitters' on the $1 \times 10^{-4}$ level, and the differential tritium spectrum agreed within $1 \times 10^{-8}$ to $1 \times 10^{-11}$. For 200 hours' worth of simulated data, CMKAT-generated Asmiov MC-generated spectrum with MC truth `mnu2` =0 were fit by another fitter, KaFit, which could recover the `mnu2` value on the $1 \times 10^{-2}$ level with errors on the $1 \times 10^{-1}$ level. The `mnu2` recovery was similar when CMKAT fit the KaFit-generated Asimov MC spectrum.

Section 3.6 shows the covergence of the CMKAT fit results on MC-generated Asimov data, which shows that it is sufficiently accurate for fitting $m_\nu^2$ with the final 1000 days' worth of neutrino mass measurement data.

# Chapter 4

# Krypton Analysis

$^{83m}$Kr was previously introduced as an excellent source for calibration and systematic studies. The decay from this second (metastable) excited state of $^{83}$Kr to its ground state (covered in Section 3.1.1) produces a number of fairly sharp (order 1 eV FWHM) lines at different energies. Krypton-mode measurements at the KATRIN experiment come in two types: one mode in which the krypton source is in a gaseous state (GKrS), and another in which the krypton source is in a condensed state ("CKrS").

In terms of utility, the GKrS and CKrS have different advantages. Because it is in a gaseous form and can occupy the WGTS simultaneously with the tritium gas, the GKrS is excellent for studying electron energy losses due to the gas in the source. It would be sensitive to the same starting potential energy conditions as the tritium, and can be used to characterize these conditions. The CKrS's main advantage is that it confines the emitted conversion electrons to a beam, which highlights a single detector pixel. This is useful for measurements which require high precision in electron position, and characterizing and calibrating the spectrometers.

In terms of experimental setup, the GKrS and CKrS also differ. In GKrS mode, the krypton (which comes from $^{83}$Rb trapped in zeolite beads) is introduced by attaching the krypton generator to the WGTS via Pump Port 2F (PP2F), and using a TMP to pump the krypton gas through a 4 mm-diameter capillary, which empties into the WGTS chamber at the centerpoint along the chamber's length[1]. During this mode of operation, the WGTS temperature must run at 100 K instead of the usual (tritium mode) 30 K to avoid freezing the krypton. Additionally, the infrastructure which in tritium mode would continuously purify the WGTS gas is deactivated, to prevent it from slowly just removing the krypton. These are the main differences between krypton and tritium operation for the GKrS. For more technical information, see

[1] Later campaigns use different circulation modes.

Section 7.7.3 of [49]. In CKrS mode, the krypton is condensed onto an Highly-Oriented Pyrolytic Graphite (HOPG) substrate at 25 K, creating a sub-monolayer film of area 4 $cm^2$ (the emitted beam size is further constrained by a 2 $cm^2$ aperture). The CKrS is then mounted to a movable carriage which sits on top of the CPS and is moved down into the beamline. More technical details are given in Section 7.7.2 of [49].

In this chapter, data taken in krypton mode using GKrS only, as well as data taken in Kr+Tr mode (GKrS and tritium simultaneously in the WGTS), are analyzed. Initial estimates at the beginning of the KNM2 campaign had pointed to source potential variation-related effects as the largest contributor to systematic uncertainty. In response to this, an investigation into the nature of the source potential was launched, making use of the Kr+Tr mode data. As part of these investigations of the source potential, we wished to estimate how much the source electrons' starting potential energies are smeared due to plasma-induced electric potential variations, where the plasma is non-neutral and consists of the charged decay products ($^3He^+$, electrons). The plasma-induced smearing has a broadening effect, and is studied in further detail in Section 4.1. Additionally, in an effort to compensate for spatial source potential inhomogeneities using hardware, Kr+Tr mode data is analyzed to predict an optimal RW voltage setting (Section 4.2).

## 4.1 Estimation of plasma-induced broadening

In tritium fits, the electric potential difference between the source and spectrometer sections affects the effective endpoint. While the spectrometer electric potential is well-known and controlled[49], variations in the source's electric potential aren't as well-known or controlled. These electric potential variations come from having a non-neutral plasma in the WGTS, which has some space charge distribution. This is what induces the electric potential variations, which affects the electrons' starting potential in the source section.

Three kinds of source electric potential (hereafter simply called "source potential") variation were identified: two related to spatial inhomogeneities, and one representing a fluctuation in time. The first spatial inhomogeneity considers a radial dependence of the mean source potential, and can be compensated by suitable choice of pixel combination during the fit (ringwise) and allowing a unique `DeltaE` for each ring-shaped region. The second spatial inhomogeneity considers the longitudinal variations of the source potential, an effect which smears the response function, and can be encoded in the form of Gaussian broadening term (as described in Section 3.4.3). Additionally, the response function terms corresponding to events with $\geq$1 scatterings tend to come

more often from decays occurring upstream in the WGTS (see Figure 4.2.1 in [66]). Thus the mean potential shift for electrons encountering inelastic scatterings is not necessarily identical to the mean potential shift for electrons experiencing no scattering. This effect can be encoded in the form of a longitudinal asymmetry parameter, $\Delta_P$[44]. This asymmetry parameter is characterized via phenomenological means[87], and will not be covered in this work.

The final kind of source potential fluctuation is a time-dependent one, which is expected to distort the tritium spectrum by (Gaussian) broadening. There is currently no way to disentangle the Gaussian broadening due to time-dependent fluctuations (on short timescales relative to runs) from the Gaussian broadening of the response function due to longitudinal effects. It is this total Gaussian broadening of potential (including the combined effects from the longitudinal potential variation and the time-dependent fluctuations) which will be studied in this chapter, and is referred to henceforth as the "plasma-induced broadening" term, $\sigma_P$. It will be studied in the context of the KNM2 measurement campaign.

Estimation of this plasma broadening necessitates a special data set: a measurement taken with both krypton and tritium in the WGTS. This special measurement is taken under the conditions similar to regular tritium measurements except at a higher source temperature; the measurement itself consists of MS scans across the various krypton lines (described in Section 3.1.1). The reason for this is two-fold: firstly, because the effect of a Gaussian broadening on a line scan is much easier to extract than a Gaussian broadening on a tritium spectrum. Secondly, the Gaussian broadening is strongly correlated with the neutrino mass parameter: in a tritium spectrum, the Gaussian broadening's effect will appear similar to a shift in neutrino mass squared.

We take into account an energy-dependent background slope `BSlope` , which could also contribute to the integrated spectrum, albeit in a more asymmetric way because there would be an excess of rates on one side of the line. This additional fit parameter was proposed after a close examination of measurements with data points extending far above a scanned krypton line (>10 eV) as depicted in Figure 4.1. Further study found that the linear increase in background, which was only discernible by eye in these "extended" measurements, was necessary to include in the model for krypton fits[96]. An underlying physics explanation has yet to be found to describe this background slope, but there is observational evidence of it (Figure 4.1).

One challenge to including a free `BSlope` fit parameter is that the data set we wish to analyze (KNM2 Kr+Tr) contains so few measurement points above the $L_3$-32 line peak. This causes a strong correlation between the `WLine` and the `BSlope` terms, resulting in unstable fit results when `BSlope` is freed. For this reason, an additional data set with a much larger range of measurement points above the line peak is

required. The only data set which fits these requirements was taken during the KNM3 measurement campaign. As long as the results from fits to the KNM3 data sets are properly normalized (as shown in Section 4.1.2), they can still be used for the KNM2 analysis.

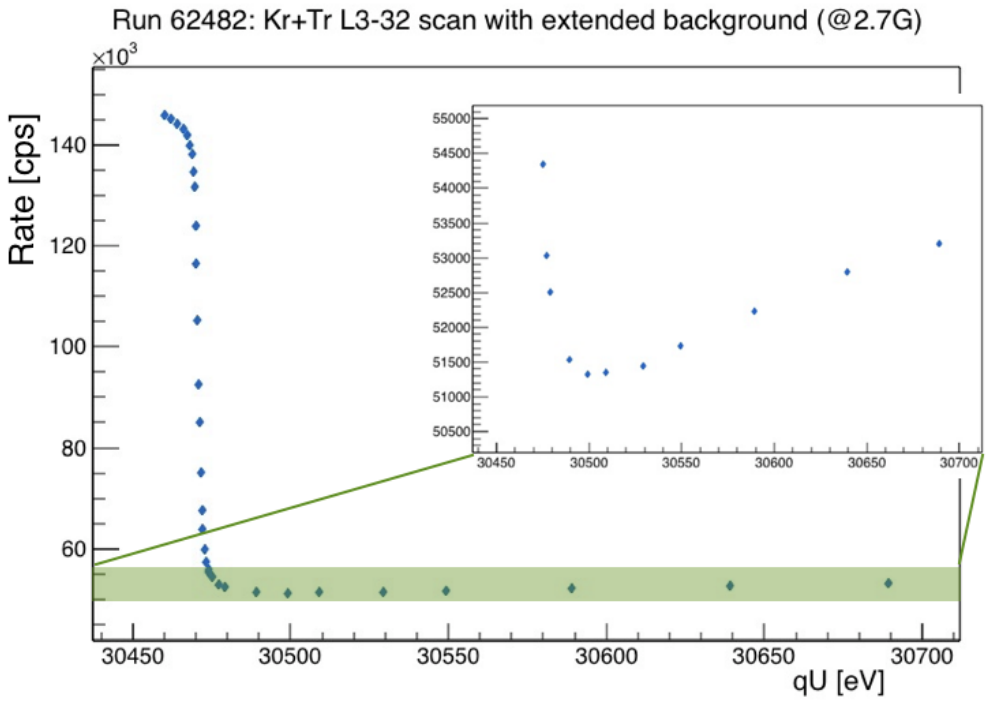


Figure 4.1: Run from the KNM3 Kr+Tr measurement campaign, with measurement points far above the $L_3$-32 line. By eye, one can see that the rate is increasing with qU in the inset (zoom-in of the green highlighted region).

### 4.1.1 Study outline

The plasma-induced broadening is extracted from the fit to KNM2 Kr+Tr data via a free `SigmaKr` fit parameter (described in Section 3.4.3). This study will analyze one of the most intense krypton lines, the $L_3$-32 line (recall Table 3.1). Motivation for the use of different data sets is given in each corresponding section.

The study is as follows:

1. Determine `BSlope` and `RLine` for each region, using KNM3 Kr+Tr data set (Section 4.1.2).

2. Determine natural line width via `WLine` , using KNM3 krypton-only data set (Section 4.1.3). To include `BSlope` information in this fit, we need to scale it properly:
    - Extract `RLine` from fit to KNM3 krypton-only data set, where `BSlope` is fixed at zero.
    - Calculate new scaled `BSlope` using `BSlope` and `RLine` from KNM3 Kr+Tr analysis, and `RLine` from KNM3 krypton-only analysis.
    - Fit KNM3 krypton-only data with `BSlope` fixed at these new scaled values. Extract `WLine` .
3. Determine plasma-induced broadening via `SigmaKr` , using the KNM2 Kr+Tr data set (Section 4.1.4).
    - Extract `RLine` from fit to KNM2 Kr+Tr data set, where `BSlope` is fixed at zero.
    - Calculate new scaled `BSlope` using `BSlope` and `RLine` from KNM3 Kr+Tr analysis, and `RLine` from KNM2 Kr+Tr analysis.
    - Fit KNM2 Kr+Tr data with `BSlope` fixed at these new scaled values, and `WLine` fixed at the value determined from the KNM3 krypton-only analysis. Extract `SigmaKr` .

The need for all these scaling steps will be elucidated in the following sections. For both the KNM2 and KNM3 data sets in the Kr+Tr configuration, only runs where WGTS contained tritium ($T_2$ gas) with a density of about 35% of nominal value were analyzed. This translates to an integrated column density d on the order of $1 \times 10^{18}$ molecule/cm$^2$. All data sets include only runs during which the RW was grounded.

### 4.1.2 `BSlope` calculation

The lack of enough measurement points above the $L_3$-32 line peak in the KNM2 Kr+Tr data results in unstable fits when the `BSlope` parameter is freed. Instead, we must turn to a different data set to get information on `BSlope` .

The data set with such an "extended measurement" in the region above the $L_3$-32 line peak comes from the KNM3 measurement campaign, and consists of just four scans of the $L_3$-32 line in the Kr+Tr configuration. The background rate is assumed to be an energy-independent term (`Bkgnd` ) plus a small correction which is linear in qU (`BSlope` ). The energy-dependent term `BSlope` is assumed to be proportional to the source count rate, as shown in Equation 3.61.

A complete run list is given in Appendix A.1.1.

For reasons explained later, this data set was fit for two different region selections (pseudoring and ring), otherwise using the same settings, outlined in Table 4.1. The pseudoring results are used in the final step, where the plasma-induced broadening $\sigma_P$ is calculated. The ring results are only used to determine the $L_3$-32 krypton natural line width, which is a single value, so it is okay to use a different region selection.

| KNM3 Kr+Tr fit settings | | |
|---|---|---|
| **Category:** | **Setting:** | **Comments:** |
| Error type | Minuit error matrix | - |
| Free params | `DeltaE` , `WLine` , `RLine` , `Bkgnd` , `BSlope` | All parameters are region-specific (none are global). |
| Fixed params | `SigmaKr` =0.052<br>`ColAdj` =0<br>`Delta10` =0 | All tritium parameters are fixed to zero.<br>`SigmaKr` comes from Table 3.2 for the corresponding measurement campaign. |
| Line position fit range | 30 462 eV-30 692 eV | - |
| Pixel combination | (1) Pseudoring<br>(2) Ring | Pseudoring includes 4 regions (Figure 4.2a)<br>Ring includes 13 regions ((Figure 4.2b)) |
| Pixel selection | KNM3 Golden Pixels | 125 pixels active |
| Response function settings | Max number scatters = 7<br>Transmission function = relativistic<br>Energy range = 0 eV-200 eV, in 0.01 eV steps | - |
| Integrated column density | Data table from SSC gas dynamics simulation for 35% nominal column density | `ColumnDensityProfiles_35.txt`<br>Described in Section 3.4 |
| Corrections | Synchrotron radiation loss | WGTS slices for synchrotron radiation = 1 |

Table 4.1: Fit settings for KNM3 Kr+Tr, to extract `BSlope` .

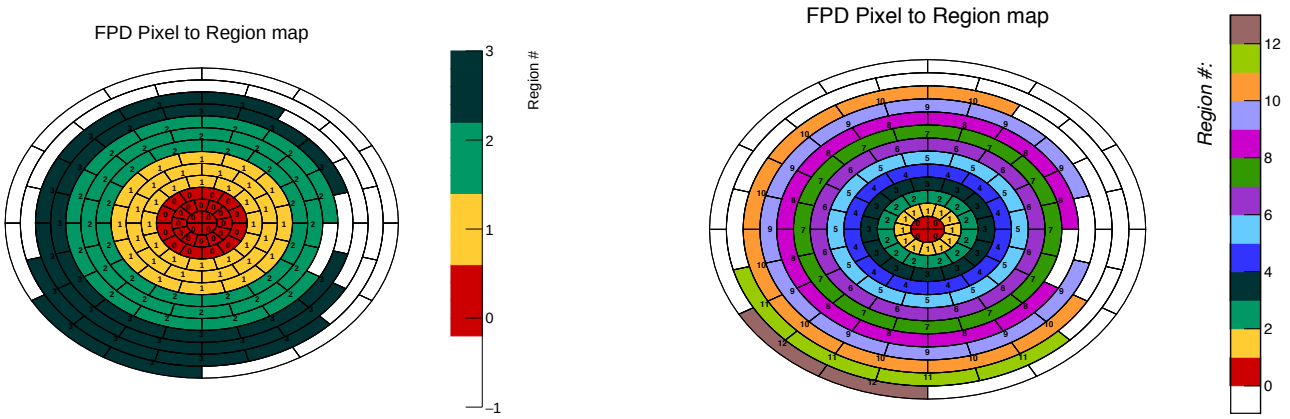


(a) Pseudoring regions.

(b) Ring regions.

Figure 4.2: KNM3 Golden Pixel selections[97], with different region mappings. Pixels in white are excluded (due to shadowing from the FBM and incomplete flux tube coverage of the outer pixels).

These measurements were taken during the KNM3 measurement campaign. Because the krypton line intensities differ from one measurement campaign to the next, we scale `BSlope` before plugging it into an other measurement campaign fit. Most experimental settings are kept the same from KNM2 to KNM3 (the measurement campaigns of interest in this study), so it is sufficient to use the line intensities `RLine` to scale.

$$\texttt{BSlope}_{\text{ other}} = \frac{\texttt{BSlope}_{\text{ KNM3Kr+Tr}}}{\texttt{RLine}_{\text{ KNM3Kr+Tr}}} \times \texttt{RLine}_{\text{ other}} \tag{4.1}$$

The factor of $\frac{\texttt{BSlope}_{\text{ KNM3Kr+Tr}}}{\texttt{RLine}_{\text{ KNM3Kr+Tr}}}$ in Equation 4.1 can be calculated now from the results of the fit, for both the pseudoring region selection (Table 4.2) and for ring region selection (Table 4.3).

| Region number: | $\texttt{BSlope}_{\text{KNM3Kr+Tr}}$ [cps/eVpixel]: | $\frac{\texttt{BSlope}_{\text{KNM3Kr+Tr}}}{\texttt{RLine}_{\text{KNM3Kr+Tr}}}$ [1/eVpixel]: |
|---|---|---|
| 0 | $-0.05882^{+0.00080}_{-0.00080}$ | $-0.0000189^{+0.0000003}_{-0.0000003}$ |
| 1 | $0.02218^{+0.00016}_{-0.00016}$ | $0.00000717^{+0.00000005}_{-0.00000005}$ |
| 2 | $0.15597^{+0.00059}_{-0.00059}$ | $0.000051^{+0.0000002}_{-0.0000002}$ |
| 3 | $0.15433^{+0.00015}_{-0.00015}$ | $0.0000699^{+0.00000007}_{-0.00000007}$ |

Table 4.2: Pseudoring values of BSlope and its estimated error (error-weighted mean over runs), and the calculated $\frac{\texttt{BSlope}_{\text{KNM3Kr+Tr}}}{\texttt{RLine}_{\text{KNM3Kr+Tr}}}$ from fit to KNM3 Kr+Tr extended data set. The $\frac{\texttt{BSlope}_{\text{KNM3Kr+Tr}}}{\texttt{RLine}_{\text{KNM3Kr+Tr}}}$ values are calculated from the BSlope and RLine fit results, and the associated errors propagated.

| Region number: | $\texttt{BSlope}_{\text{KNM3Kr+Tr}}$ [cps/eVpixel]: | $\frac{\texttt{BSlope}_{\text{KNM3Kr+Tr}}}{\texttt{RLine}_{\text{KNM3Kr+Tr}}}$ [1/eVpixel]: |
|---|---|---|
| 0 | $-0.06493^{+0.00003}_{-0.00003}$ | $-0.00002007^{+0.00000001}_{-0.00000001}$ |
| 1 | $-0.06291^{+0.0015}_{-0.0015}$ | $-0.0000194^{+0.0000005}_{-0.0000005}$ |
| 2 | $-0.04391^{+0.00003}_{-0.00003}$ | $-0.00001340^{+0.00000001}_{-0.00000001}$ |
| 3 | $-0.01337^{+0.0012}_{-0.0012}$ | $-0.0000036^{+0.0000004}_{-0.0000004}$ |
| 4 | $0.02179^{+0.00002}_{-0.00002}$ | $0.000007710^{+0.000000001}_{-0.000000001}$ |
| 5 | $0.06562^{+0.00002}_{-0.00002}$ | $0.000021940^{+0.000000007}_{-0.000000007}$ |
| 6 | $0.10918^{+0.00002}_{-0.00002}$ | $0.000036140^{+0.000000009}_{-0.000000009}$ |
| 7 | $0.15978^{+0.00002}_{-0.00002}$ | $0.00005269^{+0.00000001}_{-0.00000001}$ |
| 8 | $0.19857^{+0.0011}_{-0.0011}$ | $0.00006700^{+0.0000004}_{-0.0000004}$ |
| 9 | $0.21907^{+0.0009}_{-0.0009}$ | $0.0000768^{+0.0000003}_{-0.0000003}$ |
| 10 | $0.21112^{+0.00001}_{-0.00001}$ | $0.00007971^{+0.00000001}_{-0.00000001}$ |
| 11 | $0.12298^{+0.00001}_{-0.00001}$ | $0.00005686^{+0.00000001}_{-0.00000001}$ |

Table 4.3: Ring values BSlope and its estimated error (error-weighted mean over runs), and the calculated $\frac{\texttt{BSlope}_{KN\text{KNM3Kr+Tr}M3}}{\texttt{RLine}_{\text{KNM3Kr+Tr}}}$ from fit to KNM3 Kr+Tr extended data set. The $\frac{\texttt{BSlope}_{\text{KNM3Kr+Tr}}}{\texttt{RLine}_{\text{KNM3Kr+Tr}}}$ values are calculated from the exact BSlope and RLine fit results, and the associated errors propagated. Ring 12 wasn't fit because it has low statistics (very few active pixels).

As an example interpretation of the `BSlope` results of Table 4.2: the pixels in pseudoring Region 2 see on average 1.5 counts more (note the positive slope) at 10 eV above the tritium nominal endpoint than at the tritium nominal endpoint.

### 4.1.3 `WLine` calculation

Next, we must extract the natural line width of the $L_3$-32 line. To do this, we require a data set with just krypton gas present.

This dataset consists of 90 scans of the $L_3$-32 krypton line, with just krypton gas in the WGTS, during the KNM3 campaign. This dataset is referred to as a "krypton reference measurement", and is ideal for doing analysis free of the plasma-induced broadening. This is due to the very low scattering gas column density, which means that there is no partial ionization of the gas via scattering with the krypton conversion electrons. The Rear Wall (RW) is grounded for this set of runs.

A complete run list is given in Appendix A.1.2.

| KNM3 krypton-only fit settings | | |
|---|---|---|
| **Category:** | **Setting:** | **Comments:** |
| Error type | Minuit error matrix | - |
| Free params | `DeltaE` , `WLine` , `RLine` , `Bkgnd` | All parameters are region-specific (no global parameters). |
| Fixed params | `BSlope`<br>`SigmaKr` =0.060<br>`ColAdj` =0<br>`Delta10` =0 | `BSlope` values are fixed using the KMN3 Kr+Tr `BSlope` values from column 3 of Table 4.2 and Table 4.3, scaled by the preliminary fitted `RLine` using Equation 4.1.<br>All tritium parameters are fixed to zero.<br>`SigmaKr` rounded up from value in Table 3.2 by selecting the appropriate measurement campaign. |
| Fit range | 30 464 eV to 30 487 eV | - |
| Pixel combination | Rings | Level 3 (each region has unique `DeltaE` ) |
| Pixel selection | KNM3 Golden Pixels | 125 pixels active<br>See Figure 4.2b |
| Response function settings | Max number scatters = 1<br>Transmission function = relativistic<br>Energy range = 0 eV-200 eV, in 0.01 eV steps | - |
| Corrections | Synchrotron radiation loss | WGTS slices for synchrotron radiation = 1 |

Table 4.4: Fit settings for KNM3 krypton-only, to extract `WLine` .

As described in the study outline, in order to use the `BSlope` values found in the previous step (Table 4.2, Table 4.3), they must be properly scaled. In order to use Equation 4.1, the `RLine` value per region for this KNM3 krypton-only data set is needed. This is acquired by doing a fit using the settings in Table 4.4, except that the

BSlope parameter is fixed to zero. The extracted RLine value from this preliminary fit is then plugged into Equation 4.1, and using the appropriate BSlope values from Table 4.3, the correctly scaled BSlope values for the KNM3 krypton-only fits are found. This is done on a run-by-run basis, but the mean BSlope values are listed in Table 4.5.

| Region number: | Mean BSlope [cps/eVpixel]: |
|---|---|
| 0 | $-0.01712^{+0.00004}_{-0.00004}$ |
| 1 | $-0.01638^{+0.00157}_{-0.00157}$ |
| 2 | $-0.011380^{+0.000008}_{-0.000008}$ |
| 3 | $-0.00324^{+0.00124}_{-0.00124}$ |
| 4 | $0.005650^{+0.000005}_{-0.000005}$ |
| 5 | $0.01687^{+0.00002}_{-0.00002}$ |
| 6 | $0.02812^{+0.00003}_{-0.00003}$ |
| 7 | $0.04165^{+0.00004}_{-0.00004}$ |
| 8 | $0.0517^{+0.0012}_{-0.0012}$ |
| 9 | $0.0573^{+0.0009}_{-0.0009}$ |
| 10 | $0.05489^{+0.00005}_{-0.00005}$ |
| 11 | $0.03175^{+0.00003}_{-0.00003}$ |

Table 4.5: Mean values for scaled BSlope of each region in the KNM3 krypton-only data set, using Equation 4.1, and their associated propagated errors (which agree with the BSlope errors in column 2 of Table 4.3). Region (ring) 12 wasn't included because it has low statistics (very few active pixels). This table is meant to inform the reader on the sizes of BSlope , and are not the fixed values used in the next step.

A sample krypton spectral fit result for Region 0 of Run 61152 is shown below in Figure 4.3:

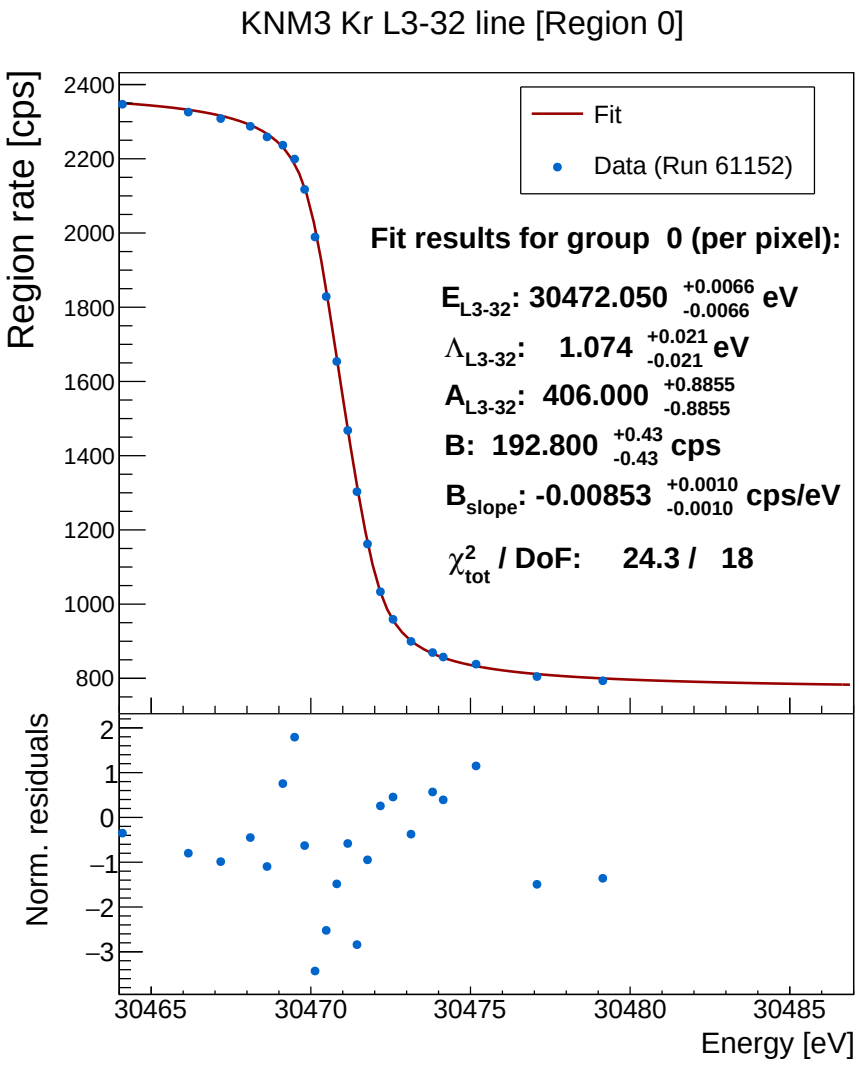


Figure 4.3: Fit results of KNM3 krypton-only data set, using the settings described in Table 4.4, with a `BSlope` value calculated for the specific run, according to Equation 4.1. $E_{L_3\text{-}32}$ is the absolute line position (`E0Line - DeltaE` ), $\Lambda_{L_3\text{-}32}$ is the natural line width (`WLine` ), $A_{L_3\text{-}32}$ is the intensity (`RLine` ), B is the background (`Bkgnd` ), and $B_{slope}$ is the linear background slope (`BSlope` ). The data rate errors are too small to see on this scale; they are $\mathcal{O}(10)$ cps. The residuals are normalized by the data rate error.

With these scaled `BSlope` values fixed, the KNM3 krypton-only data set is fit using the settings in Table 4.4. The natural line width parameter (`WLine` ) can be extracted for each of the ring regions, for each of the runs. Fit results for the free parameters, averaged over each region, are displayed in Figure 4.4 below.

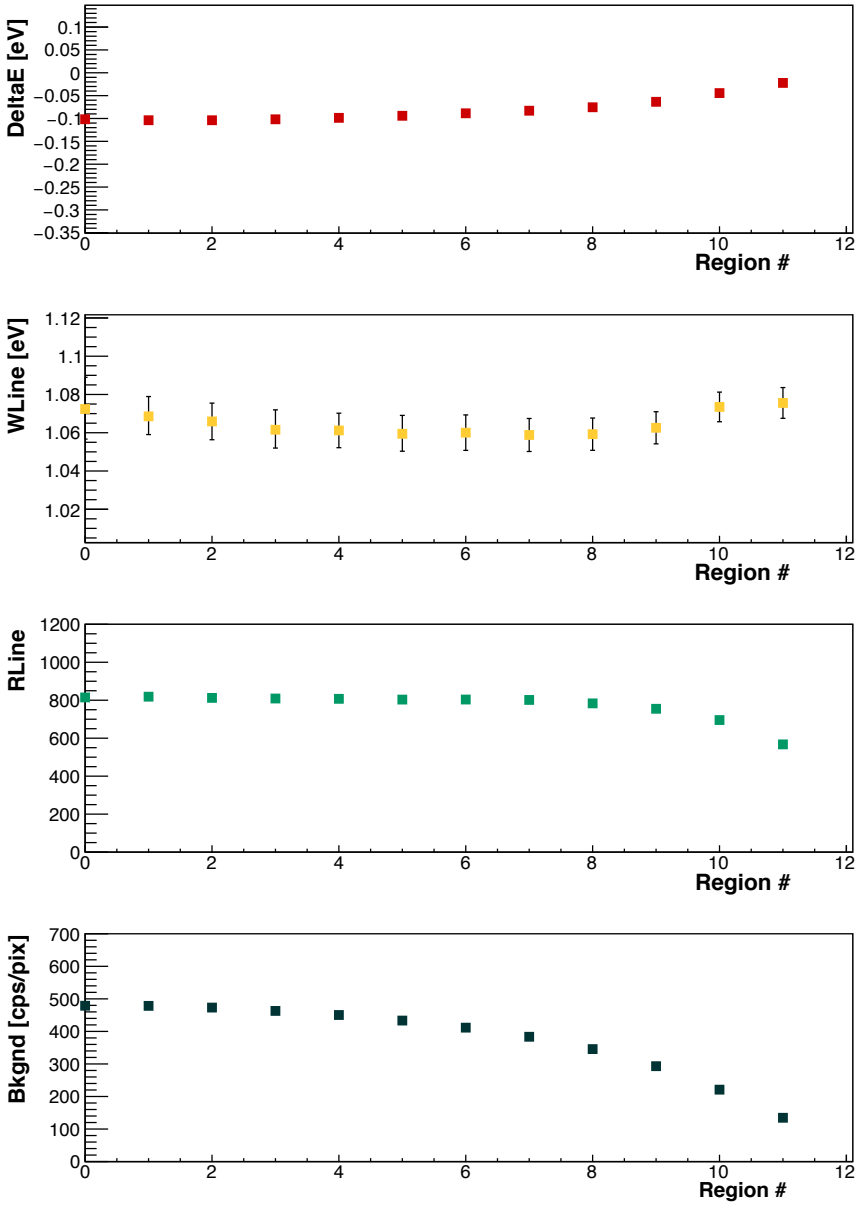


Figure 4.4: Fit results of KNM3 krypton-only data set, using the settings described in Table 4.4, and the fixed `BSlope` values calculated for each individual run, using Equation 4.1. The error bars on `DeltaE` , `RLine` , and `Bkgnd` are too small to see on the scales displayed. The radial dependence of `DeltaE` , `RLine` , and `Bkgnd` was confirmed by [98], which is likely due to reaching the flux tube limits (`RLine` ) and flux tube misalignment (`DeltaE` and `Bkgnd` ). Misalignment causes the pixel-wise calculated magnetic field and potential values to be incorrectly mapped to the true path the electrons have taken through the analyzing plane (see [98]: Section 5.9).

The `WLine` averaged over Regions 0 - 11 (shown in Figure 4.4) is:

$$\texttt{WLine} = (1.066 \pm 0.020)\,\text{eV} \tag{4.2}$$

This agrees quite well with the results of a separate analysis on the same dataset, and with an analysis using Condensed Source (CKrS) data. This first analysis on the same dataset found the $L_3$-32 natural line width to be $(1.074 \pm 0.039)$ eV[98, 99], whereas the analysis using CKrS data concluded that $(1.0606 \pm 0.0150)$ eV[100]. At a later point, it was decided that the CKrS value would be used in all analyses because it was the most conservative estimate (i.e., it is the lowest value of the three), as well as for the sake of consistency between parallel efforts.

### 4.1.4 Fit of $\sigma_P$

The main data set consists of 202 scans of the $L_3$-32 krypton line while the WGTS is filled with krypton and tritium gas ("Kr+Tr"), taken during the KNM2 campaign.

A complete run list is given in Appendix A.1.3. The scans are taken over a range of RW bias voltages between $-5$ V to 5 V, so that some preliminary conclusions could be drawn about the effect of the RW on the plasma.

| KNM2 Kr+Tr fit settings | | |
|---|---|---|
| **Category:** | **Setting:** | **Comments:** |
| Error type | Minuit error matrix | - |
| Free params | `DeltaE` , `SigmaKr` , `RLine` , `Bkgnd` | The parameters are all region-specific (no global parameters). |
| Fixed params | `BSlope` given in Table 4.2 scaled as shown in Equation 4.1<br>`WLine` =1.0606<br>`ColAdj` =0<br>`Delta10` =0 | All tritium parameters are fixed to zero. |
| Fit range | 30 464 eV-30 487 eV | - |
| Pixel combination | Pseudoring | 4 ring-shaped regions<br>See Figure 4.5 |
| Pixel selection | KNM2 Golden Pixels | 117 active pixels |
| Response function settings | Max number scatters = 1<br>Transmission function = relativistic<br>Energy range = 0 eV-200 eV, in 0.01 eV steps | - |
| Integrated column density | Data table from SSC gas dynamics simulation for 35% nominal column density | `ColumnDensityProfiles_35.txt` |
| Corrections | Synchrotron radiation loss | WGTS slices for synchrotron radiation = 1 |

Table 4.6: Fit settings for KNM2 Kr+Tr plasma broadening study.

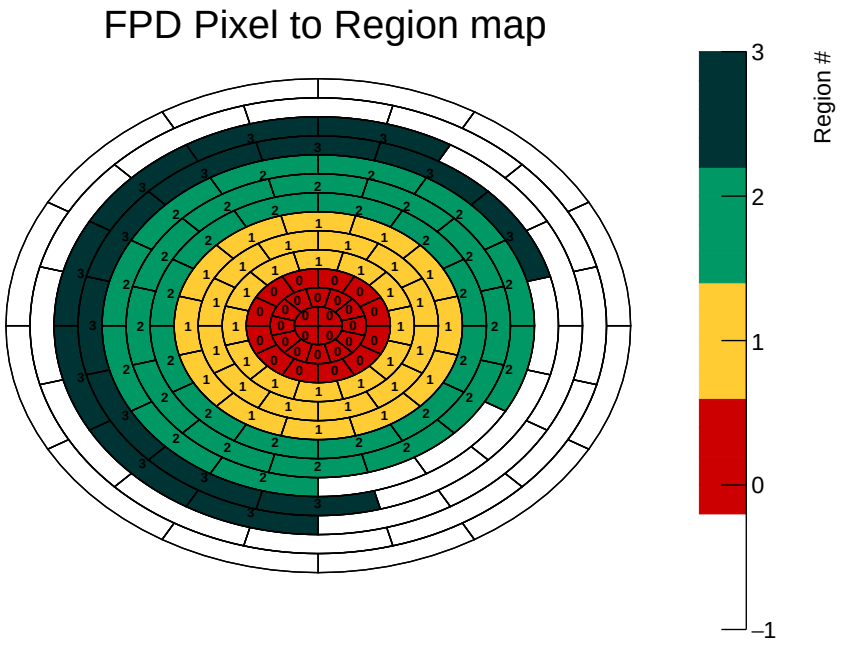


Figure 4.5: KNM2 Golden Pixel selection[101], with pseudoring region mapping. Pixels in white are excluded (due to shadowing from the FBM, incomplete flux tube coverage of the outer pixels, and relatively poor detector energy resolution). Pseudoring regions were selected as a compromise between taking into account radial effects and having enough statistics in each region to ensure stable fits.

Recalling Equation 4.1, it is necessary to do a preliminary fit of this KNM2 Kr+Tr data set to get `RLine` (= $\texttt{RLine}_{\text{other}}$) for each ring. Following the fit settings in Table 4.6 but with `BSlope` fixed at 0, this intermediate step allows us to calculate the scaled `BSlope` values for each ring using the results of Table 4.2. The fully scaled `BSlope` values are presented graphically in Figure 4.6, as they vary over both region and RW setting. Each `BSlope` value is set for its respective region- and RW setting-specific fit.

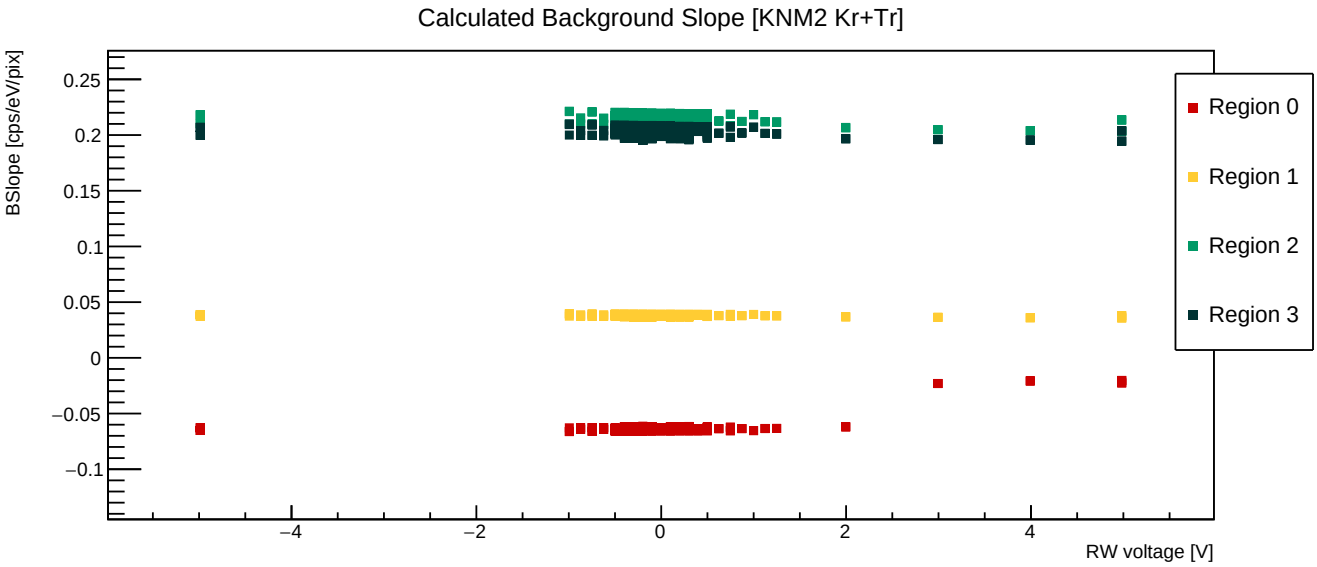


Figure 4.6: `BSlope` values calculated using Equation 4.1, for use in KNM2 Kr+Tr fits. The associated errors are expected to be on the same order as those in Table 4.2 ($1 \times 10^{-4}$ cps/eVpixel level).

With these scaled `BSlope` values (Figure 4.6) and the agreed-upon `WLine` value (1.0606 eV) in hand, the KNM2 Kr+Tr data set can be fit. The fit parameter of interest here is `SigmaKr` , which represents the total Gaussian broadening of the $L_3$-32 krypton line (on top of the line's natural width). Assuming that the only components are the Doppler broadening and the plasma-induced broadening, they add in quadrature like so:

$$\texttt{SigmaKr}^{\,2} = \sigma_{Dopp}^2 + \sigma_P^2 \tag{4.3}$$

Where:

$\texttt{SigmaKr}$ = Total Gaussian broadening extracted as a CMKAT fit parameter, in eV.
$\sigma_{Dopp}$ = Doppler broadening, given in KNM2Kr+Tr entry in Table 3.2
= 0.059 eV
$\sigma_P$ = Plasma-induced broadening, in eV.

The subset of data taken at RW voltages −0.4 V to 0.4 V is of particular interest because it is considered to be a regime which offers good coupling of RW potential

to the source potential[102]. This means that the space charge distribution (thus the plasma) is dictated by the electric potential conditions at the RW.

For this subset of scans, which were measured with the RW potential within the good coupling regime, the mean $\sigma_P$ per region is shown in Figure 4.7 below:

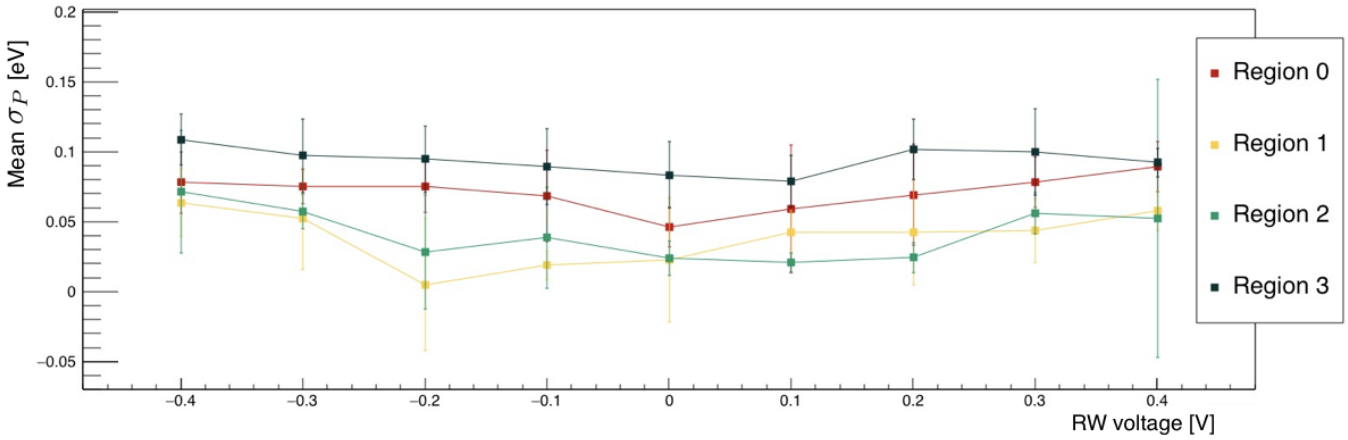


Figure 4.7: Mean $\sigma_P$ per pseudoring region.

The RW voltage setting of 0.2 V is of particular interest because it corresponds to the setting used for typical KNM2 neutrino mass measurements. For this RW setting, the mean plasma-induced broadening $\sigma_P$ for each region is given in Table 4.7.

| **Region number:** | $\sigma_P$ [eV]**:** |
|---|---|
| 0 | $0.0693 \pm 0.0011$ |
| 1 | $0.0425 \pm 0.0007$ |
| 2 | $0.0243 \pm 0.0018$ |
| 3 | $0.1019 \pm 0.0004$ |

Table 4.7: Mean Gaussian line broadening induced by the plasma, for RW set at 0.2 V. The error is the standard error from the Minuit error matrix.

To get a single mean plasma broadening value $\bar{\sigma}_P$, the results in Table 4.7 are combined in a weighted sum, where the weights correspond to the fraction of active pixel members in that region:

$$
\begin{aligned}
\bar{\sigma}_P &= \sum_{i=0}^{3} w_i \sigma_{P,i} \\
&= \left(\frac{28}{114}\right) 0.069265 + \left(\frac{36}{114}\right) 0.042514 + \left(\frac{34}{114}\right) 0.024304 + \left(\frac{16}{114}\right) 0.101908 \\
&= 0.0480\,\text{eV}
\end{aligned} \tag{4.4}
$$

The square of the error is given by the average squared sum of each region's error, weighted by $w_i^2$. Combining this with Equation 4.4:

$$
\bar{\sigma}_P = (0.0480 \pm 0.0006)\,\text{eV} \tag{4.5}
$$

This agrees with the value calculated by Raphael Ostertag in a parallel analysis: $\bar{\sigma}_P = (0.0492 \pm 0.0032)\,\text{eV}$[103].

Note that the plasma broadening value given in Equation 4.5 is lower than the value quoted in the KNM2 paper ($\sigma_P^2 = 12.4 \times 10^{-3}\,\text{eV}^2 \rightarrow \sigma_P = 0.111\,\text{eV}$ [44]) due to the fact that the KNM2 Kr+Tr runs are at lower column density than typical KNM2 tritium runs (35% and 84% of the nominal column density). The whole $\sigma_P$ extraction study can be repeated for different combinations of column densities (75% nominal column density) and krypton lines (the N2,3-32 doublet); with these data points, a value for $\sigma_P$ at higher (84% nominal) column density can be extrapolated.

## 4.2 Optimal RW setting

Previous measurement campaigns had operated under the assumption that no source (plasma-induced) potential would be created, therefore all surfaces abutting the tritium gas (WGTS beamtube and the RW) were grounded. However, once the tritium concentration was increased to non-trivial amounts (from 0.5% in a tritium commissioning campaign to $\mathcal{O}(95)$% in KNM2), a radial dependence of the effective tritium endpoint showed up (and was detected without compromising the blinding strategy). This meant that the electrons in the inner portion of the flux tube were experiencing a different starting potential than electrons in the outer portion of the flux tube. The prime candidate for causing radial source potential gradient is the unaccounted-for plasma-induced potential.

Though the radial dependence of the effective endpoint is an effect which can be taken into account by forming ring-shaped regions and assigning each region its own endpoint fit parameter, it is in the best interest of the KATRIN experiment to mitigate the radial inhomogeneity as much as possible with suitable hardware settings. In this case, it was suggested that optimizing the RW potential (voltage bias) could be a useful mitigation tool. The following study is used to inform choice of RW setting, as a first step towards a more homogeneous radial effective endpoint.

### 4.2.1 Study outline

The following study seeks to estimate an optimal RW voltage. A useful tool for this is the GKrS, because shifts in the krypton line position are much easier to track than shifts in the tritium decay spectrum. Here we choose to analyze the $L_3$-32 krypton line due to its high intensity. The study is outlined as follows:

1. Check that krypton-only ($L_3$-32 line) measurements don't show dependence on the RW voltage.
2. Fit a set of Kr+Tr ($L_3$-32 line) measurements which were taken at varying RW voltages, according to Table 4.9.
3. Extract the average `DeltaE` (a measure of the relative line position) for each region and each RW voltage.
4. Define a radial homogeneity criterion, and find the RW voltage which minimizes this criterion.

### 4.2.2 Verification of RW voltage-independence in krypton-only measurements

Plasma conditions can only be replicated with tritium in the WGTS. However, it was necessary to have a standard set of krypton reference measurements without tritium on hand. Comparing extracted fit parameters from these reference measurements to those extracted from combined Kr+Tr runs offers insight on plasma-induced effects.

**Data Selection** 43 scans of the $L_3$-32 line (using GKrS) were taken during the KNM3 campaign. The RW voltages took on values between $-5\,\mathrm{V}$ to $5\,\mathrm{V}$. A complete list of runs included in the analysis can be found in Appendix A.1.4. The

run summaries used are version `Prompt6b`. The PeriodSummary used is version `Jun2020b-32000V_2.7G`.

**Fit** The CMKAT-specific fit settings are outlined in Table 4.8:

| **Category:** | **Setting:** | **Comments:** |
|---|---|---|
| Fit level | 3 | - |
| Free params | `DeltaE` , `WLine` , `RLine` , `Bkgnd` | Unique to each region. |
| Fixed params | `BSlope` = 0<br>`ColAdj` = 0 ,<br>`SigmaKr` = 0.05<br>`Delta10` =0 | All tritium parameters set to 0.<br>`SigmaKr` is set to the Doppler broadening value. |
| Pixel selection | KNM3 Golden Pixels | 125 pixels active<br>See Figure 4.2b |
| Fit pixel combination | Pseudoring | 4 ring-shaped regions |
| Fit range (qU) | (-5, +15)eV around `E0Line` | `E0Line` = 30 472.0 eV<br>The lower fit range bound is selected to avoid increased rates due to shake-off lines (not implemented in CMKAT) |

Table 4.8: Table of fit settings for KNM3 krypton-only reference scans, at different RW voltages.

Plotting the extracted `DeltaE` (offset to krypton line position, relative to `E0Line` defined in Table 4.8) values versus RW setting:

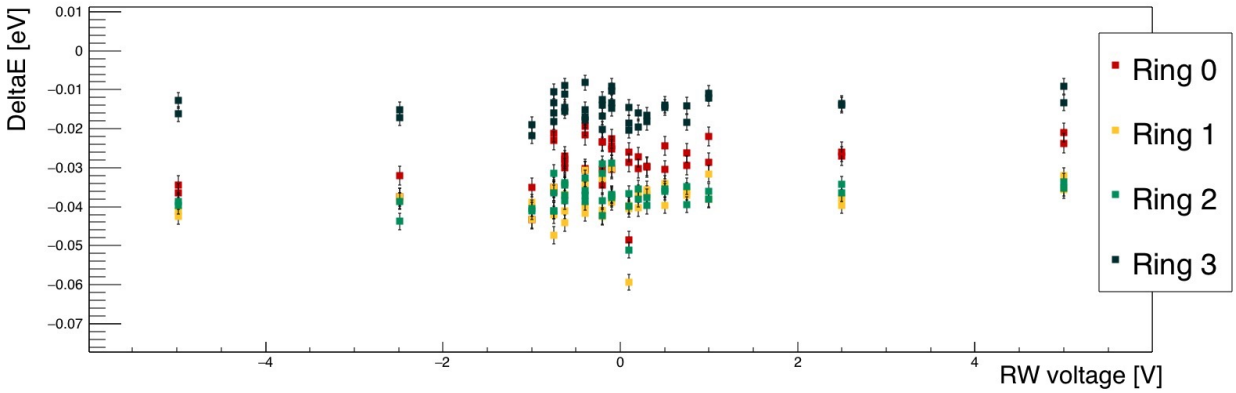


Figure 4.8: Fit results for KNM3 krypton-only data set. There appears to be no pattern in RW voltage versus line position. This behavior is expected, because we have no plasma-induced effects in the absence of tritium in the WGTS. The tiny radial dependence is a side-effect of small beamline misalignment, and is of no consequence for this analysis.

### 4.2.3 Fit to Kr+Tr data, over many RW voltages

Let the criterion for an optimal RW setting be one which minimizes the gradient in extracted krypton $L_3$-32 line position. In other terms, this optimal RW voltage would minimize the radial dependence of the starting potential.

**Data Selection** 16 scans of the $L_3$-32 line in Kr+Tr measurement mode, during the KNM3 campaign. The RW voltage settings took on a range of values between $-0.05\,\mathrm{V}$ to $0.3\,\mathrm{V}$. A complete list of runs included in the analysis is given in Appendix A.1.5. The run summaries used are version `Prompt6b`. The PeriodSummary used is version `Jun2020b-32000V_2.7G`.

**Fit** The CMKAT-specific fit settings are outlined in Table 4.9:

| Category: | Setting: | Comments: |
|---|---|---|
| Fit level | 3 | - |
| Free params | `DeltaE` , `WLine` , `RLine` , `Bkgnd` | Unique to each region |
| Fixed params | `BSlope` = 0<br>`SigmaKr` = 0.05<br>`ColAdj` = 0<br>`Delta10` = 0 | All tritium parameters set to zero.<br>`SigmaKr` is set to the Doppler broadening value. |
| Pixel selection | KNM3 Golden Pixels | 125 pixels active |
| Fit pixel combination | Ring | 12 rings + bullseye<br>See Figure 4.2b |
| Fit range (qU) | (-5, +15)eV around `E0Line` | `E0Line` = 30 472.0 eV<br>The lower fit range bound is selected to avoid increased rates due to shake-off lines (not implemented in CMKAT) |

Table 4.9: Table with fit settings for KNM3 Kr+Tr $L_3$-32 line scans.

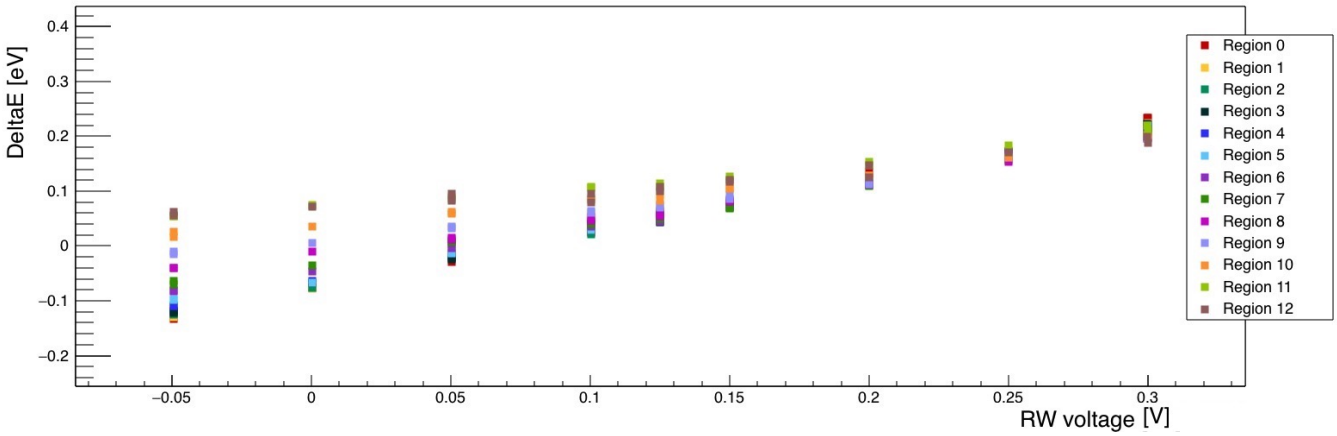


Figure 4.9: Radial dependence of energy shift, as a function of RW voltage setting. Error bars are included, but too small to see on this scale (they are $\mathcal{O}(10^{-3})$eV).

Figure 4.9 reveals a dependence of relative line position `DeltaE` on the RW voltage.

This range of RW voltages are in a "good coupling" region[102], which means that the space charge distribution (thus the non-neutral plasma) is dictated by the electric potential conditions created by the RW. This is why the region-averaged `DeltaE` at each RW voltage moves in proportion to the change in RW voltage. But more importantly, Figure 4.9 reveals a pattern in the spread in the radial `DeltaE` values: some RW settings seem to result in larger radial spread than others. Additionally, there seems to be a clear trend of decreasing radial spread up to around 0.2 V, after which the spread begins to increase again. This trend can be exploited to interpolate a RW voltage setting which would have minimal radial spread: the one which minimizes the radial `DeltaE` spread is the optimal RW voltage setting.

The criterion for optimal RW voltage setting is based on minimizing the quantity $\Delta$`DeltaE` $_{\text{outer,inner}}$, which is defined as the difference in relative line position (extracted `DeltaE` ) between an outer ring and an inner ring. The analysis group originally selected Ring 9 (outermost ring with most azimuthal pixel coverage) and Ring 1 (chosen to be near but not at center). This is shown with the red data and corresponding fit curve in Figure 4.10. Additional criteria were tested: difference between Rings 8 and 0 ($\Delta$`DeltaE` $_{8,0}$) in yellow, and difference between Rings 10 and 0 ($\Delta$`DeltaE` $_{10,0}$) in green; they are also shown in the figure.

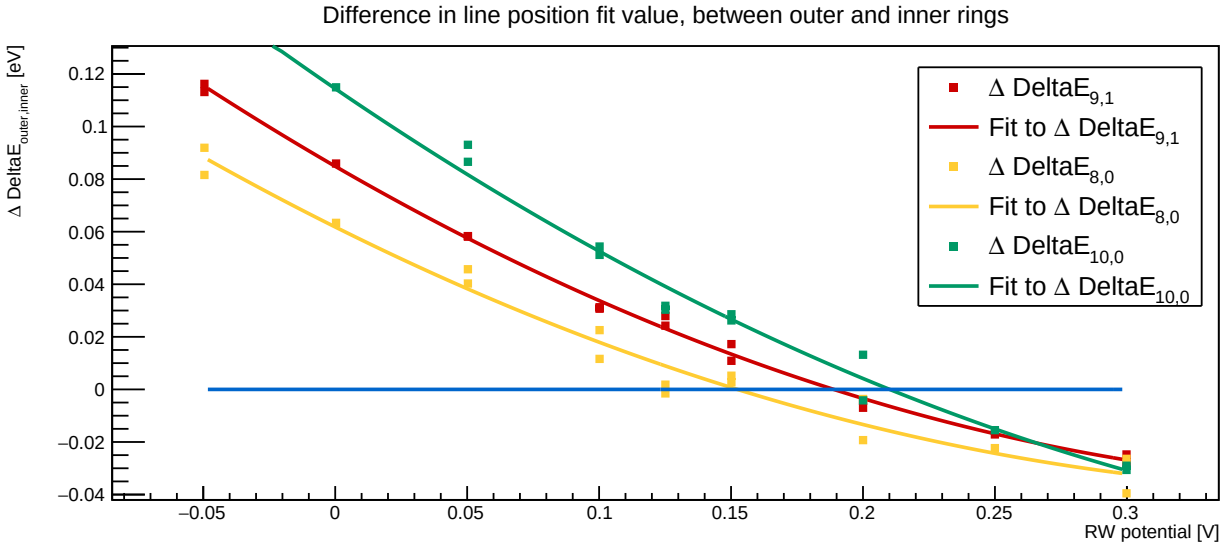


Figure 4.10: Difference in line positions ($\Delta$`DeltaE` $_{\text{outer,inner}}$) for specified criteria. The intersection between the ideal radially homogeneous `DeltaE` case (blue line at $\Delta$`DeltaE` $_{\text{outer,inner}} = 0$) and a fit (second order polynomial) to the RW-averaged differences is the estimated optimal RW voltage, $U_{RW,opt}$, for that particular criterion. For the analysis group-defined criterion $\Delta$`DeltaE` $_{9,1}$ (red), $U_{RW,opt} = 188\,\text{mV}$. Two other criteria were tested: $\Delta$`DeltaE` $_{8,0}$ (yellow) yielded $U_{RW,opt} = 152\,\text{mV}$. $\Delta$`DeltaE` $_{10,0}$ (yellow) yielded $U_{RW,opt} = 210\,\text{mV}$.

According to Figure 4.10, there is a nearly 60 mV range (±30 mV around the middle criteria, $\Delta$DeltaE $_{9,1}$) of optimum RW voltages, depending on the selected criterion. Another parallel study, using a different approach and data set, estimated the optimum RW voltage to be around $(160 \pm 20)$ mV[98]. A second parallel study using the same approach as the previous one estimated an optimal RW voltage of $(175 \pm 14)$ mV[104]. But both these studies also concluded that the extracted optimum RW voltages were highly dependent on experimental settings, so it was not possible to give a precise optimal RW voltage recommendation.

Though we could not provide an extremely precise optimal RW voltage recommendation, we were able to define a range of good RW voltage values to use. Considering that before these studies, the RW voltage hadn't been considered as a tool for mitigation of radial potential-related effects, it represents a huge leap in understanding of the plasma characteristics. Since the time of this analysis, the RW voltage has remained around 200 mV for recent neutrino mass measurements.

## 4.3 Conclusions

These studies show that the CMKAT model and fitting procedure (for both krypton and Kr+Tr) produce stable results which are in agreement with results from several other parallel analysis efforts.

The Kr+Tr analysis demonstrates the effects of a non-neutral plasma (when tritium concentrations are high) in the WGTS. The observed increase in krypton line width is likely due to variations in electric potential induced by this plasma, resulting in an RMS broadening $\bar{\sigma}_P$ of $(0.0480 \pm 0.0006)$ eV. Distortions in the spectrum due to radial-dependent potential shifts can be mitigated by introducing ring-shaped regions with independent DeltaE fit parameters for each region, and by selecting a RW voltage which minimizes radial potential inhomogeneity ($U_{RW,opt}$=150 meV-210 meV).

Neutrino mass analyses using tritium data must take this plasma-induced broadening into account in their model to avoid large systematic shifts on the extracted $m_\nu^2$ . The most recent neutrino mass analysis results take this into account[44].

# Chapter 5

# Tritium Analysis

The KNM2 neutrino mass measurement campaign, which took place between Sept-Nov 2019, provided around 31 days' worth of measurement time with a high $T_2$ purity, and a high activity rate[44].

There were extensive steps to unblinding, which were concurrently used for validation of the CMKAT framework (Section 3.5). But it was only recently (within a ∼month of this writing) that the data was analyzed unblinded. An independent analysis of this unblinded KNM2 tritium data using CMKAT is presented in this chapter.

## 5.1 Fit settings

In order to be as comparable as possible to the other KATRIN KNM2 neutrino mass analysis efforts[44], we use settings as described below in Table 5.1.

There are 317 runs included in the KNM2 neutrino mass analysis, which are listed in Appendix A.1.6. The corresponding RunSummaries used are version `Durable5g`. The PeriodSummary used is version `Apr2020b-Actual_18600V_6.0G`. These runs are combined for analysis using the stacking method presented in Section 5.2.

| **Category:** | **Setting:** | **Comments:** |
|---|---|---|
| Error type | CMKAT | See Section 3 for options |
| Free params | `DeltaE` , `mnu2` , `AScale` , `Bkgnd` , `ColAdj` | `mnu2` and `ColAdj` are global parameters. `DeltaE` , `AScale` , and `Bkgnd` are region-dependent parameters. |
| Fixed params | `BSlope` = 0<br>`SigmaTr` =0.146<br>`Delta10` =0 | All Kr-related parameters are fixed to zero.<br>`SigmaTr` value is calculated using Equation 5.1. |
| Run combination | Stacked | See Section 5.2 on how these are generated. |
| Pixel combination | Pseudoring | See Section 3.6. |
| Pixel selection | KNM2 Golden Pixel selection | 117 active pixels |
| Fit range | (E0Nominal-41, E0Nominal+136) eV | E0Nominal = 18 574 eV<br>This includes 28 subruns. |
| Column density treatment | Use RunSummary subrun-specific values | `fit.SubrunColumn DensityAdjustment` = 1 |
| Pull term | Enabled | Column density adjustment in $\chi^2$, with $\sigma_{\bar{\rho}d,err} = 0.002$ |
| Detector efficiency | 90% | `DETECTOR_EFFICIENCY` in cmFixedDefinitions.h |
| FSD | Unblinded KNM2 parametrization | From GitLab repository[105] |
| Detector ROI | 14 keV-32 keV | - |
| Theoretical corrections included | Synchrotron radiation loss<br>Relativistic Fermi function | Number of WGTS segments = 1 |

Table 5.1: Fit settings for unblinded KNM2 tritium analysis. Settings are chosen to be as close as possible to those used in the analyses shown in [44].

Additionally, there are a number of values which are read in from the RunSum-

maries. Table 5.2 lists their average values over the KNM2 neutrino mass measurement campaign.

| **Category:** | **Average value:** | **Comments:** |
|---|---|---|
| $B_S$ | $(2.52 \pm 0.04)$ T | Source magnetic field. |
| $B_{min}$ | $(6.308 \pm 0.006) \times 10^{-4}$T | Analyzing plane magnetic field. |
| $B_{max}$ | $(4.239 \pm 0.004)$ T | Pinch magnetic field. |
| $T_S$ | $(30.065 \pm 0.001)$ K | Source temperature. |
| $T_2$ concentration | $0.973 \pm 0.005$ | - |
| DT concentration | $0.0031 \pm 0.0004$ | - |
| HT concentration | $0.023 \pm 0.004$ | - |
| Tritium purity | $0.987 \pm 0.003$ | - |
| Column density | $(4.23 \pm 0.01) \times 10^{17}$cm$^{-2}$ | - |

Table 5.2: Average experimental values and their uncertainties during the KNM2 neutrino mass measurement campaign[44].

To set the `SigmaTr` broadening parameter, it is necessary to combine the contributions from the Doppler broadening of the source gas and the source plasma-induced broadening. The Doppler broadening for the KNM2 tritium was calculated in Equation 3.22: it has a standard deviation $\sigma_{Dopp} = 0.094\,\text{eV}$. The plasma-induced broadening was extrapolated for the KNM2 tritium campaign conditions, and its variance is $\sigma_P^2 = 0.0124\,\text{eV}^2$[44]. Using these values, the `SigmaTr` can be calculated:

$$\begin{aligned} \texttt{SigmaTr} &= \sqrt{(\sigma_{Dopp})^2 + \sigma_P^2} \\ &= 0.146\,\text{eV} \end{aligned} \tag{5.1}$$

## 5.2 Stacked spectrum generation

To create one stacked spectrum, many individual spectra are combined. Compared to an appended spectrum fit (which has $N_{\text{runs}} \times N_{\text{subruns per run}}$ data points), the stacked

spectrum has only $N_{\text{subruns per run}}$ data points. There are a total of 39 subruns per run in the KNM2 measurement campaign, but the fit range was set to include only the 28 subruns analyzed by other analysis teams; this corresponds to a fit range down to $-40\,\text{eV}$ below the tritium endpoint, after which some systematics begin to play a larger role. The following section describes how runs are combined into a stacked spectrum.

For every subrun of every run, the RunSummary $qU$ values which share the same $qU$ setpoint are histogrammed; this sorting takes into account that runs may have a different ordering of $qU$ setpoints ("up" scans versus "down" scans). There are 28 subruns included in the fit range, so this results in 28 $qU$ histograms with $N_{\text{runs}}$ entries in each histogram. Each $qU$ histogram is fit with a Gaussian (see Figure 5.1), and the mean values of these Gaussian fits are used as the new $qU$ values for the stacked spectrum.

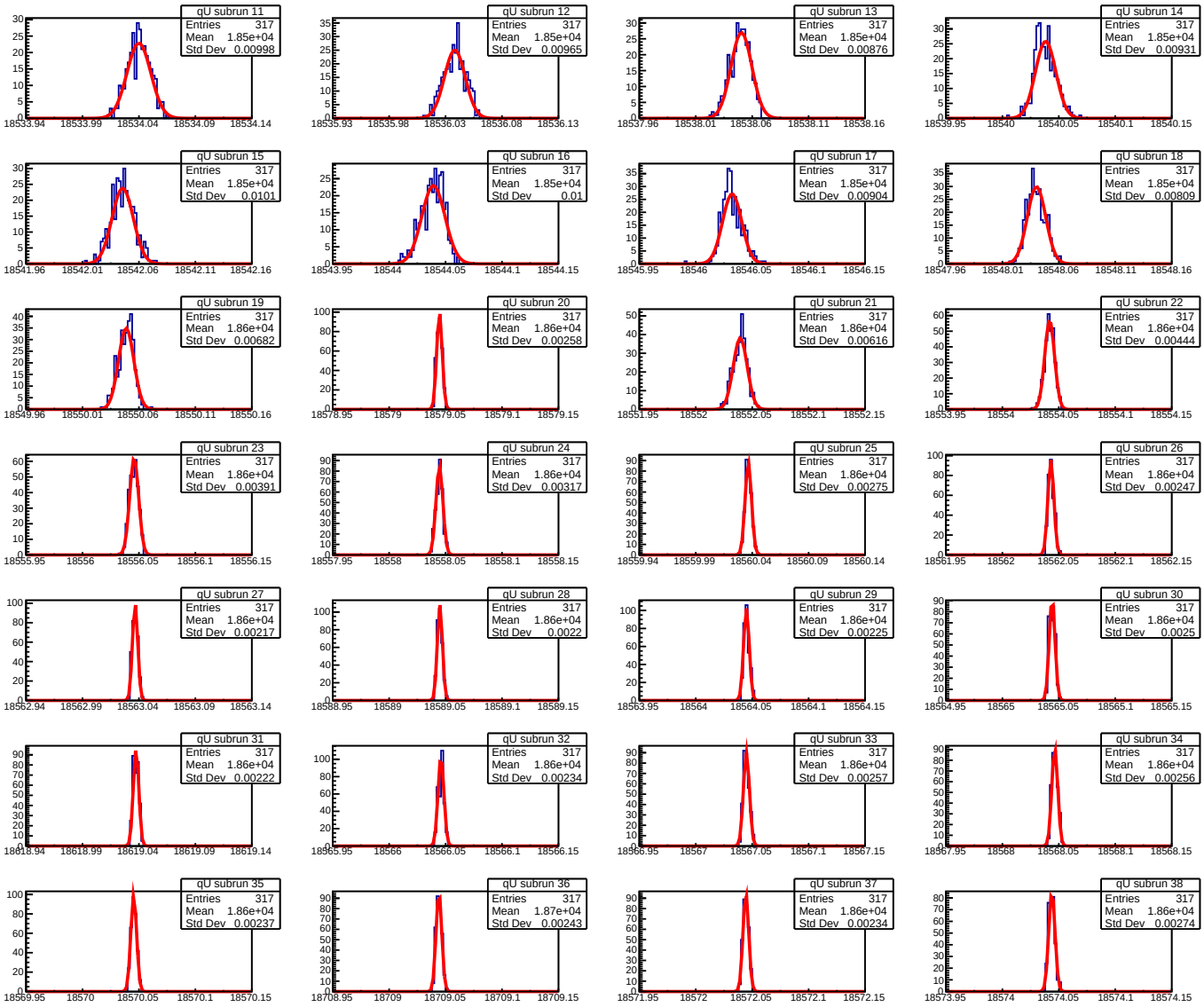


Figure 5.1: Histograms of the subrun's $qU$ values (only the 28 included in the fit range), for the 317 runs in the KNM2 campaign. All histograms are plotted on the range $\pm 0.1\,\mathrm{eV}$ around the $qU$ values taken from the first run (which is why they are not perfectly centered), and the standard deviation of the $qU$ histograms ranges from $0.002\,\mathrm{eV}$-$0.010\,\mathrm{eV}$.

For every subrun of every run, there is also a corresponding pixel-dependent detector count. The pixel-dependent detector counts corresponding to a stacked spectrum subrun $qU$ value are related to the pixel-dependent detector counts of the subrun histogram's $qU$ values in the following way:

$$n_{i,j} = \sum_{k=0}^{N_{\text{runs}}} n_{i,j,k} \tag{5.2}$$

Where $n_{i,j}$ is the detector count for subrun $i$ and pixel $j$ in the stacked spectrum, and $n_{i,j,k}$ is the detector count for subrun $i$ and pixel $j$ for run $k$.

The column density values can also be histogrammed for each subrun, in the same manner as for the $qU$ values. The process of sorting the column densities into their subrun-specific histograms occurs during the $qU$ histogramming process. The column density distributions don't have a strongly Gaussian distribution per subrun (see Figure 5.2), but it is a first approximation, and the `ColAdj` parameter can be used to compensate for the rest.

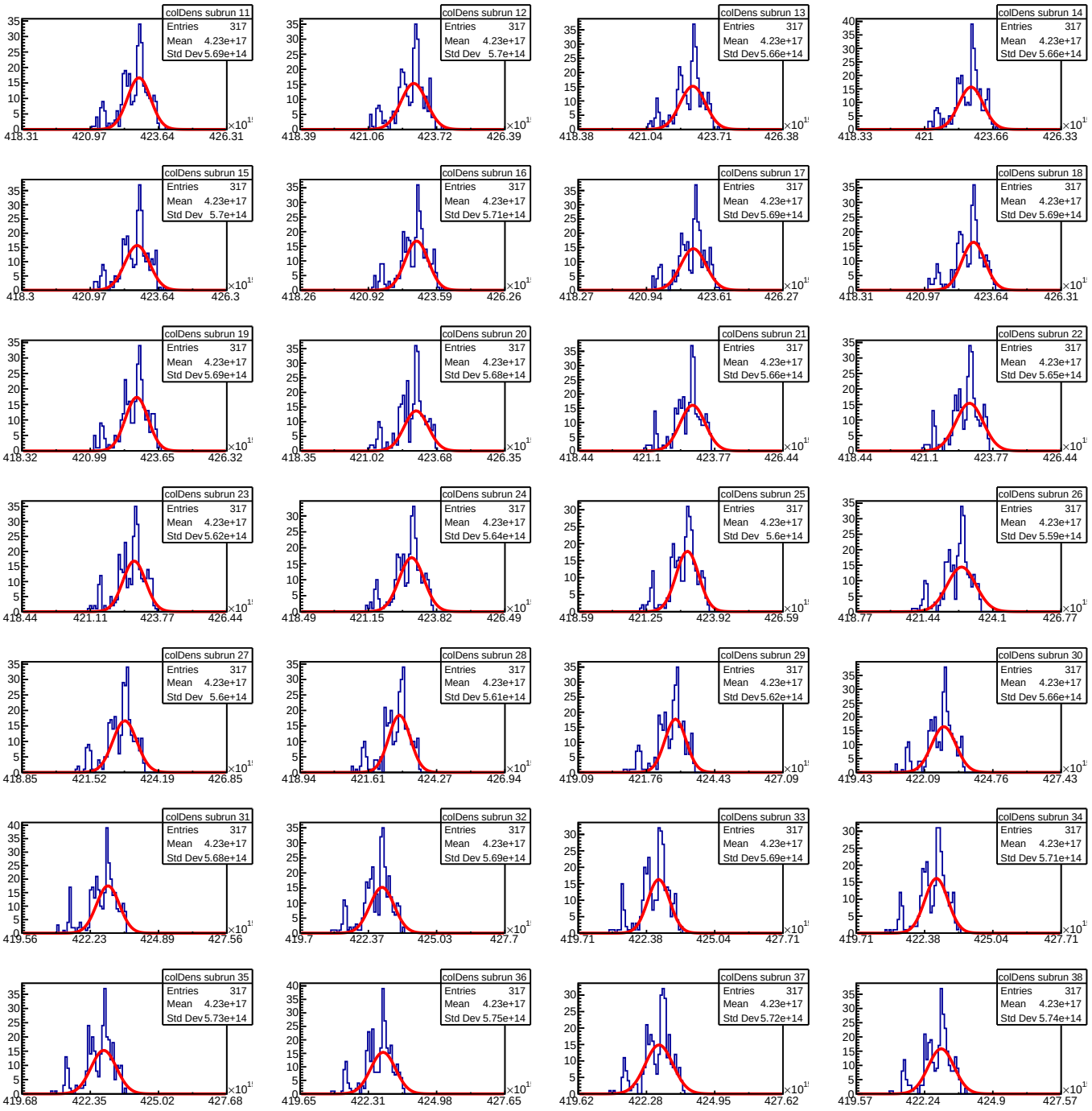


Figure 5.2: Histograms of the subruns' column density values (only the 28 included in the fit range), for the 317 runs in the KNM2 campaign. All histograms are plotted in the range $\pm 4 \times 10^{15}$ molecule/cm$^2$ around the subrun column density values for the first run, and the standard deviations of the column density histograms range from $5.61 \times 10^{14}$ molecule/cm$^2$ to $5.73 \times 10^{14}$ molecule/cm$^2$.

The new subrun live times are the sums of the runs' subrun live times. Since all subruns have the same live times throughout the campaign, this is equivalent to scaling each original live time by the number of runs in the campaign (317). The live times are used together with the detector count information to calculate rates.

Using the new set of subrun $qU$ values, pixel-dependent detector counts, column density, and live time, the stacked spectrum over all active pixels can be constructed. The stacked spectrum is shown in Figure 5.3; this version shows all 39 subruns and only includes detector counts from the 117 active pixels. Stacked spectra for individual regions can be constructed in a similar manner.

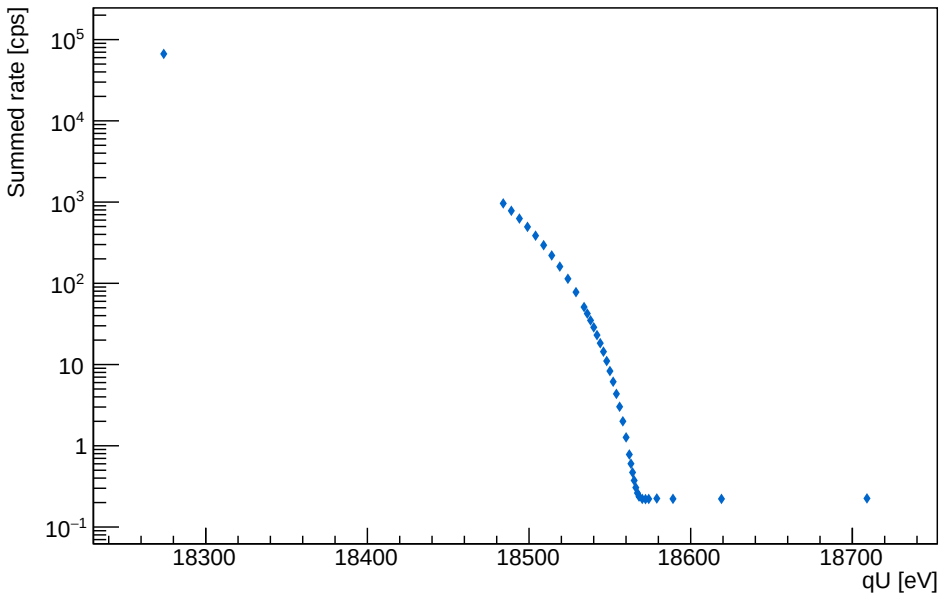


Figure 5.3: Stacked tritium spectrum summed over all active pixels, including contributions from 317 tritium runs taken during the KNM2 measurement campaign. Includes all 39 subruns and takes into account the KNM2 Golden Pixel Selection. The rate errors range from $1 \times 10^{-3}$ at lowest $qU$ to $1 \times 10^{-1}$ at highest $qU$. Note the log scale.

## 5.3 Fit results

Using the methods described in Section 5.2, a single "stacked" RunSummary can be generated (Figure 5.3). The fit to this stacked spectrum using the settings in

Table 5.1 is shown in Figure 5.4. Note that it is statistics-only, so the errors on `mnu2` are statistical only.

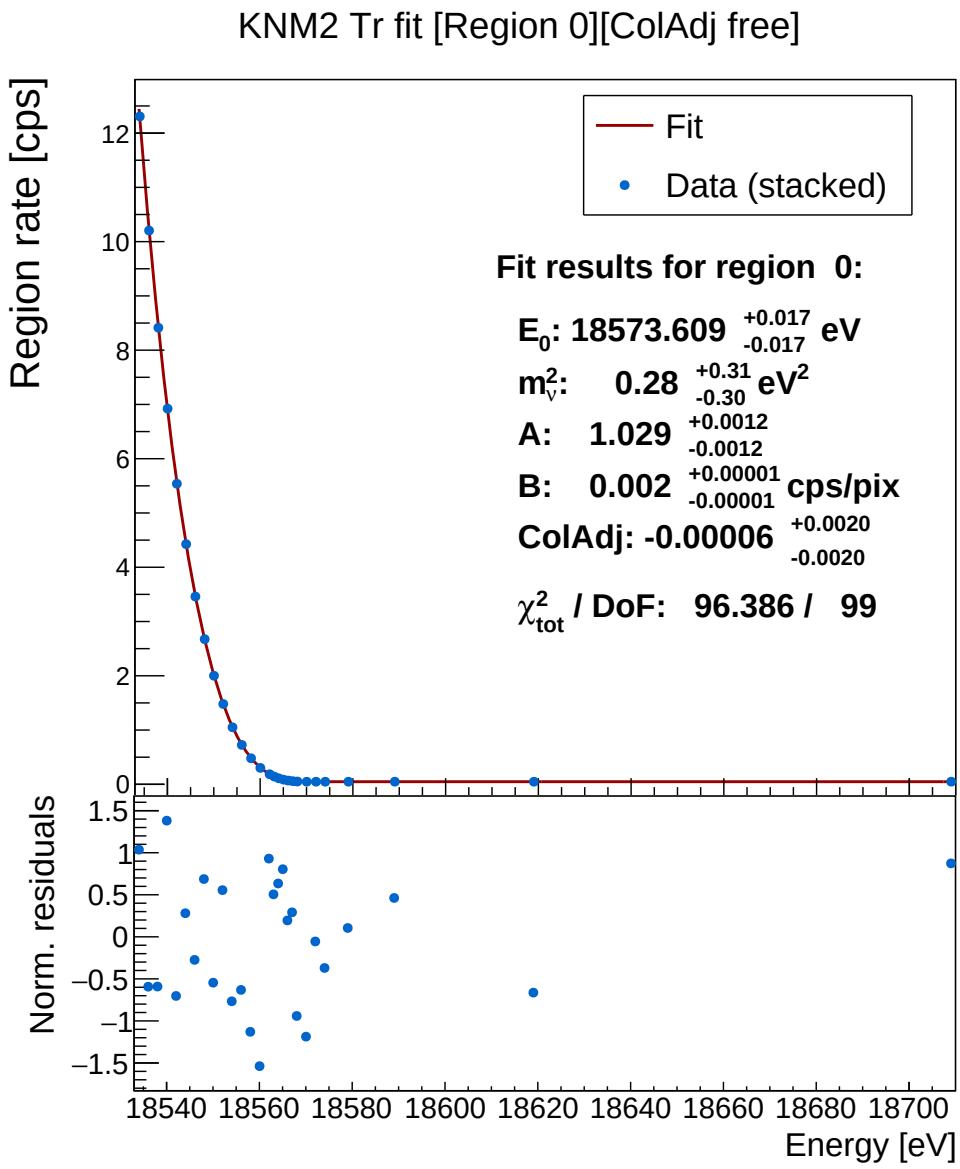


Figure 5.4: Fit to stacked KNM2 tritium spectrum, for Region 0. The effective endpoint $E_0 = \texttt{E0Nominal} - \texttt{DeltaE} = 18574.0 - \texttt{DeltaE}$ , in units of eV. The best-fit parameter values for the other three regions are given in Table 5.3. The residuals are normalized by the rate errors. Note that the rate error bars are not large enough to be seen by eye; they are $\mathcal{O}(10^{-2} - 10^{-4})$cps.

The free parameters' best fit values are shown in Table 5.3 below:

| KNM2 tritium stacked fit parameters: region-dependent | | | |
|---|---|---|---|
| **Region:** | `DeltaE` [eV]**:** | `AScale :` | `Bkgnd` [cps/pixel]**:** |
| 0 | $0.391^{+0.017}_{-0.017}$ | $1.029^{+0.0012}_{-0.0012}$ | $1.719 \times 10^{-3}{}^{+0.007 \times 10^{-3}}_{-0.007 \times 10^{-3}}$ |
| 1 | $0.433^{+0.016}_{-0.016}$ | $1.032^{+0.0011}_{-0.0011}$ | $1.826 \times 10^{-3}{}^{+0.006 \times 10^{-3}}_{-0.006 \times 10^{-3}}$ |
| 2 | $0.460^{+0.016}_{-0.016}$ | $1.033^{+0.0011}_{-0.0011}$ | $1.985 \times 10^{-3}{}^{+0.009 \times 10^{-3}}_{-0.009 \times 10^{-3}}$ |
| 3 | $0.459^{+0.022}_{-0.022}$ | $1.031^{+0.0015}_{-0.0015}$ | $2.159 \times 10^{-3}{}^{+0.006 \times 10^{-3}}_{-0.006 \times 10^{-3}}$ |

| KNM2 tritium stacked fit parameters: global | |
|---|---|
| `mnu2` [eV$^2$]**:** | `ColAdj :` |
| $0.28^{+0.31}_{-0.30}$ | $-0.0001^{+0.0020}_{-0.0020}$ |

Table 5.3: Free parameters' best fit values, for a fit of the stacked spectrum (of 317 runs), using settings shown in Table 5.1. The reduced $\chi^2$ is 96.4/99, and the asymmetry in the `mnu2` error is a sign that the chi square distribution in `mnu2` is not perfectly parabolic. Note the radially-dependent `DeltaE` is presumed to be partially due to plasma-related source potential variations.

The only fit parameter which is not a nuisance parameter is the global `mnu2` :

$$\texttt{mnu2} \ = 0.28^{+0.31}_{-0.30}\text{eV}^2 \tag{5.3}$$

Where the uncertainties quoted in Equation 5.3 are statistical uncertainties only. This is in agreement with the central $m_\nu^2$ best fit value in the recently released paper[44]:

$$m_\nu^2 = (0.26 \pm 0.34)\,\text{eV}^2 \tag{5.4}$$

Where the errors listed in Equation 5.4 represent the total uncertainty. The corresponding statistical errors calculated by the four other analyses are listed in Table 5 of [44], and range from 0.28 eV$^2$-0.31 eV$^2$. The CMKAT statistical errors of 0.31 eV$^2$ (upper) and 0.30 eV$^2$ (lower) shown in Equation 5.3 are in agreement with these results. The effect of selected systematic errors and a final estimate of the upper limit on the CMKAT-extracted neutrino mass are given in Chapter 7.

Some additional fits to test choice of fit setting are summarized in Table 5.4 below, mainly by turning off settings known to produce more accurate fit results. The last row shows the results given in Figure 5.4 and Equation 5.3.

| Stacked fit to KNM2 tritium data, with statistical errors only | | | |
|---|---|---|---|
| **Fit mode:** | `mnu2` [eV$^2$]**:** | $\chi^2$ | **Comments:** |
| Summed | $0.28^{+0.31}_{-0.30}$ | 31.89/24 | Subrun column density ON<br>`ColAdj` free ($-0.0001^{+0.0020}_{-0.0020}$) |
| Pseudorings | $0.28^{+0.30}_{-0.31}$ | 96.4/99 | Subrun column density ON<br>`ColAdj` fixed<br>Region-dependent `DeltaE` |
| Pseudorings | $0.28^{+0.31}_{-0.30}$ | 96.4/99 | Subrun column density ON<br>`ColAdj` free ($-0.0001^{+0.0020}_{-0.0020}$)<br>Region-dependent `DeltaE` |

Table 5.4: Fit results, given settings in Table 5.1 with various adjustments. The last row is the fit result using exactly the Table 5.1 settings.

## 5.4 Conclusions

The best-fit `mnu2` to the unblinded KNM2 tritium data set using this independent CMKAT-based analysis is $0.28^{+0.31}_{-0.30}$eV$^2$, as given in Equation 5.3. The central value and the (statistical-only) uncertainties agree with the results from other analyses on the same data set[44]. It is worth noting that, while the best-fit `mnu2` is positive, the result is still consistent with zero.

In order to get a more complete picture, the systematic uncertainties must be taken into account. These were generated by other working groups, and will be presented in Chapter 7.

# Chapter 6

# Sensitivity studies

The modelling capabilities of CMKAT allow us to explore the estimated accuracy of the KATRIN experiment's final neutrino mass result, as well as scenarios in which some underlying effect causes a systematic shift. Through a combination of Monte Carlo data generation and fitting, the KATRIN experiment's sensitivity to the extracted $m_\nu^2$ parameter can be investigated.

To put into perspective how much a given systematic would affect our final neutrino mass result, we must compare to the total uncertainty the experiment was designed to allow. This is broken down into the statistical and systematic uncertainties (Section 6.1, with statistics discussed in detail). Although the CMKAT model itself is nonlinear in $m_\nu^2$ , Section 6.2 will demonstrate that (to a good approximation) the confidence interval determined by the $\Delta\chi^2 = 1$ criterion corresponds to the standard symmetric $1\sigma$ uncertainties, within the 68% C.L. obtained in linear models. This same section will also discusses the various approaches available for calculating the extracted `mnu2` 's estimated error. A corresponding confidence interval prescription is introduced in Section 6.3.

With these defined, various tests can be undertaken. The dependency of the accuracy of the KATRIN experiment on the constant background is shown in Section 6.4. Systematic effects are explored next, and include studies of the impact of tritium decay in the RW and DPS (Section 6.5), small adjustments to the column density (Section 6.6), and a nonlinear rate contribution (Section 6.7). Each of these sections relies on analysis of simulated data, which we call Monte Carlo-generated data. The errors are estimated using the methods shown in Section 6.2. For systematic studies, it is possible to generate data without the usual statistical fluctuations to directly test effects. A data set generated in this manner is referred to as an Asimov data set, and amounts to evaluating the model integrated spectrum without any underlying statis-

tical treatment. This chapter will refer to any data sets generated in this manner as "MC-generated Asimov data sets". These Asimov data sets have estimated errors, which can be used for calculation of standard error matrices. To correctly interpret the fits to Asimov data sets, note that a good $\chi^2$ per degree of freedom is around zero, not 1.

## 6.1 The KATRIN uncertainty budget

The KATRIN experiment was designed to achieve its goal mass sensitivity of 0.2 eV (at 90% C.L.) with a total measurement time of 3 years[53]. This 3-year (approximately 1000 days) KATRIN design goal was chosen such that the target sensitivity is achieved when the systematic and statistical uncertainties contribute roughly equal amounts.

In this section, we seek to quantify the KATRIN experiment's total uncertainty budget. Because uncertainty estimation is highly dependent on settings, it is vital to establish a realistic set of input settings and to apply these same settings consistently throughout each study.

Since publication of [53] in 2004, a number of things have changed, and so the current nominal settings differ from those stated in the original report. In order to make the results in this section more relevant to current/future KATRIN results, we define a new set of "base case" parameters to closely mimic conditions during the KNM3b neutrino mass measurement campaign:

| Base case: Tritium MC-generation settings | | |
|---|---|---|
| **Category:** | **Setting:** | **Comments:** |
| MC truths | `DeltaE` = -0.639<br>`mnu2` = 0<br>`AScale` = 0.982<br>`Bkgnd` = 0.0017<br>`BSlope` = 0<br>`SigmaTr` = 0<br>`ColAdj` = 0<br>`Delta10` = 0 | `DeltaE` selected such that endpoint occurs at 18 573.639 eV<br>MC truths selected from time-averaged KNM3b values, to make them more realistic<br>All Kr-related parameters set to 0 |
| Integrated column density, $\bar{\rho}d$ | $3.7555 \times 10^{17}$ molecules/cm$^2$ | Run-averaged `ColumnDensity` value in reference KNM3b RunSummary |
| MTD | Scaled version of real run | Copy of MTD from reference KNM3b RunSummary (Run 63314)<br>Total MC measurement time = 1000 day |
| FSD | KNM3 blinded | `FSD_E_merge.Tr` = 0.10 |
| Corrections | Synchrotron radiation loss = ON<br>Radiative correction = ON<br>Nonlinearity $\alpha$ = 0 | Number of WGTS slices = 1 |
| Pixel selection | All pixels | 148 pixels |

Table 6.1: Monte Carlo truths and model settings for generating data set. KNM3b-like run settings were used because most settings are expected to be similar to future run conditions. Recall that MTD is the "Measurement Time Distribution".

To ensure consistency in the fitting process, we define a corresponding base case for fit settings. These also closely follow current standard KATRIN fit practice, and are shown in Table 6.2.

| Base case: Tritium fit settings | | |
|---|---|---|
| **Category:** | **Setting:** | **Comments:** |
| Error type | Minuit error matrix | See Section 3 for options |
| Free params | `DeltaE` , `mnu2` , `AScale` , `Bkgnd` | `mnu2` initialized with value of $0.1\,\mathrm{eV}^2$, not $0\,\mathrm{eV}^2$. |
| Fixed params | `BSlope` , `ColAdj` , `SigmaTr` , `Delta10` | All are fixed to zero. |
| Fit range | $-40\,\mathrm{eV}$ to $10\,\mathrm{eV}$ around E0Nominal | E0Nominal = $18\,573.0\,\mathrm{eV}$ |
| Column density treatment | Average over RunSummary template's subrun values | `fit.SubrunColumn DensityAdjustment` = 0 |
| Pixel combination | pseudo-ringwise with global `mnu2` | This is a Level 2 fit See Section 3.6. |
| Pixel selection | All pixels enabled | - |

Table 6.2: Base case fit conditions. These closely mimic the basic fit settings for the typical neutrino mass analysis.

With these MC generation and fitting standards defined, the total uncertainty budget can begin to take shape. Taking advantage of the fact that the statistical uncertainty depends on the total measurement time, this value is calculated first (Section 6.1.1) and used to pin down the corresponding total systematic uncertainty allowed (Section 6.1.2).

### 6.1.1 Statistical Uncertainty

The statistical uncertainty of $m_\nu^2$ relates to the randomness in the measured rate, which is assumed to follow a Poisson parent distribution.

First, a quick crosscheck was done using the KNM2-like MC study used as part of an unblinding step. Using settings described in [106], MC data was generated for a KNM2-like campaign (corresponding to a total measurement time of 12.86 days) and fit with a free `mnu2` parameter. The results are shown in the table below:

| Fit results for KNM2-like MC data | | |
|---|---|---|
| **Fitter:** | `mnu2` [eV$^2$]**:** | **Run, pixel combination:** |
| CMKAT | $-0.00081^{+0.32}_{-0.31}$ | MTD and $qU$ values from reference RunSummary (see Table 6.1), Level 3 fit mode (ringwise regions with global `mnu2` ) |
| KaFit | $0.003^{+0.31}_{-0.31}$ | Stacked, multi-ring |
| Fitrium | $0.00^{+0.28}_{-0.32}$ | Stacked, multi-ring |
| SAMAK | $0.000^{+0.29}_{-0.33}$ | Stacked, multi-pseudoring |

Table 6.3: Results from fits to a KNM2-like Asimov data set (part of KNM2 unblinding process). Results from KaFit, Fitrium, and SAMAK can be found in [106]. Run and pixel combinations are defined in Section 3.4.6. CMKAT used CMKAT errors to see whether the uncertainties would be symmetric (like KaFit) or slightly asymmetric (like Fitrium, Samak).

All fitters' `mnu2` errors, which correspond to the statistical uncertainty, agree to better than 10%. This demonstrates that CMKAT's $\Delta\chi^2 = 1$ error estimation method agrees with the errors produced by other fitters' methods, and serves as an important validation of CMKAT.

In order to quantify the statistical uncertainty of the 1000-day KATRIN neutrino mass results, the CMKAT framework is used to generate Asimov Monte Carlo data and fit it. Using the base case generation settings listed in Table 6.1 to generate the MC data and the base case fit settings Table 6.2 to fit, the extracted `mnu2` is:

$$\texttt{mnu2}_{\,pseudoring,Level2} = -0.00059^{+0.047}_{-0.047}\text{eV}^2 \tag{6.1}$$

The estimated errors on `mnu2` shown above come from the Minuit error matrices, and agree with the CMKAT estimated errors to within approximately 6%. The statistical uncertainty for 1000 days of KATRIN data at KNM3b-like settings correspond to the estimated errors in Equation 6.1:

$$\sigma_{stat} = 0.047\,\text{eV}^2 \tag{6.2}$$

The estimated statistical uncertainty given in Equation 6.2 is higher than the value quoted in the original design report [53] ($0.017\,\mathrm{eV}^2$), but this is due to differences in simulated conditions. Table 7 of [53] lists the settings used to arrive at the original result: they include a different MTD, magnetic field settings, and background rates. While this old statistical uncertainty value is of historical interest, it is unreasonable to use it now, given that the current settings are so different. The following sections will exclusively use Equation 6.2 as the target 1000-day KATRIN statistical uncertainty, assuming no further improvements.

To get a sense for the relationship between the statistical uncertainty and the total measurement time, we repeat the study above by generating (using Table 6.1) and fitting (using Table 6.2) spectra with different total measurement times:

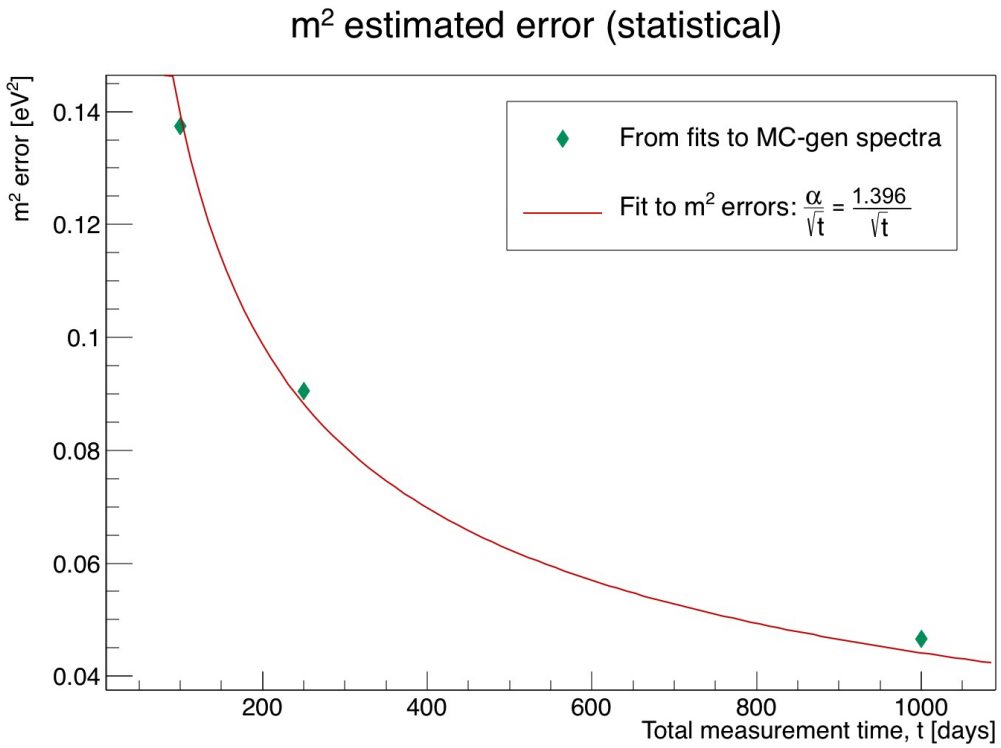


Figure 6.1: Plot of estimated $m^2$ errors for 100-, 250-, and 1000-days' worth of statistics. All spectra were generated with KNM3b-like settings. The units of fit parameter $\alpha$ are $\mathrm{eV}^2\sqrt{\mathrm{day}}$.

Because this study only tests the estimated error due to an increase in statistics, we expect it to decrease in proportion to the square root of the measurement time (large-N Poisson statistics). This allows us to construct a model to predict the measurement time-dependence of the estimated `mnu2` error (red fit curve in Figure 6.1).

### 6.1.2 Systematic Uncertainty

The systematic uncertainty on $m_\nu^2$ is the result of experimental conditions changing or behaving in a manner differing from what the model knows. Systematic uncertainties do not decrease as the amount of data increases, as statistical uncertainties do; instead, their characteristic signature is a shift in $m_\nu^2$ away from its true value. In many cases it can be difficult or computationally cost-prohibitive (but not impossible) to correct for various individual sources of systematic uncertainty. If correction is not feasible, the alternative approach is to apply no correction and instead take them into account in the systematic uncertainty budget.

Because the KATRIN experiment was designed to have roughly equal systematic and statistical uncertainty contributions, we set the total systematic uncertainty allowed at:

$$\sigma_{sys,tot} = 0.047\,\mathrm{eV}^2 \tag{6.3}$$

Some of the biggest (known) sources of systematic uncertainty are due to uncertainties on the Final State Distribution (FSD), column density, and backgrounds; the following sections explore these and select other sources of systematic uncertainty, with the goal of determining whether they play a significant role in the total systematic uncertainty budget.

## 6.2 $m_\nu^2$ error estimation methods

There are three ways which the `mnu2` error can be obtained:

1. Generate/fit MC-generated (statistically fluctuated) tritium spectrum, and histogram the (Minuit or CMKAT) error on `mnu2` fit parameter (Section 6.2.1).
2. From a chi square mapping over a range of fixed `mnu2` (Section 6.2.2).
3. Generate/fit many MC-generated (statistically fluctuated) tritium spectra, and histogram the `mnu2` distribution (Section 6.2.3).

These three methods will be demonstrated using the usual MC generation settings (Table 6.1) and fit settings (Table 6.2). Of the three methods, Method 3 (Section 6.2.3) is perhaps the most important, because it justifies the use of Minuit errors in later sections, and how they relate to statements about the confidence level.

We choose 1000 hours' worth of statistics instead of the full 1000 days to evaluate the `mnu2` error estimation methods on the currently available datasets.

### 6.2.1 Method 1

The first method for determining the estimated error on $m_\nu^2$ is the simplest:

1. Generate a single 1000 hour tritium spectrum, using the settings in Table 6.1. Let the rates for this spectrum be statistically fluctuated.
2. Fit the generated spectrum, using the settings in Table 6.2.
3. Repeat Steps 1-2 many times, with a new random seed every time.

To ensure enough statistics, 1000 spectra are generated. The extracted `mnu2` errors can then be histogrammed. See Figure 6.2.

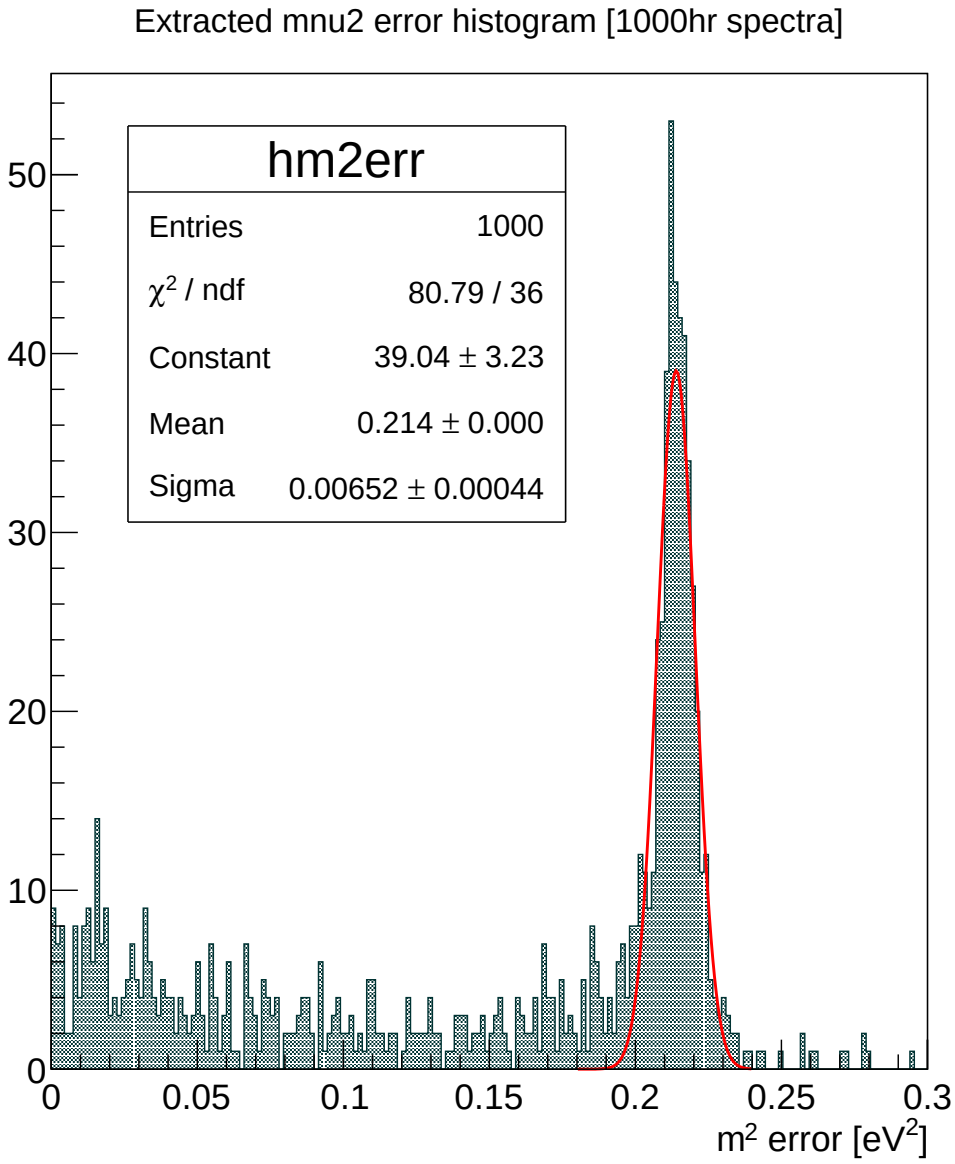


Figure 6.2: Histogram of extracted `mnu2` errors for 1000 spectra, each of which has 1000 hrs' worth of statistics, generated with $m^2_{MCtruth}$=0 eV$^2$. The `mnu2` errors are calculated using the Minuit error matrix. The excess of Minuit errors outside of the peak region are related to technical details of the Minuit error calculation (incorrect error matrices). They do not disappear with cuts on $\chi^2$ or removing fit results which did not converge.

The mean value of the `mnu2` error histogram is taken from a Gaussian fit to the

peak (red line in Figure 6.2):

$$\sigma_{m_\nu^2} = 0.21\,\mathrm{eV}^2 \tag{6.4}$$

### 6.2.2 Method 2

The second method involves mapping the $\chi^2$ values for a particular range of `mnu2` values. This "chi square map" in `mnu2` is constructed like so:

1. Generate a single 1000 hour tritium spectrum, with statistical scattering turned off (Asimov spectrum), using the settings in Table 6.1.
2. Fit the generated spectrum with `mnu2` fixed at a unique value. All other tritium parameters (`DeltaE` , `AScale` , and `Bkgnd` ) are allowed to be free, as usual. Fit in summed mode to keep computation time reasonable. All other fit settings are as stated in Table 6.2.
3. Repeat Step 2 for a range of `mnu2` values in the neighborhood of the `mnu2` MC truth.

The $\chi^2$ values are extracted for each fit, and plotted versus their corresponding fixed `mnu2` values (green data points in Figure 6.3). This also visualizes how Minuit searches for the optimum `mnu2` value when that parameter is free: by searching for the minimum $\chi^2$ value. Though the model is nonlinear in $m_\nu^2$ , the $\chi^2$ is parabolic and symmetric in the vicinity of the `mnu2` MC truth ($0\,\mathrm{eV}^2$).

As mentioned in the beginning of the chapter, by using the usual $\Delta\chi^2 = 1$ criterion, the standard $1\sigma$ uncertainty on `mnu2` is defined[107]. These $1\sigma$ uncertainties can be extracted by fitting the data with a second order polynomial (red curve in Figure 6.3) and calculating where the fitted parabola intersects with $\chi^2 = 1$ (blue line in Figure 6.3).

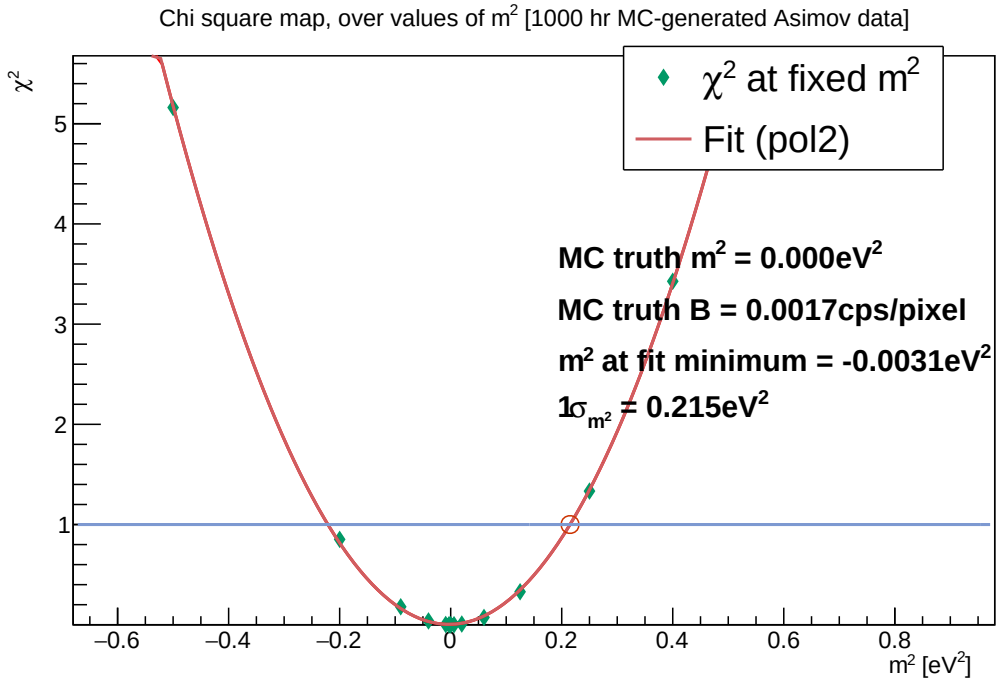


Figure 6.3: Chi square map of 1000 hr tritium spectrum, generated with $m^2_{MCtruth}$=0 eV$^2$.

This chi square mapping estimates the error on `mnu2` for 1000 hours' worth of measurement time to be:

$$\sigma_{m^2_\nu} = 0.22\,\mathrm{eV}^2 \tag{6.5}$$

As discussed in Section 3.4.6, the CMKAT errors are calculated based on this chi square mapping principle. They can be slightly asymmetric because the $\Delta\chi^2 = 1$ intercept point is evaluated in both directions (above and below the minimum $\chi^2$). For the purposes of this study, the $\chi^2$ curve minimum is close enough to zero that the difference between upper and lower intercepts is negligible.

### 6.2.3 Method 3

The third method for estimating the `mnu2` error follows a similar prescription as Method 1:

1. Generate a single 1000 hour tritium spectrum, using the settings in Table 6.1. Let the rates for this spectrum be statistically fluctuated.

2. Fit the generated spectrum, using the settings in Table 6.2.

3. Repeat Steps 1-2 many times, with a new random seed every time.

However, this method focuses on the extracted `mnu2` values themselves. With 1000 spectra generated, we can calculate the difference between extracted `mnu2` and the MC truth, and histogram this difference (see Figure 6.4).

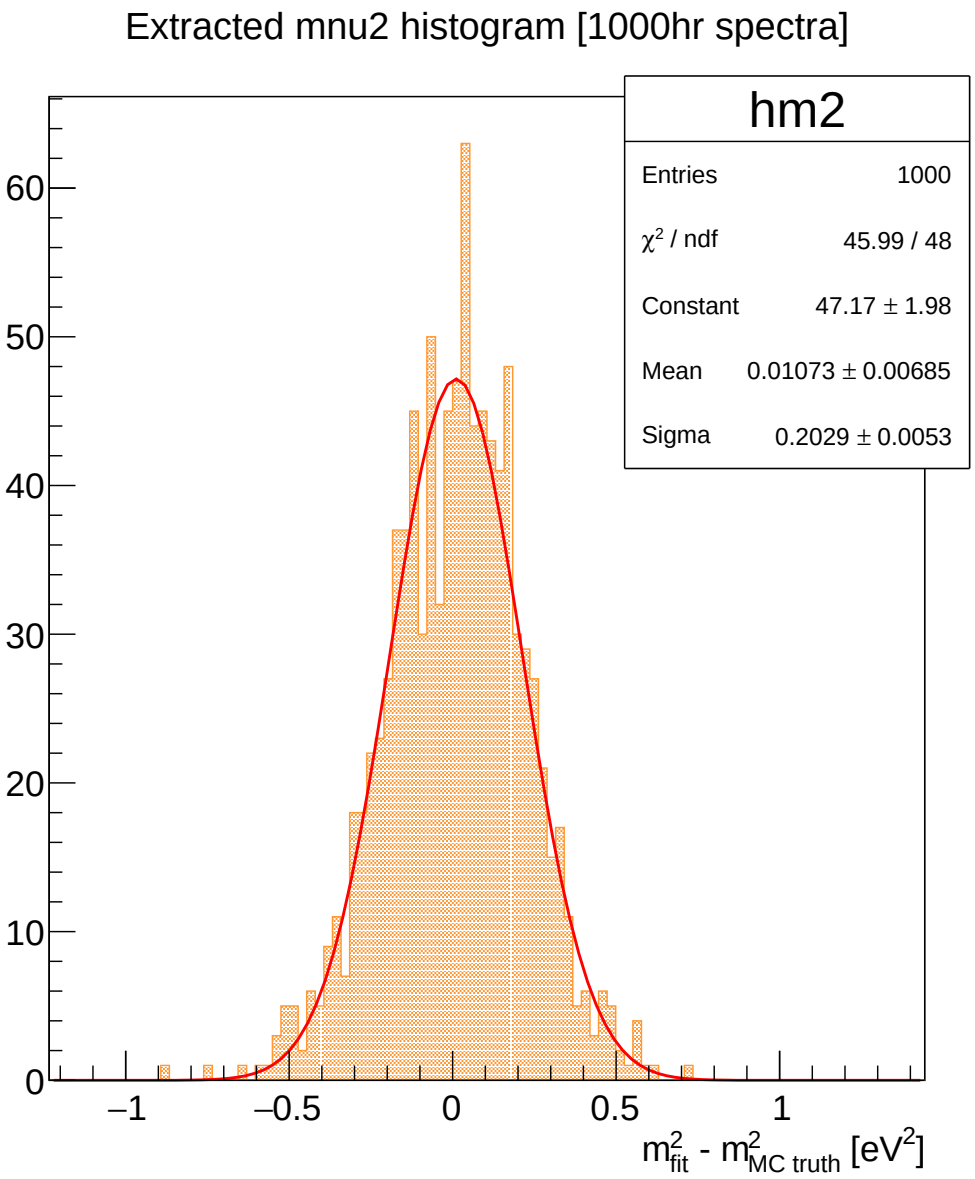


Figure 6.4: 1000 samples of 1000 hr tritium spectra, generated with $m^2_{MCtruth}$=0 eV$^2$.

The `mnu2` difference histogram (Figure 6.4) can be reasonably approximated by a Gaussian distribution. If we define the difference between extracted and true neutrino mass to be $\zeta = m^2_{fit} - m^2_{MCtruth}$, then the probability density of extracting a squared neutrino mass $\zeta$ away from the true squared neutrino mass is:

$$\frac{d\ \mathrm{Prob}(\zeta)}{d\zeta} = \frac{1}{\sqrt{2\pi}\sigma} e^{-\frac{-\zeta^2}{2\sigma^2}} \tag{6.6}$$

Equation 6.6 is used to fit the histogram (red curve in Figure 6.4), where "Sigma" (the 1-standard deviation of the Gaussian) is the `mnu2` estimated error:

$$\sigma_{m_\nu^2} = 0.20\,\mathrm{eV}^2 \tag{6.7}$$

### 6.2.4 Conclusions

Compare Equation 6.4, Equation 6.5, and Equation 6.7: as expected, they are in agreement (Table 6.4).

| `mnu2` estimated error (1000 hr) | |
|---|---|
| **Method:** | $\sigma_{m^2}$ [eV$^2$]**:** |
| Method 1 | 0.21 |
| Method 2 | 0.22 |
| Method 3 | 0.20 |

Table 6.4: Comparison of `mnu2` estimated errors for three different methods. Note that these are the errors on $m_\nu^2$ , not $m_\nu$.

In the future, unless expressly mentioned, the $m_\nu^2$ estimated error comes from Method 1: it is the value reported in each FitSummary, and requires no additional steps.

## 6.3 Confidence Interval

In Method 3, it was shown that the probability distribution of $m_\nu^2$ can be approximated by a Gaussian distribution (Equation 6.6). Using this probability distribution, we can construct a confidence interval. To do this, we must first select the confidence level.

Mathematically, the confidence level (C.L.) is defined as the percentage of total area under the probability distribution between two points $A$ and $B$, where $A$ and $B$ define the confidence interval. Using Equation 6.6:

$$\text{C.L.} = \int_A^B d\zeta \, \frac{d \, \text{Prob}(\zeta)}{d\zeta} \tag{6.8}$$

Where $\zeta = m^2_{fit} - m^2_{MCtruth}$. This is shown in Figure 6.5, where differently shaded areas correspond to different total area percentages (C.L.). Here, the probability distribution parametrization is taken from the fitted Gaussian probability in Method 3 (Figure 6.4), so it is not arbitrary.

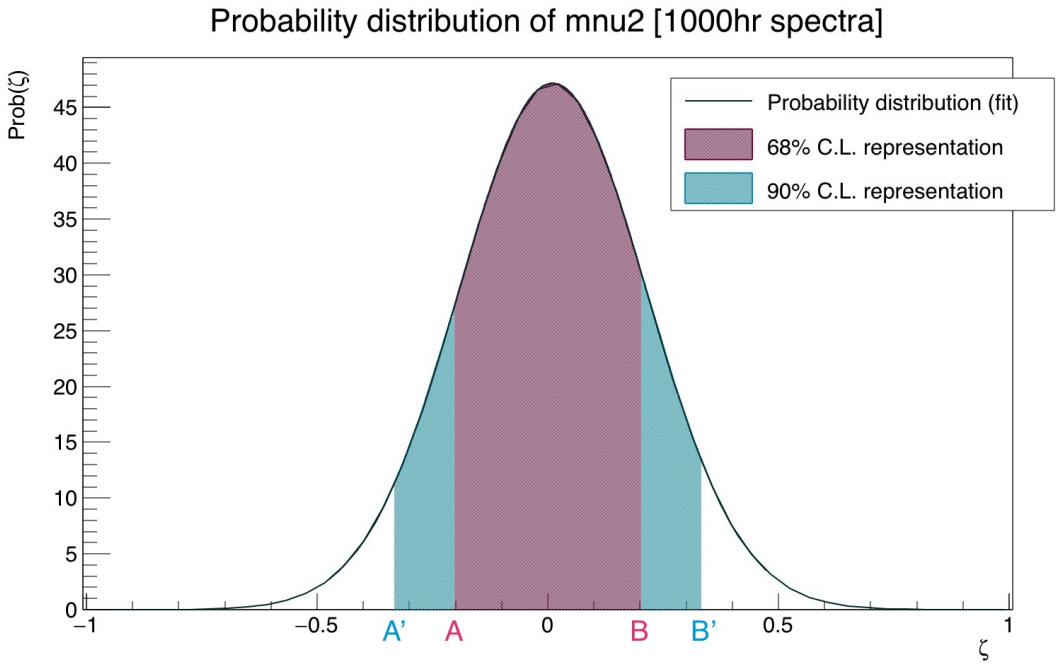


Figure 6.5: Probability distribution of $\zeta$, taken from Figure 6.4. The 68% (magenta) and 90% (blue+magenta) C.L. are shown.

The magenta region corresponds to a 68% C.L.. Mathematically, this can be expressed by plugging Equation 6.6 into Equation 6.8, the confidence level corresponding to a symmetric interval around $m^2_{fit}$ with $A = -\sigma$ and $B = +\sigma$:

$$\begin{aligned} \text{C.L.} &= \int_A^B d\zeta \frac{1}{\sqrt{2\pi}\sigma} e^{-\frac{-\zeta^2}{2\sigma^2}} \\ &= \int_{-\sigma}^{\sigma} d\zeta \frac{1}{\sqrt{2\pi}\sigma} e^{-\frac{-\zeta^2}{2\sigma^2}} \\ &= 0.68 \end{aligned} \tag{6.9}$$

This can be translated into 68% C.L. interval for $m_\nu^2$ :

$$68\%\ \text{C.I.} = \left[\ m_{fit}^2 - \sigma,\ m_{fit}^2 + \sigma\ \right] \tag{6.10}$$

If the 68% C.L. doesn't have sufficient coverage, the confidence level and corresponding confidence interval can be easily adjusted. For example, if you wish to set a 90% C.L. (blue region in Figure 6.5), corresponding to a symmetric interval around $m_{fit}^2$ with $A' = -1.64\sigma$ and $B' = +1.64\sigma$:

$$\begin{aligned} \text{C.L.} &= \int_{A'}^{B'} d\zeta \frac{1}{\sqrt{2\pi}\sigma} e^{-\frac{-\zeta^2}{2\sigma^2}} \\ &= \int_{-1.64\sigma}^{1.64\sigma} d\zeta \frac{1}{\sqrt{2\pi}\sigma} e^{-\frac{-\zeta^2}{2\sigma^2}} \\ &= 0.90 \end{aligned} \tag{6.11}$$

The corresponding 90% C.L. interval for $m_\nu^2$ is then:

$$90\%\ \text{C.I.} = \left[\ m_{fit}^2 - 1.64\sigma,\ m_{fit}^2 + 1.64\sigma\ \right] \tag{6.12}$$

Where the $m_{fit}^2$ value corresponds to the extracted CMKAT fit value `mnu2` .

Given the frequentist nature of this confidence interval construction, the physical interpretation is this: **given the true neutrino mass value, if you repeat the measurement experiment many times, the confidence interval obtained through this prescription will contain the true neutrino mass value 90% of the time**.

This confidence interval construction takes into account some assumptions, like the assumption that the probability distribution does not vary with different $m^2_{MCtruth}$. Proof that this assumption is valid, as well as confidence interval construction specifically for the KNM2 neutrino mass analysis results from Section 5, appears in Chapter 7.

### 6.3.1 From Uncertainty to Sensitivity

The rest of this chapter contains a selection of studies on the impact of certain effects on the systematic uncertainty. One can think of each systematic effect as an additional Gaussian contribution on top of the (statistics-only) `mnu2` probability distribution in Equation 6.6. The systematic uncertainties then correspond to that Gaussian's $\sigma$ value, and they add in quadrature[1]. From there, it's a straightforward task to follow the prescription in the previous section to define confidence intervals and such.

The avid reader might then wonder, what is the total uncertainty (and by extension, confidence interval) of the KATRIN experiment? For the full 1000 day measurement, the statistical and systematic uncertainties are assumed to contribute approximately equally to the total uncertainty on $m^2_\nu$ , $\sigma_{tot}(m^2_\nu)$:

$$\begin{aligned}\sigma_{tot}(m^2_\nu) &= \sqrt{2}\ \sigma_{stat} \\ &= \sqrt{2}\ (0.047\,\mathrm{eV}^2) \\ &= 0.067\,\mathrm{eV}^2\end{aligned} \tag{6.13}$$

Thus, the 90% confidence interval of $m^2_\nu$ is bounded by:

$$\begin{aligned}90\%\text{ C.I. of } m^2_\nu &= \left[\ m^2_{fit} - 1.64\sigma,\ m^2_{fit} + 1.64\sigma\ \right] \\ &= \left[\ m^2_{fit} - 0.11\mathrm{eV}^2,\ m^2_{fit} + 0.11\mathrm{eV}^2\ \right]\end{aligned} \tag{6.14}$$

The bounds associated with the $m^2_\nu$ confidence interval can be transformed into a sensitivity on $m^2_\nu$ at the corresponding confidence level, assuming $m^2_{fit} = 0$. In the case of the 90% C.L. shown above, the sensitivity $S_{m^2_\nu}(90\%\text{C.L.})$ is:

[1]This is true if the uncertainties are uncorrelated. The uncertainties selected for study in the subsequent sections are uncorrelated.

$$
\begin{aligned}
S_{m_\nu^2}(90\%\text{C.L.}) &= 1.64\sigma \\
&= 0.11\,\text{eV}^2
\end{aligned} \tag{6.15}
$$

Finally, to get the sensitivity on $m_\nu$ at 90% C.L., $S_{m_\nu}(90\%\text{C.L.})$ is:

$$
\begin{aligned}
S_{m_\nu}(90\%\text{C.L.}) &= \sqrt{S_{m_\nu^2}(90\%\text{C.L.})} \\
&= \sqrt{0.11\,\text{eV}^2} \\
&= 0.33\,\text{eV}
\end{aligned} \tag{6.16}
$$

This sensitivity value is higher than the design sensitivity of 0.2 eV, but there are plans in place to increase sensitivity by improving experimental conditions.

### 6.3.2 Negligibility threshold

Later sections in this chapter will explore specific systematic effects. In order to determine whether a particular systematic should be considered negligible or not, we must select a threshold.

With our earlier determination that the agreement of estimated error on `mnu2` to within 10% is acceptable (Section 6.1.1) and our total systematic uncertainty budget (Equation 6.3), we define a threshold `mnu2` shift below which a systematic will be considered negligible:

$$
\begin{aligned}
\Delta m^2_{threshold} &= 0.1\sigma_{sys,tot} \\
&= 0.1\sigma_{stat,tot} \\
&= 0.0047\,\text{eV}^2
\end{aligned} \tag{6.17}
$$

## 6.4 Sensitivity due to different (constant) background levels

Typical background subtraction methods aren't suitable for the KATRIN experiment. Instead, it must be taken into account in the model. We assume the simplest type

of background: a constant ("flat") background, which is energy-independent. At this time, there is no physics-motivated reason to assume it has any other shape (though some recent studies have hinted that the background isn't flat).

But regardless of the assumed background shape, whether it's a constant or something more complicated, the presence of a background will distort the true tritium spectral shape. The region near the endpoint of the tritium spectrum is particularly vulnerable to shape distortions because the fraction of signal rate per total rate is low compared to the fraction of background rate per total rate in this region. This is also the region where neutrino mass plays a strong role.

The projected accuracy of a KATRIN measurement is contingent on the model used to fit it. We call it a measurement of the "accuracy" here because it isn't really a systematic: any assumption on the background contribution will affect the statistical reach of the experiment. The following study quantifies the projected accuracy using MC-generated Asimov data, for a few different background levels. These are chosen with the expectation that future background mitigation techniques could improve (minimize) the background beyond what is currently possible.

### 6.4.1 Study outline

In order to quantify the projected accuracy, we employ the chi squared mapping method described in Section 6.2.2. This can then be directly compared to Equation 6.2, which was calculated using the error estimation method described in Section 6.2.1. They are expected to give equivalent results.

Following the above-mentioned chi square mapping prescription to evaluate $\sigma$ for the full 1000 days' worth of statistics:

1. Generate 1000 day Asimov MC spectrum, using settings given in Table 6.1. Note that the constant background term `Bkgnd` is set to a typical KNM3b-like value (1.7 mcps), and the `mnu2` $= 0\,\mathrm{eV}^2$.
2. Fit the generated spectrum with `mnu2` fixed at a unique value. All other tritium parameters (`DeltaE` , `AScale` , and `Bkgnd` ) are allowed to be free, as usual. All other fit settings are as stated in Table 6.2.
3. Repeat Step 2 for different values of `mnu2` (fixed).

Recall that CMKAT's `Bkgnd` parameter is the per-pixel background. So for a total

KNM3b-like[2] background of 220 mcps over the 125 active pixels, each pixel has an average background contribution of `Bkgnd` =1.7 mcps.

### 6.4.2 Results

With these fits completed, the relationship between $\chi^2$ and their corresponding (fixed) `mnu2` parameters can be plotted:

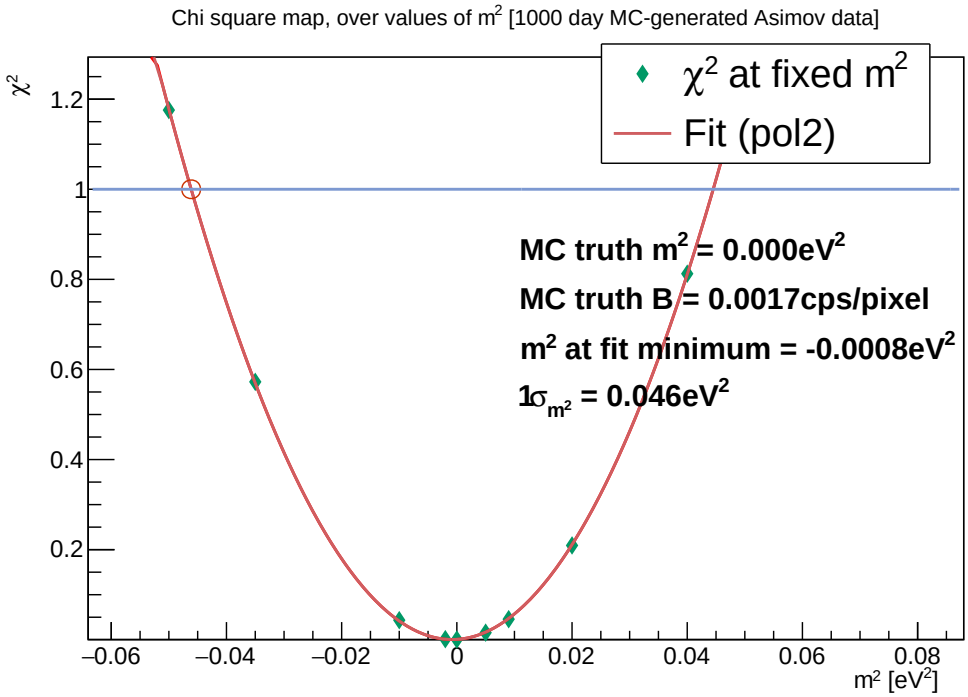


Figure 6.6: Chi squared mapping with KNM3b-like constant background terms. $1\sigma_{m^2}$ is defined as the estimated error on `mnu2` .

Figure 6.6 shows a chi square map of `mnu2` parameter space. Using this method, the $1\sigma_{m^2}$ follows the usual definition: when the $\chi^2$ increases by 1 relative to its value at the minimum, the distance between the corresponding `mnu2` and the best `mnu2` is one standard deviation error (recall Section 6.2.2). In Figure 6.6, this is graphically denoted by the intersection between the best fit parabola (red) and the constant line at $\chi^2 = 1$ (blue), and evaluates to $0.046\,\mathrm{eV}^2$. This assumes that the chi square relationship to `mnu2` is parabolic and symmetric, which is a good approximation

[2]regular, non-Shifted Analyzing Plane (SAP)

(second order polynomial fit to data points yield, on average, a chi square around $1 \times 10^{-5}$).

In order to get more insight into the influence of different constant background levels, the study is repeated for a few different values of the CMKAT parameter `Bkgnd` . Two samples at half and at double the typical KNM3b background value are chosen: `Bkgnd` =0.000 85 cps/pix and `Bkgnd` =0.003 40 cps/pix, respectively, are set in the MC. Sample backgrounds within a factor of 2 are chosen because that is the scale of plausible background improvements.

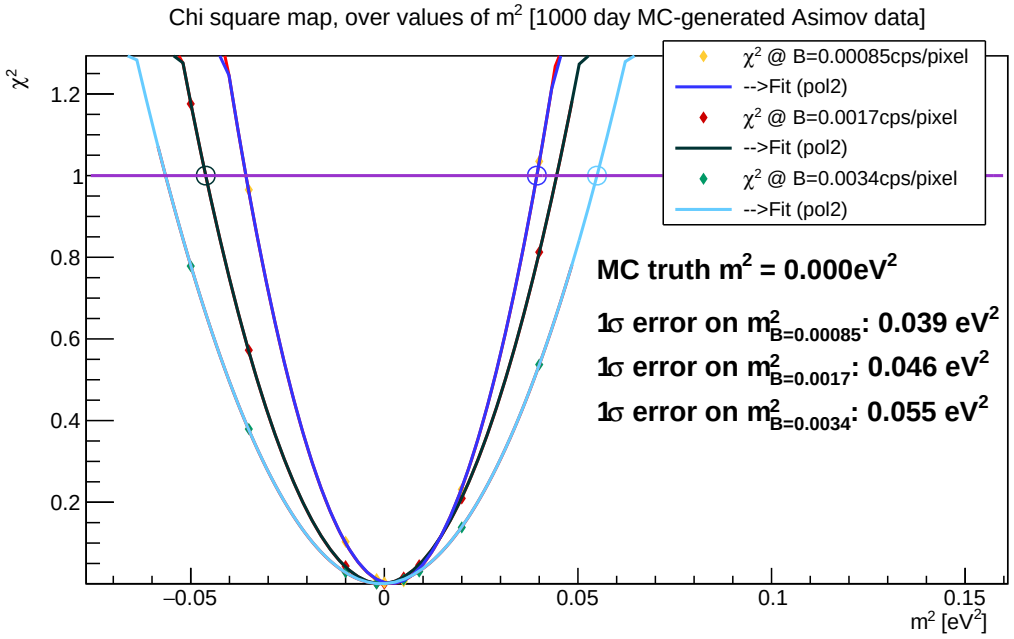


Figure 6.7: Chi square mapping with KNM3b-like MC data, for three different values of `Bkgnd` : 0.000 85 cps/pix, 0.0017 cps/pix, and 0.003 40 cps/pix. $1\sigma_{m^2}$ is defined as the estimated error on `mnu2` . According to the parabolic fits for each `Bkgnd` setting, the `mnu2` corresponding to minimum $\chi^2$ is consistent with the extracted best-fit `mnu2` value (when it is allowed to be free): on the order of $1 \times 10^{-4}\,\mathrm{eV}^2$ to $1 \times 10^{-3}\,\mathrm{eV}^2$.

As expected, the lowest background level gives the smallest estimated error on the extracted `mnu2` : it provides the smallest amount of shape distortion to the endpoint region of the tritium spectrum. This can be visualized in Figure 6.7 by a narrowing of the chi square map. The `Bkgnd` =0.000 85 cps/pix data point is of particular interest because a KNM3a-like measurement[3] would have half the background of a KNM3b-like measurement.

[3]Same in all aspects to KNM3b, but with an SAP configuration[108]

To get a sense of the dependence of $\sigma$ on any arbitrary `Bkgnd` , we repeat the chi squared mapping prescription for a few more background values, and provide a best-fit function through the points for future lookup.

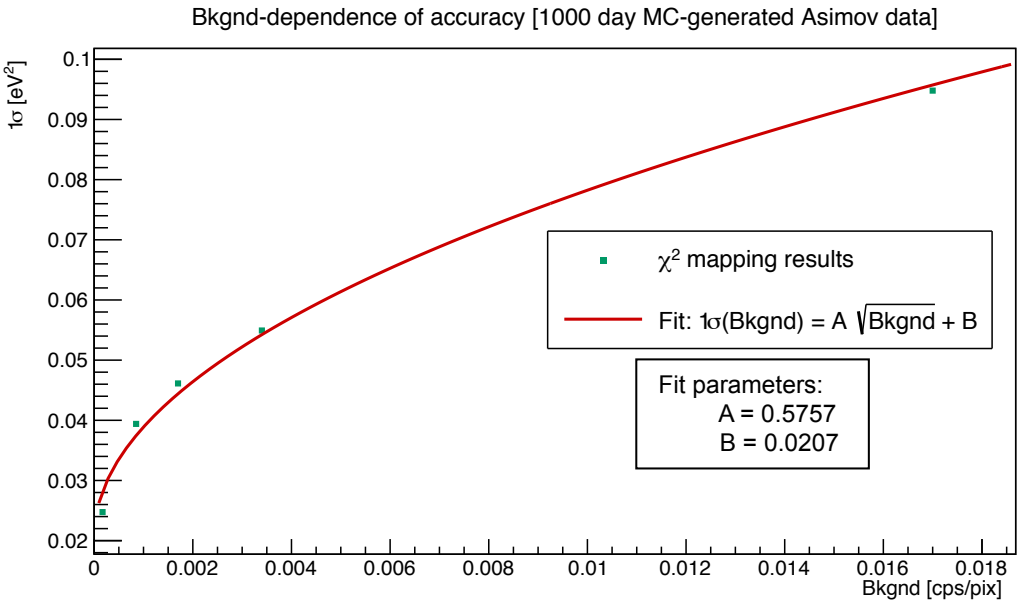


Figure 6.8: Chi square mapping's $1\sigma_{m^2}$ results vs `Bkgnd` values. The units of the $1\sigma$(`Bkgnd` ) fit function are: $\mathrm{eV}^2/\sqrt{\mathrm{cps}}$ for $A$, and $\mathrm{eV}^2$ for $B$.

The choice of fit function comes from assuming a Poisson background: the variance of a Poisson distribution is equal to the mean of the Poisson distribution [107]. The square root of the variance is our $1\sigma$ value, and the mean of the Poisson distribution is the expected event count, which is proportional to `Bkgnd` . Thus, the $1\sigma$ accuracy is expected to increase with the square root of `Bkgnd` . The offset is due to the fact that there are still event counts even after `Bkgnd` goes to zero, but those come from tritium beta electrons.

## 6.5 Impact of tritium decay in the RW and DPS

Naïvely, we expect all tritium decays to occur in the 10 m-long WGTS and nowhere else. But despite pumping to reduce the tritium flow rate downstream of the WGTS, there is still a possibility of tritium decaying in this downstream region (DPS). Likewise, the tritium decays can occur at locations which are kept at slightly different

conditions, like the RW at the WGTS' upstream end. This scenario is presented schematically in Figure 6.9 below. Electrons originating from these places are still tritium beta decay electrons, but they were not born under the same conditions as those in the WGTS. Thus we refer to them as "background tritium decay spectra".

A simple background subtraction isn't currently feasible for extracting and removing the tritium background: there is no spectral data corresponding to the background by itself. Therefore we must model the spectra, which can be done by using knowledge of run conditions and input from simulation to generate an Asimov Monte Carlo spectrum for each section.

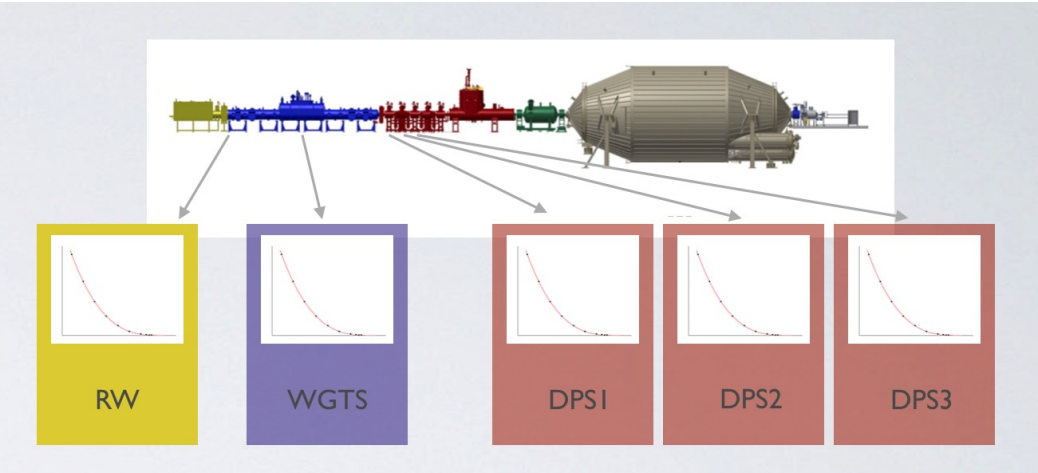


Figure 6.9: Schema of the scenario where multiple sections (RW, WGTS, and DPS1-3 each contribute to the total tritium spectra. DPS1-3) refer to the first three beamtube sections in the DPS.

### 6.5.1 Study outline

We quantify the effect of this background in terms of the neutrino mass extracted from a 1000 day MC-generated combined spectrum, fitted with a model which takes only WGTS-originating electrons into account. There will be a shift in this extracted neutrino mass compared to the neutrino mass MC truth due to the influence of the additional counts from other tritium spectra in the endpoint region, which cause a shape change in the spectrum, thus affecting the neutrino mass parameter `mnu2` . This shift will provide a handle on the sensitivity of the KATRIN experiment to tritium decays in non-WGTS sections.

The study, whose settings are given in Table 6.5 and Table 6.6, is outlined as follows:

1. Generate 1000 day tritium beta decay spectrum for RW-originating electrons, with MC $m^2_{truth} = 0$.
2. Generate 1000 day tritium beta decay spectrum for WGTS-originating electrons, with MC $m^2_{truth} = 0$.
3. Generate 1000 day tritium beta decay spectra for DPS-originating electrons, with MC $m^2_{truth} = 0$. A total of three different DPS spectra are generated: one for each of the corresponding first three subsections in the DPS section.
4. Create combined spectrum by summing RW, WGTS, and DPS spectra, as well as a constant flat background term.
5. Fit combined spectrum, with single $m^2$ parameter free ($m^2_{combined}$).
6. Compare $m^2_{combined}$ to MC truth ($m^2_{truth} = 0$).

The RW and DPS tritium spectra differ in subtle ways from the standard WGTS tritium spectra. So in order to model these RW and DPS spectra, five key ingredients must be considered: two which are simply different experimental settings (potential bias of the beamtubes and the applied magnetic fields), and three which involve tuning simulation quantities (column density, activity, and maximum number of scatterings). To make the study as relevant as possible, the MC-generated samples mimic a reference KNM2 run (56278).

**Potential bias** Firstly, the different applied potential biases of each section cause a shift in electrons' starting potential. This shifts the spectra of the RW and DPS relative to the WGTS spectrum, and have the effect of moving that spectrum's nominal tritium endpoint. These potential shifts range from order 100 meV (in the case of the RW) to order 10 eV (in the case of the DPS).

**Magnetic field** Secondly, the different magnetic fields in each section change the angular acceptance (recall Section 3.2.2), which plays a key role in the transmission condition (recall Section 3.2.1) via the maximum allowed pitch angle:

$$\theta_{max} = \arcsin\left(\sqrt{\frac{B_s}{B_{max}}}\right) \tag{6.18}$$

Here $B_s$ is the magnetic field where the electron originates. With $\theta_{max} \approx 51°$ for WGTS electrons under standard neutrino mass running conditions, Equation 6.18

shows that electrons born in a magnetic field lower than that of the WGTS will have a smaller acceptance, and vice versa.

**Column density** Recall that the column density $\bar{\rho}d$ represents the density of tritium molecules integrated over the axial length of column which the electron traverses.

For the WGTS spectra, we use the column density values reported in the reference RunSummary, $\bar{\rho}d_{WGTS}$= $4.23 \times 10^{17}$ molecules/cm$^2$. Since the electron's interactions with the gaseous tritium play such a key role, it is clear that the RW and DPS column densities must be scaled to give the correct scattering probabilities. Call these scaled column densities the effective column densities. They are used in the calculation of the model's response function.

In the case of the RW, the effective column density is twice that of the WGTS, since a RW-originating electron traverses twice the average length of a WGTS-originating electron. This effective column density is used in the calculation of the model's response function.

The DPS effective column density is a bit more complicated. The necessary scaling factor comes from a set of measurements during ion safety commissioning. These estimate a column density scaling of $5.5 \times 10^{-7}$, $5.5 \times 10^{-8}$, and $5.5 \times 10^{-9}$ times the WGTS (reference RunSummary value) for DPS1, DPS2, and DPS3, respectively [109]. On top of this, an additional scale factor is needed because these measurements were done using a non-standard setting: whereas normal neutrino mass runs are taken with the DPS beamtube electrodes in dipole mode, they were in monopole mode for the relative column density measurements. Dipole versus monopole mode refers to whether the DPS beamtube halves were at the same or different voltages. MOLFLOW+ [52] simulations by Fabian Friedel provide a mapping between dipole and monopole operational modes: the activity during measurements in taken in dipole mode is expected to be around a quarter of the activity in monopole mode[109]. Therefore, each DPS segment's effective column density needs to be scaled by an additional factor of 0.25.[4]

**Activity** Activity is defined as the rate of decays in a particular section. This value can be calculated directly given the number of tritons ($n_T$) in each section. Because of the relationship between activity and detector rate, we will use a rate scaling factor to account for differences in activity in different sections. For the CMKAT implementation, it is the rate scaling which ensures the correct activity. These rate

[4]From a CMKAT implementation perspective, it doesn't matter whether the factor of 0.25 is applied to the column density term or the activity. The column density here is so low anyways. In this study, the adjustment is applied to the column density.

scaling factors can be controlled directly by fixing the CMKAT parameter `AScale` in the Monte Carlo's truth value. This works as long as everything is relative to the WGTS rate; so for the WGTS, the parameter `AScale` = $A_{WGTS}$=1.

For the RW, there is a dedicated activity measurement from the Beta-Induced X-Ray Spectroscopy (BIXS) system by Max Aker: $R_{RW} = 43\,\text{MBq}$ [109]. In order to get the CMKAT parameter `AScale` value for the RW, we need to calculate the RW activity as a fraction of WGTS activity.

The first step is to calculate the activity in the WGTS ($R_{WGTS}$) during standard neutrino mass measurement mode. To get this, the number of tritons ($n_T$) in the WGTS must be calculated:

$$\begin{aligned} n_T &= 2\eta_T \bar{\rho} d \sigma_{BT} \\ &= 4.5 \times 10^{19} \text{ tritons} \end{aligned} \tag{6.19}$$

Where:

$n_T$ = Number of tritons
$\eta_T$ = Tritium purity (calculated from RunSummary concentrations)
$\bar{\rho}d$ = Integrated column density, in molecules/cm$^2$
$\sigma_{BT}$ = Cross sectional area of the gas in the WGTS beamtube, in cm$^2$

Knowing the number of tritons (see Equation 6.20), the WGTS activity rate can be calculated:

$$\begin{aligned} R_{WGTS} &= \frac{n_T}{\tau_T} \\ &= 80\,000\,\text{MBq} \end{aligned} \tag{6.20}$$

Where:

$\tau_T$ = Mean tritium lifetime, in seconds

Finally, the scaling factor $A_{RW}$, representing the RW activity relative to the WGTS activity, needed for the RW is:

$$A_{RW} = \frac{1}{2}\frac{R_{RW}}{R_{WGTS}} = 0.00027 \tag{6.21}$$

Where the extra factor of two takes into account the aforementioned fact that the RW effective column density is twice that of the WGTS; this is to prevent double-counting in the CMKAT implementation. For the RW simulation, then, `AScale` = $A_{RW}$.

The DPS `AScale` value can be set to $A_{DPS} = 1$, since the (simulated) effective column density already takes into account the lower activity in its model.

**Number of scatterings** Finally, one must consider the electron's interactions with the gaseous tritium. The maximum number of scatterings represents the maximum number of times an electron can scatter and still be detected.

The minimum energy loss per inelastic scattering is around 11 eV [110]. Past neutrino analyses used fit ranges extending nearly −90 eV into the spectrum, so up to 7 scatterings were considered. Current analyses use a shorter range extending −40 eV into the spectrum, but the original maximum of 7 scatterings was retained for this study.

So 7 scatterings maximum is used for the WGTS-originating electrons. Because the RW sits at the end of the WGTS, RW-originating electrons share the same maximal scattering limit. No scattering is considered for the DPS-originating electrons because there is comparatively so little tritium here that the electrons are unlikely to find other tritium molecules to scatter off of. Allowing additional scatterings in the DPS sections has no discernible effect on the DPS spectra generation, thus is superfluous.

Summarizing this information on the adjustments needed for each spectrum:

| | **RW:** | **WGTS:** | **DPS1:** | **DPS2:** | **DPS3:** |
|---|---|---|---|---|---|
| Potential bias [V]: | -1 | 0 | -15 | -35 | -85 |
| Simulated endpoint [eV]: | 18574.7 | 18573.7 | 18588.7 | 18608.7 | 18658.7 |
| B [T]: | 1.58 | 2.52 | 4.0 | 4.0 | 4.0 |
| $\bar{\rho}d_{eff}$ [mol/cm$^2$]: | $\bar{\rho}d$ $\times 2$ $= 8.454 \times 10^{17}$ | $\bar{\rho}d$ $= 4.227 \times 10^{17}$ | $\bar{\rho}d \times \frac{5.5\times10^{-7}}{4} = 5.812 \times 10^{10}$ | $\bar{\rho}d \times \frac{5.5\times10^{-8}}{4} = 5.812 \times 10^{9}$ | $\bar{\rho}d \times \frac{5.5\times10^{-9}}{4} = 5.812 \times 10^{8}$ |
| Activity [MBq]: | 43 | $8 \times 10^4$ | $1.092 \times 10^{-2}$ | $1.092 \times 10^{-3}$ | $1.092 \times 10^{-4}$ |
| `AScale` : | 0.00027 | 1 | 1 | 1 | 1 |
| Max number scatters: | 7 | 7 | 0 | 0 | 0 |

Table 6.5: Special Monte Carlo settings for each region being simulated. Note that the activity numbers are for only the active pixels (117 of 148). The selected reference RunSummary here is a KNM2 run, 56278. Potential biases are the voltages applied to beamtube (in the case of WGTS and DPS) or plate (in the case of the RW). For the RW, the bias listed is the worst-case scenario; other scenarios are explored in Table 6.8. Simulated endpoint for a given section is the WGTS's endpoint minus the potential bias.

Settings which are common to all spectra are listed on Table 6.6 below:

| MC-generation settings | | |
|---|---|---|
| **Category:** | **Setting:** | **Comments:** |
| MC truths | `DeltaE` = 0<br>`mnu2` = 0<br>`Bkgnd` = 0<br>`BSlope` = 0<br>`SigmaTr` = 0<br>`ColAdj` = 0<br>`Delta10` = 0 | `AScale` values given in Table 6.5<br>All krypton-related parameters set to 0 |
| MTD | Scaled version of real run | Copy of MTD from reference RunSummary (Run 56278), whose duration is 1.5 h<br>Total MC measurement time: 1000 day |
| FSD | KNM2 blinded | - |
| Corrections | Synchrotron radiation loss = ON<br>Radiative correction = ON | - |
| Pixel selection | KNM2 Golden Pixels | 117 of 148 pixels are considered. |

Table 6.6: Monte Carlo truths and model settings for component tritium spectra.

With these settings in mind, and using the slow control values from reference RunSummary (Run 56278, version `Durable-5g` and Period Summary `Apr2020b-Actual_18600V_6.0G`), the 5 tritium spectra can be calculated. These spectra are converted into a standard CMKAT RunSummary format so we can take advantage of all existing fitting infrastructure.

Note that during the generation process, integrated column density values' scale factors were hardcoded in the response function class (cmResponseFunction). The magnetic field values were temporarily hardcoded in the template RunSummary file. The simulated endpoints are implemented by setting `E0Nominal.Tr` in the ControlParams file. It is done in this way, instead of setting the `DeltaE` value to the potential biases given in Table 6.5, so that the response function tables are built at sensible potential settings (especially relevant for DPS3, whose potential bias setting is much higher relative to the WGTS).

Let the combined spectrum be the sum of all component tritium spectra from different sections and a background term. Let this background be a constant `Bkgnd` term of 0.0018 cps/pixel, which is the average KNM2 value. The combined spectrum rate $R_{combined}$ can then be expressed as a combination of the spectral rate contributions from each section in Table 6.6, plus the energy-independent background `Bkgnd` :

$$R_{combined} = R_{RW} + R_{WGTS} + R_{DPS1} + R_{DPS2} + R_{DPS3} + \texttt{Bkgnd} \tag{6.22}$$

The rates are $qU$-dependent, so Equation 6.22 is applied for each $qU$ (subrun).

### 6.5.2 Results

The resultant spectra (individual components, as well as combined) are shown in Figure 6.10:

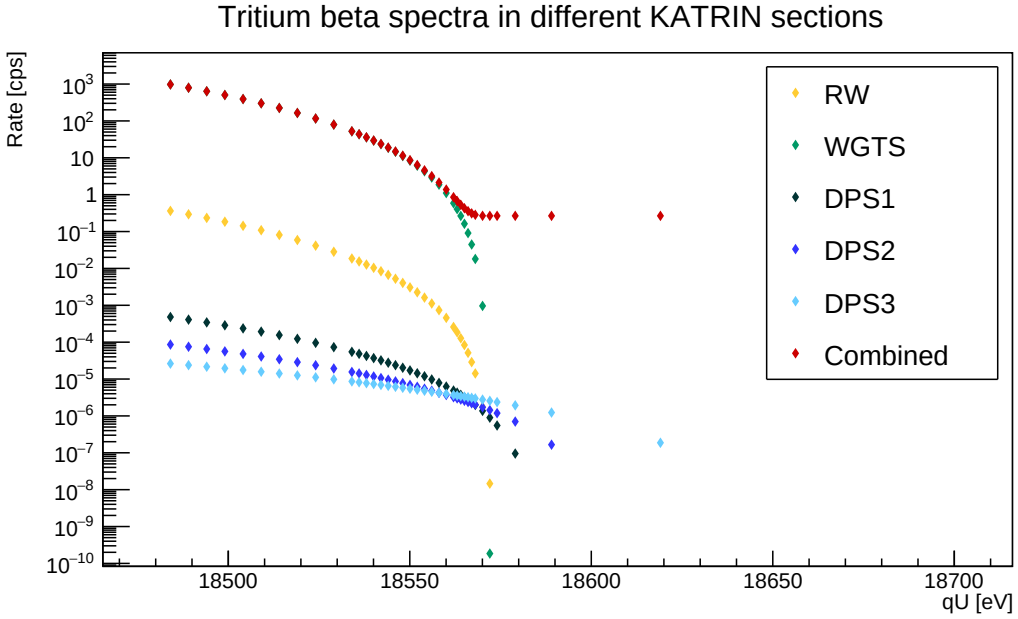


Figure 6.10: Tritium spectra for electrons created in RW, WGTS, and DPS sections 1-3. The combined spectrum is calculated using Equation 6.22, which includes the energy-independent background term. Note the log-linear scale.

Note that, as expected, the background tritium contributions from RW and DPS decays are very small, compared to the signal tritium contribution from the WGTS.

For the RW, this is due to the low activity relative to the WGTS, and is always expected to be the case. For the DPS sections, this is due to the fact that active pumping in that section has decreased the amount of tritium available for decay and scattering.

Fitting the combined spectrum from Equation 6.22 with the model for a single tritium spectrum in summed mode, we obtain the results shown in Figure 6.11.

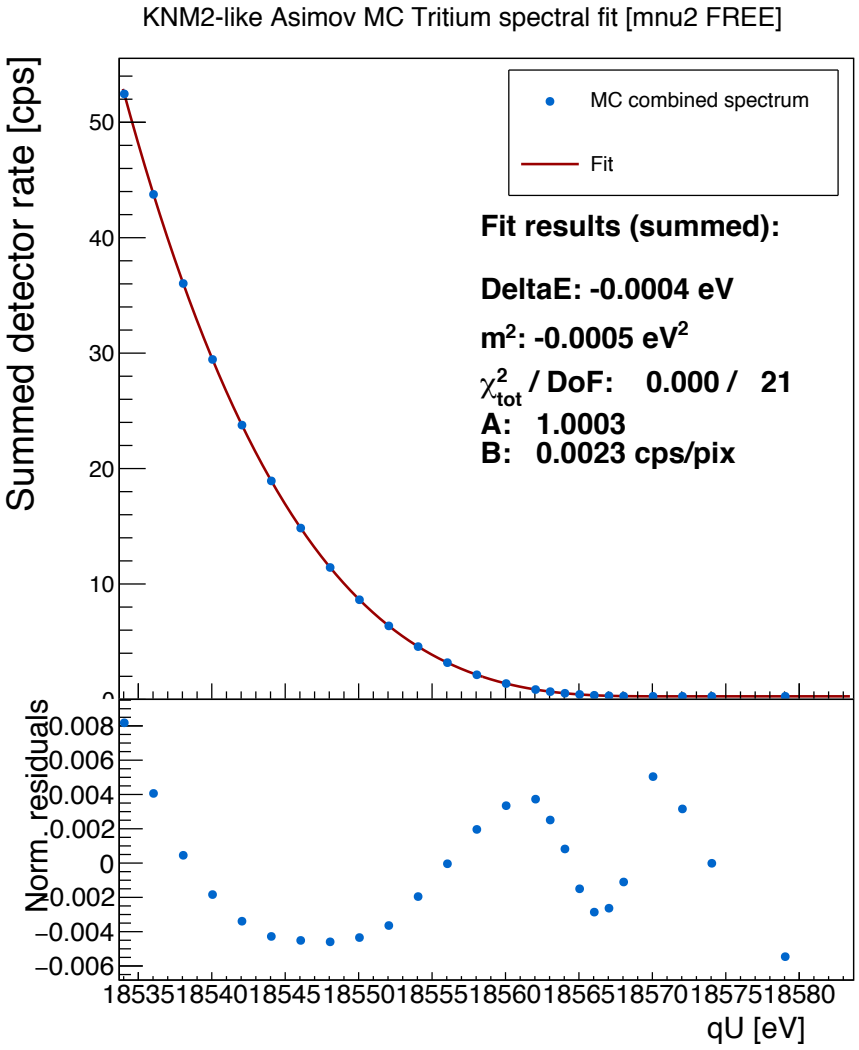


Figure 6.11: Fit to combined spectrum defined in Equation 6.22, only considering 117 active pixels. Residuals are normalized by the rate error of each subrun.

While each component spectrum was generated with $m^2_{truth} = 0\,\mathrm{eV}^2$, the combined spectrum's best-fit $m^2_{combined} = -4.58 \times 10^{-4}\,\mathrm{eV}^2$. The size of this extracted `mnu2` is very small; in fact, it is within the limit of CMKAT's fitting accuracy. The only sign of the contributions to the tritium spectrum is the increase in estimated error of `mnu2` ($0.056\,\mathrm{eV}^2$).

The shift in neutrino mass ($\Delta m^2$) due to the presence of additional tritium spectra is defined as:

$$\Delta m^2 = m^2_{combined} - m^2_{WGTS} \tag{6.23}$$

Where $m^2_{combined}$ is the extracted `mnu2` from a combined spectrum fit, and $m^2_{WGTS}$ is the extracted `mnu2` when the WGTS is the only spectrum considered (corresponds to the fit of spectrum with $R_{combined} = R_{WGTS} +$ `Bkgnd` ). In an ideal world, $m^2_{WGTS} = m^2_{truth} = 0\,\mathrm{eV}^2$, but because of the limits in Minuit convergence (Section 3.6), it actually has a small, nonzero value of $2.17 \times 10^{-3}\,\mathrm{eV}^2$ (given in Table 6.7).

Plugging in $m^2_{combined}$ and $m^2_{WGTS}$ into Equation 6.23, the result is $-2.63 \times 10^{-3}\,\mathrm{eV}^2$. This is smaller in magnitude than the negligibility threshold $\Delta m^2_{threshold}$ set in in Equation 6.17: $0.0047\,\mathrm{eV}^2$. Therefore the effect of unaccounted-for RW- and DPS-originating electrons in our spectrum is considered negligible.

### 6.5.3 Different spectral combinations

To get a feel for the amount of influence each non-WGTS component spectrum exerts on `mnu2` , the same study is repeated while only adding the RW or the DPS spectrum. The results of this study are shown in Table 6.7:

| $R_{combined}$: | $m^2_{combined}$[eV$^2$]: | $\chi^2_{combined}$: | $\Delta m^2$[eV$^2$]: | **Comments:** |
|---|---|---|---|---|
| $R_{WGTS}$ + `Bkgnd` | $2.17 \times 10^{-3}$ | 0.000043/21 | 0 | This is the case where $m^2_{combined} = m^2_{WGTS}$, as shown in Equation 6.23 |
| $R_{WGTS} + R_{DPS1} + R_{DPS2} + R_{DPS3}$ + `Bkgnd` | $1.49 \times 10^{-3}$ | 0.00015/21 | $-6.80 \times 10^{-4}$ | |
| $R_{RW} + R_{WGTS}$ + `Bkgnd` | $2.04 \times 10^{-4}$ | 0.0003/21 | $-1.97 \times 10^{-3}$ | |
| $R_{RW} + R_{WGTS} + R_{DPS1} + R_{DPS2} + R_{DPS3}$ + `Bkgnd` | $-4.58 \times 10^{-4}$ | 0.0003/21 | $-2.63 \times 10^{-3}$ | |

Table 6.7: Fits with different combinations of tritium spectral contributions. To calculate $\Delta m^2$ (Equation 6.23), $m^2_{WGTS}$ is the value given in the table's first row. The last row reflects the results of Figure 6.11.

It is clear that the additional RW spectrum contributes most to the shift in `mnu2` . This is corroborated by the fact that the RW spectrum (yellow data points in Figure 6.10) has the highest rates in the tritium endpoint region, second only to the WGTS signal itself.

It is important to note here that the RW bias voltage selected represents a worst-case scenario. In reality, it is set at a value smaller than $-1$ V. Some RW setpoints are given in Table 6.8, which correspond to three different real setpoints used during the KNM2 measurement period, as well as the case where the RW is grounded and the worst-case covered previously. The study is repeated with new RW spectra generated corresponding to the given setpoints. These RW spectra are combined with the same WGTS and DPS spectra as before, following the prescription given in Equation 6.22. The results are given below:

| **RW bias voltage** [mV]: | `E0Nominal.Tr`: | $m^2_{combined}$[eV$^2$]: | $\chi^2_{combined}$: | $\Delta m^2$[eV$^2$]: |
|---|---|---|---|---|
| $-1000$ | 18 574.7 | $2.04 \times 10^{-4}$ | 0.0003/21 | $-1.97 \times 10^{-3}$ |
| $-50$ | 18 573.75 | $9.62 \times 10^{-4}$ | 0.0002/21 | $-1.21 \times 10^{-3}$ |
| $-8$ | 18 573.708 | $10.0 \times 10^{-4}$ | 0.0002/21 | $-1.17 \times 10^{-3}$ |
| 0 | 18 573.7 | $10.1 \times 10^{-4}$ | 0.0003/21 | $-1.16 \times 10^{-3}$ |
| 200 | 18 573.5 | $10.1 \times 10^{-4}$ | 0.003/21 | $-1.16 \times 10^{-3}$ |

Table 6.8: Fits with combined tritium spectra with different RW bias voltages. Note that $\Delta m^2$ is calculated using Equation 6.23, with $m^2_{WGTS}$ from the first row of Table 6.7.

As expected, because the RW bias voltages are smaller in magnitude than the worst-case, there isn't as dramatic an increase in rates in the endpoint region, so the `mnu2` parameter doesn't shift as much. In any case, the shifts are still less than the threshold 0.0047 eV$^2$, and are therefore still negligible.

This begs the question: what kind of conditions would create a mass shift which could compete with the final sensitivity of the KATRIN experiment? How big would the RW/DPS background contributions need to be to blow the entire systematic uncertainty budget of 0.047 eV$^2$?

In Equation 6.17, we had considered 10% of the total systematic budget as appropriate limit for negligible mass shift. Assuming the only contributor to the systematic error is from an unaccounted-for RW/DPS background, a mass shift which represents the entire systematic uncertainty budget would correspond to:

$$\begin{aligned} \Delta m^2 &= \sigma_{sys} \\ &= 0.047\,\text{eV}^2 \end{aligned} \tag{6.24}$$

Because the RW contributes orders of magnitude more than any of the DPS sections, this is the lever we'll play with. The results of Table 6.8 show that changing the potential bias don't have a huge effect on the mass shift. The most dramatic effect would likely be a change in RW activity, since this would directly increase the fraction of electrons from the RW versus from the WGTS, in each energy bin.

The simplest way to scale the RW activity is to scale the RW `AScale` parameter, $A_{RW}$. New RW contributions with different $A'_{RW}$ values are generated (using the worst-case RW potential again) and combined in the usual way with the WGTS and DPS contributions. These new combined spectra are fit as if the only contribution was from the RW; results are given in Table 6.9.

| **Scaled $A'_{RW}$:** | $m^2_{combined}$[eV$^2$]**:** | $\chi^2_{combined}$**:** | $\Delta m^2$[eV$^2$]**:** |
|---|---|---|---|
| $1 \times A_{RW} = 43\,\text{MBq}$ | $-4.58 \times 10^{-4}$ | $0.0003/21$ | $-2.63 \times 10^{-3}$ |
| $2 \times A_{RW} = 86\,\text{MBq}$ | $-26.1 \times 10^{-4}$ | $0.001/21$ | $-4.78 \times 10^{-3}$ |
| $10 \times A_{RW} = 430\,\text{MBq}$ | $-191 \times 10^{-4}$ | $0.05/21$ | $-21.2 \times 10^{-3}$ |
| $50 \times A_{RW} = 2150\,\text{MBq}$ | $-997 \times 10^{-4}$ | $1.2/21$ | $-102 \times 10^{-3}$ |
| $100 \times A_{RW}$ $= 4300\,\text{MBq}$ | $-1970 \times 10^{-4}$ | $4.8/21$ | $-199 \times 10^{-3}$ |
| $300 \times A_{RW}$ $= 12\,900\,\text{MBq}$ | $-5640 \times 10^{-4}$ | $123.939/21$ | $-564 \times 10^{-3}$ |

Table 6.9: Fitting with different combinations of tritium spectral contributions, with different RW activities. Recall that the first row ($1 \times A_{RW}$) corresponds to the last entry in Table 6.7. Note that $\Delta m^2$ is calculated using Equation 6.23, with $m^2_{WGTS}$ from the first row of Table 6.7.

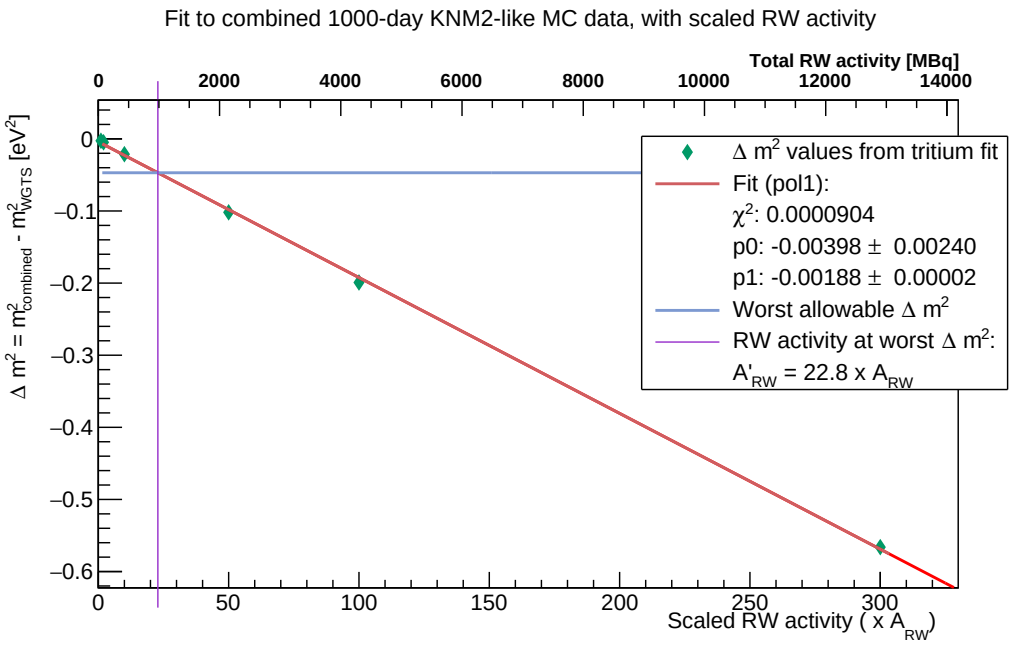


Figure 6.12: Results from Table 6.9, to extrapolate which RW activity scaling would give the worst-case mass shift.

According to a first-order polynomial fit in Figure 6.12, the current RW activity (43 MBq) would need to be scaled by a factor of 22.8 (for a total RW activity $A'_{RW}$ of 980.4 MBq) to cause a mass shift big enough to take up the entire systematic uncertainty budget (0.047 eV$^2$). Based on RW activity measurements by Max Aker, while it is possible that the RW activity could increase by a factor of 2-3, it seems unlikely to increase by an order of magnitude.

However, it is worth noting that even a factor of 2 increase in RW activity will put this systematic just above the negligibility threshold (second row in Table 6.9), so this systematic would be a good candidate for further study. The most promising method to correct for the RW spectral contribution is to include it in the model, but with fixed parameters gained from dedicated RW spectral measurements. Preliminary work on measuring the RW spectrum is currently in progress.

## 6.6 Sensitivity to Column Density parameters

As discussed in Section 3.4.3, the column density corresponds to the amount of material (gas molecules) in the source section. Beta decay electrons traveling through

the source section can encounter and inelastically scatter off these molecules, causing the electrons to lose some energy.

For this reason, the column density $\bar{\rho}d$ is a key parameter: it plays a major role in the calculation of the integrated spectrum, and has the potential to influence the extracted neutrino mass parameter, `mnu2` .

This section aims to quantify how sensitive the extracted `mnu2` is to the column density, which can be explored via the behavior of the CMKAT column adjustment fit parameter, `ColAdj` . Recall how this parameter modifies the column density read directly from the RunSummary, $\bar{\rho}d_{measured}$:

$$\bar{\rho}d_{true} = \bar{\rho}d_{measured} \times (1 + \texttt{ColAdj}\ ) \tag{6.25}$$

We begin by first quantifying the shift in extracted `mnu2` due to an underestimation of the measured column density (Section 6.6.1).

Having established this, we examine how the accuracy in actual column density measurements affect the extracted `mnu2` (Section 6.6.1). The lever we have on this is the column density measurement error, whose value (0.2%) is provided by a dedicated column density working group [86].

While exploring the effects of column density on the KATRIN results is not new, the studies done here are novel in the sense that CMKAT presents a new approach to modelling the column density and assessing its corresponding uncertainties.

### 6.6.1 Effect of column density underestimation

In order to quantify the effect of underestimating the column density on the extracted `mnu2` , we must build in a column density mismatch between the model (fit) and the Monte Carlo-generated data.

#### 6.6.1.1 Study outline

The study, in which `ColAdj` is not treated as a fit parameter and is instead kept fixed, goes as follows:

1. Generate a 1000-day Asimov MC tritium spectrum, according to settings listed in Table 6.1 (note the `mnu2` =0), but with `ColAdj` =0.

2. Fit this spectrum with settings listed in Table 6.2, but with fixed `ColAdj` =0.002 and no additional pull term.

3. Compare fit results via the shift of extracted `mnu2` .

The value of `ColAdj` =+0.002 is selected to complement the real KATRIN column density measurement error estimation.

#### 6.6.1.2 Results

The result of this study is shown in the first row of Table 6.10. In order to put this into context, the study must be repeated where there is no mismatch between data and model. To get the "no mismatch" results, the exact same procedure was used as outlined above, but with `ColAdj` fixed at 0 (in Step 2). In this case, with data and model containing no mismatch, the extracted `mnu2` should be zero (modulo the accuracy of Minuit). The second row of Table 6.10 verifies this.

| **Fitted** `ColAdj` **:** | `mnu2` [eV$^2$]**:** | `mnu2` **est. err** [eV$^2$]**:** | $\chi^2$: | **Comments:** |
|---|---|---|---|---|
| fixed (=0.002) | 0.011 | 0.053 | 0.0570 | No pull term<br>Mismatch between model and data |
| fixed (=0) | −0.00054 | 0.046 | 0.0002 | No pull term<br>No mismatch between model and data |
| free | −0.00060 | 0.047 | 0.0002 | With pull term: $\sigma_{\bar{\rho}d,err}$ = 0.002<br>Extracted `ColAdj` =−0.000005 ± 0.0019 |
| free* | -0.00052 | 0.069 | 0.0009 | **Sanity check:** manually changed RunSummary column density value to be x1.002 higher after MC generation (with `ColAdj` =0)<br>Fit with pull term: $\sigma_{\bar{\rho}d,err}$ = 0.08<br>Extracted `ColAdj` =−0.0020 ± 0.0083 |

Table 6.10: Fit to spectra with underestimated column densities (data: `ColAdj` =0), using settings in Table 6.2. Results are in the `test` directory. Minuit errors used. Not shown in this table is a test of the case where `ColAdj` was fixed at 0.002, but including a pull term. As expected, this resulted in the same extracted `mnu2` value as the no-pull case, but with a chi squared increased by 1 (in agreement with Equation 6.27). The row marked with * is a sanity check, described below.

An additional study with a freed `ColAdj` fit parameter is done to confirm that it would converge to the MC truth value (row three of Table 6.10). This was confirmed as well, with the extracted `mnu2` again being nearly zero (modulo the accuracy of Minuit). It also reproduces the MC `ColAdj` value of 0.

To ensure that a free `ColAdj` is behaving as expected (case of `ColAdj` =0 could be an edge case that hides weird behavior), a quick sanity check is done. First, an Asimov MC data set is generated with the settings listed in Table 6.1, but with `ColAdj` =0. After generation, the column density listed in the MC RunSummary is increased by

a factor of 1.002. This mimics the effect of overestimating the true column density, independent of the model; it corresponds to data which is being overestimated by 0.2%. Fitting this spectrum with a free `ColAdj` and with pull term included (large measurement error for reasons explained in Section 6.6.2), the free `ColAdj` parameter compensates for the hardcoded overestimation by swinging to `ColAdj` =-0.002. The MC truth for `mnu2` is recovered, to within our numerical accuracy. This validates the implementation of the `ColAdj` parameter.

Finally, the shift in extracted `mnu2` when there is a column density underestimation of 0.2% can be calculated:

$$\begin{aligned}\Delta m^2_{underest} &= \texttt{mnu2}_{\,\texttt{ColAdj=0.002}} - \texttt{mnu2}_{\,\texttt{ColAdj=0}} \\ &= 0.011\,\mathrm{eV}^2 - -0.000\,58\,\mathrm{eV}^2 \\ &= 0.012\,\mathrm{eV}^2 \end{aligned} \tag{6.26}$$

This systematic shift in `mnu2` is larger than the negligibility threshold (Equation 6.17) of $0.0047\,\mathrm{eV}^2$. Clearly, a column density underestimation of 0.2% has a large impact on $m^2_\nu$ . But there is hope: Table 6.10 demonstrates that fitting with a free `ColAdj` parameter and a pull term can compensate for underestimation of the data. The next section (Section 6.6.2) will go more into depth on the behavior of the free `ColAdj` and pull term in the chi square.

### 6.6.2 Effect of column density measurement accuracy

The previous section established that unwittingly underestimating the column density and not including any information on the column density measurement error (no pull term) can cause a significant systematic shift in extracted `mnu2` .

If `ColAdj` is allowed to be treated as a fit parameter, and the model is given access to column density measurement error information, the fit can be improved. Whether it is or not depends on the accuracy of column density measurement, which is estimated by the column density measurement error.

The column density measurement error ($\sigma^2_{\bar{\rho}d,err}$) enters into the fit via pull term as described in Equation 3.60:

$$\chi^2_{tot} = \chi^2 + \frac{\texttt{ColAdj}^{\,2}}{\sigma^2_{\bar{\rho}d,err}} \tag{6.27}$$

The inclusion of the pull term is equivalent to adding another measurement. Because the pull term is strongly tied to the accuracy of this measurement, the studying the impact of different values of $\sigma^2_{\bar{\rho}d,err}$ is the clear next step.

#### 6.6.2.1 Study outline

The first step builds on the quick sanity check in the last section (Section 6.6.1), except now the column density underestimation is built into the data via the MC `ColAdj` truth. We choose a nonzero value for this MC truth to track changes in the extracted fit `ColAdj` for different values of $\sigma^2_{\bar{\rho}d,err}$:

1. Generate a 1000-day MC Asimov tritium spectrum, according to settings listed in Table 6.1, except with `ColAdj` =0.002.
2. Fit this spectrum with free `ColAdj` , and the pull term enabled. All other fit settings are described in Table 6.2.
3. Repeat Step 2 for different values of the column density measurement error.

#### 6.6.2.2 Results

Following this procedure, we can fill Table 6.11 for a range of measurement errors, spanning values much smaller and much larger than what is currently possible ($\sigma_{\bar{\rho}d,err} = 0.2\%$):

| Fit results, with MC truth ColAdj =0.002 | | | | | |
|---|---|---|---|---|---|
| $\sigma_{\bar{\rho}d,err}$ [%]: | mnu2 [eV$^2$]: | mnu2 est. err [eV$^2$]: | ColAdj : | ColAdj est. err: | $\chi^2$: |
| 0.05 | −0.012 | 0.045 | 0.0000084 | 0.00050 | 0.071 |
| 0.1 | −0.012 | 0.046 | 0.000035 | 0.0010 | 0.070 |
| 0.2 | −0.011 | 0.047 | 0.00015 | 0.0019 | 0.067 |
| 0.5 | −0.0085 | 0.052 | 0.00061 | 0.0042 | 0.050 |
| 1.0 | −0.0047 | 0.058 | 0.0013 | 0.0060 | 0.026 |
| 5.0 | −0.00075 | 0.063 | 0.0020 | 0.0075 | 0.0018 |
| 8.0 | −0.0006 | 0.063 | 0.0020 | 0.0075 | 0.00084 |
| 10.0 | −0.00059 | 0.063 | 0.0020 | 0.0075 | 0.00062 |

Table 6.11: Fit results. Technical note: due to some edge-case settings, the fitting script and ControlParams file used were provided by Gregg Franklin. This includes initialization with mnu2 =0.1 instead of 0, for fit stability reasons.

If the measurement of the column density is assumed to be very precise (small $\sigma_{\bar{\rho}d,err}$), then ColAdj plays a big role in the total chi square, predominantly through the pull term. This is at the cost of pulling mnu2 away from its MC truth value, and results in a worst fit. Conversely, if one makes a very imprecise column density measurement (large $\sigma_{\bar{\rho}d,err}$), the pull term's contribution to the total chi square becomes smaller, and ColAdj can be pushed closer to its MC truth value.

Testing this behavior on data with purposefully underestimated column density is a good way to demonstrate these expected outcomes. In a real situation, this would be unlikely because nonzero ColAdj is itself evidence of an inaccurate column density measurement; a consistently positive or negative ColAdj would be evidence of a systematic error in the measurement. However, testing first with nonzero ColAdj is useful because it solidly differentiates between cases where the ColAdj fit value is being minimized to 0, and where it's being driven to its MC truth.

Having demonstrated how the extracted ColAdj attempts to compensate for underestimated column densities in data, we can move forward and assume the column density is known perfectly (no column density underestimation). This is done by setting the ColAdj MC truth to 0. Repeating the fitting procedure (defined above with ColAdj =0 in Step 1) over the same set of column density measurement errors:

| Fit results, with MC truth ColAdj =0 | | | | | |
|---|---|---|---|---|---|
| $\sigma_{\bar{\rho}d,err}$ [%]: | mnu2 [eV$^2$]: | mnu2 est. err [eV$^2$]: | ColAdj : | ColAdj est. err: | $\chi^2$: |
| 0.05 | −0.00050 | 0.045 | −0.00000011 | 0.00050 | 0.00022 |
| 0.1 | −0.00049 | 0.046 | 0.00000033 | 0.0010 | 0.00022 |
| 0.2 | −0.00031 | 0.047 | 0.0000000012 | 0.0019 | 0.00025 |
| 0.5 | −0.00051 | 0.051 | 0.0000037 | 0.0042 | 0.00024 |
| 1.0 | −0.00041 | 0.058 | 0.000079 | 0.0060 | 0.00074 |
| 5.0 | −0.00055 | 0.063 | −0.000000058 | 0.0075 | 0.00022 |
| 8.0 | −0.00069 | 0.063 | −0.000033 | 0.0075 | 0.00025 |
| 10.0 | −0.00043 | 0.064 | 0.0000025 | 0.0076 | 0.00022 |

Table 6.12: Fit results on data whose column density was not underestimated.

In this case, there isn't much shift in mnu2 or ColAdj with increase in measurement error because this is the special case of ColAdj =0, so the pull term is already really small. What is of interest is the estimated errors on mnu2 and ColAdj , which both get larger with larger measurement error. This implies that the less accurately the column density is known, the less accurately mnu2 can be pinned down.

Repeating the study once more on data with an underestimated column density, but with the pull term disabled, we get insight on the neutrino mass shift free of the column density measurement error information:

| Fit results, with MC truth ColAdj =0.002 (no pull term) | | | | | |
|---|---|---|---|---|---|
| $\sigma_{\bar{\rho}d,err}$ [%]: | mnu2 [eV$^2$]: | mnu2 est. err [eV$^2$]: | ColAdj : | ColAdj est. err: | $\chi^2$: |
| N/A | −0.00021 | 0.063 | 0.000018 | 0.0076 | 0.00025 |

Table 6.13: Fit results, without pull term. Note that results will be same regardless of $\sigma_{\bar{\rho}d,err}$ value, because the only place it appears is in the pull term.

It is clear that this (Table 6.13) is analogous to the case where no information on the column density accuracy is supplied (i.e., the limit of large $\sigma_{\bar{\rho}d,err}$ in Table 6.12).

The following figure collates the results of Table 6.11, Table 6.12, and Table 6.13:

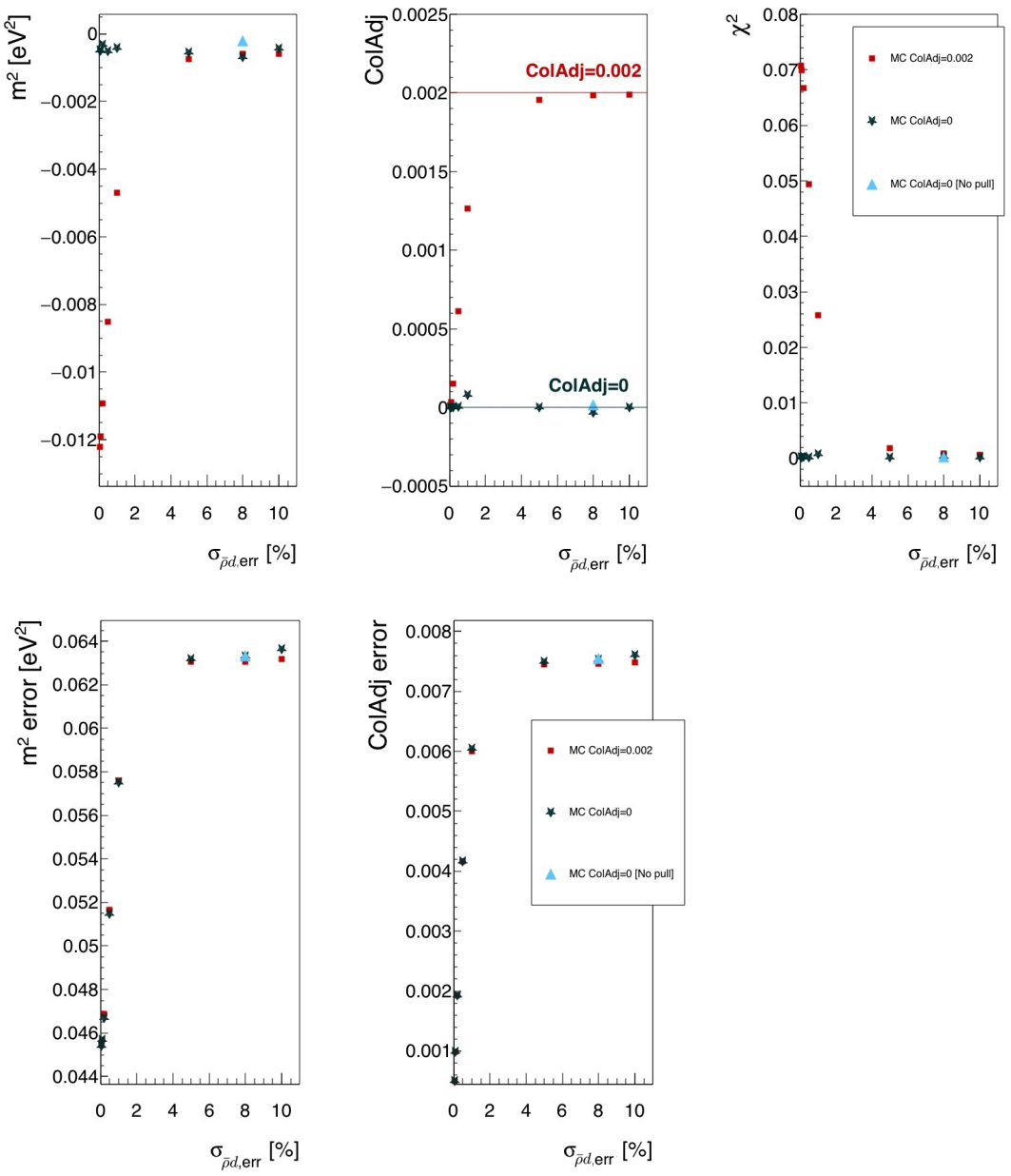


Figure 6.13: Compare $\sigma_{\bar{p}d,err}$ versus shift in extracted `mnu2` and `ColAdj` values, as well as their respective estimated errors. Note that the error bars on `mnu2` and `ColAdj` plots are supplied separately in the bottom row of plots. The "no pull" data point's corresponding $\sigma_{\bar{p}d,err}$ value has no significance and was chosen for best visibility.

It's clear that, for data whose column density has not been underestimated (`ColAdj` =0 case), choice of $\sigma_{\bar{\rho}d,err}$ doesn't affect the extracted `mnu2` much. The shift in `mnu2` (order $1 \times 10^{-4}\,\mathrm{eV}^2$) is on the same order as the CMKAT accuracy regardless of $\sigma_{\bar{\rho}d,err}$. This shift in extracted `mnu2` is far below the negligibility threshold (Equation 6.17) of $0.0047\,\mathrm{eV}^2$, its contribution to the systematics budget is negligible.

But once the column density has been underestimated appreciably (`ColAdj` =0.002), column density measurements with an assumed error smaller than 5% (alternatively, "more accurate than 5%") can shift the extracted `mnu2` enough to play a major role in the entire systematics uncertainty budget (converging to an `mnu2` shift of $-0.012\,\mathrm{eV}^2$, which is about 25% of the $0.047\,\mathrm{eV}^2$ allotted to systematics).

Assuming the column density measurement error remains at 0.2%, the maximum `ColAdj` which passes the negligibility threshold of $0.0047\,\mathrm{eV}^2$ can be extrapolated with the following study:

1. Generate 1000 day MC Asimov spectrum for a given `ColAdj` , using settings defined in Table 6.1.
2. Fit the spectrum with the current column density measurement error $\sigma_{\bar{\rho}d,err} = 0.002$. All other fit settings are defined in Table 6.2.
3. Calculate $\Delta m^2 = m^2_{\texttt{ColAdj}} - m^2_{\texttt{ColAdj}=0(fix)}$, where $m^2_{\texttt{ColAdj}=0(fix)}$ is the extracted `mnu2` from a spectrum generated with `ColAdj` =0 and fitted with fixed `ColAdj` =0 (value taken from the second row of Table 6.10).
4. Repeat Steps 1-2 for a range of `ColAdj` values between 0 and 0.002.

The results for a few points are shown in Figure 6.14:

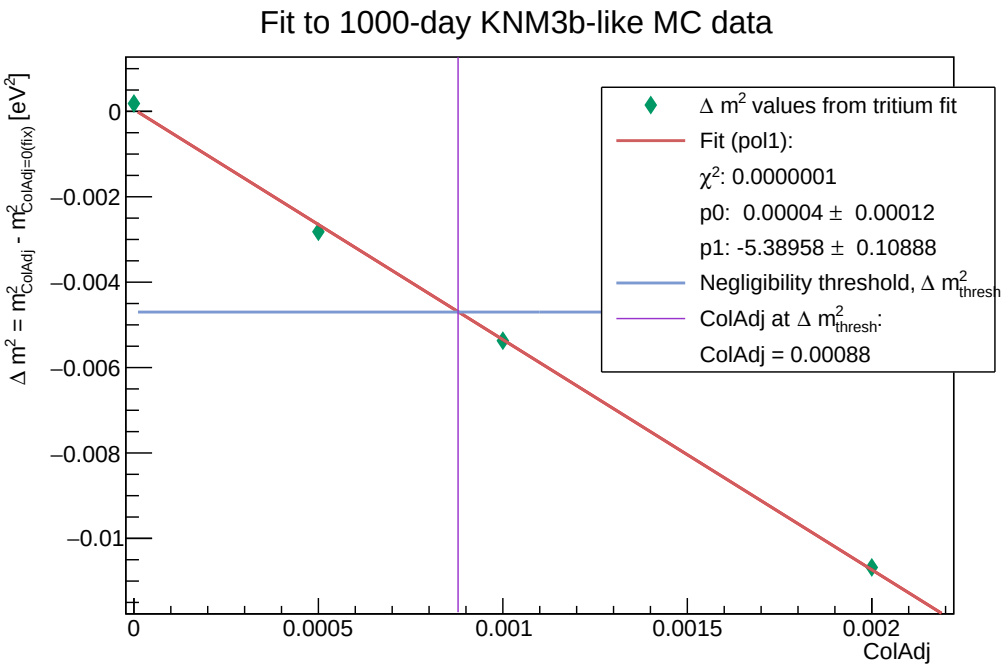


Figure 6.14: For $\sigma_{\bar{\rho}d,err} = 0.002$: extrapolation of how much column underestimation can be tolerated before the negligibility threshold is hit. A first order polynomial provides a good fit to the data points, and is used to evaluate the `ColAdj` at the negligibility threshold.

This study estimates that for $\sigma_{\bar{\rho}d,err} = 0.002$, a maximum underestimation of 0.088% (`ColAdj` =0.00088) can be tolerated before the negligibility threshold of $0.0047\,\mathrm{eV}^2$ is hit. This relationship is symmetric: 0.088% column density overestimation (`ColAdj` =-0.00088) fulfills this requirement as well.

The qualitative lesson here is the importance of ensuring that the column density used by the model is as close as possible to the true column density, or else that apparently precise $\sigma_{\bar{\rho}d,err}$ will shoot the unwary fitter in the foot. This underscores the need to be careful when combining measurement campaigns with even slightly different column densities. One possible way to address this in CMKAT is to allow the model access to column density values for each subrun (rather than using a single, averaged value for all subruns).

## 6.7 Nonlinear rate adjustment

As described in Section 2.2, there is an intermediate step between raw data collection and the output RunSummary file. This intermediate step seeks to correct some of the detector-related effects by correcting the rates directly.

To understand why this rate correction step is important, it must be understood that incident electron rate is not the same thing as detector rate. In translating from detector rates to the electron rate (RunSummary's `EventCounts`), one must consider competing effects which can cause loss/gain/shifts of counts: backscattering, reflection, pile-up, detector dead layer, ROI cut, and readout deadtime. In addition to these, one still cannot assume that detector rates are Poisson because of the presence of correlated physical processes, such as generation of secondary background electrons via cascades, discharges, etc.

Categorizing the above mentioned detector-related effects will not be the topic of the section; for more information on this, see [111].

However, some of these detector effects have a rate-dependence which can be easily modeled. To first order, these can be modeled by a nonlinear correction to the rate:

$$R' = R \times (1 + \alpha R) \tag{6.28}$$

Where $R'$ is the corrected rate, $R$ the uncorrected rate, and $\alpha$ is the nonlinear correction factor. $R'$ should be closer to the incident electron rate. Equation 6.28 makes no assumptions about whether $R$ or $R'$ is larger, as the process of applying rate corrections can move events in or out of the detector region of interest.

### 6.7.1 Study outline

To characterize this nonlinearity, we map out what an unaccounted-for detector rate nonlinearity would do to the extracted `mnu2` . The study goes as follows:

1. Generate 1000-day Asimov MC data, according to the settings in Table 6.1. The data is to be generated with some value $\alpha$.
2. Fit the spectrum, using the settings listed in Table 6.2.
3. Repeat Steps 1-2 for a range of $\alpha$.

### 6.7.2 Results

Note that the fitting model assumes linearity ($\alpha = 0$). The table below tabulates fit results for data sets generated with different values of $\alpha$:

| $\alpha$ [s]: | `mnu2` [eV$^2$]: | `mnu2` **est. error** [eV$^2$]: | $\chi^2$: |
|---|---|---|---|
| -0.004 | 0.14 | 0.043 | 15.32 |
| -0.0005 | 0.017 | 0.046 | 0.24 |
| -0.0001 | 0.0029 | 0.044 | 0.0099 |
| 0 | -0.00083 | 0.044 | 0.00036 |
| 0.0001 | -0.0039 | 0.045 | 0.0099 |
| 0.0004 | -0.015 | 0.043 | 0.15 |
| 0.001 | -0.036 | 0.046 | 0.95 |
| 0.005 | -0.18 | 0.045 | 23.68 |
| 0.01 | -0.37 | 0.044 | 94.10 |

Table 6.14: Fit results for different nonlinear factors $\alpha$. Fits at/above $\alpha$=0.01 stopped converging, likely because the unaccounted-for nonlinear rate component became significant. Unaccounted-for nonlinearities at this level simply disturb the fit sufficiently to the point where Minuit gives up.

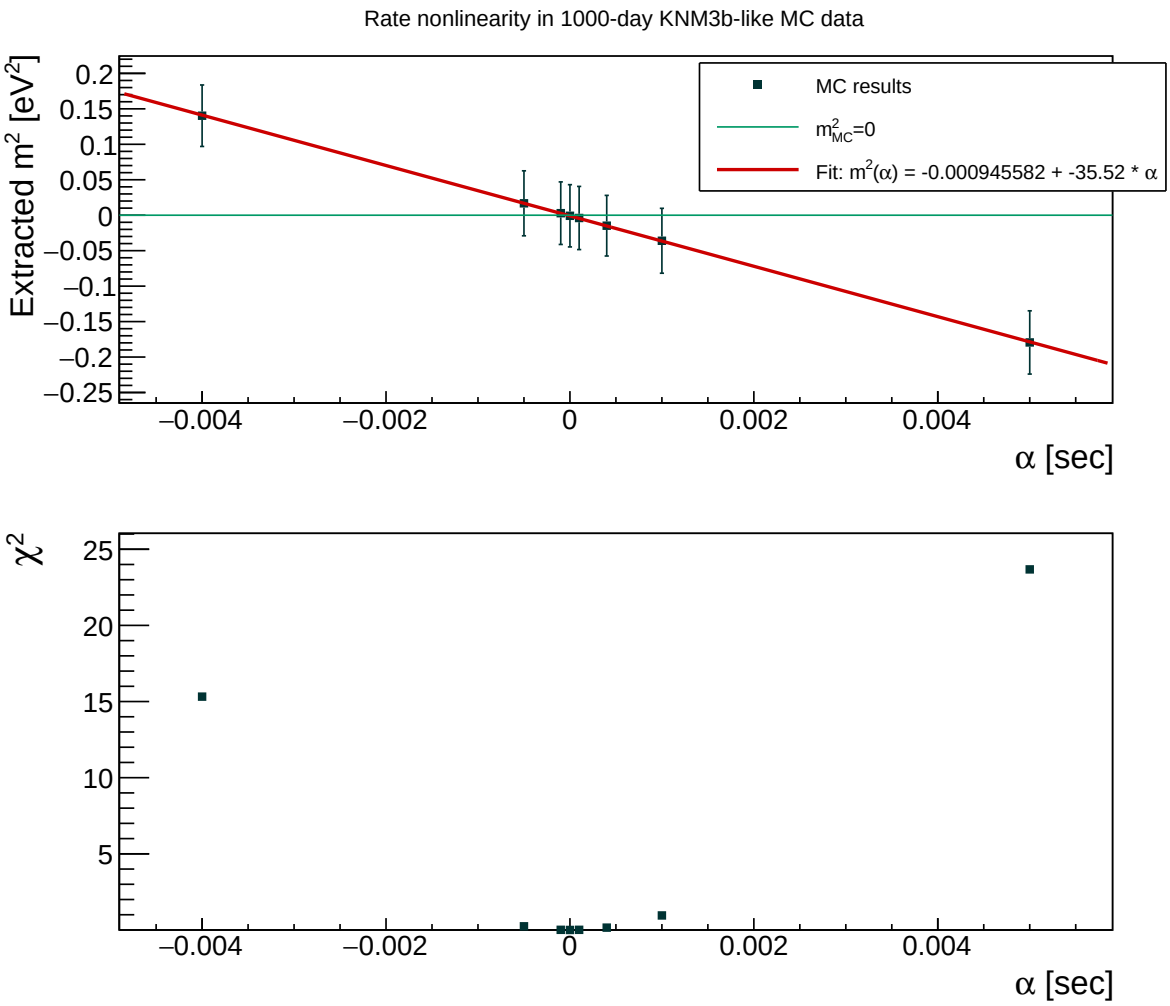


Figure 6.15: Results from Table 6.14, with first order polynomial fit through MC data points.

Given the first order polynomial fit (red line in Figure 6.15) and the negligibility threshold (Equation 6.17), nonlinearity effects can be considered negligible if the nonlinearity factor is less than:

$$|\alpha_{thresh}| = 1.1 \times 10^{-4}\,\mathrm{s} \tag{6.29}$$

### 6.7.3 In the case of pile-up

To get a sense for how much nonlinearity there is in the real data and whether it is negligible, we reference a study of various detector effects[111]. One such effect which contributes to the rate like in Equation 6.28 is pile-up. The simplest case of pile-up is the case of two electrons arriving within $\leq t_{pileup}$ of each other at the same detector pixel: the DAQ will record a single event with a higher energy, corresponding to the sum of the two electrons' energies.

For the case of pile-up, we can estimate how the nonlinearity due to pile-up compares to our $\alpha_{thresh}$ (Equation 6.29). This is done by relating to one of the properties of the DAQ double trapezoidal filter[49, 56] (which is responsible for time and energy reconstruction of electron hits). The property of interest is the shaping length, $L$, which is set to $1.6 \times 10^{-6}$ s. The $L$ corresponds approximately to the time window during which events are being recorded[5], so if two events occur within $t_{pileup} \leq L$, they could be recorded as a single event.

This could move events into or out of the FPD region of interest[111], depending on the data cuts, resulting in a gain of events ($\alpha > 0$) or a loss of events ($\alpha < 0$). For a given event, the probability that the next event comes within the shaping length $L$ =1.6 $\times 10^{-6}$ s on the same pixel is $\frac{RL}{N_{pix}}$, where $N_{pix}$ is the number of pixels. In the case that both events are lost, $\alpha = -\frac{2L}{N_{pix}} = \frac{-3.2 \times 10^{-6}\,\mathrm{s}}{148 pix} = -2.16 \times 10^{-8}\,\mathrm{s/pix}$, which is four orders of magnitude smaller than the negligibility threshold $\alpha_{thresh}$ defined in Equation 6.29.

The detector effects document [111] presents results from extensive studies on FPD-related effects and defines a set of corrections to detector counts, including a pile-up correction. Results from the pile-up correction study in [111] can be used to estimate the nonlinearity factor due to pile-up.

The detector effects document defines the rate-dependent detector efficiency correction to be:

$$R' = \epsilon R \tag{6.30}$$

Where $R'$ and $R$ are the same corrected and uncorrected detector rates as used in Equation 6.28, and $\epsilon$ is the efficiency correction. Note that $\epsilon$ is an efficiency correction on top of the rate-independent detector efficiency (`DETECTOR_EFFICIENCY`

[5]This does not include the gap length $G$=200 ns, which would make the true event time window somewhere between $L$ and $L$+$G$.

value in CMKAT's cmFixedDefinitions class, which is fixed to 90%).

Setting Equation 6.30 equal to Equation 6.28, we arrive at the relationship:

$$\epsilon = 1 + \alpha R \tag{6.31}$$

As noted earlier, the $\alpha$ (and by extension, the $\epsilon$) can take on positive or negative values, depending on whether events are being moved into or out of the FPD region of interest.

To calculate the nonlinearity factor $\alpha = \alpha_{pileup}$ in Equation 6.31, we require $\epsilon$ and $R$. At 17.75 keV, Figure 7 of [111] estimates a pile-up efficiency correction $\epsilon$ of 99.99%. The uncorrected rate $R$ comes from an MC spectrum. The plot below (Figure 6.16) shows the tritium spectrum in the range 17 750 eV to 18 710 eV, which was generated without statistical fluctuation and for 1000 days' worth of measurement time, in accordance with the usual settings in Table 6.1:

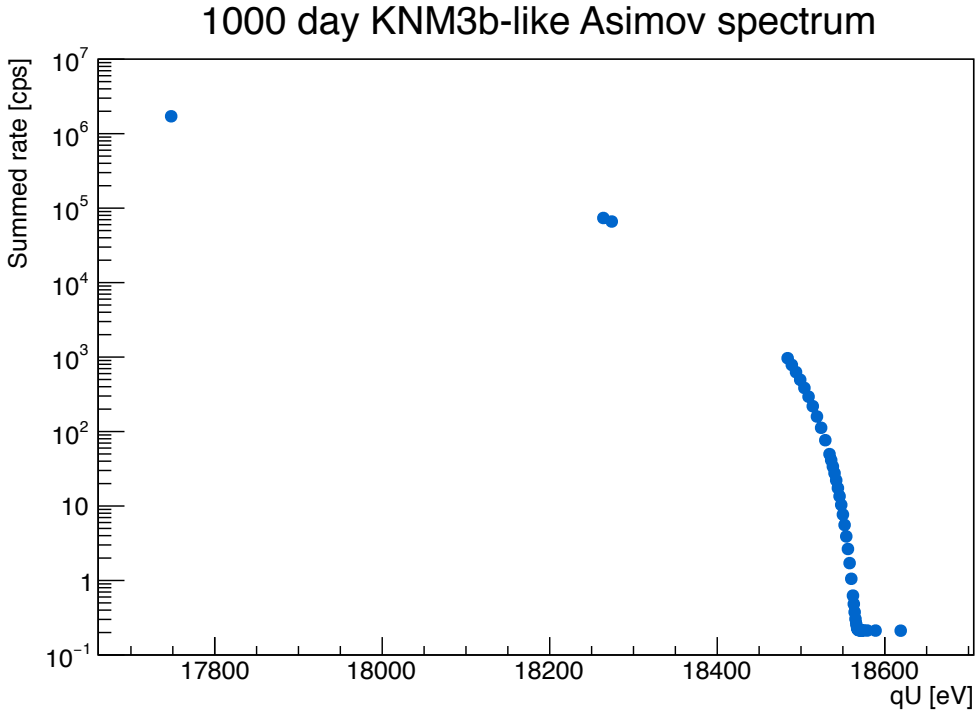


Figure 6.16: 1000 day KNM3b-like MC-generated Asimov spectrum (generated in accordance with Table 6.1 settings), to estimate $\alpha_{pileup}$.

According to Figure 6.16, the rate far the endpoint is on the order of $1 \times 10^6$ cps. Plugging this in for $R$, and an efficiency correction of $\epsilon = 0.9999$[111], the estimated $\alpha_{pileup}$ from Equation 6.31 is:

$$|\alpha_{pileup}| = 1 \times 10^{-10}\,\mathrm{s} \tag{6.32}$$

Comparing to the result in Equation 6.29, the requirement that $\alpha_{pileup} < \alpha_{thresh}$ is met, and we consider it negligible.

In conclusion, even if the rate nonlinearity were not corrected, the effect on the neutrino mass analysis would be negligible. In any case, corrections for these nonlinear effects are implemented[111] (with a correction error on the 10% level), so no further action is needed.

# Chapter 7

# Conclusions

The absolute mass scale of the neutrino is of great interest to modern physics, and the KATRIN experiment is poised to make major contributions to the field. In the short time since data-taking with tritium began in spring 2019, the KATRIN experiment has already set new world-best upper limits on the neutrino mass[39, 61, 44], and pushed the limit into the sub-eV range for the first time in 2021 ([44] and this work).

The KATRIN experiment's high precision measurements are made possible by standing on the shoulders of giants, taking advantage of lessons learned with past MAC-E filter-equipped spectrometer-based experiments at Mainz[38] and Troitsk[37]. Through upgrades and implementation of new techniques, the resulting hardware setup (described extensively in Section 2 and in [49]) is expected to meet all the design requirements.

Analysis of this data using the CMKAT analysis framework was the main focus of this work. The CMKAT framework was developed by Gregg Franklin and Larisa Thorne (the author), and consists of a set of custom classes for handling, modelling, and fitting both real and Monte Carlo-simulated data. The CMKAT framework is written in C++ and uses ROOT libraries. It includes both a tritium beta decay (Section 3.1.2: for neutrino mass analysis) and $^{83m}$Kr conversion electron (Section 3.1.1: for krypton calibration) models, as well as the KATRIN experiment response function (Section 3.2). The $\chi^2$ minimization is optimized by using a special 3-level algorithmic structure which takes advantage of the linear fit parameter terms. A description of CMKAT on the technical level is given in Section 3.4. Validation (Section 3.5) and convergence tests (Section 3.6) demonstrated that CMKAT neutrino mass analysis results were in agreement with those of other analysis teams.

With the CMKAT framework checked and validated, analysis of real data could be

done. Because the conversion electrons from $^{83m}$Kr have such well-defined peaks (of order 1 eV wide), they are excellent for characterizing the electrons' starting potential in the WGTS. In KNM2, studies with blinded data found that the influence of non-neutral plasma in the WGTS had a systematic effect on neutrino mass analysis, when in the presence of large amounts of tritium. By injecting krypton and tritium gas simultaneously into the WGTS, the krypton conversion electrons would be subject to the same starting potential conditions as the beta decay electrons, so analysis of the krypton lines in this measurement mode could help characterize this systematic effect. There are a few components necessary to fully characterize these plasma-induced effects. One of them is a Gaussian plasma-induced broadening , $\sigma_P$, which is calculated in Section 4.1. It was also found that the choice of RW voltage setting had an effect on the electrons' starting potential. By studying the radial dispersion in krypton line energy, a range of optimal RW voltages could be identified which would minimize this radial dispersion. This is studied in Section 4.2.

CMKAT was also used to fit the KNM2 neutrino mass measurement campaign data. With its validation process completed using one of the KNM2 unblinding milestones, the CMKAT team met the requirement to fit the KNM2 unblinded data. In an independent analysis in Section 5, a fit using CMKAT on unblinded KNM2 tritium data found the best-fit extracted neutrino mass squared `mnu2` $=0.28^{+0.31}_{-0.30}\text{eV}^2$ (Equation 5.3). The central value agrees with the value quoted ($m^2_\nu = 0.26\text{eV}^2$) in a recent paper[44]. The uncertainty on `mnu2` ($0.31\,\text{eV}^2$ (upper) and $0.30\,\text{eV}^2$ (lower)) is statistical only, and agrees with the statistical uncertainties found by others (range from $0.28\,\text{eV}^2$-$0.31\,\text{eV}^2$)[44].The fit to the KNM2 data also extracted a radially-dependent energy shift, presumed to be partially due to plasma-related source potential variations (also observed in krypton line studies in Section 4.1).

The ingredients to construct a confidence interval (as defined in Section 6.3) are the best-fit neutrino mass squared $m^2_{fit}$ and the total uncertainty $\sigma$. The $m^2_{fit}$ is given in Equation 5.3. The statistical uncertainty and the systematic uncertainty add in quadrature to yield the total uncertainty:

$$\sigma = \sqrt{\sigma^2_{stat} + \sigma^2_{sys}} \tag{7.1}$$

The mean of the upper and lower statistical uncertainties in Equation 5.3 is taken, such that $\sigma_{stat}$=$0.31\,\text{eV}^2$. For the systematic uncertainty, we use the systematic uncertainty presented in [44]. This can be calculated using Table 2 of [44], and comes to $\sigma_{sys}$=$0.18\,\text{eV}^2$. Plugging the statistical and systematic uncertainties into Equation 7.1 and solving for the total uncertainty yields:

$$\sigma = 0.35\,\text{eV}^2 \tag{7.2}$$

The study in Section 6.2.3 demonstrated that the extracted `mnu2` fit parameter

distribution is well-represented by a normal distribution. Therefore, using Equation 7.2, we can now construct a confidence interval. For the 90% confidence level, the corresponding 90% confidence interval (Equation 6.12) is:

$$\begin{aligned} 90\%\ \text{C.I.} &= [\ m^2_{fit} - 1.64\sigma,\ m^2_{fit} + 1.64\sigma\ ] \\ &= [\ 0.28\,\text{eV}^2 - 1.64(0.35\,\text{eV}^2),\ 0.28\,\text{eV}^2 + 1.64(0.35\,\text{eV}^2)\ ] \\ &= [\ -0.30\,\text{eV}^2,\ 0.86\,\text{eV}^2\ ] \end{aligned} \tag{7.3}$$

The approach for confidence interval construction in Equation 7.3 relies on a standard $\Delta\chi^2$ error estimation procedure, where the confidence intervals are valid for both linear and near-linear model parameters. Section 6.2.3 made an initial demonstration of the validity of this approach using Monte Carlo, with two other approaches ($\chi^2$ mapping in Section 6.2.2, and error matrix in Section 6.2.1)) to confirm. This was done for the 1000 hour MC `mnu2` error estimation.

In order to more rigorously validate this confidence interval construction, some additional tests are proposed. These involve calculating the likelihood distributions over a relevant range of $m^2_{true}$, using the Monte Carlo approach.

Starting with the statistics-only case, we generate MC spectra which have the same measurement time as the KNM2 neutrino mass campaign (27 days). The rates are statistically fluctuated, fit, and repeated for 6000 MC samples. A histogram of the shift in extracted `mnu2` from the MC truth ($m^2_{fit} - m^2_{MCtruth}$) is constructed. This process is repeated for two different $m^2_{MCtruth}$ values ($0.5\,\text{eV}^2$ and $0\,\text{eV}^2$ were chosen); the results of the histogramming are shown below in Figure 7.1.

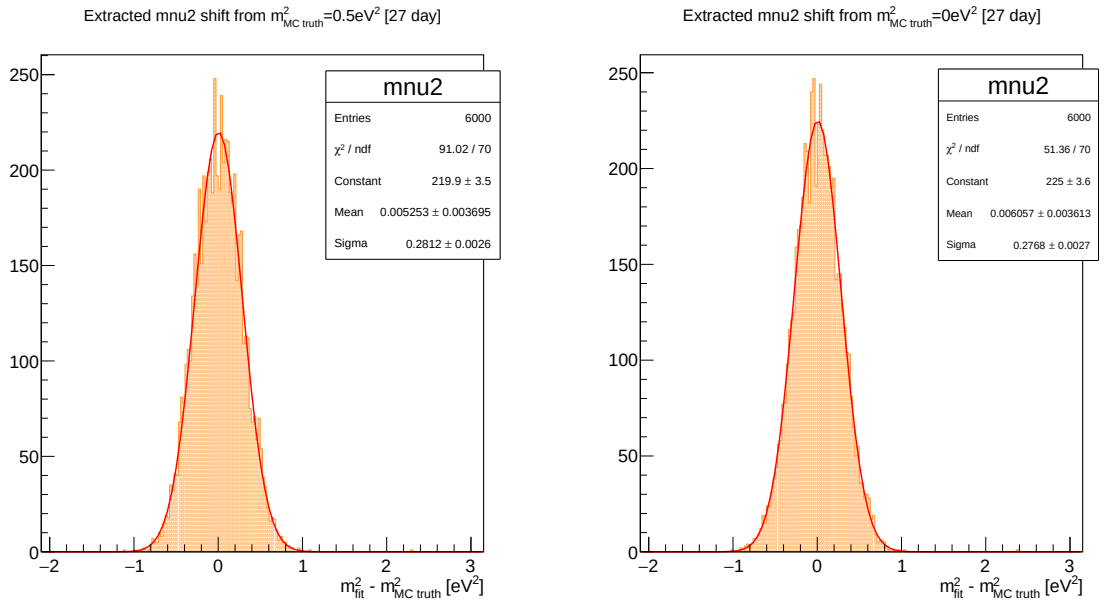


Figure 7.1: Histograms of the shift for $m^2_{MCtruth} = 0.5\,\mathrm{eV}^2$ (left) and $m^2_{MCtruth} = 0\,\mathrm{eV}^2$(right), for 6000 MC samples.

The histogram quantities $m^2_{fit} - m^2_{MCtruth}$ in Figure 7.1 are both "statistics"[112]. "Statistics" are quantities which can be calculated using the data, and are independent of unknown parameters. In this case, $m^2_{fit} - m^2_{MCtruth}$ is a "statistic" because $m^2_{MCtruth}$ is known.

These histograms are the likelihood distributions, and can be approximated by Gaussian distributions. Their respective "Sigma" Gaussian fit parameters are within 2% of each other. Because they are close enough and the likelihood distributions do not appear to be functions of $m^2_{MCtruth}$, we can construct a single (Gaussian) likelihood distribution, whose "Sigma" is the average Gaussian width:

$$\sigma = 0.28\,\mathrm{eV}^2 \tag{7.4}$$

The probability that the confidence interval $[\ m^2_{fit} - B,\ m^2_{fit} + A\ ]$ will cover its $m^2_{MCtruth}$ value is given by:

$$\mathrm{Prob}(-B < m^2_{fit} - m^2_{MCtruth} < A) = \int_{-B}^{A} d\zeta \frac{1}{\sqrt{2\pi}\sigma} e^{-\frac{-\zeta^2}{2\sigma^2}} \tag{7.5}$$

Where $\zeta = m^2_{fit} - m^2_{MCtruth}$. Choosing $A = +1.64\sigma$ and $-B = -1.64\sigma$ for Equation 7.5, the probability Prob($-1.64\sigma < m^2_{fit} - m^2_{MCtruth} < +1.64\sigma$) corresponds to the 90% C.L..

Now we introduce the pivot quantity $m^2_{fit} - m^2_{true}$, where $m^2_{true}$ is the true $m^2_\nu$ . This is not a "statistic" because it cannot be calculated from the data ($m^2_{true}$ is unknown). We do, however, know the pivot quantity's probability distribution: it is the same as the likelihood distribution of the "statistic", as described above. This is true for any value of $m^2_{MCtruth}$ in the region of interest, including $m^2_{MCtruth} = m^2_{true}$.

Using this likelihood distribution, we can calculate a statistics-only confidence interval for the KNM2-like MC simulated data. Since Equation 7.5 is true for all values of $m^2_{MCtruth}$, that includes the case where $m^2_{MCtruth} = m^2_{true}$. Thus, the probability that the confidence interval $[\ m^2_{fit} - B,\ m^2_{fit} + A\ ]$ will cover the $m^2_{true}$ value is given by:

$$\text{Prob}(-B < m^2_{fit} - m^2_{true} < A) = \int_{-B}^{A} d\zeta' \frac{1}{\sqrt{2\pi}\sigma} e^{-\frac{-\zeta'^2}{2\sigma^2}} \tag{7.6}$$

Where $\zeta' = m^2_{fit} - m^2_{true}$. Choosing $A = +1.64\sigma$ and $-B = -1.64\sigma$ for Equation 7.6, the probability Prob($-1.64\sigma < m^2_{fit} - m^2_{true} < +1.64\sigma$) corresponds to the 90% C.L.. The 90% confidence interval can be constructed using the $\sigma$ given in Equation 7.4:

$$\begin{aligned} 90\%\ \text{C.I. (stat)} &= [\ m^2_{fit} - 1.64\sigma,\ m^2_{fit} + 1.64\sigma\ ] \\ &= [\ m^2_{fit} - 0.45\,\text{eV}^2,\ m^2_{fit} + 0.45\,\text{eV}^2\ ] \end{aligned} \tag{7.7}$$

Now we can fold in the systematics. This has the effect of broadening the likelihood distribution. Using the average systematic value from earlier ($\sigma_{sys}$=0.18 eV$^2$) and adding it in quadrature with the histograms' average $\sigma$ (statistics only, from Equation 7.4), the total uncertainty $\sigma_{tot}$=0.33 eV$^2$. Using $\sigma_{tot}$, we can calculate a total confidence interval for the KNM2-like MC simulated data. For the 90% confidence level, the corresponding 90% confidence interval is given by:

$$\begin{aligned} 90\%\ \text{C.I. (tot)} &= [\ m^2_{fit} - 1.64\sigma_{tot},\ m^2_{fit} + 1.64\sigma_{tot}\ ] \\ &= [\ m^2_{fit} - 0.54\,\text{eV}^2,\ m^2_{fit} + 0.54\,\text{eV}^2\ ] \end{aligned} \tag{7.8}$$

Equation 7.8 represents the total 90% confidence interval for the KNM2-like MC-simulated data, for 27 days' worth of measurement time. It is worth noting that if the

likelihood distributions had a stronger $m_\nu^2$ dependence, the confidence intervals would need to be constructed via the general Neyman construction[113]. The likelihood distributions don't appear to have an $m_\nu^2$ dependence, so this is unnecessary.

Assuming the experimental conditions don't change and the systematic uncertainty is the same as in KNM2, we can estimate the 3-year sensitivity of the KATRIN experiment. Using the relation between statistical uncertainty and total measurement time (Section 6.1.1), the projected statistical uncertainty is $0.04\,\mathrm{eV}^2$. The total uncertainty is then $0.19\,\mathrm{eV}^2$, and, per Equation 6.16, the worst-case sensitivity on the neutrino mass at 90% C.L. is:

$$S_{m_\nu}^{worst}(90\%\mathrm{C.L.}) = 0.55\,\mathrm{eV} \tag{7.9}$$

This sensitivity is worse than the KATRIN experiment design sensitivity (0.2 eV) because it assumes the current KNM2 systematic budget, but there is active work being done on improvement to both the experimental conditions and control of systematics. The final sensitivity is expected to be much better than this.

The rest of this work consists of estimations of the sensitivity of the KATRIN experiment to various effects, for the full 3 years' worth of data. The data used in these estimations is Monte Carlo-generated. Following tests of different error estimation methods (Section 6.2) and calculation of the total uncertainty budget (Section 6.1), a few studies are presented. In order of appearance, these include a study of the effect of different constant background levels (Section 6.4), impact of tritium decay at the RW and DPS (Section 6.5), tests of the sensitivity to column density adjustments (Section 6.6), and nonlinearities in the detected rate (Section 6.7). Using the 3-year total uncertainty budget, we can establish which effects are negligible, and project their contributions to the uncertainty budget. These projections are useful tools which future KATRIN collaborators can use for uncertainty estimation when conditions change, and can be used to inform decision-making.

One example of the importance of these projections in decision-making involves the study of the impact of tritium decays from the RW and DPS. The result of the study was that the biggest contributor to systematic shift in `mnu2` came from tritium decaying at the RW. By parameterizing the relationship between RW activity and the shift in `mnu2` , we were able to project which levels of RW activity would create non-negligible contributions to the uncertainty budget (as defined by a negligibility threshold). This led to a decision to try measuring the tritium decay spectrum of electrons originating at the RW. That measurement effort is currently under way.

In conclusion, the CMKAT framework was developed and demonstrated the abil-

ity to successfully model and fit the many kinds of data gathered by the KATRIN experiment. It offers the ability to conduct independent analyses, and, with a more complete systematics treatment in the future, CMKAT can be used for the primary KATRIN mission: to extract the effective neutrino mass squared $m_\nu^2$ from tritium beta decay measurements.

# Bibliography


[1] E. Rutherford. "Uranium radiation and the electrical conduction produced by it". In: *The London, Edinburgh, and Dublin Philosophical Magazine and Journal of Science* 47 (1899), pp. 109–163. DOI: 10.1080/14786449908621245. URL: https://doi.org/10.1080/14786449908621245.

[2] L. Gerward and A. Rassat. "Paul Villard's discovery of gamma rays - A centenary". In: *Comptes Rendus de l'Academie des Sciences: Physique et Astrophysique* (2000), pp. 965–973. URL: http://inis.iaea.org/search/search.aspx?orig_q=RN:32010858.

[3] Lise Meitner. "Über die Entstehung der Beta-Strahl-Spektren radioaktiver Substanzen". In: *Zeitschrift für Physik* 9 (1922), pp. 131–144. URL: https://doi.org/10.1007/BF01326962.

[4] F. Reines and C. L. Cowan. "Detection of the free neutrino". In: *Phys. Rev.* 92 (1953), pp. 830–831. DOI: 10.1103/PhysRev.92.830.

[5] G. Danby et al. "Observation of High-Energy Neutrino Reactions and the Existence of Two Kinds of Neutrinos". In: *Phys. Rev. Lett.* 9 (1962), pp. 36–44. DOI: 10.1103/PhysRevLett.9.36.

[6] K. Kodama et al. "Observation of tau neutrino interactions". In: *Physics Letters B* 504 (Apr. 2001), pp. 218–224. ISSN: 0370-2693. DOI: 10.1016/s0370-2693(01)00307-0. URL: http://dx.doi.org/10.1016/S0370-2693(01)00307-0.

[7] Bruce T. Cleveland et al. "Measurement of the Solar Electron Neutrino Flux with the Homestake Chlorine Detector". In: *The Astrophysical Journal* 496 (Mar. 1998), pp. 505–526. DOI: 10.1086/305343. URL: https://doi.org/10.1086/305343.

[8] John N. Bahcall. "Solar neutrinos: Theory versus observation". In: *Space Science Reviews* 24 (1979), pp. 227–251. DOI: 10.1007/BF00167710. URL: https://doi.org/10.1007/BF00167710.

[9] L. Wolfenstein. "Neutrino oscillations in matter". In: *Phys. Rev. D* 17 (9 May 1978), pp. 2369–2374. DOI: 10.1103/PhysRevD.17.2369. URL: https://link.aps.org/doi/10.1103/PhysRevD.17.2369.

[10] S. P. Mikheev and A. Y. Smirnov. "Resonance enhancement of oscillations in matter and solar neutrino spectroscopy". In: *Soviet Journal of Nuclear Physics* 42 (1985), pp. 913–917. URL: http://inis.iaea.org/search/search.aspx?orig_q=RN:17075812.

[11] Q. R. Ahmad et al. "Direct Evidence for Neutrino Flavor Transformation from Neutral-Current Interactions in the Sudbury Neutrino Observatory". In: *Physical Review Letters* 89 (June 2002), p. 011301. ISSN: 1079-7114. DOI: 10.1103/physrevlett.89.011301. URL: http://dx.doi.org/10.1103/PhysRevLett.89.011301.

[12] Y. Fukuda et al. "Evidence for Oscillation of Atmospheric Neutrinos". In: *Physical Review Letters* 81 (Aug. 1998), pp. 1562–1567. ISSN: 1079-7114. DOI: 10.1103/physrevlett.81.1562. URL: http://dx.doi.org/10.1103/PhysRevLett.81.1562.

[13] S. M. Bilenky. "Neutrino in standard model and beyond". In: *Physics of Particles and Nuclei* 46 (2015), pp. 475–496. DOI: 10.1134/S1063779615040024. URL: https://doi.org/10.1134/S1063779615040024.

[14] F. R. Klinkhamer. "Neutrino mass and the Standard Model". In: *Modern Physics Letters A* 28 (Feb. 2013), p. 1350010. ISSN: 1793-6632. DOI: 10.1142/s0217732313500107. URL: http://dx.doi.org/10.1142/S0217732313500107.

[15] C. Giganti, S. Lavignac, and M. Zito. "Neutrino oscillations: The rise of the PMNS paradigm". In: *Progress in Particle and Nuclear Physics* 98 (Jan. 2018), pp. 1–54. ISSN: 0146-6410. DOI: 10.1016/j.ppnp.2017.10.001. URL: http://dx.doi.org/10.1016/j.ppnp.2017.10.001.

[16] R.B. Patterson. "Prospects for Measurement of the Neutrino Mass Hierarchy". In: *Annual Review of Nuclear and Particle Science* 65 (2015), pp. 177–192. DOI: 10.1146/annurev-nucl-102014-021916. eprint: https://doi.org/10.1146/annurev-nucl-102014-021916. URL: https://doi.org/10.1146/annurev-nucl-102014-021916.

[17] Ivan Esteban et al. "The fate of hints: updated global analysis of three-flavor neutrino oscillations". In: *Journal of High Energy Physics* 2020 (Sept. 2020), p. 178. ISSN: 1029-8479. DOI: 10.1007/jhep09(2020)178. URL: http://dx.doi.org/10.1007/JHEP09(2020)178.

[18] Particle Data Group, PA Zyla, et al. "Review of particle physics". In: *Progress of Theoretical and Experimental Physics* 2020 (2020), p. 083C01.

[19] Martin W. Gruenewald et al. "Precision electroweak measurements on the Z resonance". In: *Physics Reports* 427 (May 2006), pp. 257–454. ISSN: 0370-1573. DOI: https://doi.org/10.1016/j.physrep.2005.12.006. URL: https://www.sciencedirect.com/science/article/pii/S0370157305005119.

[20] G. Mention et al. "Reactor antineutrino anomaly". In: *Physical Review D* 83 (Apr. 2011), p. 073006. ISSN: 1550-2368. DOI: 10.1103/physrevd.83.073006. URL: http://dx.doi.org/10.1103/PhysRevD.83.073006.

[21] Shin'ichiro Ando and Alexander Kusenko. "Interactions of keV sterile neutrinos with matter". In: *Physical Review D* 81 (June 2010), p. 113006. ISSN: 1550-2368. DOI: 10.1103/physrevd.81.113006. URL: http://dx.doi.org/10.1103/PhysRevD.81.113006.

[22] M. Fukugita and T. Yanagida. "Baryogenesis Without Grand Unification". In: *Phys. Lett. B* 174 (1986), pp. 45–47. DOI: 10.1016/0370-2693(86)91126-3.

[23] Vedran Brdar et al. "Type-I Seesaw as the Common Origin of Neutrino Mass, Baryon Asymmetry, and the Electroweak Scale". In: *Phys. Rev. D* 100 (2019), p. 075029. DOI: 10.1103/PhysRevD.100.075029. arXiv: 1905.12634 [hep-ph].

[24] B. Aharmim et al. "Low-energy-threshold analysis of the Phase I and Phase II data sets of the Sudbury Neutrino Observatory". In: *Physical Review C* 81 (May 2010), p. 055504. ISSN: 1089-490X. DOI: 10.1103/physrevc.81.055504. URL: http://dx.doi.org/10.1103/PhysRevC.81.055504.

[25] K. Abe et al. "Atmospheric neutrino oscillation analysis with external constraints in Super-Kamiokande I-IV". In: *Physical Review D* 97 (Apr. 2018), p. 072001. ISSN: 2470-0029. DOI: 10.1103/physrevd.97.072001. URL: http://dx.doi.org/10.1103/PhysRevD.97.072001.

[26] S. Gariazzo et al. "Neutrino masses and their ordering: global data, priors and models". In: *Journal of Cosmology and Astroparticle Physics* 2018 (Mar. 2018), p. 011. ISSN: 1475-7516. DOI: 10.1088/1475-7516/2018/03/011. URL: http://dx.doi.org/10.1088/1475-7516/2018/03/011.

[27] J. H. Choi et al. "Observation of Energy and Baseline Dependent Reactor Antineutrino Disappearance in the RENO Experiment". In: *Phys. Rev. Lett.* 116 (21 May 2016), p. 211801. DOI: 10.1103/PhysRevLett.116.211801. URL: https://link.aps.org/doi/10.1103/PhysRevLett.116.211801.

[28] Y. Abe et al. "Improved measurements of the neutrino mixing angle $\theta_{13}$ with the Double Chooz detector". In: *Journal of High Energy Physics* 2014 (Oct. 2014), p. 86. ISSN: 1029-8479. DOI: 10.1007/jhep10(2014)086. URL: http://dx.doi.org/10.1007/JHEP10(2014)086.

[29] F. P. An et al. "Measurement of electron antineutrino oscillation based on 1230 days of operation of the Daya Bay experiment". In: *Physical Review D* 95 (Apr. 2017), p. 072006. ISSN: 2470-0029. DOI: 10.1103/physrevd.95.072006. URL: http://dx.doi.org/10.1103/PhysRevD.95.072006.

[30] Mark Scott et al. "Latest oscillation results from T2K". In: *Journal of Physics: Conference Series* 1342 (Jan. 2020), p. 012043. DOI: 10.1088/1742-6596/1342/1/012043. URL: https://doi.org/10.1088/1742-6596/1342/1/012043.

[31] M. G. Aartsen et al. "Determining neutrino oscillation parameters from atmospheric muon neutrino disappearance with three years of IceCube DeepCore data". In: *Physical Review D* 91 (Apr. 2015), p. 072004. ISSN: 1550-2368. DOI: 10.1103/physrevd.91.072004. URL: http://dx.doi.org/10.1103/PhysRevD.91.072004.

[32] P. Adamson et al. "Measurement of Neutrino and Antineutrino Oscillations Using Beam and Atmospheric Data in MINOS". In: *Physical Review Letters* 110 (June 2013), p. 251801. ISSN: 1079-7114. DOI: 10.1103/physrevlett.110.251801. URL: http://dx.doi.org/10.1103/PhysRevLett.110.251801.

[33] N. Aghanim et al. "Planck 2018 results". In: *Astronomy Astrophysics* 641 (Sept. 2020), A6. ISSN: 1432-0746. DOI: 10.1051/0004-6361/201833910. URL: http://dx.doi.org/10.1051/0004-6361/201833910.

[34] W. David Arnett and Jonathan L. Rosner. "Neutrino Mass Limits From Sn1987a". In: *Phys. Rev. Lett.* 58 (1987), p. 1906. DOI: 10.1103/PhysRevLett.58.1906.

[35] Georg G. Raffelt. "Particle physics from stars". In: *Annual Review of Nuclear and Particle Science* 49 (Dec. 1999), pp. 163–216. ISSN: 1545-4134. DOI: 10.1146/annurev.nucl.49.1.163. URL: http://dx.doi.org/10.1146/annurev.nucl.49.1.163.

[36] M. Agostini et al. "Final Results of GERDA on the Search for Neutrinoless Double-$\beta$ Decay". In: *Phys. Rev. Lett.* 125 (25 Dec. 2020), p. 252502. DOI: 10.1103/PhysRevLett.125.252502. URL: https://link.aps.org/doi/10.1103/PhysRevLett.125.252502.

[37] V. N. Aseev et al. "Upper limit on the electron antineutrino mass from the Troitsk experiment". In: *Physical Review D* 84 (Dec. 2011), p. 112003. ISSN: 1550-2368. DOI: 10.1103/physrevd.84.112003. URL: http://dx.doi.org/10.1103/PhysRevD.84.112003.

[38] Ch Kraus et al. "Final results from Phase II of the Mainz neutrino mass searching tritium $\beta$ decay". In: *The European Physical Journal C* 40 (Apr. 2005), pp. 447–468. ISSN: 1434-6052. DOI: 10.1140/epjc/s2005-02139-7. URL: http://dx.doi.org/10.1140/epjc/s2005-02139-7.

[39] M. Aker et al. "Improved Upper Limit on the Neutrino Mass from a Direct Kinematic Method by KATRIN". In: *Physical Review Letters* 123 (Nov. 2019), p. 221802. ISSN: 1079-7114. DOI: 10.1103/physrevlett.123.221802. URL: http://dx.doi.org/10.1103/PhysRevLett.123.221802.

[40] Ali Ashtari Esfahani et al. "Determining the neutrino mass with cyclotron radiation emission spectroscopy—Project 8". In: *J. Phys. G* 44 (2017), p. 054004. DOI: 10.1088/1361-6471/aa5b4f. arXiv: 1703.02037 [physics.ins-det].

[41] A. Nucciotti et al. “The Use of Low Temperature Detectors for Direct Measurements of the Mass of the Electron Neutrino”. In: *Advances in High Energy Physics* 2016 (2016), pp. 1–41. ISSN: 1687-7365. DOI: 10.1155/2016/9153024. URL: http://dx.doi.org/10.1155/2016/9153024.

[42] W. Urban et al. “Precise measurement of energies in $^{115}$Sn following the $(n, \gamma)$ reaction”. In: *Phys. Rev. C* 94 (1 July 2016), p. 011302. DOI: 10.1103/PhysRevC.94.011302. URL: https://link.aps.org/doi/10.1103/PhysRevC.94.011302.

[43] Marco Kleesiek. “A Data-Analysis and Sensitivity-Optimization Framework for the KATRIN Experiment”. PhD thesis. KIT, 2014.

[44] M. Aker et al. “First direct neutrino-mass measurement with sub-eV sensitivity”. In: (2021). arXiv: 2105.08533.

[45] L. Gastaldo et al. “The Electron Capture $^{163}$Ho Experiment ECHo: an overview”. In: *Journal of Low Temperature Physics* 176 (2014), pp. 876–884. DOI: 10.1007/s10909-014-1187-4. arXiv: 1309.5214 [physics.ins-det].

[46] Giovanni Gallucci et al. “$^{163}$ Ho Distillation and Implantation for HOLMES Experiment”. In: *J. Low Temp. Phys.* 194 (2019), pp. 453–459. DOI: 10.1007/s10909-018-2086-x.

[47] S. Eliseev et al. “Direct Measurement of the Mass Difference of Ho163 and Dy163 Solves the Q-Value Puzzle for the Neutrino Mass Determination”. In: *Physical Review Letters* 115 (Aug. 2015), p. 062501. ISSN: 1079-7114. DOI: 10.1103/physrevlett.115.062501. URL: http://dx.doi.org/10.1103/PhysRevLett.115.062501.

[48] J. Clarke. *The SQUID handbook, Volume 1: Fundamentals and Technology of SQUIDs and SQUID systems*. Wiley VCH, 2004. URL: http://inis.iaea.org/search/search.aspx?orig_q=RN:38047859.

[49] M. Aker et al. “The Design, Construction, and Commissioning of the KATRIN Experiment”. In: (2021). arXiv: 2103.04755 [physics.ins-det].

[50] Ana Paula Vizcaya. “PhD thesis in preparation”. PhD thesis. Carnegie Mellon University, 2021.

[51] COMSOL Multiphysics. “Introduction to COMSOL multiphysics®”. In: *COMSOL Multiphysics* 9 (1998), p. 2018. URL: http://www.comsol.com/products/multiphysics/.

[52] Roberto Kersevan and J.-L Pons. “Introduction to MOLFLOW+: New graphical processing unit-based Monte Carlo code for simulating molecular flows and for calculating angular coefficients in the compute unified device architecture environment”. In: *Journal of Vacuum Science  Technology A: Vacuum, Surfaces, and Films* 27 (Aug. 2009), pp. 1017–1023.

[53] J. Angrik et al. "KATRIN design report 2004". In: (Feb. 2005).

[54] O Rest et al. "A novel ppm-precise absolute calibration method for precision high-voltage dividers". In: *Metrologia* 56 (July 2019), p. 045007. DOI: 10.1088/1681-7575/ab2997. URL: https://doi.org/10.1088/1681-7575/ab2997.

[55] M. Arenz et al. "Reduction of stored-particle background by a magnetic pulse method at the KATRIN experiment". In: *The European Physical Journal C* 78 (Sept. 2018), p. 778. ISSN: 1434-6052. DOI: 10.1140/epjc/s10052-018-6244-8. URL: http://dx.doi.org/10.1140/epjc/s10052-018-6244-8.

[56] J.F. Amsbaugh et al. "Focal-plane detector system for the KATRIN experiment". In: *Nuclear Instruments and Methods in Physics Research Section A: Accelerators, Spectrometers, Detectors and Associated Equipment* 778 (Apr. 2015), pp. 40–60. ISSN: 0168-9002. DOI: 10.1016/j.nima.2014.12.116. URL: http://dx.doi.org/10.1016/j.nima.2014.12.116.

[57] FPD working group. *The new FPD wafer of 2020*. Document available at https://de.overleaf.com/project/5eae89482a176000016ada2a (Accessed 2021/04/30).

[58] K Altenmüller et al. "High-resolution spectroscopy of gaseous 83m Kr conversion electrons with the KATRIN experiment". In: *Journal of Physics G: Nuclear and Particle Physics* 47 (May 2020), p. 065002. ISSN: 1361-6471. DOI: 10.1088/1361-6471/ab8480. URL: http://dx.doi.org/10.1088/1361-6471/ab8480.

[59] M. Arenz et al. "First transmission of electrons and ions through the KATRIN beamline". In: *Journal of Instrumentation* 13 (Apr. 2018), p. 4020. ISSN: 1748-0221. DOI: 10.1088/1748-0221/13/04/p04020. URL: http://dx.doi.org/10.1088/1748-0221/13/04/P04020.

[60] Max Aker et al. "First operation of the KATRIN experiment with tritium". In: *The European Physical Journal C* 80 (Mar. 2020), p. 264. ISSN: 1434-6052. URL: http://dx.doi.org/10.1140/epjc/s10052-020-7718-z.

[61] M. Aker et al. "Analysis methods for the first KATRIN neutrino-mass measurement". In: (2021). arXiv: 2101.05253 [hep-ex].

[62] Fons Rademakers et al. *ROOT - An Object-Oriented Data Analysis Framework. root-project/root: v6.10/04*. Version v6-10-04. Aug. 2017. DOI: 10.5281/zenodo.848819. URL: https://doi.org/10.5281/zenodo.848819.

[63] Kleesiek, M. et al. "$\beta$-Decay spectrum, response function and statistical model for neutrino mass measurements with the KATRIN experiment". In: *Eur. Phys. J. C* 79 (2019), p. 204. DOI: 10.1140/epjc/s10052-019-6686-7. URL: https://doi.org/10.1140/epjc/s10052-019-6686-7.

[64] D. Vénos et al. "Properties of 83mKr conversion electrons and their use in the KATRIN experiment". In: *Journal of Instrumentation* 13 (Feb. 2018), pp. 2012–2012. URL: https://doi.org/10.1088/1748-0221/13/02/t02012.

[65] Martin Slezak. "Monitoring of the energy scale in the KATRIN neutrino experiment". PhD thesis. Charles University, Prague, Dec. 2015. URL: https://cds.cern.ch/record/2243754.

[66] Moritz Machatschek. "Simulation of the 83mKr Mode of the Tritium Source of the KATRIN Experiment". MA thesis. KIT, May 2016. URL: https://www.katrin.kit.edu/publikationen/mth-machatschek.pdf.

[67] M Zbořil et al. "Ultra-stable implanted 83Rb/83mKr electron sources for the energy scale monitoring in the KATRIN experiment". In: *Journal of Instrumentation* 8 (2013), pp. 3009–3009. URL: https://doi.org/10.1088/1748-0221/8/03/p03009.

[68] NIST. *CODATA Value: Boltzmann constant*. Available at website https://physics.nist.gov/cgi-bin/cuu/Value?k (accessed 2021/04/05).

[69] NIST. *CODATA Value: electron mass*. Available at website https://physics.nist.gov/cgi-bin/cuu/Value?me (accessed 2021/04/05).

[70] NIST. *Atomic Weights and Isotopic Compositions for All Elements*. Available at website https://physics.nist.gov/cgi-bin/Compositions/stand_alone.pl (accessed 2021/04/05).

[71] W. W. Repko and Chong-En Wu. "Radiative corrections to the endpoint of the tritium beta decay spectrum". In: *Phys. Rev. C* 28 (1983), pp. 2433–2436. DOI: 10.1103/PhysRevC.28.2433.

[72] E. W. Otten and C. Weinheimer. "Neutrino mass limit from tritium beta decay". In: *Reports on Progress in Physics* 71 (July 2008), p. 086201. URL: https://doi.org/10.1088/0034-4885/71/8/086201.

[73] Natasha Doss et al. "Molecular effects in investigations of tritium molecule beta decay endpoint experiments". In: *Phys. Rev. C* 73 (2006), p. 025502. DOI: 10.1103/PhysRevC.73.025502.

[74] V. Sibille. *LARA parameters for KATRIN*. Document available at https://ikp-katrin-wiki.ikp.kit.edu/katrin/images/4/49/LARA_parameters.pdf (Accessed 2021/04/05).

[75] G. Zeller. *Remarks on updates in RunSummary 2f*. Document available at https://ikp-katrin-wiki.ikp.kit.edu/katrin/images/0/09/RemarksOnRunSummary2f-LARA.pdf (Accessed 2021/04/05).

[76] Wayne W. Repko and Chong-en Wu. "Radiative corrections to the end point of the tritium $\beta$ decay spectrum". In: *Phys. Rev. C* 28 (6 Dec. 1983), pp. 2433–2436. DOI: 10.1103/PhysRevC.28.2433. URL: https://link.aps.org/doi/10.1103/PhysRevC.28.2433.

[77] Meng Wang et al. "The AME 2020 atomic mass evaluation (II). Tables, graphs and references*". In: *Chinese Physics C* 45 (Mar. 2021), p. 030003. DOI: 10.1088/1674-1137/abddaf. URL: https://doi.org/10.1088/1674-1137/abddaf.

[78] John David Jackson. *Classical electrodynamics*. 2nd edition. Wiley, 1975. URL: http://cdsweb.cern.ch/record/490457.

[79] Stefan Groh. "Modeling of the response function and measurement of transmission properties of the KATRIN experiment". PhD thesis. KIT, 2015. URL: https://publikationen.bibliothek.kit.edu/1000046546.

[80] Rudolf Sack. "Measurement of the energy loss of 18.6 keV electrons on deuterium gas and determination of the tritium Q-value at the KATRIN experiment". PhD thesis. Westfälischen Wilhelms-Universität Münster, 2020. URL: http://nbn-resolving.de/urn:nbn:de:hbz:6-59069498754.

[81] M. Aker et al. "Precision measurement of the electron energy-loss function in tritium and deuterium gas for the KATRIN experiment". In: (2021). arXiv: 2105.06930 [physics.ins-det].

[82] Yong-Ki Kim and M. Eugene Rudd. "Binary-encounter-dipole model for electron-impact ionization". In: *Phys. Rev. A* 50 (5 Nov. 1994), pp. 3954–3967. URL: https://link.aps.org/doi/10.1103/PhysRevA.50.3954.

[83] Larisa Thorne. *FirstTritium KATRIN response function*. Analysis note available at https://nuserv.uni-muenster.de:8443/katrin-pub/analysisreview/-/tree/master/OfficialPlots/KatrinModel/CMKat/ResponseFunction-2019 (Accessed 2021/05/09).

[84] G. B. Franklin. *Synchrotron Energy Loss Formula*. Documentation available in CMKAT directory /doc/gbfSynchrotronRadiation.pdf (2020/03/13).

[85] Valerian Sibille. *KNM2 Blinded FSDs*. Presentation available at https://ikp-katrin-wiki.ikp.kit.edu/katrin/images/7/7d/KNM2_blind_FSDs_-_October_2019.pdf (2019/10/08).

[86] F. Block and C. Koehler. *KATRIN KNM3 Reference Report Systematic Uncertainty of Column Density and Column Density Times Inelastic Scattering Cross-Section*. Presentation available at https://www.overleaf.com/project/5f68aa9245e32c0001efb51d (Accessed 2021/03/09).

[87] Moritz Machatschek. "A Phenomenological Theory of KATRIN Source Potential Systematics and its Application in Krypton-83m Calibration Measurements". PhD thesis. KIT, 2020.

[88] Nikolaus Trost. "Modeling and measurement of Rydberg-State mediated Background at the KATRIN Main Spectrometer". PhD thesis. KIT, 2018. URL: https://publikationen.bibliothek.kit.edu/1000090450.

[89] J. Behrens et al. *KNM2 Systematic Uncertainties: Uncertainties of magnetic field in analyzing plane, pinch magnet and WGTS*. Analysis note available at https://ikp-katrin-wiki.ikp.kit.edu/katrin/images/3/3d/KNM2_magFields_sysUncFinal.pdf (2021/05/25).

[90] Jan Behrens. "Design and commissioning of a mono- energetic photoelectron source and active background reduction by magnetic pulse at the KATRIN experiment". PhD thesis. Westfälischen Wilhelms-Universität Münster, 2016. URL: https://www.katrin.kit.edu/publikationen/phd_behrens.pdf.

[91] Seba Smith. "The Money Diggers". In: *Burton's Gentleman's Magazine and Monthly American Review*. Ed. by Edgar A. Poe and William E. Burton. Burton, 1840, pp. 81–91.

[92] L. Thorne. *CMKAT: model, validation and outlook*. Presentation available at https://fuzzy.fzk.de/bscw/bscw.cgi/1318701?op=preview&back_url=15294 (Accessed 2021/03/15).

[93] Various. *Wiki: KNM2 MC fitter comparison*. Available at https://ikp-katrin-wiki.ikp.kit.edu/katrin/index.php/KNM2_MC_fitter_comparison (accessed 2021/03/15).

[94] Energy loss function working group. *KNM1-T2 energy loss function parameterization)*. Data files available at https://nuserv.uni-muenster.de:8443/katrin-git/KATRIN-eloss/-/tree/master/parameters/KNM1/t2-tofonly_withpu_chisq1-v1) (accessed 2021/05/21).

[95] Alexey Lokhov and Christian Weinheimer. *Transmission function for pixels patches in SAP configuration*. Presentation available at https://ikp-katrin-wiki.ikp.kit.edu/katrin/images/1/15/2020-06-30_sap_transmission.pdf (2020/06/30).

[96] Raphael Ostertag. *KNM2 Krypton Analysis with Background Slope*. Presentation available at https://ikp-katrin-wiki.ikp.kit.edu/katrin/images/5/50/KNM2_BackgroundSlope.pdf (2020/07/21).

[97] Martin Slezak. *KNM3 pixel selection proposal*. Presentation available at https://ikp-katrin-wiki.ikp.kit.edu/katrin/images/9/9b/KNM3_pixel_selection.pdf (2020/05/26).

[98] Raphael Ostertag. "Investigation of Plasma Effects in the KATRIN Source with 83mKr". MA thesis. KIT, June 2020. URL: https://www.katrin.kit.edu/downloads/mth_ostertag.pdf.

[99] R. Ostertag. *KNM2 Krypton Analysis with Background Slope*. Presentation available at https://ikp-katrin-wiki.ikp.kit.edu/katrin/images/5/50/KNM2_BackgroundSlope.pdf (2020/07/21).

[100] Alexander Fulst. *Reanalysis of the 2017 CKrS data*. Presentation available at https://ikp-katrin-wiki.ikp.kit.edu/katrin/images/9/97/Ckrs_l3-32.pdf (2019/05/11).

[101] Florian Fränkle. *Pixel Selection for KNM2*. Presentation available at https://ikp-katrin-wiki.ikp.kit.edu/katrin/images/3/3b/AnaCallPixelCut190924.pdf (2019/09/24).

[102] PRO-KATRIN working group. *Radial plasma potential from coupling strength (PRO-KATRIN)*. Presentation available at https://ikp-katrin-wiki.ikp.kit.edu/katrin/index.php/Radial_plasma_potential_from_coupling_strength_(PRO-KATRIN) (accessed 2021/04/26).

[103] R. Ostertag. *KNM2 Krypton Line Broadening with Background Slope Consideration and CKrS Reference Lorentzian Width*. Presentation available at https://ikp-katrin-wiki.ikp.kit.edu/katrin/images/0/08/KNM2_LineBroadening_CKrSReference.pdf (2020/08/06).

[104] V. Gupta. *Kr analysis update: Plasma call*. Presentation available at https://ikp-katrin-wiki.ikp.kit.edu/katrin/images/e/e1/Kr_analysis-7-July.pdf (2020/07/07).

[105] V. Sibille. *KATRIN FSDs)*. Data files available at https://nuserv.uni-muenster.de:8443/vsibille/KATRIN_FSD (accessed 2021/05/25).

[106] *KNM2 Unblinding presentations*. Presentation available at https://ikp-katrin-wiki.ikp.kit.edu/katrin/index.php/Nu_Mass_2#Unblinding_presentations_.28w.2Fo_Penning_.2F_BG-time-slope_systematics.29_.2803.11.2020.29 (2020/11/03).

[107] Philip Bevington. *Data Reduction and Error Analysis for the Physical Sciences*. McGraw-Hill, 1969.

[108] Alexey Lokhov for the SAP team. *Shifted analyzing plane*. Presentation available at https://ikp-katrin-wiki.ikp.kit.edu/katrin/images/2/20/SAP_update_2019_05_28.pdf (2019/05/28).

[109] L. Thorne, C. Karl, and L. Koellenberger. *Impact of RW and DPS spectrum on the neutrino mass*. Presentation available at https://ikp-katrin-wiki.ikp.kit.edu/katrin/images/6/68/07-04-2020_impactOfRWandDPSonNeutrinomass.pdf (2020/04/07).

[110] V. Hannen et al. "Deconvolution of the energy loss function of the KATRIN experiment". In: *Astroparticle Physics* 89 (Mar. 2017), pp. 30–38. ISSN: 0927-6505. DOI: 10.1016/j.astropartphys.2017.01.010. URL: http://dx.doi.org/10.1016/j.astropartphys.2017.01.010.

[111] S. Enomoto. *Detector Count Corrections for First Tritium*. Document available at https://ikp-katrin-wiki.ikp.kit.edu/katrin/images/d/d2/FirstTritiumDetectorSystematics_20190203.pdf (2019/02/03).

[112] G. B. Franklin. *Least Square Confidence Regions and Confidence Levels*. Private communication (document: LSF_Confidence_Levels.pdf). Dec. 2020.

[113] Gary J. Feldman and Robert D. Cousins. "Unified approach to the classical statistical analysis of small signals". In: *Physical Review D* 57 (Apr. 1998), pp. 3873–3889. ISSN: 1089-4918. DOI: 10.1103/physrevd.57.3873. URL: http://dx.doi.org/10.1103/PhysRevD.57.3873.

# Acronyms

**BAO** Baryon Acoustic Oscillations.

**BIXS** Beta-Induced X-Ray Spectroscopy.

**CKrS** Condensed $^{83m}$Kr Source.

**CMB** Cosmic Microwave Background.

**CPS** Cryogenic Pumping Section.

**DAQ** data acquisition.

**DET** detector magnet.

**DPS** Differential Pumping Section.

**DVM** precision digital voltmeter.

**e-gun** electron gun.

**EMCS** Earth Magnetic field Compensation System.

**FBM** Forward Beam Monitor.

**FFT** Fast Fourier Transform.

**FPD** Focal Plane Detector.

**FSD** Final State Distribution.

**GKrS** Gaseous $^{83m}$Kr Source.

**HOPG** Highly-Oriented Pyrolytic Graphite.

**HVac** high vacuum.

**IE** inner wire electrode system.

**KATRIN** KArlsruhe TRitium Neutrino.

**KIT** Karlsruhe Institute of Technology.

**LARA** Laser Raman Spectroscopy.

**LFCS** Low-Field Correction System.

**MAC-E** Magnetic Adiabatic Collimation with Electrostatic.

**MS** Main Spectrometer.

**MTD** Measurement Time Distribution.

**NEG** non-evaporable getter.

**ORB** optical receiver board.

**OSB** optical sender board.

**PAC** power and control.

**PAE** Post Acceleration Electrode.

**PCH** pinch magnet.

**PP2F** Pump Port 2F.

**PP5** Pump Port 5.

**PS** Pre-Spectrometer.

**PS2** Pre-Spectrometer magnet 2.

**PULCINELLA** Precision Ultra-Low Current Integrating Normalization Electrometer for Low-Level Analysis.

**RS** Rear System.

**RW** Rear Wall.

**SAP** Shifted Analyzing Plane.

**SDD** Silicon Drift Detector.

**SiPM** Silicon Photomultiplier.

**SM** Standard Model of particle physics.

**TLK** Tritium Laboratory Karlsruhe.

**TMP** turbo-molecular pump.

**UHV** ultra-high vacuum.

**UV** ultra violet.

**WGTS** Windowless Gaseous Tritium Source.

**WLS** Wave-Length Shifting.

# Appendix A

# Appendix

## A.1 Run lists

### A.1.1 `BSlope` calculation runs

KNM3 Kr+Tr extended background runs, used for analysis in Section 4.1.2:

{62482, 62483, 62484, 62485}

### A.1.2 `WLine` calculation runs

KNM3 krypton-only runs, used for analysis in Section 4.1.3:

{61152, 61153, 61155, 61156, 61158, 61336, 61337, 61441, 61442, 61443, 61444,61445, 61446, 61469, 61470, 61475, 61476, 61477, 61478, 61479, 61868, 61869, 61871,61872, 61874, 61875, 61877, 61878, 61880, 61881, 61883, 61884, 61886, 61887, 61889,61890, 61892, 61893, 61895, 61896, 61898, 61899, 61901, 61902, 61904, 61905, 61907,61908, 61910, 61911, 61913, 61914, 61916, 61917, 61919, 61920, 61922, 61923, 61925,61926, 61928, 61929, 61931, 61932, 61934, 61935, 61937, 61938, 61940, 61941, 61943,61944, 61946, 61947, 61949, 61950, 61952, 61953, 61955, 61956, 61958, 61959, 61961,61962, 61964, 61965, 61967, 61968, 61970, 61971}

### A.1.3 Fit of $\sigma_P$ calculation runs

KNM2 Kr+Tr runs, used for analysis in Section 4.1.4:

{58443, 58442, 58440, 58439, 58437, 58436, 58434, 58433, 58431, 58430, 58428,58427, 58425, 58424, 58422, 58421, 58419, 58418, 58416, 58415, 58413, 58412, 58410,58409, 58407, 58406, 58404, 58403, 58401, 58400, 58398, 58397, 58395, 58394, 58392,58391, 58389, 58388, 58386, 58385, 58383, 58382, 58380, 58379, 58377, 58376, 58374,58373, 58371, 58370, 58368, 58367, 58365, 58364, 58362, 58361, 58359, 58358, 58356,58355, 58353, 58352, 58350, 58349, 58347, 58346, 58344, 58343, 58341, 58340, 58338,58337, 58305, 58304, 58302, 58301, 58299, 58298, 58296, 58295, 58293, 58292, 58290,58289, 58287, 58286, 58284, 58283, 58281, 58280, 58278, 58277, 58275, 58274, 58271,58270, 58268, 58267, 58265, 58264, 58262, 58261, 58253, 58252, 58250, 58249, 58247,58246, 58244, 58243, 58241, 58240, 58238, 58237, 58235, 58234, 58232, 58231, 58229,58228, 58226, 58225, 58223, 58222, 58220, 58219, 58217, 58216, 58214, 58213, 58211,58210, 58208, 58207, 58202, 58201, 58199, 58198, 58196, 58195, 58193, 58192, 58190,58189, 58187, 58186, 58184, 58183, 58181, 58180, 58178, 58177, 58175, 58174, 58172,58171, 58169, 58168, 58166, 58165, 58163, 58162, 58160, 58159, 58157, 58156, 58154,58153, 58151, 58150, 58148, 58147, 58145, 58144, 58142, 58141, 58139, 58138, 58136,58135, 58133, 58132, 58130, 58129, 58127, 58126, 58124, 58123, 58121, 58120, 58118,58117, 58115, 58114, 58112, 58111, 58109, 58108, 58106, 58105, 58103, 58102}

### A.1.4 RW voltage-independence in krypton-only runs

KNM3 krypton-only, used for analysis in Section 4.2.2:

{61304, 61305, 61308, 61309, 61312, 61313, 61316, 61317, 61320, 61321, 61324,61325, 61328, 61329, 61332, 61333, 61340, 61341, 61344, 61345, 61348, 61349, 61352,61353, 61356, 61357, 61360, 61361, 61364, 61365, 61368, 61369, 61449, 61450, 61453,61454, 61457, 61458, 61461, 61462, 61465, 61466, 61474}

### A.1.5 Kr+Tr over many RW voltages runs

KNM3 Kr+Tr, used for analysis in Section 4.2.3:

{62570, 62571, 62573, 62574, 62575, 62576, 62577, 62578, 62579, 62580, 62581,62582, 62583, 62584, 62586, 62587}

### A.1.6 KNM2 unblinded tritium fit runs

KNM2 tritium-only, used for analysis in Section 5.1:

{ 56278, 56279, 56280, 56281, 56282, 56284, 56285, 56286, 56287, 56288, 56289, 56290, 56291, 56292, 56293, 56294, 56301, 56302, 56303, 56304, 56305, 56306, 56307, 56308, 56309, 56310, 56311, 56312, 56313, 56314, 56315, 56316, 56317, 56319, 56320, 56321, 56322, 56323, 56324, 56325, 56326, 56327, 56328, 56329, 56330, 56333, 56334, 56335, 56336, 56337, 56338, 56341, 56342, 56343, 56344, 56345, 56346, 56347, 56348, 56349, 56350, 56351, 56352, 56353, 56354, 56355, 56356, 56357, 56358, 56359, 56360, 56361, 56362, 56363, 56364, 56365, 56366, 56367, 56368, 56369, 56370, 56379, 56380, 56381, 56382, 56383, 56384, 56385, 56386, 56387, 56388, 56389, 56390, 56391, 56392, 56393, 56394, 56395, 56396, 56397, 56398, 56399, 56400, 56401, 56402, 56403, 56404, 56405, 56406, 56407, 56409, 56412, 56413, 56414, 56415, 56416, 56417, 56418, 56472, 56473, 56474, 56475, 56476, 56477, 56478, 56479, 56560, 56561, 56562, 56563, 56564, 56565, 56566, 56575, 56576, 56577, 56578, 56579, 56580, 56581, 56582, 56583, 56584, 56585, 56586, 56587, 56588, 56589, 56590, 56591, 56592, 56593, 56594, 56595, 56598, 56599, 56600, 56601, 56602, 56603, 56604, 56605, 56606, 56607, 56608, 56609, 56610, 56611, 56612, 56613, 56621, 56622, 56623, 56624, 56625, 56626, 56627, 56628, 56629, 56636, 56639, 56640, 56641, 56642, 56643, 56644, 56645, 56646, 56647, 56648, 56654, 56655, 56656, 56657, 56658, 56659, 56660, 56661, 56662, 56663, 56664, 56669, 56670, 56671, 56672, 56673, 56674, 56684, 56685, 56688, 56689, 56690, 56691, 56692, 56693, 56706, 56707, 56708, 56709, 56710, 56711, 56712, 56713, 57015, 57016, 57017, 57018, 57019, 57020, 57022, 57023, 57024, 57025, 57026, 57035, 57036, 57038, 57039, 57040, 57041, 57042, 57043, 57044, 57045, 57046, 57047, 57048, 57049, 57050, 57051, 57052, 57053, 57054, 57055, 57056, 57057, 57058, 57059, 57060, 57061, 57062, 57068, 57069, 57070, 57071, 57072, 57073, 57074, 57075, 57076, 57077, 57078, 57079, 57080, 57081, 57082, 57083, 57084, 57085, 57086, 57087, 57088, 57089, 57090, 57091, 57092, 57093, 57094, 57095, 57096, 57103, 57104, 57105, 57106, 57107, 57108, 57109, 57110, 57111, 57120, 57121, 57122, 57123, 57124, 57125, 57126, 57127, 57128, 57129, 57130, 57131, 57132, 57133, 57134, 57135, 57136 }

## A.2 Sample code

### A.2.1 Sample fitting script

```
1 /*
2  * sampleTritiumFitScript.C
3  *
```

```
 * Date: 2021-05-17
 * Author: Larisa Thorne <lthorne@andrew.cmu.edu>
 *
 * Description: summed fit of real KNM2 tritium data. Blinded FSD.
 ↪  Fixed mnu2. One run.
 */


#ifndef FITTR_SUMMED_H_
#define FITTR_SUMMED_H_
#include "TF1.h"
#include "TCanvas.h"
#include "TMath.h"
#include "lib/cmKatrin.h"
#include "lib/KatrinParams.h"
#include "lib/tritiumSource.h"
#include "lib/cmM2Fit.h"
#include "lib/FitContainer.h"
#include "TStopwatch.h"
#include <vector>
#endif


void sampleTritiumFitScript(){

        // Groups of runs are terminated with a -1
        // First run in group used for Response Function parameters,
        ↪  etc.
        Int_t runList[] = { 56278, -1 }; // KNM2 tritium data runs

        TStopwatch timeKeeper;
        timeKeeper.Start();


        /*
         * Initializate class instances:
         */
        auto theKatrin = new cmKatrin();
        auto theControlParams = new KatrinParams();
        auto theRunParams = new KatrinParams();
        auto theData = new betaData();
        auto theFit = new cmM2Fit();
```

```
44          auto theSourceTr = theKatrin->getTritiumSource();
45
46
47          /*
48           * Set input files:
49           */
50          char runFile[100];
51          sprintf(runFile, "run_%07d.ktf", runList[0]);
52          theRunParams->openFile(runFile);
53          theControlParams->openFile("cmControlParams_summed.txt");
54          char fitSummaryFile[100];
55          sprintf(fitSummaryFile, "fitSummary_%07d.ktf", runList[0]);
56
57
58          /*
59           * Call updateParams():
60           */
61          theKatrin->updateParams(theControlParams, theRunParams);
62          theData->updateParams(theControlParams, theRunParams);
63          theFit->updateParams(theControlParams, theRunParams);
64          theData->print(1);
65          theFit->setData(theData);
66          theFit->setSimulator(theKatrin);
67
68
69          /*
70           * Build response function:
71           */
72          theKatrin->getResponseFunction()->enableSynchRadELoss(true);
            ↪  // Synchrotron correction ON
73          theKatrin->getResponseFunction()->setRelApprox(false); // Use
            ↪  exact relativistic factor
74          theKatrin->buildResponseTable();
75          theSourceTr->setFinalStatesEnabled(true); // FSD ON
76          theSourceTr->enableRadiativeCorrection(false); // Radiative
            ↪  correction OFF
77
78          Int_t NumPixelsEnabled = theData->getNumberPixelsEnabled();
79          Double_t E0Nominal = theKatrin->getE0NominalTritium();
80          printf("Number of pixels enabled: %d\n", NumPixelsEnabled);
81
82          Double_t qU0ffset = E0Nominal;
```

```
83          Int_t numberOfRuns=0;
84          Int_t numberOfSubRunsInDataFile=0;
85          Int_t indx=0;
86
87
88          /*
89           * Add runs to betaData:
90           */
91          while (runList[indx]>=0){
92                  sprintf(runFile,
                    ↪  "dataFiles/KNM2_Tr/RunSummaries/run_%07d.ktf",
                    ↪  runList[indx]);
93                  printf("Adding run %d to chain...\n", runList[indx]);
94                  numberOfSubRunsInDataFile =
                    ↪  theData->addRunData(runFile);
95                  printf("Number of Runs = %d,  Number of SubRuns =
                    ↪  %d\n", theData->getNumberOfRuns(),
                    ↪  theData->getNumberOfSubruns());
96                  if(numberOfSubRunsInDataFile==0){
97                          char* runFileName =
                            ↪  theData->getRunFileName(indx);
98                          printf("*** ERROR:  No subruns found, run file
                            ↪  = %s\n", runFileName);
99                  }
100                 indx++;
101         }
102
103         // Set fit range to "-40eV range", which should include 28
            ↪  subruns.
104         // Has to be here, after addRunData or it gets ignored.
105         Double_t qULowerCut = E0Nominal - 41;
106         Double_t qUUpperCut = E0Nominal + 136.;
107         theData->setqULowCut(-1, qULowerCut);
108         theData->setqUHiCut(-1, qUUpperCut);
109
110
111         /*
112          * Set fit mode:
113          */
114         Bool_t valid = theFit->setFit(fitMethod::Level_2,
            ↪  fitSources::Tritium, fitParameters::TritiumPars,
            ↪  pixelGrouping::Summed);
```

```
115         if (!valid){ printf("Aborted\n");}
116 
117         Int_t numSubruns = theData->getNumberOfSubruns();
118         theData->print(0); // Check that data input was successful.
119 
120 
121         /*
122          * Fix/free fit parameters before the fit begins:
123          */
124         theFit->FixGlobalParameter("m_nu2"); // Part of data blinding
            ↪  scheme, in addition to using blinded FSDs!
125         theFit->FixGlobalParameter("ColAdj");
126         theFit->setGlobalParameter("E0Line", E0Nominal);
127         theFit->setGlobalParameter("BSlopeOffset", E0Nominal);
128         theFit->setGlobalParameter("SigmaTritium", 0.146);
129         theFit->FixGlobalParameter("SigmaTritium");
130         theFit->FixGlobalParameter("BSlope");
131 
132         theFit->setUseCMKatErrors(true);
133 
134         Int_t NParams = theFit->getNumberOfGlobalParameters();
135 
136 
137         /*
138          * Begin the fit:
139          */
140         FunctionMinimum minReturn = theFit->minimize();
141         cout << minReturn << endl;
142         theFit->printSetup();
143         theFit->printResults();
144 
145 
146         /*
147          * Store fit results to file (FitSummary):
148          */
149         auto theFitResults= new FitContainer();
150         theFitResults->setSimulator(theKatrin);  // This is needed if
            ↪  FitContainer used to plot fit result function.
151         theFitResults->loadFitResults(theFit);  // Store latest fit
            ↪  in a FitContainer.
152         theFitResults->Print(); // Check the fit results being
            ↪  written to file.
```

```
153         printf("\n");
154 
155         ofstream outputFile;
156         outputFile.open(fitSummaryFile);
157         theFitResults->writeResults(outputFile, 0, theData,
            ↪  theControlParams, theRunParams);
158 
159         Double_t RWbias;
160         theRunParams->getFloat("RearWallPotential/0", RWbias);
161         outputFile << "RWpotential :  " << RWbias << "   ; Taken from
            ↪  first subrun" << endl;
162         outputFile.close();
163 
164         printf("Results written to FitSummary file.\n");
165 
166         timeKeeper.Stop();
167         timeKeeper.Print();
168 
169         return;
170 }
```

### A.2.2 Sample ControlParams file

```
1  ;
2  ; Sample ControlParams file
3  ; As of 2021-05-17
4  ; Blinded KNM2 FSDs
5  ;
6 
7  ;
8  ; FSD file paths:
9  ;
10 FSDfilename_T2 = FSD_KNM2_T2.txt
11 FSDfilename_DT = FSD_KNM2_DT.txt
12 FSDfilename_HT = FSD_KNM2_HT.txt
13 FSD_E_merge.Tr = 0.10  ; use 0.100 to match KaFit
14 
15 ;
16 ; For correction terms:
17 ;
18 cntrl.ExtendToUnphysical = 1    ; =1 to extend to negative m^2
```

```
cntrl.NumberWGTSsegments = 1 ; For synch radiation loss treatment

;
; Response function controls:
;
cntrl.NumberScatters = 7  ; Number of inelastic scatterings folded into response function. Set to 0 for transmission function (Krypton mode)
eloss.model = knm2-t2 ; Options: aseev, abdurashitov, sts3a-official, sts3a-test-kimrudd, sts3a-test-volker, knm1-t2, knm2-t2
ExcessEnergyMax = 100 ; Speedup for response function generation if not doing deep scans!
FixedGaussianSigma = 0 ; Gregg tested with 0.050, but for most analyses using 0 is ok
FixedFlatWidth = 0 ; Gregg tested with 0.100, but for most analyses using 0 is ok
fit.SubrunColumnDensityAdjustment = 0 ; =1 to use subrun column densities. =0 to use run average.

;
; Monte Carlo controls:
;
MC.totalTime =  12.86;
MC.totalTimeUnits = timeInDays ; Options: timeInHours, timeInDays, or timeInMonths (==30 days), or timeInYears (==365 days)
MC.enableStatFluct = 0   ; To turn on/off statistical fluctuations in Monte Carlo data

;
; Nominal electron energies:
; Electron energy used for nominal endpoint in calculating qUDiff = qU - ENominal:
; Used in the cmKatrin, fits, response function, e-loss, tritium source, and all data classes.
;
E0Nominal.Tr = 18574.0 ; For Tritium, 18573.7eV
E0Nominal.Kr = 30472.0 ; For L3-32 = 30472.0eV. For K-32 = 17824.0eV
E0Nominal.Table =  18574.0 ; Change depending on mode
E0BkgndSlope = 18574.0 ; Energy-dep background term goes to zero at this qU. \Anchor"

;
```

```
; Gas density profile info:
; Use this when running in Kr+Tr mode!
;
UseDualGasProfiles = 0 ; Simultaneous Kr, Tr
UseProbScatterLookup = 0 ; Use the generated lookup tables instead of calc from scratch. Faster with tables.
GasDensityFile = datafiles/KNM3_KrAndTr/ColumnDensityProfiles.txt

;
; Pull term controls:
;
fit.ColumnDensityMeasurementError= 0.002  ;estimate fractional Column Density Measurement Accuracy. Number from KNM2 column density analysis: 0.2% runwise


;
; Fit parameter initialization:
; [ initial value, est. accuracy, lower bound, upper bound]
; Note: estimated accuracy / 10 determines step size of chi square!
;
fit.param.DeltaE = [0.0, 0.5, -3., 3.]
fit.param.m_nu2 =  [0.1, 2.0, -20., 20.]
fit.param.AScale = [0., 0.01]
fit.param.SigmaTritium = [0., 0.01]
fit.param.Bkgnd = [0., 0.01]
fit.param.E0Line = [0., 0.001]
fit.param.WidthLine = [1.0, 0.01, 0.1, 20.]
fit.param.RateLine = [1.0, 0.1]
fit.param.SigmaKrypton = [0.0523, 0.002, 0.0, 2.0]
fit.param.ColAdj = [0.0, 0.01, -0.05, 0.05]
fit.param.BSlope = [0.0, 0.001, -0.3, 0.3]
fit.param.Delta10 = [0.0, 0.01, -2., 2.]
;
; *** FPD list of enabled pixels ***
;  Comment out entire row to exclude a ring
;  use "-" sign in from of pixel number to exclude an individual pixel

;
; KNM2 Golden Pixel list:
;
FPD.ring/0 =   [ 0, 1, 2, 3 ]
```

```
88 FPD.ring/1 =   [ 4, 5, 6, 7, 8, 9, 10, 11, 12, 13, 14, 15 ]
89 FPD.ring/2 =   [ 16, 17, 18, 19, 20, 21, 22, 23, 24, 25, 26, 27 ]
90 FPD.ring/3 =   [ 28, 29, 30, 31, 32, 33, 34, 35, 36, 37, 38, 39 ]
91 FPD.ring/4 =   [ 40, 41, 42, 43, 44, 45, 46, 47, 48, 49, 50, 51 ]
92 FPD.ring/5 =   [ 52, 53, 54, 55, 56, 57, 58, 59, 60, 61, 62, 63 ]
93 FPD.ring/6 =   [ 64, 65, 66, 67, 68, 69, 70, 71, 72, 73, 74, 75 ]
94 FPD.ring/7 =   [ 76, 77, 78, 79, 80, 81, 82, 83, 84, 85, 86, 87 ]
95 FPD.ring/8 =   [ 88, 89, 90, 91, 92, 93, 94, 95, 96, -97, -98, 99 ]
96 FPD.ring/9 =   [ -100, 101, 102, 103, 104, 105, 106, 107, 108, 109,
   ↪  -110, -111 ]
97 FPD.ring/10 = [ -112, -113, 114, 115, 116, 117, 118, 119, 120, -121,
   ↪  -122, -123 ]
98 FPD.ring/11 = [ -124, -125, -126, -127, -128, -129, -130, 131, 132,
   ↪  133, -134, -135 ]
99 ;FPD.ring/12 = [ 136, 137, 138, 139, 140, 141, 142, 143, 144, 145,
   ↪  146, 147 ]
```